Simulating the Chemical Enrichment of the Intra-Group Medium

by

Aviv Padawer-Blatt
B.Sc., University of Waterloo, 2022

A Thesis Submitted in Partial Fulfillment of the
Requirements for the Degree of

MASTER OF SCIENCE

in the Department of Physics and Astronomy

We acknowledge and respect the Lək̓ʷəŋən (Songhees and Xʷsepsəm/Esquimalt) Peoples on whose territory the university stands, and the Lək̓ʷəŋən and W̱SÁNEĆ Peoples whose historical relationships with the land continue to this day.

Simulating the Chemical Enrichment of the Intra-Group Medium

by

Aviv Padawer-Blatt
B.Sc., University of Waterloo, 2022

Supervisory Committee

Dr. Arif Babul, Supervisor
(Department of Physics and Astronomy)

Dr. Jon Willis, Departmental Member
(Department of Physics and Astronomy)

Abstract

The channels by which heavy elements are produced through nucleosynthesis in stars, ejected from stars into the surrounding interstellar medium (ISM) of host galaxies, and dispersed (both spatially and in thermodynamic phase, i.e. density, temperature, and velocity) into their gaseous atmospheres are fundamental to the formation and evolution of galaxies, as well as gravitationally bound collections of galaxies - groups and clusters. These massive systems host hot diffuse gas throughout their volume, known as the intragroup medium (IGrM), which can become substantially enriched with metals, informing us about stellar populations, chemical production and enrichment mechanisms, large-scale gas flows, and gas- and metal-mixing. This thesis investigates the chemical enrichment of the IGrM using cosmological simulations. Specifically, I compare results from the SIMBA and SIMBA-C simulations, focusing on the distribution of metal abundances in galaxy groups. SIMBA-C incorporates an updated and more realistic chemical enrichment and stellar feedback model (`Chem5`), leading to notable differences in IGrM abundances compared to SIMBA. I examine projected emission-weighted abundance profiles, finding that SIMBA-C generally produces lower-amplitude abundance profiles with flatter cores, aligning better with observational data across a range of X-ray relevant metals. However, the agreement between simulations and observations for both SIMBA-C and SIMBA worsens with decreasing group mass through an increase in the amplitudes of the simulated abundance profiles relative to those of the observed profiles; this agreement is also somewhat sensitive to the specific element under consideration. Moreover, I investigate the 3D mass-weighted abundance profiles to deepen my understanding of the physical mechanisms driving the changes found between SIMBA and SIMBA-C and between low and high mass groups. The results indicate that SIMBA-C enriches the IGrM to a lesser degree than SIMBA across all studied metals and mass scales, and produces less total metal mass in the hot diffuse phase. I ascribe these features to reduced metal yields in `Chem5` compared to SIMBA and the replacement of SIMBA's instantaneous enrichment model with `Chem5` in SIMBA-C. On the other hand, SIMBA-C actually contains more total hot gas mass in low mass groups than does SIMBA, which may be due to slight changes in the stellar and AGN feedback models. My study reveals that accurate sub-grid models for chemical enrichment, as well as metal dispersal and mixing processes, are required to realistically reproduce observed group environments in cosmological simulations.

Table of Contents

List of Tables

List of Figures

Acknowledgements

I would like to thank:

Arif Babul, for supervising and educating me, providing input and feedback on this research, spending time iterating on applications and paper drafts with me, and financial support.

Jon Willis, for being a member of my supervisory committee, and providing a neutral but informed perspective.

Renier Hough, for providing guidance and technical support with SIMBA-C, and very helpful discussion.

Zhiwei Shao, for providing the script upon which I based my pipeline, and much technical support.

Romeel Davé, for stimulating discussion about my results, and developing the SIMBA model in the first place.

Weiguang Cui, for being *extremely* patient the many times I asked him to run my memory-intensive script, as well as providing ideas for direction in my research.

Franois Mernier, for providing the main set of observations from the CHEERS project, taking the time to explain the details of it, and balancing the theoretical perspective with observationally-driven arguments.

Douglas Rennehan and Vida Saeedzadeh, for helping me get set up with the simulations and learn how to manipulate them, and the ongoing support.

Ruxin Barré, for the tea sessions, allowing me to bounce ideas around, and being physically present and supportive throughout this process.

The Digital Research Alliance of Canada, the Niagara Compute Cluster, and their support staff, for providing the computational resources necessary to undertake such a study, a continually available Jupyter Hub, and technical support every time I ran into an error or ran out of memory.

Dedication

I dedicate this thesis to:

The children of Palestine, Lebanon, Syria, Yemen, the Congo, and all nations where oppression, colonization and genocide have reared their heads; we have have failed you.

The indigenous stewards of this stolen land - Turtle Island - and all lands, who took care of the earth we now live on and destroy day by day, and who have endured the horrors of inter-generational trauma caused by our ancestors and upheld by current institutions.

My Ema and Aba, for their unending efforts to understand and support me, and their openness, honesty, and care. You and your love are irreplaceable; I would not be here without you.

My sister Noa, my polar opposite but also the one who I believe understands me the best. Your moments of pure love and care for me have never stopped resonating; I will always be there for you when you need me.

The rest of my family, for their support, love, and inspirational personalities.

Maia and Jayde (hopefully that is still your name by the time this is done); I am forever grateful for your loyalty and friendship through everything. You will always be the ones I go to when things feel hopeless, and who I want to be with when life is looking up. I intend to keep you by my side forever (figuratively speaking).

My partner, my other half; I'm not sure what I'd have done if we hadn't found each other. Your presence has kept me sane through grad school, and I have learned so much about life from you. I love you deeply, and am excited for a future with you.

My friends, without whose consistent companionship, support, conversations, and advice I would not be the person I am; I love you all so much.

My music, which has been there for me in the darkest of times, and in which I can always trust.

Myself, for learning to give up, hold onto hope, and forgive myself; I'm proud of you for making it this far.

Chapter 1

Introduction

1.1 Overview

The spatial distributions of element abundances in the intragroup medium (IGrM) are critical to our understanding of the formation and evolution of galaxy groups and clusters. These distributions may be indicative of such characteristics as the spatial and temporal distribution of enrichment sources across cosmic time, the metal yields of these different sources, the initial mass function (IMF) of stars, and the efficiency of feedback and gas- and metal-mixing in the IGrM. Our understanding of the details of these processes in the real universe is typically relatively limited, but much progress has been made since the advent of X-ray astronomy, especially in recent years (see Werner et al., 2008; Böhringer & Werner, 2010; Mernier et al., 2018a; Werner & Mernier, 2020; Gastaldello et al., 2021; Mernier & Biffi, 2022, and references therein). Likewise, the ability to numerically simulate chemical enrichment and other phenomena at the group and cluster scale - taking into account many components and physical processes, and a large range of scales - has improved greatly in the past few decades (see Tornatore et al., 2007; Borgani et al., 2008; Wiersma et al., 2009b; Somerville & Davé, 2015; Biffi et al., 2018a; Vogelsberger et al., 2020; Oppenheimer et al., 2021; Gastaldello et al., 2021; Mernier & Biffi, 2022; Crain & van de Voort, 2023, and references therein). This progress has refined - and continues to refine - our identification and understanding of the key drivers of the evolution of the hot diffuse gas in groups and clusters, and the physical processes that mold its properties.

Many modern simulations of galaxy formation and evolution are evolved in a cosmological context with galaxy interactions and mergers and gaseous inflows and outflows, as well as under the influence of large scale environments. Collectively, these are called "cosmological simulations", which are critical to disentangle the complex sets of physical mechanisms underlying observed features, to constrain models and their parameters, and to predict and

guide observations. These massive simulations involve "sub-grid" models[1] for feedback and chemical enrichment, permitting the study of metal distributions in the simulated IGrM. In the context of chemical enrichment, cosmological simulations have contributed substantial knowledge: the potential need for active galactic nucleus (AGN) feedback to generate realistic intracluster medium (ICM) radial abundance profiles (e.g. Biffi et al., 2017); the effect of different sub-grid feedback models on enrichment (e.g. Short et al., 2013; Bradley et al., 2022; Tuominen et al., 2023; Khrykin et al., 2024; Padawer-Blatt et al., 2025); the importance of metal cooling to fuel galaxies with gas (e.g. Dubois et al., 2011; Saeedzadeh et al., 2023); constraints on the epoch of the bulk of enrichment and the relative contributions of different metal sources to enrichment (e.g. Oppenheimer & Davé, 2008; Liang et al., 2016); and biases present in both observations and simulations.

While AGN feedback, especially at early times in the universe ($z \sim 2-3$), has been shown to possibly play a significant role in obtaining realistic metal distributions in present-day groups and clusters from simulations (e.g. Sijacki & Springel, 2006a; Fabjan et al., 2010; Biffi et al., 2017, 2018b), the models of chemical enrichment (e.g. metal sources, yields, stellar IMFs) and galactic-scale metal dispersal (i.e. stellar feedback, winds and outflows, heating of gas), as well as the mechanisms for mixing (e.g. turbulent diffusion), are just as important. In particular, simulations suggest that stellar feedback may be partly responsible for the widespread distribution of metals in galaxies and protogroup/protocluster environments (Mernier & Biffi, 2022). This enables the cooling of gas and subsequent feeding of AGN, the feedback from which further mixes the metals into the hot diffuse gas and produces uniformly enriched IGrM and ICM environments, as observed in local clusters (e.g. Ghirardini et al., 2019). Additionally, it is known that various components of chemical enrichment models, such as the IMF and yields, can be uncertain, up to factors of ~ 2 in the latter case. In these ways, the specific implementations of chemical enrichment models have the potential to substantially alter the simulated properties of the hot gas in groups and clusters. It is therefore of appreciable import to develop and utilize realistic and physically motivated chemical enrichment models, and to characterize their effects on the enrichment of the IGrM.

Currently, progress in two primary areas of observational research is required to better pin down enrichment in the real universe: improved observations of the X-ray emitting gas in groups and clusters to minimize uncertainties and biases through increased spectral

[1]Sub-grid - or sub-resolution - models are phenomenological or empirically-driven models that aim to describe real physical processes in the universe without the need to simulate the fundamental components and interactions (e.g. real particles, electromagnetism, etc...), either due to the driving forces existing below the mass, spatial, or temporal limits of the simulation, limited computational resources, or a lack of physical understanding.

and spatial resolution, as well as greater sensitivity; and improved spectral modelling to account for all significant astrophysical processes and conditions, allowing the procurement of accurate abundance measurements. Simultaneously, simulations must advance in their implementation of physical models to produce realistic galactic evolution and astrophysical observables, allowing simulations to guide and predict observations, and elucidate the physical processes driving observed features. In particular, research into the physical mechanisms most significantly impacting chemical enrichment and evolution in galaxy groups is required, including how the physics shaping these processes operate at large scales, methods for accurately modelling these phenomena, and the effects of different models.

Overall, there are many open questions in the field of group- and cluster-scale enrichment: Are groups enriched similarly to clusters? When does the bulk of enrichment occur? What are the dominant enrichment pathways? How are metals transferred from the colder denser interstellar medium (ISM) localized in galaxies to the hot diffuse phase extending throughout groups and clusters? Before it is possible to use cosmological simulations to interpret observations in terms of their underlying physical mechanisms, or predict future observations, it is necessary to understand how accurate and robust the simulations are with respect to to existing observations. For example, can simulations reproduce important features of observed IGrM and ICM abundance profiles, like overall measured metal abundances and distributions, flat outskirts in the ICM, and the abundances' trends with radius and halo mass? And what changes to sub-grid models are required to improve these predictions?

I broadly address all of these questions, but focus on the last two, as well as understanding the physical processes responsible for setting the spatial distributions of metal abundances in the IGrM. My work is grounded in a theoretical and computational approach, utilizing cosmological hydrodynamic simulations to study these phenomena. I analyze $z = 0$ radial abundance profiles in galaxy groups and clusters from a cosmological simulation incorporating a new chemical enrichment and stellar feedback model. This latter model, known as `Chem5` (Kobayashi et al., 2020a,b), tracks many elements not previously considered in cosmological simulations, treats stellar feedback and chemical enrichment self-consistently, and evolves star particles over time. These characteristics enhance the model's realism, making it more physically motivated than those employed in past cosmological simulations. It has been implemented in the hydrodynamics and gravity solver code GIZMO by my colleague Dr. Renier Hough, using the SIMBA galaxy formation model (Davé et al., 2019), augmented to produce the new cosmological simulation SIMBA-C (Hough et al., 2023, 2024; Padawer-Blatt et al., 2025). This thesis represents a step forward in our understanding of cosmic chemical enrichment and the group-scale effects of increasingly realistic chemical enrichment models

simulated in a cosmological context.

1.2 X-ray Astronomy and the History of Galaxy Groups

1.2.1 First we saw clusters...

The first reference to an observed clustering of galaxies (or "galaxy cluster") in literature was likely that of the Virgo Cluster, some of the brightest galaxies of which were optically identified in the late 1770s and early 1780s by the astronomer Charles Messier (Messier, 1781). Messier catalogued it as a "nebula without stars" due to the appearance of the many fuzzy objects in the same region of the sky. The nature of galaxy clusters became clearer in the early 20th century, when Heber Curtis argued that the Andromeda galaxy resides outside of our own Milky Way galaxy[2]. His reasons included: Curtis' finding that the novae in Andromeda are, on average, 10 magnitudes fainter than those in the Milky Way (Curtis, 1988); there exist dark lanes in Andromeda that resemble the dust lanes in the Milky Way; and many nebular spectra, including of Andromeda, taken by Vesto Slipher showed high Doppler shifts, indicating stellar velocities exceeding those of the Milky Way and demonstrating that many of these nebulae must be moving away from us (Slipher, 1913, 1915). Subsequently, Ernst Öpik calculated a distance to Andromeda that placed it outside the Milky Way (Opik, 1922). Shortly after, Edwin Hubble used the then-new 100-inch Mt. Wilson telescope to resolve the outer parts of spiral nebulae as collections of individual stars. By identifying special types of stars with periodic changes in brightness (called Cepheid variables), he estimated distances that ended up being far too large for these structures to reside in the Milky Way (Hubble, 1926, 1929), collectively demonstrating that these "nebulae" were individual galaxies beyond the Milky Way.

Max Wolf had already been performing extensive photographic work as early as 1901, leading to detailed descriptions of the Coma and Perseus clusters (Wolf, 1901, 1902, 1906). The first systematic study of galaxy clusters was conducted by George Abell in and before 1958. He published the Abell Catalogue of Rich Clusters of Galaxies, listing 2,712 galaxy clusters identified in the northern sky (Abell, 1958). The Local Group, which includes the Milky Way, Andromeda, and around 50 or more other smaller galaxies, was recognized as a gravitationally bound system in the early 20th century, with Hubble and his contemporaries noting its structure (e.g. Hubble, 1936).

[2]On April 26, 1920, Harlow Shapley and Heber Curtis took part in a debate - colloquially known as the Great Debate - held at the Smithsonian Museum of Natural History on the nature of so-called spiral nebulae and the size of the Universe, in which Curtis was a proponent of the "island universes" hypothesis.

In 1962, Riccardo Giacconi headed an experiment that, for the first time, launched an X-ray detector above the atmosphere, aboard an Aerobee rocket. Though it was "in space" for a mere 350 seconds, it managed to identify one X-ray source (Scorpius-1, a "compact star" later determined to be a neutron star) and what later came to be known as the X-ray background (Giacconi et al., 1962). X-ray emission was subsequently detected in 1966 around the region of the galaxy M87 at the centre of the Virgo cluster, the first known source of extragalactic X-rays (Byram et al., 1966; Bradt et al., 1967); a few years later, the same was detected in the direction of the Coma and Perseus clusters (Fritz et al., 1971; Gursky et al., 1971; Meekins et al., 1971). Cavaliere et al. (1971) suggested that all clusters of galaxies may be X-ray sources.

Using the *Uhuru* satellite, the first Earth-orbiting X-ray observatory, Giacconi and his team performed an all-sky X-ray survey, finding that this indeed was the case (Giacconi et al., 1972). Specifically, the X-ray sources were spatially extended, with sizes comparable to the extent of the clusters' galaxy distributions (Kellogg et al., 1972; Forman et al., 1972), and temporally invariant in their brightness (Elvis, 1976). This discovery marked the beginning of X-ray astronomy's role in studying galaxy clusters, and provided evidence that clusters contain a significant amount of hot diffuse gas emitting X-rays primarily via thermal bremsstrahlung[3]. The temperature of this "intracluster medium" (ICM) ranged from $\sim 5 - 15$ keV.

In the late 1970's, the first evidence of metals[4] existing in the hot diffuse gas was obtained through observations of the Fe-K emission line complex in nearby clusters: Perseus by the *Ariel 5* satellite (Mitchell et al., 1976), and Virgo, Perseus and Coma by OSO-8 (Serlemitsos et al., 1977).

1.2.2 . . . And then we saw groups

Clusters of galaxies are not the only mega-structures; so-called "groups" of galaxies exist. While clusters can contain many hundreds to thousands of member galaxies and numerous highly luminous galaxies, groups consist of fewer galaxies, i.e. a few to a couple hundred at most, and generally only a few luminous galaxies. Groups also have overall less bound mass than clusters. During the second half of the 1900s, redshift surveys of the local universe showed that the majority of galaxies reside in small groups, setting the stage for the importance of group environments to galaxy formation and evolution (e.g. Holmberg, 1950; Humason et al., 1956; Humason, 1956; de Vaucouleurs, 1965; Materne, 1979; Huchra & Geller, 1982; Geller & Huchra, 1983; Tully, 1987; Nolthenius & White, 1987).

[3] German for "braking radiation".

[4] In astronomy, metals are all elements heavier than helium.

Early observations suggested that to first order groups could be viewed as scaled-down clusters (Mulchaey, 2000). For example, given the relation between cluster X-ray luminosity (L_X) and temperature (T), groups were often found to lie in the $L_X - T$ region that would be predicted by this same relation. But even in the 1900s, many observations indicated important differences. Clusters and groups were found to have similar velocity dispersions despite the differences in their mass, temperature, and luminosity scales. This implied that processes like galaxy merging may be more common in groups than clusters, while other processes, like ram-pressure stripping and galaxy harassment, may be less important.

For galaxy groups, X-ray observations followed later, as the fainter emission from the cooler and less dense gas in groups (in comparison to clusters) posed more of a challenge. It was not until the late 1970s and early 1980s, with more sensitive X-ray telescopes than *Uhuru*, such as *Ariel 5* and the *Einstein* Observatory, that the X-ray emission of groups was seen. In particular, *Einstein* first observed Fe L shell emission in the early 1980's (Mushotzky et al., 1981; Lea et al., 1982).

While not quite at the group scale, Schwartz et al. (1980) demonstrated that several of the objects in the 2A catalogue of 105 bright X-ray sources (Cooke et al., 1978), which came from the Leicester Sky Survey Instrument on-board *Ariel 5*, were low-mass, few-member "poor" clusters. *Einstein* observations showed that some poor clusters with bright central galaxies, i.e. the Morgan, Kayser, and White (MKW; Morgan et al., 1975) and Albert, White, and Morgan (AWM; Albert et al., 1977) clusters, were also X-ray sources with X-ray luminosities $\sim 10^{41} - 10^{43}\,\mathrm{erg\,s^{-1}}$, extended X-ray emission up to ~ 0.5 Mpc, and X-ray temperatures $\sim 1 - 5$ keV (Kriss et al., 1980, 1983; Burns et al., 1981; Price et al., 1991; dell'Antonio et al., 1994).

Finally, extended X-ray emission was detected in the galaxy groups NGC 3607 and NGC 5846 (Biermann et al., 1982; Biermann & Kronberg, 1983). This emission was viewed past the optical extent of the groups. Similar to clusters, this suggested that groups contain a hot diffuse volume-filling gas. In analogy to the ICM, it was dubbed the "intragroup medium" (IGrM).

1.2.3 Eyes in the sky - the early X-ray IGrM

With the advent of two major X-ray observatories in the 1990s, the ROentgen SATellite (ROSAT; Trümper, 1982; Aschenbach, 1991; Voges, 1992) and the Advanced Satellite for Cosmology and Astrophysics (ASCA; Tanaka et al., 1994), X-ray studies of galaxy groups progressed greatly. These two facilities had simultaneous imaging and spectroscopic capabili-

ties, as well as large fields of view (with the former having a better spatial resolution and the latter having a better spectral resolution), allowing for more detailed studies of the soft X-ray emission from dimmer and cooler groups. ROSAT pointed observations were the first to separate X-ray emission sources within galaxies (e.g. massive compact binary stars that emit X-rays, very hot interstellar gas, and accretion that heats material around massive black holes residing in the centres of galaxies) from the hot diffuse component spread throughout groups, firmly establishing the existence of the IGrM in NGC 2300 and HCG 62 (Mulchaey et al., 1993b; Ponman & Bertram, 1993). Additionally, with ROSAT, Fukazawa et al. (1998) demonstrated that the metallicities[5] of these two galaxy groups were a fair bit lower than that found for the average cluster.

Shallower data from the ROSAT All-Sky Survey (RASS) demonstrated that X-ray-selected galaxy *groups* lie on the smooth extrapolation of the *cluster* X-ray luminosity and temperature functions, consistent with groups being scaled-down clusters (Henry et al., 1995). On the other hand, Mahdavi et al. (1997, 2000) optically selected groups from RASS using the CfA redshift survey (Ramella et al., 1995a,b), and found a shallower X-ray luminosity - velocity dispersion scaling relation for groups than for clusters. The IGrM was turning out to be an interesting discovery, and possibly a medium distinct from the ICM.

Through ROSAT and ASCA X-ray spectroscopy and subsequent spectral fitting, gas temperatures of $\sim 0.3-1.8$ keV were found for dim groups (Ponman et al., 1996a,b; Mulchaey et al., 1996; Mulchaey & Zabludoff, 1998; Helsdon & Ponman, 2000a,b). Further, a limited number of spatially resolved radial profiles of these gas temperatures suggested that, similar to the ICM, the IGrM was approximately isothermal (characterized by a single temperature), as long as an often-observed central temperature drop in the inner ~ 50 kpc was excluded (Ponman & Bertram, 1993; David et al., 1994; Doe et al., 1995; Davis et al., 1985; Trinchieri et al., 1997; Mulchaey & Zabludoff, 1998; Helsdon & Ponman, 2000a,b; Buote, 2000a). This central drop was thought to be consistent with the effects of a "cooling flow"[6] (Fabian, 1994).

[5]Metallicity is the combined mass fraction of all elements (in a substance) more massive than helium (known as metals in astronomy), defined by $X + Y + Z = 1$, where X is the mass fraction of Hydrogen, Y is that of helium, and Z is that of all other elements. Primordial gas is by definition purely H and He, and therefore has $Z = 0$.

[6]The gas densities of the IGrM and ICM increase towards the centres of groups and clusters, as evidenced by observations of centrally peaked X-ray emission. Since the cooling rate is proportional to the square of the density, gas in the core should cool substantially faster than gas at larger radii. As this gas cools, it loses thermal pressure support, succumbing to the effects of gravity and "falling" inwards. The pressure of the outer "shells" of the IGrM or ICM should cause more gas to flow inwards (the quintessential *cooling flow*) and replace the gas that cooled out. In modern astronomy, central cooling flows are not seen in groups or clusters as often as expected, leading to the so-called "cooling flow problem". The most commonly invoked resolution to this issue is the energy output by active black holes at the centres of groups/clusters keeping the gas hot.

Unlike the ICM, which was found to be dominated by bremsstrahlung emission, the emission of groups showed significant contributions from bound-free continuum and line emission from highly ionized trace elements. Spectral fitting allowed determination of the overall metallicity of the gas, as well as individual abundances of elements, both in clusters and groups.

The element iron (Fe) is the most prominent feature in spectra of both groups and clusters (see Figure 1.1[7]), and its abundance is often employed as a proxy for the total gas-phase metallicity in the IGrM and ICM (Renzini, 1997; Urban et al., 2017; Vogelsberger et al., 2018; Pearce et al., 2021; Gastaldello et al., 2021; Mernier & Biffi, 2022). While the Fe K-α line and Fe K complex are generally clear in spectra of clusters, the Fe L complex is more pronounced in spectra of groups. Not only is the production of the latter driven by more complex physics, but the lower temperatures of the IGrM promote a greater number and rate of electron transitions between energy shells in elements, resulting in more emission lines that blend together to a greater degree than in the ICM, as seen in Figure 1.1. As such, the abundances and metallicities of the IGrM are more difficult to obtain than those of the ICM. This is an issue that still plagues observations to this day.

Early observations with ROSAT and ASCA found diversity in the metallicities of groups, ranging from $\sim 10 - 60\%$ Solar[8] (Mulchaey et al., 1993a,b; Ponman & Bertram, 1993; David et al., 1994; Davis et al., 1985, 1995; Saracco & Ciliegi, 1995; Davis et al., 1996; Ponman et al., 1996a; Mulchaey et al., 1996; Fukazawa et al., 1996, 1998; Mulchaey & Zabludoff, 1998; Davis et al., 1999; Finoguenov et al., 1999; Hwang et al., 1999; Helsdon & Ponman, 2000a,b) compared to the more consistent $\sim 20 - 30\%$ for clusters (Fukazawa et al., 1998). At the time, the general expectation was that groups would be found to have on average higher metallicities than clusters because groups tended to have higher stellar to gas mass ratios. The range of measured metallicities in groups indicated that other physical processes may be at play. While the assumption of isothermality worked well for clusters, studies showed that multi-temperature and/or multiphase spectral models may be more appropriate for groups (Trinchieri et al., 1997; Buote, 1999, 2000b; Mulchaey & Zabludoff, 1998). This permitted improved fits to observed ASCA X-ray spectra of groups, which gave higher derived gas metallicities (Buote, 2000b). This came to be known as the "Fe-bias". Alternatively, studies

[7]Note that all figures in this section have been reprinted from a selection of review articles, all published under the gold standard open access CC-BY 4.0 (Creative Commons Attribution v4.0 International) Licence, which permits readers to freely copy and redistribute the material in any medium or format, provided the original author is credited (as has been done here).

[8]"Solar" indicates that the metallicity or abundance is measured in units of our sun's metallicity or abundance.

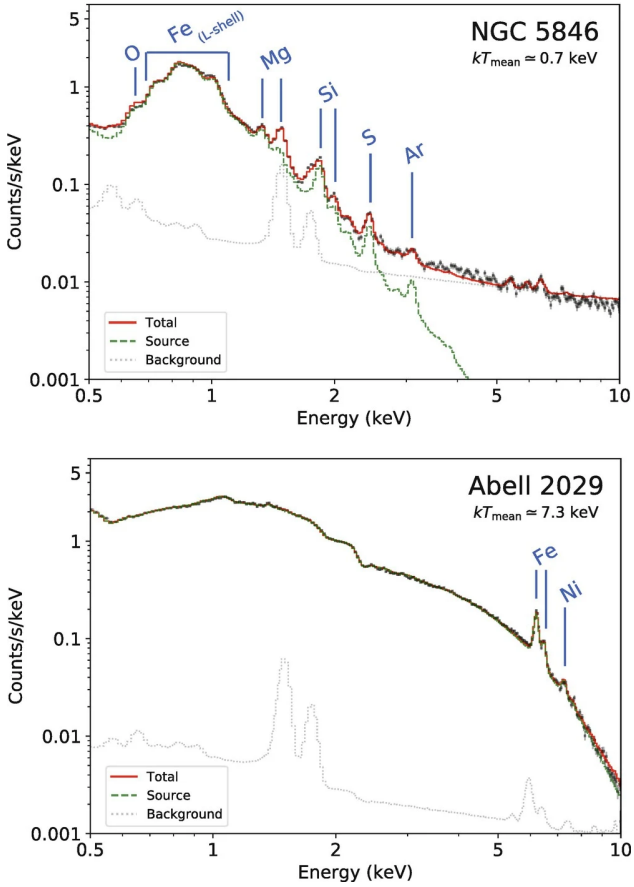

Figure 1.1: Reproduced from Werner & Mernier (2020). Observed XMM-*Newton*/EPIC MOS X-ray spectra of the giant elliptical galaxy/poor galaxy group NGC 5846 (*top*) and the galaxy cluster Abell 2029 (*bottom*), both extracted in the central regions within a halocentric radius of $0.1R_{500}$. The visible metal emission lines, unless otherwise labeled, are a result of K-shell transitions.

suggested that the abundances of other metals in the IGrM, specifically the α elements (i.e. O, Ne, Mg, Si, S), may be degenerate to some degree with the abundance of Fe. As such, it was possible that the total metallicity could not be uniquely constrained unless the abundances of these other elements were linked to that of Fe in the spectral models. Implementing this also resulted in increased IGrM metallicities derived from observations (Matsushita et al., 2000).

1.2.4 The modern X-ray IGrM

The following era of X-ray astronomy beginning in the early 2000s primarily involved the telescopes *Chandra* (Weisskopf et al., 2000), XMM-*Newton* (Kahn, 1999; Jansen et al., 2001), and *Suzaku* (Mitsuda et al., 2007; Kelley et al., 2007), all three of which made use of CCD

(charge-coupled device) detectors (and still do in the case of *Chandra* and XMM-*Newton*). The advancing technologies of these observatories allowed improved spatial and spectral resolutions, as well as enhanced sensitivities, compared to their older counterparts. In particular, this permitted the study of the spatial distribution of metals in the IGrM (out to larger halocentric distances) and the investigation of metal abundances for elements other than Fe.

While significantly more data has been collected by *Chandra* and XMM-*Newton* owing to their earlier launches and much longer-than-planned mission durations (continuing to this day), allowing statistically significant studies of galaxy groups, *Suzaku* provided a lower instrumental background and superior soft X-ray response. This opened up X-ray observations to the low surface-brightness outskirts of galaxy groups and accurate metal abundances in those regions. A combination of results from all three telescopes has given a more holistic view on the enrichment of the IGrM.

Studies on the IGrM metal content and distribution using these observatories (e.g. Buote, 2002; Buote et al., 2003; O'Sullivan et al., 2003a,b; Buote et al., 2004; O'Sullivan et al., 2005b, 2007; Rasmussen & Ponman, 2007; Sivanandam et al., 2009; Rasmussen & Ponman, 2009; Johnson et al., 2009, 2011; Humphrey et al., 2012; Sun, 2012; Rafferty et al., 2013; Sasaki et al., 2014; Su et al., 2015; Panagoulia et al., 2015; Thölken et al., 2016; Su et al., 2017; Mernier et al., 2017; Hu et al., 2019; Lovisari & Reiprich, 2019; Sarkar et al., 2022) have largely produced consistent findings that appear to broadly match some ICM observations (e.g. Grandi & Molendi, 2001; Leccardi & Molendi, 2008; Urban et al., 2011; Werner et al., 2013; Simionescu et al., 2017; Urban et al., 2017; Ghizzardi et al., 2021). For more information, see Mernier et al. (2018a) and Gastaldello et al. (2021), and references therein. Some of these results can be seen summarized in Figure 1.2 and, most importantly, they include the following:

- A metallicity increase towards the group cores, with a peaked central metallicity, and sub-solar to slightly super-solar values.

- Increased central metallicity on average in groups with low levels of energetic feedback and those classified as "cool-cores" (see Sec. 1.5 & 1.6 for a definition and brief discussion of cool-core and non-cool-core systems).

- Approximately similar levels of total enrichment between groups and clusters, with the IGrM at least as metal-rich as the ICM, although this has been shown to be somewhat sensitive to the spectral modelling code employed.

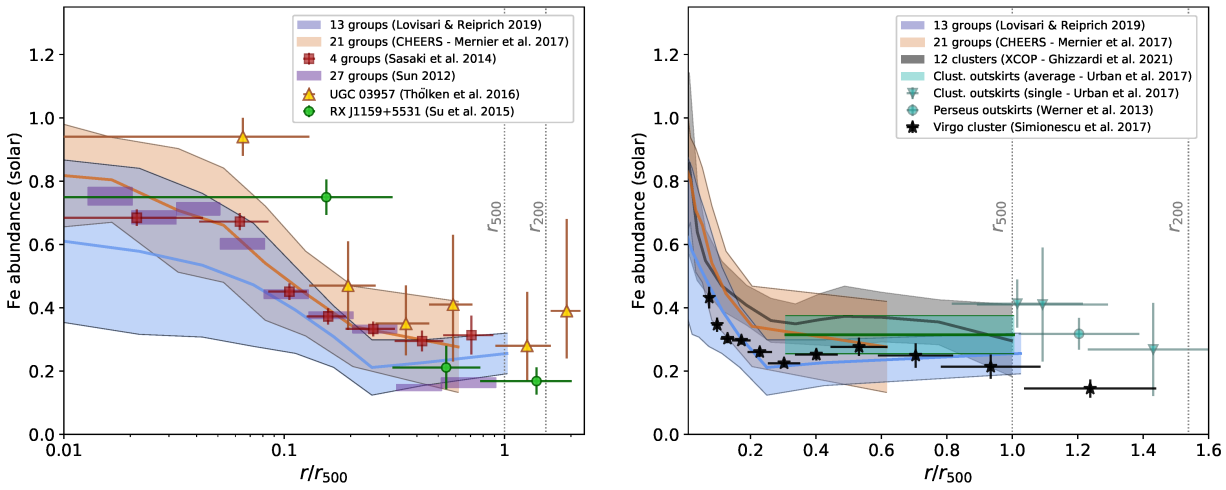

Figure 1.2: Reproduced from Gastaldello et al. (2021). Radial Fe abundance profiles derived from X-ray observations of various galaxy groups (and clusters) from the literature. (**Left**) Group-scale abundance profiles. (**Right**) Group-scale compared to cluster-scale abundance profiles. All measurements have been re-scaled into radial units of R_{500} (following the values given in the corresponding papers and/or the conversion proposed by Reiprich et al. (2013)) and into Solar units of Asplund et al. (2009).

- Flat *or decreasing* metallicity profiles in the outskirts of groups, the latter trend being different than what is observed in clusters; this may again be dependent on the spectral fitting code.
- Outskirt metallicities around *or slightly below* $0.3Z_{\odot}$ (the "universal" value), where the latter result is again not generally found in clusters.

These findings suggest that, with respect to chemical enrichment, groups are in some ways scaled down versions of clusters; however, overall, the IGrM has distinct features from the ICM. In particular, those decreasing and/or lower outskirt metallicities in groups hint at different formation histories and evolutionary pathways for groups compared to clusters (as well as for their member galaxies) and physical processes having varying impacts in different environments. This idea remains an open question today.

The total metallicity (or for observational purposes, the Fe abundance) of the IGrM is a key property, but abundances of other individual elements impart even more detailed understanding. This is because different metals originate from different astrophysical sources (primarily nucleosynthesis in stellar cores of different types of stars and the subsequent supernovae (SNe) releasing them, namely type Ia and core-collapse SNe), in different places, at different times (see Sec. 1.7 for a more detailed discussion). Modern studies largely find

similar radial distributions of multiple metals (including Fe and the α elements O, Mg, Si, S, Ar, and Ca) in the IGrM, that are also relatively consistent from the group to cluster scale (Gastaldello & Molendi, 2002; Buote et al., 2003; Kim & Fabbiano, 2004; Xue et al., 2004; Werner et al., 2006b; de Plaa et al., 2006; Kazuyo et al., 2008; Komiyama et al., 2009; Simionescu et al., 2009; Sato et al., 2009a,b, 2010; Sasaki et al., 2014; Mernier et al., 2017; Sarkar et al., 2022).

In-depth studies of the cores of systems produced similar results (Grandi & Molendi, 2009; Mernier et al., 2016, 2018b). In the mid-2010s, the *Hitomi* X-ray satellite (Takahashi et al., 2014, 2016) was launched. Unlike *Chandra*, XMM-*Newton*, and *Suzaku*, it employed a micro-calorimeter for extremely high energy resolution X-ray spectroscopy, allowing it to obtain highly accurate metal abundances. Unfortunately, it only operated for a little over a month due to multiple incidents leading to the destruction of structurally weak components. However, *Hitomi* was able to confirm that the ratios of metal abundances in the core of the Perseus cluster are consistent with Solar values at high precision (Aharonian et al., 2017; Simionescu et al., 2019).

All of these modern measurements favour an approximately uniform chemical composition across the majority of the volume of groups and clusters. This has led to our current understanding of a scenario in which enrichment of the IGrM from different metal sources occurred similarly across space and time.

1.3 The Formation and Growth of Galaxy Groups and the IGrM

To build up a consistent and holistic picture of galaxy group and IGrM enrichment, it is necessary to have knowledge of their formation and evolution. The Λ Cold Dark Matter[9] (ΛCDM) model of cosmology (Efstathiou et al., 1990; Ostriker & Steinhardt, 1995) fosters the growth of matter in our universe into galaxies and the halos in which they reside, as well as these groups and clusters of galaxies, which are some of the largest known structures. As a basic definition, galaxy groups are groups of individual galaxies, gas, stars, and dark matter, all bound together by their mutual gravity (Einasto et al., 2024).

[9]"Cold" refers to the fact that this matter has velocities much less than the speed of light, resulting in a vanishing equation of state; "dark" refers to the idea that dark matter interacts with itself and normal matter gravitationally, but only does so very weakly through the weak force (and hence is "collisionless"), and further only interacts with photons very weakly through the electromagnetic force.

1.3.1 Early universe density perturbations

According to ΛCDM, galaxy group formation began in the early universe. To fully understand and appreciate this, one must start by considering the first fraction of a second of the universe. The theory of cosmic inflation posits that, during this time, the universe rapidly exponentially expanded many times in size, smoothing out inhomogeneities and anistropies and reducing the curvature of space (hence, the postulated and observed homogeneity, isotropy, and flatness of the universe) (Guth, 1981; Linde, 1982; Albrecht & Steinhardt, 1982). Another consequence arose: minute quantum fluctuations in the nascent universe were inflated to cosmic proportions, seeding real density perturbations throughout the dark matter and primordial plasma, the latter composed of tightly coupled photons and ionized baryonic matter[10].

During the epochs following inflation and prior to recombination, radiation pressure resulting from the plasma's strong coupling to photons stabilized perturbations in the baryon-photon fluid, effectively "suspending" the baryons and photons by preventing them from falling into gravitational potential wells. This inhibited the cooling and collapse of the gas and forced it to remain a nearly uniform medium. However, cold dark matter - undergoing no (non-gravitational) interactions with the radiation field, and thus under no such constraint - was free to begin evolving purely under the effects of gravity and cosmic expansion. The mass-density perturbations, often considered to initially follow a homogeneous and isotropic Gaussian random field, eventually led to the gravitational collapse of dark matter into structures called halos.

While the magnitude of density contrasts (over- and under-densities), characterized by $\delta(\vec{x},t) \equiv \big(\rho(\vec{x},t) - \overline{\rho}(t)\big)/\overline{\rho}(t)$, remained small ($|\delta(\vec{x},t)| \ll 1$), this process began with approximately linear growth, i.e. the density perturbations evolved according to linearized versions of the gravitational equations (Edwards & Heath, 1976; Kravtsov & Borgani, 2012). In linear perturbation theory, the amplitude of an over-density (and, in fact, all the different Fourier modes $\delta(\vec{k})$) evolves in direct proportion to the linear growth factor $D_+(a)$[11], which is determined from the specific cosmology (its form in ΛCDM is given in Heath (1977)). Upon reaching an over-density of $\delta_{\rm turn-around} \gtrsim 1$, a region is dense enough to decouple from the overall expansion (or "Hubble flow") of the Universe, and initiate collapse (i.e., reach its "turn-around" radius) (Press & Schechter, 1974; Edwards & Heath, 1976; Heath, 1977; Kravtsov & Borgani, 2012). This is also approximately the epoch at which the density

[10] In astronomy, baryons or baryonic matter refers to all matter that is not dark matter.

[11] In an expanding universe, the scale factor $a(t)$ is the relative size of the universe at a given time compared to the present, and is related to redshift as $a(t) = 1/(1+z)$.

perturbation's evolution enters the non-linear regime.

As the universe expanded, it "dragged" matter with it. Gravity opposed this, by foremostly pulling matter towards regions with deeper gravitational wells (i.e., denser volumes), in effect increasing the density and drawing more matter in through a positive feedback loop. To use an example, in the spherical collapse model (Gunn & Gott, 1972; Lahav et al., 1991), in which one often assumes a simple Einstein-de Sitter (EdS) universe (flat universe with cold dark matter only) since the non-linear collapse over-density is analytically tractable in that case, a top-hat constant-mass perturbation δ_i has a spherical "perturbation radius" R that increases with a decreasing velocity, i.e. it decelerates as it expands outwards, under the assumption that the enclosed mass is conserved. If it is initially sufficiently dense relative to the mean density of the universe, R reaches a maximum value $R_{\rm ta} \equiv R_{\rm turn-around}$ with a *nonlinear* over-density of $\delta_{\rm ta} \sim 4.55$ - corresponding to a *linearly-extrapolated* over-density of $\delta_{\rm ta} \sim 1.06$ - at a time $t_{\rm ta}$, after which it accelerates inward (Gunn & Gott, 1972; Mota, 2004; Pace et al., 2017; Albuquerque et al., 2024). Eventually, the perturbation collapses, virializes[12] (during which time the dark matter is redistributed in phase space through a process called violent relaxation), and settles at a final radius $R_{\rm f} = R_{\rm vir} = R_{\rm ta}/2$. This collapse occurs roughly on the gravitational free-fall timescale $t_{ff} = \sqrt{3\pi/(32G\rho_{\rm ta})}$, such that the *nonlinear* density contrast after virialization is $\delta_{\rm vir} \sim 177$ (compared to a *linearly-extrapolated* over-density at collapse of $\delta_{\rm coll} \sim 1.686$, demonstrating how rapidly structures grow when perturbations enter the non-linear regime). In more realistic scenarios, e.g. a non-spherical density perturbation in a ΛCDM cosmology, all of these values can change; for example, $\delta_{\rm vir}$ can range from $100 - 200$. In general, they depend on the specific cosmology and redshift (see e.g. Bryan & Norman, 1998; Percival, 2005; Komatsu et al., 2011; Kravtsov & Borgani, 2012, and references therein).

Because cold dark matter cannot interact electromagnetically, it is not able to release energy as radiation, and therefore net cooling cannot occur[13]; in this way, virialization marks the stage at which the system is supported by the "pressure" from the random motion of the dark matter particles. Finally, the collapsed dark matter object is deemed a "halo", and at first order evolves in isolation from the expansion of the universe.

[12] Virial equilibrium occurs when the kinetic energy is half of the potential energy of the system, $K = -\frac{1}{2}U$.

[13] Regardless of their ability to release electromagnetic radiation, dark matter particles can transfer energy as they interact gravitationally, resulting in an effective "cooling" and "heating" of individual particles, but no collective change in the "temperature" (internal energy) of the system.

1.3.2 Dark matter structure

In a ΛCDM cosmology, larger objects are built up through the successive merging of smaller objects in a process called hierarchical structure growth (Bardeen et al., 1986; Babul & Rees, 1992; Shapiro et al., 1994), with the dark matter halos of groups, clusters, and super-clusters being the ultimate examples (Springel, 2005). In this paradigm, less massive halos form earlier than more massive halos as a consequence of the specific density power spectrum resulting from inflation: for a given density contrast δ, the progenitor density perturbations of less massive halos have smaller characteristic sizes (i.e., less volume) and larger physical densities ρ than those of more massive halos. Therefore, the gravitational instability of the former can overcome the expansion of the universe earlier than the latter.

Following the pathway of hierarchical mass assembly leads to the coalescing of low mass dark matter halos into higher mass halos. Regions of initially larger over-densities and/or higher clustering of density perturbations seed the halos that go on to form groups, clusters, and super-clusters (although smaller systems, like poor groups, can form and exist in environments with a wider range of densities compared to their higher mass counterparts). On the other hand, smaller and/or more isolated perturbations grow into dwarf galaxy- and galaxy-scale halos.

Simultaneously with all this, the "sheets" and "filaments" of the so-called cosmic web form as a result of the tidal and shear velocity fields underlying the dark matter density field. Tidal forces between each pair of objects (most significantly between neighbouring halos) pull matter into the region between each pair, elongating it into filaments tenuously connecting the halos. The full cosmic web is built up out of the hierarchical growth of halos, filaments, and "nodes" (the regions where filaments intersect, which house - at any given epoch - the most massive of halos). Over time, mergers incorporate smaller filaments and their halos into larger filaments, which are then incorporated into even larger filaments, mirroring the hierarchical growth of the halos themselves.

Under-dense volumes follow an opposite evolutionary pathway: these regions are emptied of matter over time, which accretes onto surrounding collapsing over-densities, halos, and filaments, further increasing their masses. These low-density volumes are termed cosmic voids. Hence, dark matter halos grow through both mergers and large-scale accretion of matter from their surrounding environments.

1.3.3 Gas accretion and hot diffuse atmosphere formation

About 380,000 years after the Big Bang, expansion had cooled the Universe to sufficiently low temperatures ($T \sim 3000$ K at $z \sim 1100$) for electrons and photons in the cosmic plasma to decouple, as well as for protons and electrons to recombine into neutral hydrogen, largely forming expansive clouds. At this point, the Universe transitioned from opaque to photons, to transparent, allowing them to freely stream across vast expenses and generating what is known as the cosmic microwave background (CMB). Importantly, decoupling removed the radiative pressure support preventing baryons from following a similar process as that described above for dark matter. Since the dark matter had at least partially undergone gravitational growth and collapse by this time, semi-formed structures to full halos were already in place, allowing the baryonic matter a "head-start" on gravitationally-induced evolution. It was therefore free to evolve under the influence of the gravitational attraction of these structures, and was pulled into halos and filaments.

Broadly, there are two "places" this gas can accrete onto: dark matter halos, or the galaxies forming at their centres in the bottom of the gravitational potential wells. This thesis mainly focuses on the gas that ends up in a hot diffuse state in the halo; in galaxy-scale halos, it is called the circumgalactic medium (CGM), while at more massive scales it is the IGrM and ICM. This work specifically addresses the IGrM (and, to an extent, the ICM); therefore, the following descriptions will primarily centre on the formation and evolution of this hot diffuse gas. However, while these two gas accretion pathways naively appear as two distinct processes, they are actually intimately intertwined. The gas that winds up in cooler denser phases in galaxies, denoted as the interstellar medium (ISM), is also critical to the evolution of the IGrM - in particular its chemical enrichment because the vast majority of metals are produced and released from the stars birthed in galaxies. Additionally, as explained in following paragraphs, gas accretion onto a halo can - in certain regimes - depend on energetic feedback from member galaxies.

As laid out by Rees & Ostriker (1977), van de Voort et al. (2011) discuss the three main regimes of gas cloud cooling that exist post-virialization. In the first case, if the characteristic cooling time $t_{\rm cool} \equiv E/\dot{E} \sim \rho\epsilon/C$ (where $\dot{E} \equiv {\rm d}E/{\rm d}t$ is the output power, $C \equiv {\rm d}\dot{E}/{\rm d}V$ is the volumetric cooling rate, and $\epsilon \equiv {\rm d}E/{\rm d}M$ is the energy per unit mass of the gas and depends on its temperature and composition) is larger than the Hubble time $t_{\rm H}$[14], there

[14]The Hubble time $t_{\rm H}(z) = (H(z))^{-1}$, where $H(z)$ is the Hubble parameter at redshift z, is the age the universe would be at redshift z if its expansion up to that point was linear. Though the universe's expansion has been nonlinear, at the current epoch, $t_{\rm H}$ is still approximately the age of the universe (~ 14 Gyr for $t_{H,0}$ depending on the assumed value of H_0, and ~ 13.8 Gyr for the age of the universe).

is not sufficient time for the gas to radiate away its energy, leaving it in a non-collapsing equilibrium state suspended by thermal pressure support. If $t_{\rm cool} < t_{\rm H}$, but $t_{\rm cool}$ is still larger than the dynamical (or free-fall) time-scale of the gas $t_{\rm dyn} \equiv t_{ff}$, the gas cloud will slowly contract while maintaining quasi-hydrostatic equilibrium, by increasing its temperature and density in response. Lastly, if $t_{\rm cool} < t_{\rm dyn} < t_{\rm H}$, then cooling occurs rapidly in comparison to gravitational contraction, resulting in catastrophic cooling and lowering of the Jeans mass[15], and therefore possible fragmentation. This also causes the gas to plummet towards the bottom of the gravitational potential well of the system. The first and second of these regimes are thought to be the approximate states of the CGM, IGrM, and ICM. On the other hand, galaxies are believed to form in the third regime (Rees & Ostriker, 1977; Silk, 1977a,b,c).

Such radiative cooling occurs via two-body processes like collisional ionization, recombination, collisional excitation, and bremsstrahlung, with the former three dominant at gas temperatures of $10^4\,{\rm K} \lesssim T \lesssim 10^6\,{\rm K}$ and the last at $T \gtrsim 3 \times 10^7\,{\rm K}$, at which gas is mostly ionized. Although not as much within the scope of this thesis, below $T \sim 10^4\,{\rm K}$, gas is primarily neutral and the aforementioned two-body processes become negligible, such that cooling by these methods is inefficient. Instead, in molecular clouds, cooling mechanisms like molecular line cooling (e.g. by the CO molecule, the second most astrophysically abundant molecule after H_2), fine-structure cooling, and dust thermal radiation[16] play important roles in bringing the gas temperature down to the conditions required for star formation. The volumetric cooling rate itself depends on the temperature T, metallicity Z, and density ρ of the gas as $C = n_e n_i \Lambda(Z,T)$, where n_e is the electron number density, n_i is the ion number density, and $\Lambda(Z,T)$ is called the cooling function (as shown in Figure 1.3), such that higher densities result in increased cooling rates and shorter cooling times. In this way, higher density regions, possibly induced by gravitational instabilities in the gas that increase the local density, result in an increase in the cooling rate, leading to enhanced cooling.

Early works (e.g. Rees & Ostriker, 1977; Silk, 1977a,b,c; White & Rees, 1978; Fall & Efstathiou, 1980; White & Frenk, 1991; Mo et al., 1998) described gas accretion under the incorrect approximation of spherically symmetric collapse, as well as often under the incorrect assumption that only gravity and cooling dictate the thermodynamics of the gas (i.e., no energetic output from feedback). In reality, these assumptions do not hold true in most

[15]The Jeans mass M_J is the critical mass of a gas cloud, at a given size (i.e. radius in the case of spherical symmetry) and temperature, above which the cloud is unstable to runaway contraction until some other force can impede the collapse, such as the nuclear fusion in stellar cores.

[16]Dust grains are blackbody emitters, but for them to efficiently cool the gas, the two must be thermally well-coupled. This occurs when densities are sufficiently high, which happens at $\sim 10^4\,{\rm cm}^{-3}$ and is not reached in molecular clouds (but is in the regions of molecular clouds collapsing to form stars, e.g. pre-stellar cores).

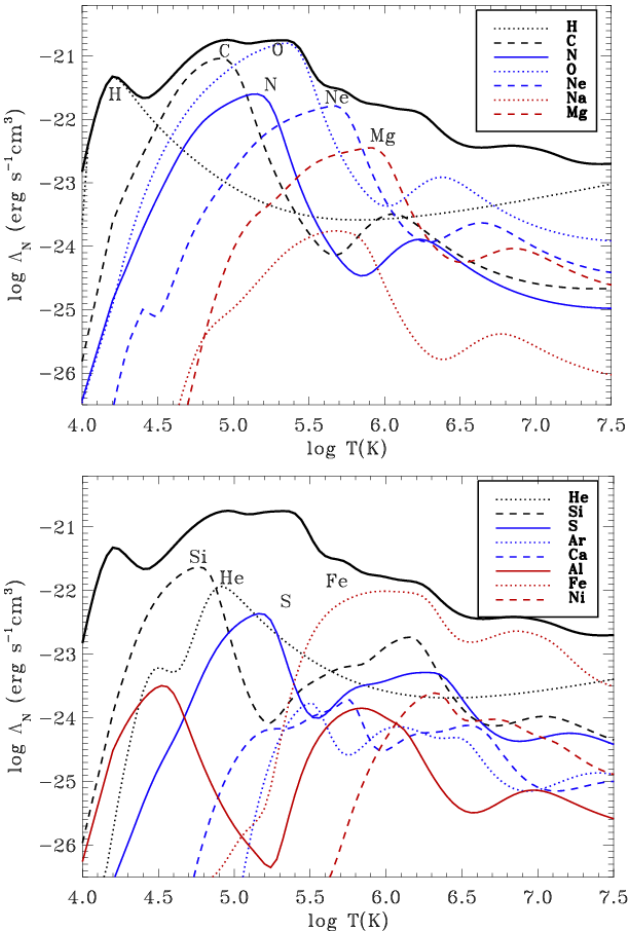

Figure 1.3: Reproduced from Schure et al. (2009). Contributions of different elements to the cooling curve. Each of the plots shows a different set of elements. Important peaks are labelled with the name of the element. The total cooling curve (black solid line) is an addition of the individual elemental contributions.

cases. Gas accretion may be substantially asymmetric, especially when cosmic structure, like the cosmic web, has become well-established. Nearly all collections of gas that become dense enough to form stars (i.e., galaxies) inject energy from stellar feedback into the ISM, generating galactic-scale winds that may exit the galaxy and enter the surrounding halo, supplying it with gas and heating it. Finally, AGN feedback can be orders of magnitude more energetic than that from stars, producing outflows that can inflate bubbles in the hot gas and inhibit its cooling.

Emerging from a combination of the dark matter halo large-scale structure and the three regimes of gas cooling are two dominant modes of smooth gas accretion: hot-mode and cold-mode (Katz et al., 2003; Kereš et al., 2005). To understand these mechanisms well, the concept of a "cooling radius" $r_{\rm cool}$ is useful. A consistent quantitative definition is not clear in

the literature; it may be considered the radius at which - based on the gas temperature and density, and the gravitational field - the cooling and the dynamical times are equal, $t_{\rm cool} = t_{\rm dyn}$. Alternatively, it is the radius at which $t_{\rm cool} = t_{\rm H}$. Regardless, the qualitative implication of $r_{\rm cool}$ is that for $r < r_{\rm cool}$, accreting gas has $t_{\rm cool}$ less than the compression time to establish a stable shock and is therefore generally able to cool and collapse, whereas for $r > r_{\rm cool}$, $t_{\rm cool}$ is greater than the compression time so gas remains hot and thermally supported (van de Voort et al., 2011; Stewart, 2017). The two modes of accretion are described in the following points:

- *Cold-Mode Accretion.* If $r_{\rm cool} > r_{\rm vir}$, infalling gas may never shock heat to $T_{\rm vir}$. Typically, then, this cooler gas will be in the third regime of gas cooling ($t_{\rm cool} < t_{\rm dyn}$), or at least the second ($t_{\rm cool} < t_{\rm H}$), allowing its descent to be primarily governed by its infall rate (i.e. gravity), and not its cooling rate (White & Frenk, 1991). The gas can then cool rapidly, as has been shown to occur in simulations (Rees & Ostriker, 1977; White & Rees, 1978). In this case, a hot diffuse baryonic halo does not form. The cosmic web results in preferential feeding of halos and galaxies with new gas along filaments; mergers also bring in gas asymmetrically. Accreting gas originating from these sources has higher density on average than otherwise. Consequently, it has lower $t_{\rm cool}$, and the probability that the gas will undergo cold-mode accretion is higher. Studies show that, especially at high redshift, "cold streams" are able to breach the hot diffuse atmospheres and directly feed central galaxies with cooler gas, sparking star formation and the resultant stellar feedback (Kereš et al., 2005; Dekel & Birnboim, 2006; Ocvirk et al., 2008; Dekel et al., 2009a,b; Kereš et al., 2009).

- *Hot-Mode Accretion.* Baryonic matter gains kinetic energy as it falls towards dark matter halos. If the cooling radius is well within the virial radius of a dark matter halo, i.e. $r_{\rm cool} \ll r_{\rm vir}$, as is largely the case for high-mass halos, upon reaching the halo, the gas meets resistance in the form of supersonic collisions with itself, known as shocks, transforming its kinetic energy into thermal energy. Most of the infalling gas will shock heat somewhere between $r_{\rm vir}$ and $r_{\rm cool}$. This process halts its infall as the gas pressure balances the gravitational pull. It also leaves the hot "baryonic halos" virialized at the virial temperature of their host dark matter halos ($T_{\rm vir} \sim$ few $\times 10^5 -$ few $\times 10^6$ K, depending on halo mass), in a state of thermal pressure-induced quasi-hydrostatic equilibrium, and filling the volume of the halos, thus resulting in a quasi-static hot atmosphere (van de Voort et al., 2011; Sokołowska et al., 2018). In the early universe, when the filaments of the cosmic web are dense and relatively thin, this process is quite non-spherically symmetric, and hot-mode accretion is generally sub-dominant to

cold-mode accretion in most halos; however, as time progresses, the filaments widen, becoming comparable in size to the halos themselves and resulting in an increasing fraction of the gas accreting quasi-spherically and via hot-mode. Gas collects to a larger degree in the minima of the gravitational wells, leading to higher density inner regions. Therefore, following this, the denser gas within $r_{\rm cool}$ can radiatively cool out of the hot gaseous halo, infall and sink to the centre according to the cooling function, accrete onto the central galaxy, and, by conserving angular momentum, settle into a rotationally supported disk, in which stars form (e.g. Binney, 1977; Rees & Ostriker, 1977; Silk, 1977a; White & Rees, 1978; Fall & Efstathiou, 1980; White & Frenk, 1991; Maller & Bullock, 2004). This mechanism for fueling galaxies with colder gas (that is necessary to initiate the pathway to star formation) may not be common earlier in the universe because of the limited time such gas has had to cool and the aforementioned prominence of cold-mode accretion in directly shuttling gas to the central galaxy. It is possible the slow quasi-spherical cooling of the hot gas may play a larger role at later times (Sokołowska et al., 2018), although - as mentioned - AGN feedback (and, to a lesser degree in massive halos, stellar feedback) may inhibit this by heating the halo gas.

While cold-mode accretion is prominent in filamentary environments (where groups and clusters tend to reside), both accretion modes can co-exist in a single halo. In general, the more massive a halo, the more important hot-mode accretion is and the less important cold-mode accretion is, and vice versa (Birnboim & Dekel, 2003; Katz et al., 2003; Kereš et al., 2005, 2009; Ocvirk et al., 2008; Brooks et al., 2009; Crain et al., 2010; van de Voort et al., 2011). Broadly, the fraction of gas accreted in the hot-mode (the "hot fraction") increases with increasing halo mass: $\lesssim 10\%$ at $M_{\rm halo} \sim 10^{11}\,{\rm M}_{\odot}$ to $\gtrsim 90\%$ at $M_{\rm halo} \sim 10^{13}\,{\rm M}_{\odot}$, at $z = 0$ (van de Voort et al., 2011). The reason for this is that higher mass halos have higher virial temperatures, and therefore longer cooling times. They are also larger in comparison to their cooling radii. Specifically, in high mass halos ($T_{\rm vir} \gtrsim 10^6\,{\rm K}$), the hot fraction directly reflects the fraction of the accreted gas that has experienced an accretion shock near the virial radius (van de Voort et al., 2011).

Further, the relative contribution of the two cooling modes depends on redshift, since the universe is denser at higher z and less dense at lower z. Although the Hubble time is shorter in the early universe in line with $t_{\rm H} \propto \rho^{-1/2}$, the cooling time is also shorter but with a stronger dependence on density as $t_{\rm cool} \propto \rho^{-1}$, i.e. the ratio $t_{\rm cool}/t_{\rm H} \propto \rho^{-1/2}$ decreases with increasing age of the universe. Accordingly, cold-mode accretion is more significant relative

to hot-mode accretion at high z than at low z.

To first order, the rate of gas accretion onto halos parallels the rate of dark matter accretion. Both the rate of accretion and the relative importance of the two accretion modes are relatively insensitive to metal-line cooling and energetic feedback from AGNs and SNe in galaxies (van de Voort et al., 2011). However, even up to the scale of groups, the establishment of hot atmospheres can critically rely upon the presence of energy output.

Employing a set of four hydrodynamical zoom-in simulations (*Eris* (Guedes et al., 2011; Sokołowska et al., 2016), *ErisNFB*, *Eris2k* (Sokołowska et al., 2016, 2017) and *Venus* (Sokołowska et al., 2017)) of MW-like galactic systems ($M_{\rm halo} \sim 10^{11} - 10^{12}\,{\rm M}_{\odot}$), Sokołowska et al. (2018) demonstrate that their warm-hot ($T = 10^5 - 10^6\,{\rm K}$) gaseous atmospheres and hot super-virial ($T > 10^6\,{\rm K}$) coronae, collectively comprising the CGM, originate from gas expelled from the galaxies by merger-induced shock heating and SN feedback. Specifically, at $z \gtrsim 2$, the CGM is majority composed of (cold-mode accreted) gas ejected from the central galaxy that subsequently cooled upon expansion, resulting in "inside-out" growth of the hot diffuse halo. At $z \lesssim 2$, the process inverts, with the late-time mass budget of the CGM dominated by gas accreted in the hot-mode.

Babul & Rees (1992) show that dwarf galaxies can expel gas through SN-driven winds given they reside in an environment of sufficiently low density and pressure; otherwise, the gas will shock-heat, cool on a relatively short time-scale, and fall back onto the ISM, or never escape the ISM in the first place. Photoionizing radiation from massive stars and SNe additionally heats the gas, extending its cooling time and preventing it from flowing back into the galaxy.

Therefore, if a galaxy resides in a dense environment, like a group or cluster, in which the deeper gravitational potential wells are more effective at retaining gas and induce shorter compression timescales, photoionization and stellar winds are inadequate to play a marked role in the formation and development of the hot diffuse gas, effectively "decoupling" these processes from its evolution. As discussed, although quasi-spherical hot-mode accretion becomes more important with increasing halo mass, cold flows may still be prominent in filamentary environments, such as the nodes of the cosmic web, where groups and clusters form. As such, energetic feedback giving rise to inside-out growth may remain a critical component of the establishment of the IGrM, at least in isolated massive elliptical galaxies and lower mass galaxy groups. Specifically in these systems, AGN feedback may be reasonably energetic enough to fill this role. Clusters, on the other hand, are so massive that, in general, even AGN feedback is expected not to be able to expel gas.

1.3.4 IGrM maintenance and interaction with feedback

Many physical processes work in tandem to craft the specific features and characteristics of galaxy groups and clusters. Feedback cycles play a prominent role in the maintenance (and potentially formation, e.g. Sokołowska et al., 2018) of the IGrM, and are likely important contributors to the quenching[17] of massive central galaxies.

In the absence of any forms of feedback, the ISM gas would continue cooling and condensing until the ongoing star formation ran out of fuel (Katz, 1992; Benson, 2010), producing small galaxies over-massive in stars compared to observations by factors of $\sim 10-100$ (e.g. Tomczak et al., 2014; Somerville & Davé, 2015) and large galaxies over-massive in stars by factors of $\sim 3-5$ (e.g. Lewis et al., 2000; Liang et al., 2016).

Stellar feedback, in which massive amounts of energy are injected into the surrounding medium through mechanisms like supernova (SN) explosions (e.g. SNe Ia and SNe II) and stellar winds (e.g. from asymptotic giant branch (AGB) stars) (Doherty et al., 2014b), heats the ISM and physically blows gas out of galaxies, supplying the hot atmospheres with heated and potentially enriched gas. This energy also suppresses further cooling of the ISM, thus inhibiting star formation (i.e. quenching) and establishing a negative feedback loop (e.g. Hopkins et al., 2014, also see Naab & Ostriker (2017), and references therein).

Stellar feedback is only sufficient to regulate star formation in this way in less massive halos ($M_{\rm halo} \lesssim M_{\rm halo,MW} \sim 10^{12}\,{\rm M}_{\odot}$, where $M_{\rm halo,MW}$ is the total mass of our Milky Way galaxy including its halo (Cautun et al., 2020)) (e.g. Davé et al., 2016; Bassini et al., 2023). This is a result of the decreasing impact of stellar feedback as systems become more massive, i.e. the net energy output by stellar feedback does not grow as rapidly as the depth of the gravitational potential well with increasing halo mass. The same argument implies that stellar feedback can impact the extended hot diffuse gas of the CGM in less massive systems, but its effects remain confined to central galaxies and their ISM in more massive systems (even localized in the ISM depending on the mass and type of the galaxy).

The total efficiency of feedback in removing gas from the colder, denser, star-forming phase, or stopping it from entering that phase in the first place, is lowest at $M_{\rm halo} \sim M_{\rm halo,MW}$, resulting in relatively efficient star formation around that halo mass, as shown in Figure 1.4. This is found both in observations (e.g. Connelly et al., 2012; Mok et al., 2013; Gonzalez et al., 2013; van Uitert et al., 2016; Kravtsov et al., 2018; Loubser et al., 2018; Erfanianfar et al., 2019; Girelli et al., 2020) and simulations (e.g. Liang et al., 2016; Oppenheimer et al.,

[17] Quiescent refers to the state of a galaxy that has a low star formation rate (SFR) per unit stellar mass, or specific star formation rate (sSFR). The process of reducing the sSFR over time in a galaxy is called quenching.

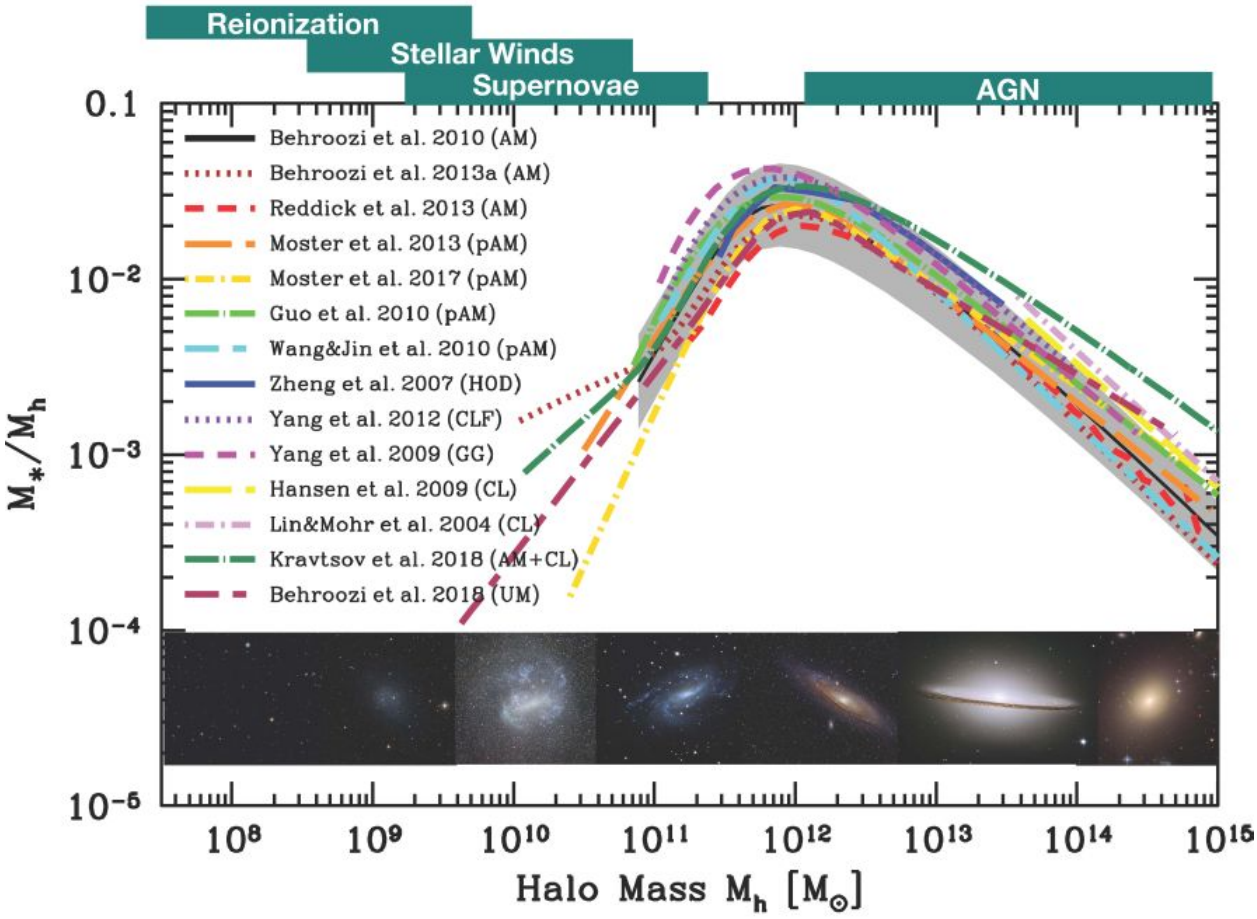

Figure 1.4: Reproduced from Wechsler & Tinker (2018), based on data compiled by Behroozi et al. (2019). The $z = 0$ stellar mass - halo mass relation for massive galaxies derived from various methods. The labels at the top indicate the key physical processes most likely responsible for ejecting or heating gas and suppressing star formation at those mass scales, while the bottom panel depicts example galaxies that are hosted by halos in the specified mass range.

2021; Jung et al., 2022).

AGNs are relatively weak in small systems (relative to stellar feedback), but become more efficient as the central supermassive black holes (SMBHs) are fed with increasingly large gas supplies drawn in by increasingly deep gravitational potential wells. Indeed, it is thought that in massive halos, the gaseous fueling of SMBHs by accretion within galaxies, and subsequent expulsion of enormous amounts of energy, takes over in stifling star formation and keeping the galactic stellar masses lower than otherwise predicted (Springel, 2005; Springel et al., 2005; Nelson et al., 2019; Kurinchi-Vendhan et al., 2024). This is known as AGN feedback

(as has already been discussed to some degree), which is observed in a large percentage of galaxies (Perna et al., 2017b; Fiore et al., 2017).

Although there is still much to be understood about AGN, broadly, they likely operate as follows in massive systems like groups and clusters (see Eckert et al., 2021, for a detailed review on AGN self-regulation and thermodynamics in galaxy groups). After gas has accreted onto a halo via hot- or cold-mode accretion, it flows from the large "macro" scales (kpc to Mpc) through infalling gas clouds, multiphase condensation and precipitation, and/or filamentary cold flows (e.g. Prasad et al., 2015, 2018; Saeedzadeh et al., 2023), initially generated by nonlinear turbulent thermal instabilities in the hot halo of the IGrM in a process known as chaotic cold accretion (CCA; McCourt et al., 2012; Sharma et al., 2012; Gaspari et al., 2013, 2017; Voit, 2018), to the "micro" scales (order of ∼parsecs) at the centre of the galaxy (Gaspari et al., 2020). Due to conservation of angular momentum, the gas settles into a rotationally-supported disk-like structure, which heats to extreme temperatures from the intense friction. This "accretion disk" thermally radiates, and can power galactic-scale outflows in the form of gaseous winds and relativistic jets of ionized gas, the latter of which are observable in radio waves due to their synchrotron radiation.

In galaxy groups and clusters, the most massive of AGN in the universe (located in their central galaxies) are not radiatively efficient, but rather operate largely in a "mechanical" mode with powerful jets. These inject energy into the surrounding IGrM or ICM (Babul et al., 2002; Croton et al., 2006; McNamara & Nulsen, 2007), preventing the gas from cooling efficiently and falling back onto the galaxy (Fabian, 2012).

Specifically, it has been found that these jets can inflate bubbles and cavities in the hot gas, which may offset cooling (Nusser et al., 2006; McCarthy et al., 2008a; Zhuravleva et al., 2014; Reynolds et al., 2015; Jennings et al., 2025). This occurs because the bubbles rapidly expand to reach pressure equilibrium with their surroundings, in the process generating shocks and waves that dissipate and heat the IGrM; also, as the bubbles rise due to their buoyancy, the viscosity of the IGrM induces a drag force that further heats the gas (Nusser et al., 2006; Werner & Mernier, 2020). A schematic of the cycle of SMBH feeding and AGN feedback is illustrated in Figure 1.5. Thus, a new negative feedback loop is set, in which AGN activity prevents gas from cooling and finding its way back to the SMBH for continuous fueling. This heating helps maintain the hot diffuse state of the gaseous atmosphere. In addition to regulating cooling, the outflows may entrain nearby enriched ISM gas and thus expel metals into the IGrM.

Importantly, as has been discussed, galaxies and halos evolve over time through various processes, both external (e.g. mergers, large-scale accretion) and internal (e.g. feedback from

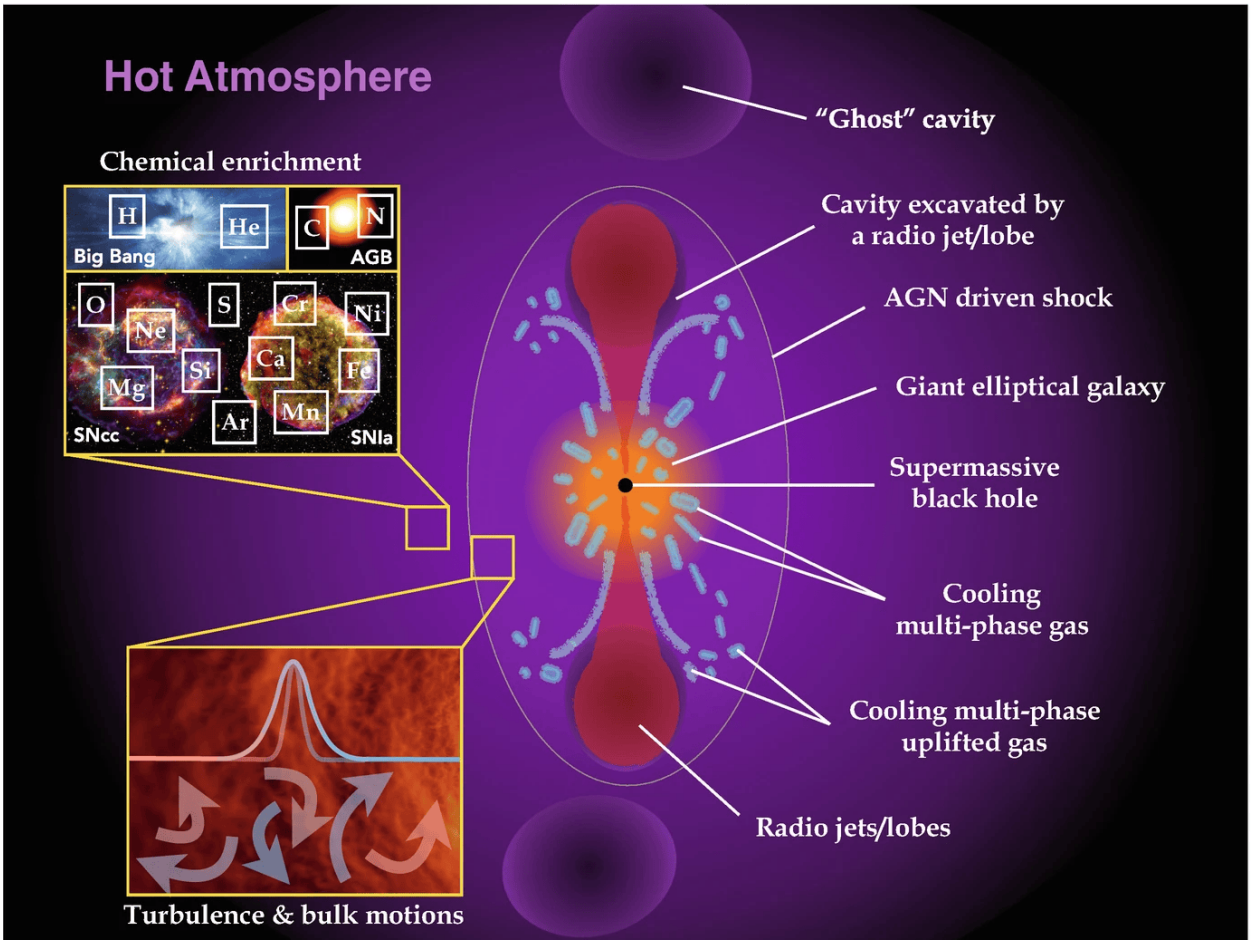

Figure 1.5: Reproduced from Werner & Mernier (2020). An illustration showing a chemically enriched (by SNIa, core-collapse SN, and AGB stars), hot, X-ray emitting atmosphere, stabilized by AGN feedback. Within a radius where the cooling time of the atmospheric gas is shorter than $\sim$ 1 Gyr the thermally unstable atmospheric gas "precipitates" by condensing into cooler clouds that may fall towards the centre, increasing the accretion rate onto the central supermassive black hole and driving the formation of jets. The jets inflate lobes, displacing the hot atmospheric gas and creating X-ray dark cavities. Initially, the lobes/cavities expand supersonically, driving weak shocks into the surrounding medium and increasing its entropy. After detaching from the jets, the lobes/cavities rise buoyantly in the hot atmosphere, driving turbulence and uplifting low entropy gas in their updraft. The uplifted low entropy gas may cool and fall back towards the centre. As the relativistic plasma filling the bubbles loses energy it stops shining in the radio band and the cavities become "ghost" cavities. By mechanically perturbing the gas, e.g. driving shocks, uplifting the lowest entropy gas from the centre, driving turbulence, the AGN heats the atmosphere preventing its radiative cooling. AGN driven turbulent motions cause Doppler broadening of spectral lines, which can be observed by high-resolution X-ray spectrometers.

stars and AGN). Within galaxies, metals are primarily produced through nucleosynthesis in stars, with the specific formation pathway varying by stellar type. Generally, in massive stars, nuclear fusion in their cores creates elements up to iron, while in low- and intermediate-mass stars, elements like carbon, nitrogen, and oxygen are synthesized (Arnett, 1996; Nomoto et al., 2013). Over their lifetimes, stars expel these elements into the ISM through stellar winds, particularly from AGB stars (Doherty et al., 2014a,b). At the end of their life cycle, most massive stars undergo SNe, ejecting metals and enriching the surrounding ISM further (Nomoto et al., 2013). This enriched gas mixes with other ISM components and phases and is then lifted out of galaxies through feedback mechanisms such as SNe- and AGN-driven galactic-scale outflows (Hopkins et al., 2012); see Section 1.7.2 for more detail on how metals become part of the IGrM. Once outside the galaxy, these metals contribute to the chemical enrichment of the IGrM by transitioning into the hot, diffuse gas phase due to shock heating from gravitational infall and feedback processes (Biffi et al., 2018a; Werner & Mernier, 2020).

1.4 Observing the IGrM

How do we actually observe the IGrM and ICM in the real universe? The gas temperatures are very high ($\gtrsim 5\times10^5$ K in general) and the densities - and thus optical depths - tend to be quite low (hence the term *diffuse* to describe the hot gas), so much of the gas is optically thin and can be treated under the collisional ionization equilibrium (CIE) approximation[18]. However, dense and highly rarefied gas - or regions of gas - may require more careful consideration, the former because the gas is no longer optically thin and radiative transfer must be accounted for, and the latter because the large mean free paths of particles in the plasma reduce the frequency of interactions, making it difficult to establish CIE (Wiersma et al., 2009a). X-ray emission from the hot gas arises from various processes, primarily thermal bremsstrahlung (free-free emission), line emission from ionized metals ("line cooling"), recombination radiation (free-bound emission), and, to a lesser extent, (inverse) Compton scattering, thermal synchrotron emission, and resonant scattering (important to account for in those denser regions).

Thermal bremsstrahlung is the dominant mechanism at temperatures $T \gtrsim 3\times10^7$ K, which occurs when charged particles, like electrons, are deflected by the electric fields of ions, decelerating them and producing X-ray photons. The generated continuous spectrum therefore underlies the spectra from other processes, especially at the high temperatures of the ICM. Recombination is the process of an ion capturing a free electron, with the resulting

[18]CIE refers to the dynamic balance in a plasma at a given temperature between collisional ionization (i.e. collisions between particles resulting in a bound electron becoming free) and the process of recombination (i.e. the capture of a free electron by an atom or ion, resulting in a bound electron) (Dopita & Sutherland, 2003).

quantum mechanical electron transition producing an X-ray photon. The overall mechanism also generates a continuous spectrum, but is generally less dominant than bremsstrahlung. However, it becomes more relevant in cooler regions of clusters, like the outskirts, as well as in the cooler IGrM, where gas may be actively cooling and recombining (Oppenheimer et al., 2021). These two processes generate the background continua seen in the spectra of Figure 1.1. Additionally, metal line emission from ionized species, such as O, Si, S and Fe, contributes significantly to the X-ray spectrum and to the cooling of the hot gas (see Figure 1.3), in particular in the IGrM (Eckert et al., 2021). This occurs when an electron transitions between energy levels and produces a distinct emission line. The balance between these emission processes is influenced by the temperature, density, and metal content of the gas, making the X-ray spectrum a valuable tool for probing the physical conditions of the IGrM and ICM.

Observations of the IGrM and ICM using X-ray telescopes allow astronomers to measure these X-ray spectra and infer temperatures and chemical abundances by fitting the observed spectra to models of total emission. Abundances can be derived either from the analysis of the strength of specific emission lines, or from full spectral fitting. The accuracy of both methods relies on the degree to which metal emission lines and other spectral features can be distinguished from the underlying continuous spectrum, as well as from each other (termed spectral resolution). Spectral resolution is both a fundamental and technological issue. For the former, the widths of spectral features, including the broadening of emission lines, are affected by the temperature of the gas, the relative ionization states of different elements, and the spread in bulk motions of the gas: the higher the temperature, the more ionization states and the greater the velocity dispersion, the wider and less resolved spectral lines are. In this way, different spectral features are more prominent in groups versus clusters (see Sec. 1.6). In terms of the latter, instrumental designs and capabilities govern the minimum wavelength difference that can be resolved. The sensitivity of X-ray instruments impacts the observable radial extent of a group or cluster, while the spatial resolution controls the coarseness of observed structures and melding of different regions, which, for example, partially determines the accuracy of radial profiles. These broadly cover the observational limitations that exist in measuring the X-ray IGrM and ICM, though there are other, often more instrument-specific, ones as well.

1.5 Thermodynamic state of the IGrM

The IGrM plays a key role in mediating galaxy evolution, hosting a significant fraction of the gas in groups. There is broad consensus that star formation in a galaxy is primarily fueled by the large scale inflows of gas into the galaxy (e.g. Saeedzadeh et al., 2023). Whether a galaxy is actively star-forming (SF) or quenched depends on how freely this gas flows (Tumlinson et al., 2017; Peeples et al., 2019). Like the CGM, observations show that that the IGrM and ICM are multiphase media characterized by rich dynamics (e.g. Prasad et al., 2015, 2017, 2018; Saeedzadeh et al., 2023); they comprise gas with a wide range of kinematics, ionization states, densities, phases, and temperatures (Zhan et al., 2003; McCabe et al., 2021; McCabe & Borthakur, 2023, see also Sec. 4.3 of Oppenheimer et al. (2021), and references therein). The rate and detailed manner in which the hot gas cools and flows into the central galaxy galaxy, and thus whether this galaxy is actively forming stars, depends critically on the nature of this structure (Bildfell et al., 2008).

The median thermodynamic states (i.e., not the detailed multiphase structure) of the observed IGrM and ICM are relatively well characterized. X-ray observations with telescopes like *Chandra* , XMM-*Newton*, and *Suzaku*, indicate low-redshift global X-ray temperatures ranging from $\sim 0.3-3$ keV ($\sim 10^6-10^7$ K) for the IGrM and $\sim 3-15$ keV ($\sim 10^7-10^8$ K) for the ICM, but can vary depending on the specific measurement (e.g. X-ray band employed) (Sun, 2012; Werner & Mernier, 2020). This roughly corresponds to masses $M_{500} \sim 10^{13}-10^{14} M_\odot$ and $M_{500} \sim 10^{14}-$ a few $\times\, 10^{15} M_\odot$, respectively (Oppenheimer et al., 2021; Eckert et al., 2021), though poor groups like our own Local Group and rich clusters - even super-clusters (clusters of clusters) - exist at the extremes with lower and higher masses. Combining X-ray observations with observations of the Sunyaev-Zel'dovich (SZ) effect[19] (Zeldovich & Sunyaev, 1969; Sunyaev & Zeldovich, 1970), from observatories like *Planck* and the Wilkinson Microwave Anisotropy Probe (WMAP), shows that the hot gas has radially decreasing gas density ρ_{gas}, electron number density n_e, and pressure $P = n_e k_B T_{\rm gas}$ profiles (e.g. Sun et al., 2009; Lovisari et al., 2015).

It is commonly assumed that the hot gas in groups and clusters exists in hydrostatic equilibrium (HSE); that is, there is a net balancing of external forces, like gravity, and internal fluid forces, namely those induced by pressure gradients. Therefore, the radially decreasing pressure profiles demonstrate how the maintenance of HSE provides pressure-support against gravitational collapse (Kravtsov & Borgani, 2012). However, non-thermal

[19]The SZ effect is the scattering of CMB photons by high-energy electrons in the ionized plasma of galaxy clusters via inverse Compton scattering, leading to a distortion in the CMB spectrum by the thermal SZ effect and an overall shift in the CMB intensity by the kinematic SZ effect.

processes, such as turbulence and AGN feedback (which can also provide pressure support), influence the thermodynamic state, leading to deviations from HSE (e.g. Mahdavi et al., 2008; Hoekstra et al., 2015). This is, in fact, quite important for quantifying the total gravitating mass in a system. Ideally, for a group or cluster, the total enclosed mass within some radius would be determined via a method that is independent of such assumptions, like gravitational lensing (e.g. Hoekstra et al., 2015) or galaxy kinematics (although neither method is inherently unbiased - see, for example, the discussion in Braspenning et al. (2025)); unfortunately, this is often not feasible. Indeed, estimates are typically obtained from a gas proxy under the assumption of HSE. Specifically, observations of a group's X-ray surface brightness distribution can be used to extract a gas density profile (e.g. Pratt & Arnaud, 2002; Ettori et al., 2013; Ghirardini et al., 2019). Concurrently, assuming an emission model, a spatially resolved X-ray spectrum can be converted into a temperature profile (e.g. Arnaud, 1996). Fits to these profiles with an analytic function, assuming HSE, can be then used to compute the enclosed mass (e.g. Sarazin, 1986). Issues with this procedure include: (i) deprojection of 2D profiles into 3D profiles (Turner et al., 2025) can introduce significant bias, especially if a group is very non-spherically symmetric; (ii) the outskirts of these systems, in particular low mass groups, have rather low X-ray surface brightnesses, resulting in substantial error bars on measurements, which, given that the computed mass depends on the spatial derivative, can translate into large uncertainties on the mass estimates (e.g. Rossetti et al., 2024); (iii) the total hydrostatic mass estimate is linearly dependent on the inferred absolute temperature, which can differ by up to $\sim 30\%$ depending on the X-ray telescope employed (e.g. Schellenberger et al., 2015; Migkas et al., 2024); (iv) the multiphase nature of the IGrM/ICM can result in temperature inhomogeneities within a single radial bin, leading to errors on the mass of $\sim 10\%$, in general biasing the mean temperature (and thus the mass) low due to unaccounted-for clumpy cold gas (Mazzotta et al., 2004; Rasia et al., 2014; Henson et al., 2017); (v) contributions from non-thermal pressure, such as from magnetic fields and cosmic rays (Ruszkowski & Pfrommer, 2023), and turbulent pressure can significantly impact the hydrostatic mass estimate by pushing the gas away from hydrostatic equilibrium (e.g. Kay et al., 2004; Nagai et al., 2007; Martizzi & Agrusa, 2016; Ettori & Eckert, 2022), with the latter's contribution exceeding $\sim 30\%$ in some simulations (e.g. Nelson et al., 2014); and (vi) if a group or cluster is out of equilibrium, for example due to a recent merger, the reconstructed mass may be affected. The cumulative effect of these uncertainties (in particular the last two) is known as the hydrostatic mass bias, whose magnitude is commonly characterized by comparing observed hydrostatic mass estimates to weak lensing mass estimates or comparing true masses to forward-modelled hydrostatic masses of groups/clusters from cosmological

hydrodynamic simulations. The hydrostatic mass bias can range from $\sim 10-40\%$, both as an overestimate and underestimate (e.g. Hurier & Angulo, 2018; Ettori & Eckert, 2022; Gianfagna et al., 2023; Jennings & Davé, 2023; Kay et al., 2024; Kelleher & Lelli, 2024; Muñoz-Echeverría et al., 2024; Turner et al., 2025; Braspenning et al., 2025); Hoekstra et al. (2015) provide an estimate for clusters - derived directly from observations - of $\sim 24\%$.

Measurements of IGrM and ICM temperature $T_{\rm gas}$ and entropy $K = k_B T_{\rm gas}/n_e^{2/3}$ [20] illuminate differences in the thermodynamic states of these systems' cores. Observations find two general classifications: systems with so-called "cool-cores", known as CC groups/clusters, and those without, known as non-cool-core (NCC) groups/clusters. Broadly, CC systems are characterized by one or a combination of the following: temperature profiles with a central drop, low central entropies, short central gas cooling times ($t_{\rm cool}$), and X-ray bright cores, such that they are generally associated with central cooling flows (McCarthy et al., 2008b; O'Sullivan et al., 2017). Sub-classifications such as "strong CC" and "weak CC" are often used in literature to distinguish between large and small temperature, entropy, and cooling time drops (e.g. Hudson et al., 2010). The opposite is true for NCC systems, with the aforementioned non-thermal processes, as well as mergers, often being attributed as the source of the high central temperatures and densities. There are also important distinctions between CC/NCC *groups* and CC/NCC *clusters* in terms of their identifying features and their effects on abundances, the latter of which is briefly discussed in Sec. 1.6.

1.6 Galaxy Groups vs Clusters

Up to this point, I have mentioned various differences between groups and clusters, and their hot diffuse atmospheres. It is clear that groups and clusters are not necessarily one fundamental entity with overall similar properties existing on some extended scale, like number of member galaxies or system mass or temperature, with only minor differences. There are bimodalities in their properties and physical processes, mechanisms that operate in different modes at the different scales, and other properties that scale with total mass. Currently,

[20] This quantity, known as the "astrophysical entropy", is actually the adiabatic constant, but serves as a proxy for the classical thermodynamic entropy s (with the two related by $s = k\ln(K^{3/2}) + \text{constant}$; see Sec. 3.2.1 of Balogh et al. (1999)) to describe the thermal properties of the IGrM and ICM, as it combines temperature and density in a way that highlights the heating/cooling history and distribution of gas (McCarthy et al., 2008b; Werner & Mernier, 2020). Gas with low entropy naturally sinks to the centre of a system's potential, while high entropy gas rises. When gas is moved (e.g. by AGN activity or galaxy interactions), its temperature and density will generally change due to adiabatic expansion or compression, but its entropy will remain unchanged, thus preserving the "memory" of its thermodynamic history. On the other hand, cooling always decreases entropy and heating always raises it, which is not the case with density or temperature (McCarthy et al., 2008b).

there is also open debate on whether galaxy groups act more like small clusters or massive individual galaxies, and if they provide the "missing link" between the two (Oppenheimer et al., 2021). So how are groups and clusters - and the IGrM and the ICM - different, and how are they similar?

Before broaching this topic, it is important to clarify what is meant by "similar". There are at least two - if not more - distinct connotations to this term in the context of galaxy groups and clusters, and one must therefore be careful with the semantics. In the first instance, a group and cluster are the "same" if their properties of interest have the same values. For example, their temperatures, luminosities, etc... are near-identical or their hot gaseous atmospheres are enriched to the same level. On the other hand, "similar" may refer to the idea that groups' and clusters' properties scale as expected with, for example, total gravitating mass or the global temperature of the IGrM/ICM, based on theory, logical reasoning, analytical or numerical modelling, or empirically-motivated trends. If the latter definition holds in a scenario, then an observer holding the former definition would instead deem the objects "different", and vice versa. Further, as is fairly obvious, there can be distinctions even within the second definition, as in the case when the expectation from a self-similarity argument (e.g. with only gravity and gas cooling playing a role in cosmic structure formation) is at odds with the result from a cosmological simulation including feedback processes. As such, moving forward, I will endeavor to be clear about under which interpretation I am operating.

The first difference concerns the impact of different gas temperatures on their observed spectra. The higher temperatures of the ICM promote thermal bremsstrahlung radiation as the dominant emission process, but inhibit both radiative recombination and electron shell transitions, as the atoms are largely ionized. In the X-ray regime, this leads to a brighter ICM with a broader and smoother X-ray spectrum, greater flux at higher energies (depending on the gas temperature, the spectrum may only start to significantly drop off above $5-10$ keV), and fewer metal emission lines. On the other hand, the cooler temperatures of the IGrM allow recombination and electron shell transitions to increase in prominence (sometimes becoming dominant over bremsstrahlung), generating X-ray spectra that drop off rapidly at higher energies ($E \gtrsim 1-2$ keV) and contain many metal emission lines. Such spectral features in these different temperature regimes can be seen in Figure 1.1. Note that these differences between groups and clusters are as expected by conventional and current knowledge. This results in some key factors when attempting to derive elemental abundances. While the limited number of emission lines in clusters (such as the Fe-K shell lines at ~ 6.7 keV) allows them to typically be fairly well resolved by current instruments, this also means

fewer metals can have their abundances constrained. In groups, the increased number of emission lines causes these lines to overlap and blend together, creating what are known as "line complexes", such as the Fe-L complex between 0.7 and 1.3 keV. These complexes are completely unresolved at the spectral resolution of CCD cameras, and even remain blended for the high-spectral resolution micro-calorimeter on-board XRISM (the X-Ray Imaging and Spectroscopy Mission - the most recent observatory to join the array of humanity's X-ray telescopes), yielding more poorly constrained abundances (for more details, see Werner & Mernier, 2020; Gastaldello et al., 2021; Mernier & Biffi, 2022, and references therein).

Despite existing on a continuum, the second major difference is in the depths of their gravitational potential wells, and the impact this has on the hot diffuse gas. Massive clusters have very deep gravitational wells. They are typically treated as "closed-box" - or, more accurately, "closed-trap" - environments, in which there is minimal exchange of matter (e.g. gas and metals) with the surrounding large-scale environment (see early works, such as Gunn, 1977; Davis et al., 1985; White et al., 1993, discussing this issue). Specifically, baryons and dark matter flow in from voids and the cosmic web, and, having fallen into the gravitational potential well, largely remain in the system from then on. There is thus no significant outflow of material into the inter-galactic medium (IGM), the diffuse gas spanning the rest of the universe outside of isolated galaxies, groups, and clusters. Observations (e.g. Sun et al., 2009; Pratt et al., 2009; Gonzalez et al., 2013; Ettori, 2015; Chiu et al., 2018; Eckert et al., 2019) show that the baryonic mass fractions of sufficiently massive galaxy clusters are similar to the universal baryonic mass fraction $f_b \approx 0.165 - 0.155$ derived from CMB observations (Komatsu et al., 2009; Planck Collaboration et al., 2020, respectively), as illustrated in Figure 1.6 and corroborated by expectations from modern simulations (Figure 1.7). Both figures show the hot gas fraction as a function of halo mass, which can be taken as a proxy for the baryon fraction under the assumption that the total contribution to the baryonic mass from cold gas and stars is negligible compared to that from hot gas over the spatial extent of a group or cluster[21]. This implies that all baryons, including metals, that were originally associated with a cluster's dark matter halo, were ejected by cluster galaxies over time, or that have fallen into a cluster in its past are retained (Donahue & Voit, 2022; Mernier & Biffi, 2022). In this model, fully-formed clusters evolve in a manner somewhat decoupled from their surrounding environment, although infalling gas and galaxies drive shocks and deepen the potential wells, and mergers occasionally churn the gas. Broadly, the primary processes affecting the gas

[21]Although this assumption starts breaking down for lower mass groups, the inclusion of cold gas mass and stellar mass is still typically insufficient to raise the group baryon fractions to the cosmic baryon fraction expected from a self-similar structure formation scenario governed only by gravity and gas cooling (e.g. Hough et al., 2024).

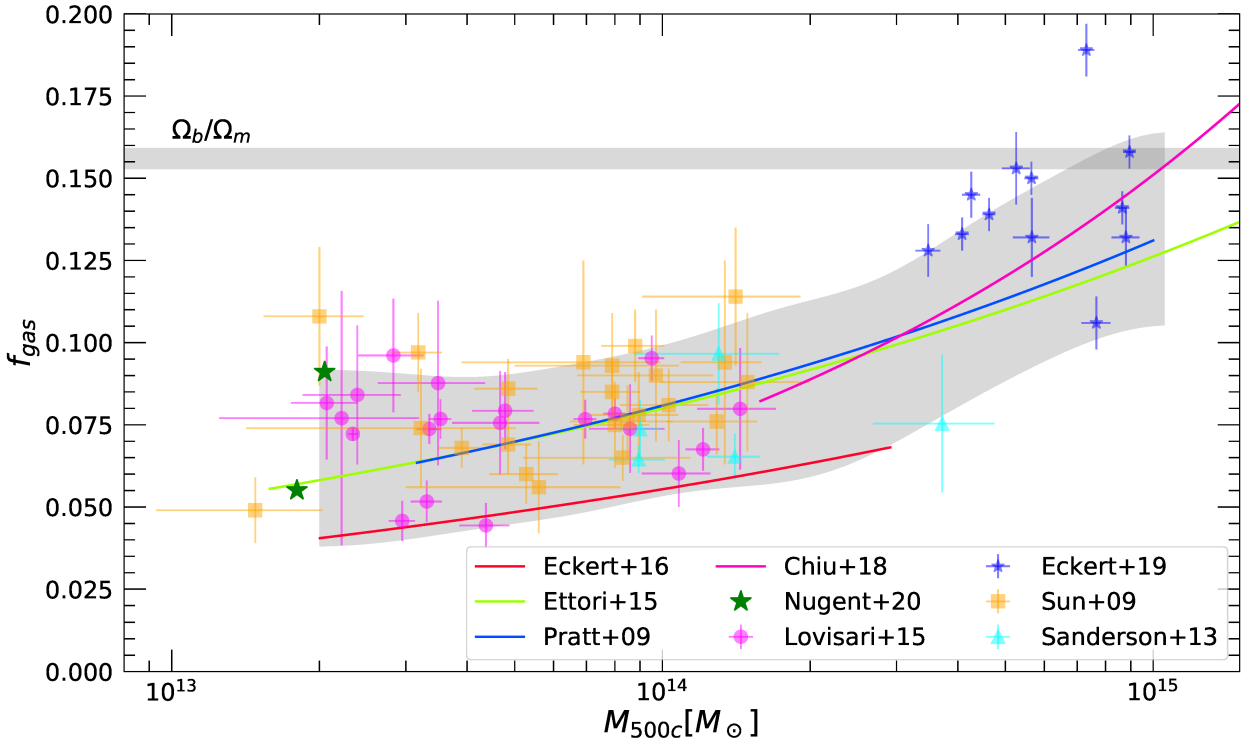

Figure 1.6: Reproduced from Eckert et al. (2021). Compilation of existing measurements of the hot gas fraction at R_{500} in galaxy groups and clusters as a function of halo mass M_{500}. The data points show the galaxy group samples of Sun et al. (2009) (orange), Lovisari et al. (2015) (magenta), Sanderson et al. (2013) (cyan), and Nugent et al. (2020) (green). The data from the X-COP sample Eckert et al. (2019) at the high-mass end are shown as the blue points for comparison. The solid lines show the $f_{\rm gas} - M$ relations that are derived from REXCESS (blue, Pratt et al. (2009)), XMM-XXL (red, Eckert et al. (2016)), SPT-SZ (magenta, Chiu et al. (2018)), and the literature sample of Ettori (2015). The gray shaded area shows the 90% confidence range encompassing the existing observational data and their corresponding uncertainties. The horizontal gray band shows the cosmic baryon fraction.

and metal content of a cluster are therefore internal, such as gravity, star formation, SNe, and AGN feedback. As a result, the enrichment of the ICM nearly depends solely on the internal star formation history and the efficiency of feedback mechanisms (relative to gravity) that redistribute metals within a cluster, allowing the ICM to retain the memory of its metal enrichment.

Conversely, galaxy groups and poor clusters are less massive with shallower potential wells. This means they should not generally be considered closed-trap systems (Mernier & Biffi, 2022); instead, they act like open-box systems, permitting the exchange of matter between the IGrM and IGM, and are potentially able to fully eject metals, losing them to the IGM

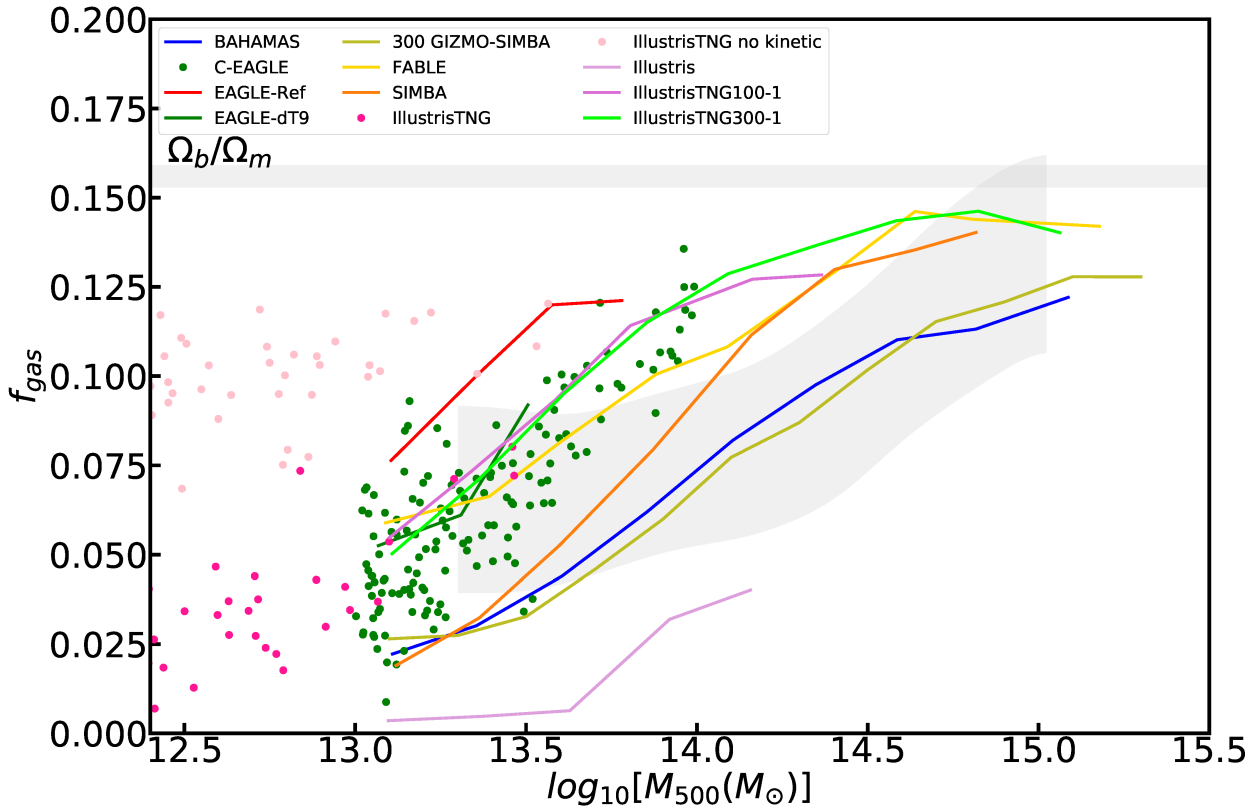

Figure 1.7: Reproduced from Eckert et al. (2021). Compilation of gas fractions within R_{500} from modern simulations as a function of M_{500}. The blue line corresponds to BAHAMAS (McCarthy et al., 2017), the red and green lines to the Reference and dT9 models of EAGLE (Schaye et al., 2015), the green symbols to C-EAGLE and `Hydrangea` (Barnes et al., 2017; Bahé et al., 2017), as it uses the same sub-grid model as EAGLE-dT9, the olive line to the 300 clusters run with the GIZMO-SIMBA code (Cui et al., 2022) as part of `The Three Hundred Project` (Cui et al., 2018), the salmon line to HORIZON-AGN (Dubois et al., 2014), the gold one to FABLE (Henden et al., 2018), the orange one to SIMBA (Davé et al., 2019; Robson & Davé, 2020), and the pink and deep pink symbols, as well as the plum, orchid, and lime lines correspond to various models from the `Illustris` and `IllustrisTNG` suites (Vogelsberger et al., 2014; Springel et al., 2018). The compilation of observations presented in Figure 1.6 is shown as a gray band.

(e.g. Figure 1.5). As such, their baryon fractions are lower than in clusters[22] (e.g. Pratt et al., 2009; Sun et al., 2009; Gonzalez et al., 2013; Ettori, 2015; Lovisari et al., 2015; Eckert et al., 2016; Nugent et al., 2020); again, see Figures 1.6 & 1.7. Additionally, these low masses enable

[22]In actuality, it is currently unclear whether the lower baryon fractions in groups compared to clusters originate from processes occurring after group assembly or during the proto-group stage, when the shallower gravitational potential wells (both compared to clusters and compared to present day) would have permitted substantial expulsion of gas, and subsequent slow - but not full - re-capturing of the gas. The latter scenario appears to be more likely.

complex baryonic physics (e.g. cooling, heating, galactic winds, AGN feedback, turbulence) to begin to dominate above gravity, again making groups more than simple scaled-down versions of galaxy clusters (e.g. Ponman et al., 2003; McCarthy et al., 2010; Lovisari et al., 2021; Eckert et al., 2021). In particular, the typical injected energy from AGN feedback in a group setting has a similar magnitude to or exceeds the gravitational binding energy of its gas, leading to the potential for substantial thermal and dynamical effects on the IGrM, such as fully ejecting the hot gas from a group; contrastingly, in massive clusters, energy injection from AGN feedback is normally lower than the gravitational binding energy, impeding its ability to alter gas properties, especially at large cluster-centric radii (Eckert et al., 2021); see Figure 1.8. Galaxy groups and the IGrM therefore sit in a special regime where they can provide key information on the processes resulting in the redistribution and loss of gas and metals (Gastaldello et al., 2021).

Following the same logic, one may expect groups to have a lower overall metallicity than clusters since they are able to eject metals over their evolution. Early observational works did find such results (e.g. Baumgartner et al., 2005; Rasmussen & Ponman, 2007, 2009; Sun, 2012; Mernier et al., 2016; Yates et al., 2017). However, many of these studies failed to use consistent regions for their abundance measurements between different systems. More recent - more spatially consistent - studies with improved observations and updated spectral models indicate that these previous works underestimated the core abundances in galaxy groups. This has led to the current knowledge - but a lack of simultaneous comprehensive understanding - of an essentially mass-invariant enrichment from groups to massive clusters (Mantz et al., 2017; Mernier et al., 2018c), at least in the systems' inner regions, which is reflected in many simulations (e.g. Davé et al., 2008; Fabjan et al., 2010; Planelles et al., 2014; Liang et al., 2016; Barnes et al., 2017; Dolag et al., 2017; Yates et al., 2017; Mernier et al., 2018c; Truong et al., 2019; Robson & Davé, 2020; Hough et al., 2024). An example of this is shown in Figure 1.9. In this way groups and clusters are similar according to my first definition of "similarity", but different according to my second definition (employing logical reasoning as the motivator for one's expectations on the IGrM/ICM abundances.

Regarding metallicity and abundances, cosmological simulations including feedback processes are generally found to be in better agreement with observations at the cluster scale, and may over-predict iron abundance in the group regime (e.g. Fabjan et al., 2010; Barnes et al., 2017; Braspenning et al., 2024; Hough et al., 2024; Padawer-Blatt et al., 2025). Additionally, irregardless of whether the enrichment at the group and cluster scales is similar or different, cosmological simulations generally exhibit greater scatter in the global IGrM metallicity than the global ICM metallicity (e.g. Davé et al., 2008; Fabjan et al., 2010; Planelles et al., 2014;

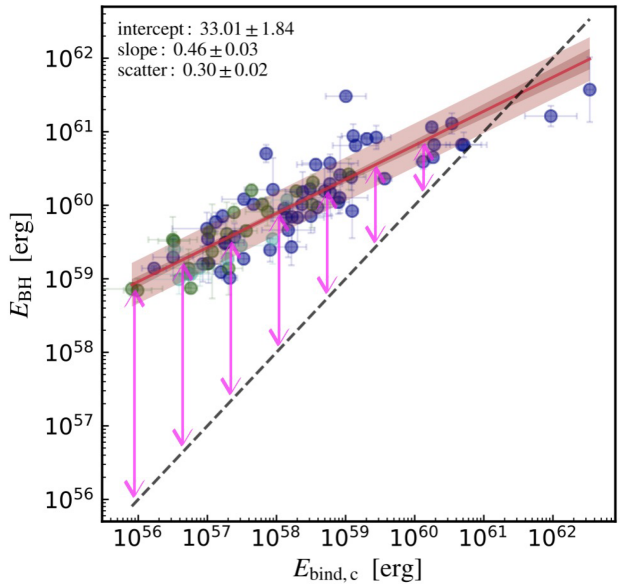

Figure 1.8: Reproduced from Eckert et al. (2021). Available mechanical feedback energy of the central SMBH versus gravitational binding energy of the hot gas within the core of the host halo ($R \lesssim 0.15R_{500}$). The SMBH energy is $E_{\rm BH} = 10^{-3}M_{\rm BH}c^2$, while the binding energy is related to the thermal energy via the virial theorem $E_{\rm bind} \approx 2E_{\rm th} \propto M_{\rm gas}T_{\rm x}$. The 85 points are taken from Gaspari et al. (2019), which include the observed direct/dynamical SMBH mass with the X-ray halo detected in the host group or cluster. The solid red curve shows a fit to the the relation with a power law, with the 16-84 percentile interval being indicated by the red shaded area. The $1-\sigma$ intrinsic scatter is plotted as a light red band on top of the mean fit. The circle colors reflect the morphological type of the central galaxy: elliptical (blue), lenticular (green), and spiral (cyan). The black dashed line demarks the one-to-one energy equivalence, whereas the magenta arrows highlight the excess BH energy when compared to the binding energy.

Liang et al., 2016; Barnes et al., 2017; Truong et al., 2019; Robson & Davé, 2020; Hough et al., 2024); see Figure 1.9. These characteristics are potentially a result of the greater susceptibility of group-scale enrichment patterns to gas-dynamical processes and AGN feedback, given their smaller sizes and shallower potential wells (Biffi et al., 2018a).

While groups and clusters are shown to have similar levels of enrichment, there are further divergences between CC and NCC systems. Observed CC clusters have higher core abundances and steeper metallicity profiles than their NCC counterparts (Leccardi & Molendi, 2008; Johnson et al., 2011; Ettori et al., 2015; Mernier et al., 2017; Ghizzardi et al., 2021). The same dichotomy is typically found in cosmological simulations (Rasia et al., 2015; Biffi et al., 2017; Vogelsberger et al., 2018; Barnes et al., 2017, 2018; Braspenning et al., 2024). This implies that central metallicity scales inversely with core entropy at the cluster scale, i.e.

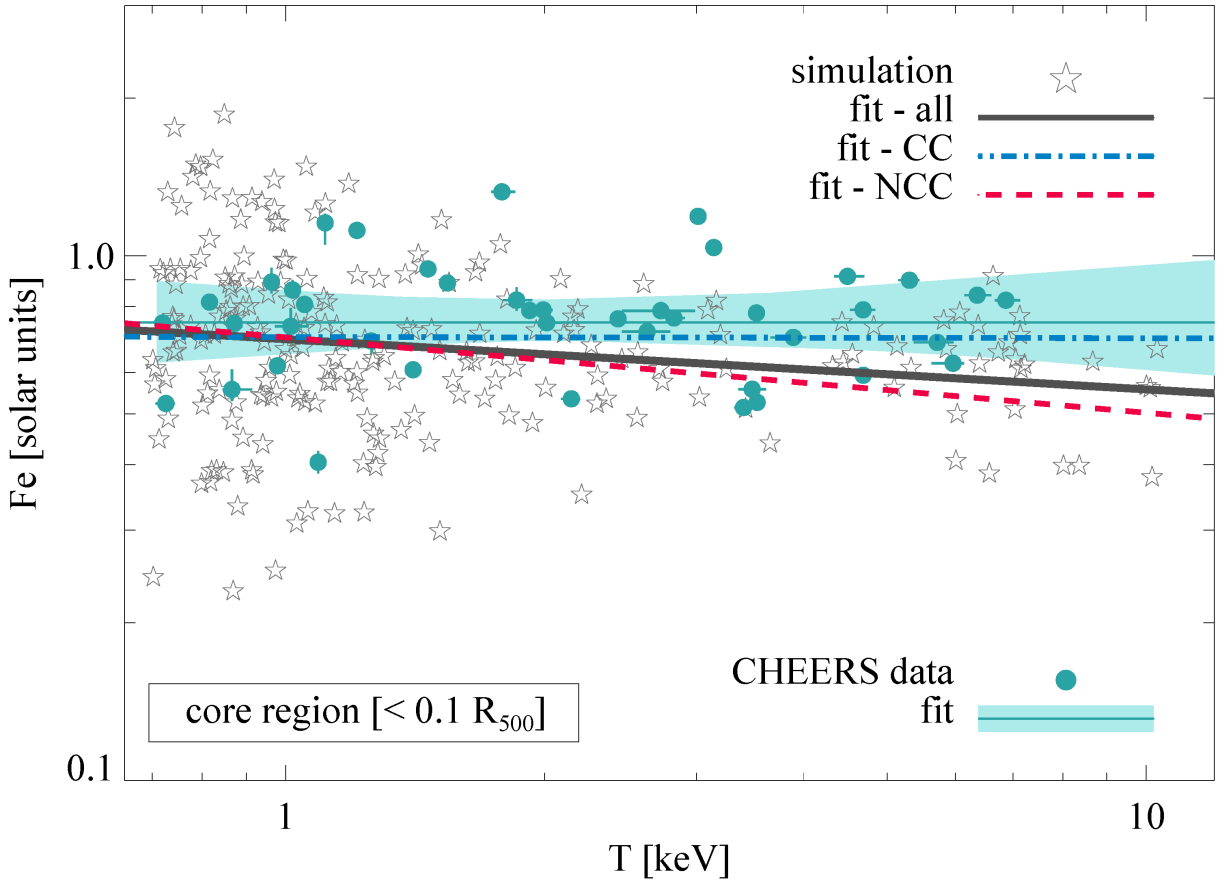

Figure 1.9: Reproduced from Gastaldello et al. (2021); originally adapted from Truong et al. (2019). Relation between gas iron abundance and temperature in the cores ($R < 0.1R_{500}$) of groups and clusters, with a comparison between cosmological simulations (empty stars) and X-ray observational results from the CHEERS sample (filled circles). Also reported are the best-fit relations for the whole simulated sample (solid grey line), and for the CC and NCC subsamples (blue dot-dashed and red dashed lines, respectively), as well as the relation determined from the CHEERS data (turquoise line and shaded area, for the associated 68.3% confidence region). Iron abundances, relative to hydrogen, are reported with respect to the Solar reference value by Asplund et al. (2009).

CC systems retain a higher fraction of their metals in their core, while NCC systems tend to more easily lose them either to the outskirts or out of the cluster altogether. The situation at the group scale is less evident due to the lack of statistically significant observational X-ray surveys of groups and larger uncertainties in abundance measurements. As a result, there has been little investigation of this in cosmological simulations, and so is an open area of research.

Thus, galaxy groups and clusters are found in many ways to present as rather distinct

systems. Clearly, while clusters host a wealth of information, groups are also very interesting systems to study, with their potential for unveiling the complex physical processes controlling IGrM properties and dynamics.

1.7 Cosmic Chemical Enrichment

The field of cosmic chemical enrichment is rich and multifaceted - spanning many orders of magnitude in scale, from stellar interiors to the gaseous nebulae surrounding stars and the ISM, out to the hot diffuse atmospheres surrounding galaxies. Uncertainties abound: exact formation processes and their reaction rates for different elements; the elemental yields for different types of stars and stellar populations; how metals escape from stars and diffuse into the surrounding gaseous medium; the relative number of different types of stars; and the list goes on. When attempting to understand chemical enrichment in galaxy groups, many assumptions must be made, and generally only broad conclusions can be drawn. However, even these overarching results are able to unveil significant and interesting information on the formation, evolution, and enrichment history of these massive structures. Still, there are many outstanding questions as to how the universe is enriched with metals. In this section, I will give a brief overview of the current understanding of cosmic enrichment in the IGrM and then discuss the `Chem5` enrichment model.

1.7.1 Where do metals come from?

The majority of the information in this section is sourced from the review by Mernier & Biffi (2022); more detail is available in Nomoto et al. (2013).

Metals in the universe are produced primarily through nucleosynthesis processes in stars. These processes occur at different stages of stellar evolution and involve various nuclear reactions that synthesize heavier elements. The origin and production of these metals depend on the specific nuclear processes and the mass and type of the star. Various types of stellar events then release metals into the surrounding ISM, where they can later contribute to the formation of new stars, planets, and other celestial bodies.

The first generation of stars, known as Population III stars, was likely composed almost entirely of hydrogen and helium, with virtually no metals (Katz et al., 2023). As the universe aged, metals produced and released by stars were reincorporated into new stars at their time of formation, resulting in later stellar populations (Population II and I stars) having greater metallicities. Low-mass stars, like the Sun, mainly produce lighter elements such as carbon, nitrogen, and oxygen through thermonuclear fusion processes like the proton-proton chain

and the CNO (carbon-nitrogen-oxygen) cycle. In contrast, more massive stars can create heavier elements up to iron (Fe) in their cores through successive stages of fusion (e.g., helium burning, carbon burning, and so on).

Supernovae (SNe) - the explosive "deaths" of massive stars - are key events for dispersing metals into the universe. For elements heavier than Fe, the nuclear fusion process is endothermic (i.e. net input of energy, instead of output), and the energy required to fuse them is too great to be sustained by a star's energy output. This leads to a loss of fusion-induced pressure support against gravity once the lower-mass elements have all been fused, which is only able to occur in sufficiently massive stars (typically more than $10\times$ the mass of the Sun). When this exhaustion of fuel ensues, the stars undergo core-collapse SNe, in which the stellar material falls in successive layers toward the solid core, ultimately "bouncing" off of it. These explosions release tremendous amounts of energy, triggering the synthesis of elements heavier than Fe (e.g. gold, platinum, uranium) through rapid neutron capture, also known as the r-process. The shockwaves from these explosions eject the star's outer layers, which are rich in metals (mainly the α elements from O to Ca on the periodic table), into the ISM.

Type Ia supernovae (SNe Ia) occur in binary systems where a white dwarf (WD; the compact remnant of a low-mass star, typically $\lesssim 8\,M_{\odot}$) gains mass until it reaches - or nears - a critical mass (the Chandrasekhar mass of $\sim 1.4\,M_{\odot}$) such that the temperature reaches that required for fusion of C, igniting a thermonuclear explosion. There are two such scenarios: i) two WDs in a binary system, which eventually merge, triggering the explosion, and ii) a WD-companion binary system, in which the WD accretes H-rich matter from the companion (e.g. a star) until it reaches the mass threshold. The explosion triggers a chain reaction creating and fusing elements up to Fe. Thus, SNe Ia are another significant source of metals, particularly Fe and Ni, as well as other intermediate-mass "iron-peak" elements (from Cr to Ni on the periodic table), although they also produce a substantial amount of some α elements.

Stellar winds also contribute to metal release, especially from evolved stars. For example, asymptotic giant branch (AGB) stars, which are evolved low-to-intermediate-mass ($1 - 8\,M_{\odot}$) stars in a thermally pulsing phase, shed large amounts of material via strong winds, enriching the ISM mainly with carbon and nitrogen, but also with elements produced through the s-process (slow neutron capture), such as strontium and barium. Massive stars experience strong stellar winds, particularly during their Wolf-Rayet phase, which release the aforementioned metals into the ISM. Whereas the production of metals and their yields, as well as the specific energy output, for SNe II and AGB stars depend on their intrinsic properties, i.e. initial stellar mass and metallicity, that is not the case for SNe Ia, i.e. all SNe Ia (at least of a

similar sub-type) output approximately the same amount of energy, mass, and metals.

A collection of stars formed temporally and spatially coherent (i.e. at the same time in a similar region) of common initial metallicity, but of varying masses as a result of their IMF, can be approximated as a single homogeneous population, called a simple stellar population (SSP). In cosmological simulations, this is the dominant approach to treating the evolution, feedback, and enrichment from stars. Each stellar particle (of mass thousands to many millions times that of the Sun) is assumed to represent a SSP formed with a chosen IMF and initial metallicity of the gas particle that was converted into it. The metal output of a star particle is then computed at each time step by integrating the yields over the IMF, with contributions from the discussed metal enrichment processes, though there are models which include fewer or greater numbers of enrichment channels. SIMBA-C (see Sec. 1.8.3), our flagship cosmological simulation (Hough et al., 2023, 2024), uses the `Chem5` chemical enrichment model (Kobayashi et al., 2020a,b), which I discuss in Sec. 1.7.4, whereas the original SIMBA simulation (Davé et al., 2019) employs its own model composed of instantaneous and delayed components (see Sec. 1.8.1).

1.7.2 How do metals become part of the IGrM?

The exact range of processes that bring metals both physically out of galaxies and out of the ISM phases into the hot diffuse phase of the IGrM, and how they work in different contexts, are not comprehensively understood at present. Outflows have been observed ubiquitously in galaxies across a range of redshifts (McCarthy et al., 1987; Heckman et al., 1990, 2000, 2015; Martin, 1999, 2006; Martin et al., 2012; Rupke et al., 2005; Weiner et al., 2009; Sturm et al., 2011; O'Sullivan et al., 2012; Maiolino et al., 2012, 2024; Bradshaw et al., 2013; Veilleux et al., 2013; Sell et al., 2014; Turner et al., 2014; Villar Martín et al., 2014; Arribas et al., 2014; Ford et al., 2014; Harrison et al., 2014; Williams et al., 2015; Perna et al., 2017a,b; Fiore et al., 2017; Davies et al., 2019; McQuinn et al., 2019; Fluetsch et al., 2021; Perrotta et al., 2023; Xu et al., 2023; Cresci et al., 2023; Carniani et al., 2024; Weldon et al., 2024; Vayner et al., 2024; Torres-Papaqui et al., 2024; Salehirad et al., 2025; Gianolli et al., 2024; Ferrara, 2024; Dan et al., 2025). These outflows are capable of shuttling metals to various distances from their production sites (Moll et al., 2007; Barai et al., 2011; Chisholm et al., 2018; Martín et al., 2024), and such energetic feedback is probably required to do so (e.g. Scannapieco et al., 2005). Prior to the full assembly of a group or cluster, its gravitational potential well was shallower, likely enabling outflows to be more effective at shuttling gas fully out of galaxies (e.g. Mori et al., 2002; Ferrara, 2024). Therefore, it is thought that much

of the enrichment may have occurred in the protogroup/protocluster phases (e.g. Scannapieco et al., 2005; Mantz et al., 2017; Flores et al., 2021; Brauer et al., 2024; Blackwell & Bregman, 2025).

Because the sources of metals and stellar feedback, like stellar winds and SNe, coincide (i.e. they both originate from stars), stellar feedback is expected to play a critical role in redistributing metals. Galactic outflows - or "superwinds" - driven by energy and momentum input from SNe, as well as photoheating and radiation pressure from massive stars, can propel metal-enriched gas from star-forming regions out of the galactic disk into the halo (Murray et al., 2009; Hopkins et al., 2012, 2014; Krumholz & Thompson, 2013; Bradshaw et al., 2013; Geach et al., 2014a,b; Sell et al., 2014; Somerville & Davé, 2015; Chisholm et al., 2018). Energy injection by SNe is potentially also able to heat the gas-phase metals to temperatures closer to that of the IGrM. Many theoretical studies have investigated such a scenario, finding considerable but varying levels of success in matching a wide range of enrichment-related observations (e.g. Davé et al., 2006, 2008, 2016; Davé, 2008; Oppenheimer & Davé, 2006, 2008, 2009; Oppenheimer et al., 2009; Finlator & Davé, 2008; Finlator et al., 2011a,b; Hirschmann et al., 2013, 2016; Hirschmann & De Lucia, 2016; Hirschmann, 2016; Somerville & Davé, 2015; Liang et al., 2016; Sun et al., 2024; Wijers et al., 2024).

Simultaneously, though, it has also been found that stellar feedback on its own is not necessarily sufficient to quench galaxies and maintain their quiescence to the degree observed in the real universe (e.g. Geach et al., 2014a; Su et al., 2019a; Bassini et al., 2023), and some combination of stellar and AGN feedback is more likely to be how quenching proceeds (e.g. Hopkins et al., 2016), as briefly discussed in Sec. 1.3.4. In general, the collective energy output of stellar feedback is likely not sufficient to overcome the deeper gravitational potential wells of more massive systems, like rich clusters, even in their protocluster phases. It may, however, contribute to gas expulsion more significantly in lower mass groups, albeit still potentially hand in hand with - or even sub-dominant to - other mechanisms.

Therefore, in concert with stellar feedback, it is possible that AGN feedback must also contribute to metal redistribution, with a relative importance that may increase with halo mass. AGN can power much more energetic and efficient outflows than SNe, including the collimated jets and wide-angle winds discussed in Sec. 1.3.4. Jets may be able to transport gas to large distances from the galaxy centre, while radiative feedback could heat the gas, reducing the cooling efficiency and enabling it to be dispersed more effectively throughout the IGrM (e.g. Murray et al., 2005; McCarthy et al., 2011; Taylor & Kobayashi, 2015; Nelson et al., 2019). If this gas were to already be enriched with metals from stars (i.e. pre-enriched), such feedback could be important for the enrichment of the IGrM (Gaspari et al., 2011a,b;

Taylor & Kobayashi, 2015); see the schematic in Figure 1.5.

Simulations that reproduce the observed flat outskirt metallicity profiles in the ICM (e.g. Sijacki & Springel, 2006a; Fabjan et al., 2010; Short et al., 2013; Martizzi et al., 2016; Biffi et al., 2018b; Choi et al., 2020, see the inset of Figure 1.10) indicate that early AGN activity in the protocluster phase (when the gravitational potentials of halos are shallower, as discussed) is necessary on top of stellar feedback to eject metals out of galaxies prior to the fully-fledged formation of clusters, since stellar feedback alone is not as effective at distributing enriched material far from star formation sites (Biffi et al., 2018a; Werner & Mernier, 2020). This could occur via the generation by jets of buoyant X-ray bubbles (e.g. Jennings et al., 2025; Duan et al., 2024; Duan & Guo, 2024), lifting metals from the core out to the ICM (Dalla Vecchia et al., 2004; Sijacki & Springel, 2006a,b; Roediger et al., 2007). Whether this applies at the group scale - or even is the dominant mechanism - is unclear, but, as discussed, AGN feedback has the potential to be more effective at gas redistribution from central galaxies to halos in groups than in clusters.

Possible evidence of this process in the low-z universe has been found in the clusters M87 (Simionescu et al., 2008), Hydra A (Simionescu et al., 2009; Kirkpatrick et al., 2009), the *Teacup* quasar (Martín et al., 2024), and a host of other massive systems (e.g. Kirkpatrick et al., 2011; David et al., 2011; Doria et al., 2012), in which metal-rich gas is observed within galaxies (outside the central nuclei) along the radio jets of the central AGN and around their ionized X-ray cavities. Examples of this are shown in Figure 1.11. Such a phenomenon is likewise found in cosmological simulations (e.g. Gaspari et al., 2011a,b; Pillepich et al., 2021). X-ray observations of clusters at high redshift ($1 \lesssim z \lesssim 2$) also provide indirect evidence inferred from the time evolution of ICM metallicity that the majority of enrichment did occur at early times (e.g. Flores et al., 2021).

On the flipside, this characteristic is not ubiquitous, i.e. there are observed clusters that do *not* have metal enrichment along galactic outflows, jets, or bubbles/cavities (c.f. Harrison et al., 2014). Although there are hints of a similar process at the group scale (O'Sullivan et al., 2005a, 2011; Laganá et al., 2015), equivalent observational studies are still lacking (Gastaldello et al., 2021). Furthermore, some examples of the *anti*correlation of AGN jets and metallicity have been found in observations of groups (e.g. Randall et al., 2015; Gendron-Marsolais et al., 2017). The same process has also not been seen at high redshift ($z \gtrsim 2$) in protocluster environments, so direct evidence of the dominant metal redistribution process(es) in groups and clusters is not yet available.

Moreover, high resolution simulations have shown that AGN outflows originating from the centres of galaxies likely do not interact with most of the galactic disk; rather, the

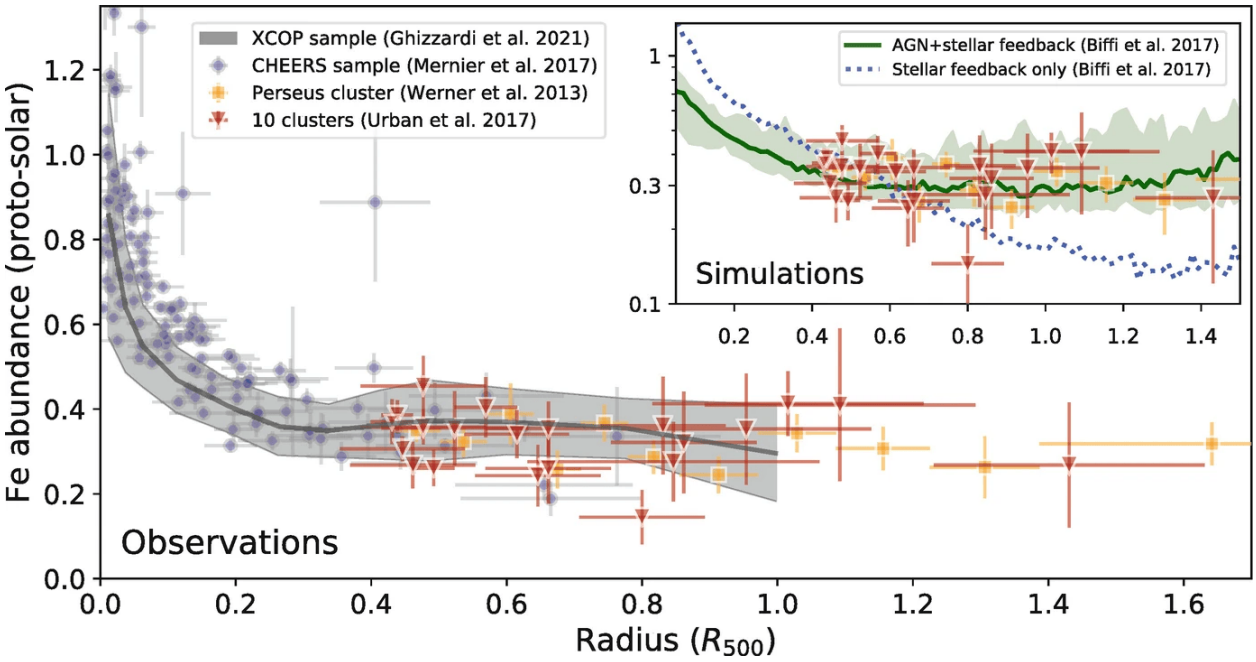

Figure 1.10: Reproduced from Mernier & Biffi (2022). Compilation of radial profiles of Fe abundance in cool-core clusters from the literature. The main panel shows measurements from observations: the XCOP (Ghizzardi et al., 2021) and CHEERS samples (Mernier et al., 2017) using XMM-*Newton*/EPIC and measurements at cluster outskirts using *Suzaku*/XIS (Werner et al., 2013; Urban et al., 2017). The inset panel compares the latter outskirt measurements with predictions from the DIANOGA cosmological hydrodynamical simulations (Biffi et al., 2017), assuming either solely stellar feedback or including AGN feedback as well. Abundances are all expressed in units of Asplund et al. (2009).

high-velocity nuclear outflows shock in the inner ∼kpc, transitioning into an expanding wind that, upon encountering the disk, takes the path of least resistance such that it is funneled through the less dense regions (the "cavities" of the sponge-like ISM) and exits the ISM close to the centre of the galaxy and perpendicular to the disk (e.g. Faucher-Giguère & Quataert, 2012; Gabor & Bournaud, 2014, see also Borodina et al. (2025) for a recent study). These winds are found to leave the metal-enriched ISM unaffected. In this way, AGN-induced metal redistribution does not necessarily provide a concrete solution as to how metals become part of the IGrM.

Other processes may also play a role to varying degrees (Schindler & Diaferio, 2008; Werner & Mernier, 2020; Gastaldello et al., 2021), including:

- Ram-pressure stripping. As galaxies traverse the IGrM (for example, during a minor merger, or even a major merger), the pressure exerted by the hot gas can strip away the galaxy's own gas, including the metal-rich ISM, contributing to enrichment of the IGrM

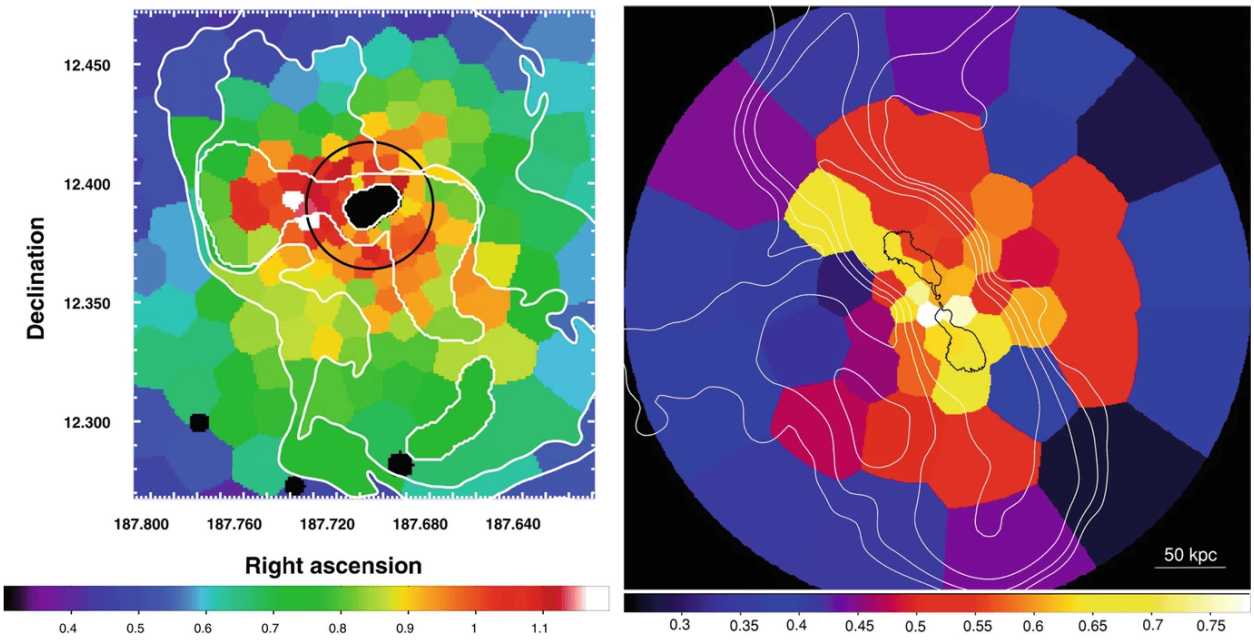

Figure 1.11: Reproduced from Werner & Mernier (2020). Projected Fe abundance maps for the hot atmospheres of M87 (left panel; Simionescu et al. (2008)) and the Hydra A cluster (right panel; Kirkpatrick et al. (2009)). The 330 MHz and 1400 MHz radio contours, over-plotted in white and black, respectively, trace the jets from the central supermassive black hole.

(e.g. Ehlert et al., 2013; Eckert et al., 2017b; O'Sullivan et al., 2019). This process is especially effective in environments like massive groups or clusters, where the densities and relative velocities are higher.

- Tidal stripping. A galaxy that experiences a gradient in an external gravitational potential, like that of a galaxy group, can have the outer layers of its ISM preferentially stripped via differential tidal forces, adding metal-enriched gas to the IGrM (e.g. Sheardown et al., 2019).

- Sloshing. When the bulk or a portion of the IGrM is slightly displaced from its potential well, e.g. by a minor merger, oscillatory motions occur due to the positive entropy gradients in the IGrM being stable against convection, i.e. after a perturbation, a "parcel" of IGrM oscillates rather than continuing to rise or sink (Tittley & Henriksen, 2005; Ascasibar & Markevitch, 2006; Roediger et al., 2024). This leads to a characteristic, outwards-moving coherent pattern of local compressions and rarefactions, which has the potential to redistribute metals on large scales (e.g. ZuHone et al., 2011, 2012, 2014, 2016a,b; ZuHone, 2011; Roediger et al., 2011, 2013; Brzycki & ZuHone, 2019).

Sloshing has been observed in multiple clusters (e.g. Markevitch et al., 2003; Markevitch & Vikhlinin, 2007; Simionescu et al., 2010; Ghizzardi et al., 2010, and see ZuHone & Roediger (2016) for a review), with some studies finding indications that metal redistribution has occurred (e.g. Kraft et al., 2006; Gu et al., 2007; Gitti et al., 2010; Rafferty et al., 2013; O'Sullivan et al., 2014; Hu et al., 2019).

- Intra-group stars. A significant fraction of stars reside in the IGrM itself and do not belong to any galaxy. They can produce metals via nucleosynthesis, and directly release them into the IGrM through stellar winds and SNe (e.g. Sivanandam et al., 2009; Liang et al., 2016).

- Cosmic rays. Cosmic ray-driven winds may contribute to the transport of metals from the ISM to IGrM (e.g. Hopkins et al., 2021).

While the aforementioned mechanisms heat gas-phase metals and drive their redistribution from galaxies into the IGrM, a critical physical process for mixing these metals throughout the hot diffuse gas is known as turbulent diffusion. As described in Rennehan et al. (2019):

> Turbulence occurs when inertial forces dominate viscous forces in a gaseous environment, and kinetic energy on large scales cannot immediately dissipate as heat. This leads to the formation of a kinetic energy cascade, as coherent turbulent eddies on large scales spawn eddies on successively smaller scales, until the energy thermalizes.

Turbulent diffusion hence refers to the mixing and spreading of energy and material, such as metals, due to small-scale turbulent fluctuations. In astrophysical contexts, this process is propelled by the energy injection from the discussed mechanisms, such as stellar feedback events, AGN outflows, and satellite wakes. Unlike molecular diffusion, which occurs due to random motions of individual particles and is relatively slow, turbulent diffusion significantly enhances mixing by transporting substances across larger distances and shorter timescales due to turbulent eddies and vortices. The irregular, chaotic motions in turbulent diffusion break up concentration gradients, leading to more homogeneous distributions across a medium. This process is crucial in the IGrM and ICM, where injected metals are mixed with the surrounding hot gas to produce approximately uniform metallicity distributions at large radii (Sharma et al., 2009; Banerjee & Sharma, 2014). Turbulence generated during mergers, galactic motions, or gas sloshing further enhances mixing, spreading metals even to outer regions of groups (Gaspari & Churazov, 2013; Rasia et al., 2015). Interactions with bulk

flows and AGN-driven outflows further extend the impact of turbulent diffusion on the metal distribution, making it a vital process in the chemical evolution of the IGrM (Sembolini et al., 2013; Bourne & Sijacki, 2017).

The relative contributions of all of these processes are not well pinned down, and likely depend on factors like system mass and temperature, as well as surrounding environment. Based on a range of studies, Gastaldello et al. (2021) conclude that, broadly speaking, the primary physical mechanisms responsible for the observed 2D metallicity maps of the IGrM are AGN feedback and ongoing mergers, likely often operating in unison (e.g. Kraft et al., 2004; Su et al., 2019b). Liang et al. (2016) employ a cosmological hydrodynamical simulation (*without* AGN feedback) to investigate the growth and enrichment of the IGrM. They find that in lower mass ($k_{\rm B}T \lesssim 0.8$ keV) $z = 0$ groups, the largest source of Fe is intragroup stars (IGS; stars in a group halo not bound to any galaxies), with central, satellite, and "external" (other) galaxies each providing a similar lower level of IGrM Fe enrichment. On the other hand, higher mass groups ($k_{\rm B}T \sim 0.8 - 2$ keV) have more similar contribution across Fe enrichment sources, with central galaxies leading slightly. The situation is somewhat different for Si and O: for Si, the IGS and external galaxies are slightly more prominent in very low mass groups while the central galaxy again leads in higher mass groups, whereas for O, external galaxies lead in lower mass groups and both central and external galaxies lead in higher mass groups. This demonstrates a complex dependence of the dominant and sub-dominant enrichment sources on not just mass/temperature scale, but also on the specific metal under consideration.

Our understanding of cosmic chemical enrichment is continually evolving, from the details of element production pathways in stellar interiors, to the modes by which different elements are ejected from stars, to the dominant mechanisms through which these elements become part of different phases. It is crucial to upgrade the models of chemical enrichment used in cosmological simulations to reflect the state of the art in knowledge, and assess how they impact many aspects of these simulations. However, this is tempered by computational limitations of large-scale simulations, including available computational resources and running time, as well as the maximum resolution possible given these restrictions. Therefore, compromises must be made in terms of which aspects of a model are most relevant to the formation and evolution of galaxies, groups, and clusters.

1.7.3 What are the outcomes of different enrichment scenarios?

The IGrM is primarily composed of gaseous H and He, but contains trace amounts of heavier metals from C up to Ni, as produced according to the processes described in Sec. 1.7.1 and brought to the IGrM by the mechanisms discussed in Sec. 1.7.2. As a result, the absolute and relative abundances of these metals in the IGrM, as well as their spatial and temporal distributions, can provide information on the underlying physical mechanisms operating in galaxy groups and the IGrM and clues as to how they form, evolve, and interact with their environments.

A key current question is: When did the majority of cosmic enrichment occur? And by association, which physical mechanisms are responsible for the transport of metals from stellar-scales out to group and cluster scales? These questions are highly relevant for current and upcoming X-ray observational facilities, like the X-Ray Imaging and Spectroscopy Mission (XRISM), the Advanced Telescope for High-ENergy Astrophysics (ATHENA; see Mernier et al. (2020) for predictions of its constraining abilities), the Advanced X-ray Imaging Satellite (AXIS), and *Lynx*. Diversity can (and likely does) exist in the exact enrichment pathways of individual systems, and even across general classifications (e.g. CC vs NCC systems), mass scales, and other properties (e.g. Biffi et al., 2017; Mernier et al., 2017; Biffi et al., 2018b; Mernier et al., 2022). Broadly, though, there are two main enrichment scenarios: i) pre-/early enrichment and ii) late/ongoing enrichment.

The early enrichment (or pre-enrichment) scenario for galaxy groups and clusters posits that a significant fraction of the metals observed in the IGrM and ICM was produced and distributed at high redshift, well before the assembly of these large-scale structures. During the early universe (at $z \gtrsim 2-3$; Werner & Mernier (2020); Mernier & Biffi (2022)), prior to or during the main epoch of star formation and AGN activity (Madau & Dickinson, 2014), intense star formation and SN activity in young galaxies led to the production and enrichment of heavy elements. Feedback mechanisms such as SN-driven winds and AGN outflows then ejected these metals into the surrounding IGM, enriching it with heavy elements[23]. This enrichment process occurred before or during the early stages of group and cluster formation, resulting in the widespread distribution of metals throughout the protogroup and protocluster environments. As groups and clusters formed via gravitational collapse and hierarchical merging, the pre-enriched gas was incorporated into the IGrM and ICM. Potential consequences of this scenario include: a limited metallicity evolution at lower redshifts ($z \lesssim 2$)

[23] Blackwell & Bregman (2025) discuss the previously-theorized existence of such an "Early Enrichment Population" of stars at high redshifts ($z \sim 10$), the properties (e.g. IMF) it must have to reproduce observations, and predictions it makes.

due to the "fixing" of abundances in stars and the hot gas; relatively flat radial abundance profiles from the significant amount of time peri- and post-enrichment to mix metals into the IGrM and ICM; and similar levels of enrichment between the IGrM and ICM.

In contrast, the late enrichment scenario suggests that metal enrichment predominantly occurred after the primary assembly of galaxy groups and clusters, through continuous star formation and feedback in the group and cluster galaxies, primarily at lower redshifts ($z \lesssim 1$). In this case, metals are injected into the IGrM and ICM by ongoing SNe, stellar winds, and AGN activity within the galaxies. Consequently, the late enrichment scenario would predict a more centrally concentrated metal distribution, with metallicity decreasing towards the cluster outskirts, as well as more time- and mass-dependent levels of enrichment.

In fact, the well-stratified entropy of today's IGrM and ICM would inhibit the mixing of metals and "freeze" their spatial distribution to some extent (Mernier & Biffi, 2022), providing us with a simple test to differentiate between the two enrichment scenarios. It is important to note, however, that other factors, such as the efficiency of metal mixing and diffusion and the repeated churning of the hot gas due to mergers (which can alter its entropy), may be just as significant and result in IGrM properties (e.g. degree of metallicity temporal evolution, abundance profile shapes, enrichment contrast between groups and clusters) that are less sensitive to the epoch at which the majority of enrichment occurs. Further, in reality, both enrichment scenarios likely operate in most systems, especially in lower mass groups in which the central galaxy remains star-forming at late times (since the quenching of a galaxy limits the available metals for enrichment, sustained star formation in this fashion enhances the contribution by late enrichment).

X-ray observations of local galaxy clusters out to and past R_{500}, and even in some cases R_{200} or the virial radius R_{vir}, exhibit abundance profiles that flatten and reach a uniform enrichment of ~ 0.3 Solar (see Figures 1.2 and 1.10), assuming recent reference solar values, like from Asplund et al. (2009) (e.g. Leccardi & Molendi, 2008; Sivanandam et al., 2009; Simionescu et al., 2009; Werner et al., 2013; Molendi et al., 2016; Urban et al., 2017; Lovisari & Reiprich, 2019; Ghizzardi et al., 2021; Sarkar et al., 2022). Observations also show minimal or no redshift evolution of the metallicity of both cluster cores (Ettori et al., 2015; Mantz et al., 2017; Liu et al., 2020) and outskirts (McDonald et al., 2016; Mantz et al., 2017; Flores et al., 2021) at $z \lesssim 1-2$, with cosmological simulations providing similar results (Biffi et al., 2017; Vogelsberger et al., 2018; Robson & Davé, 2021; Pearce et al., 2021; Hough et al., 2024). Examples of this are shown in Figure 1.12. Lastly, the level of enrichment from group to cluster scales appears quite uniform (Mantz et al., 2017; Mernier et al., 2018c; Gastaldello et al., 2021, see Figure 1.9). Observational evidence therefore appears to support the early

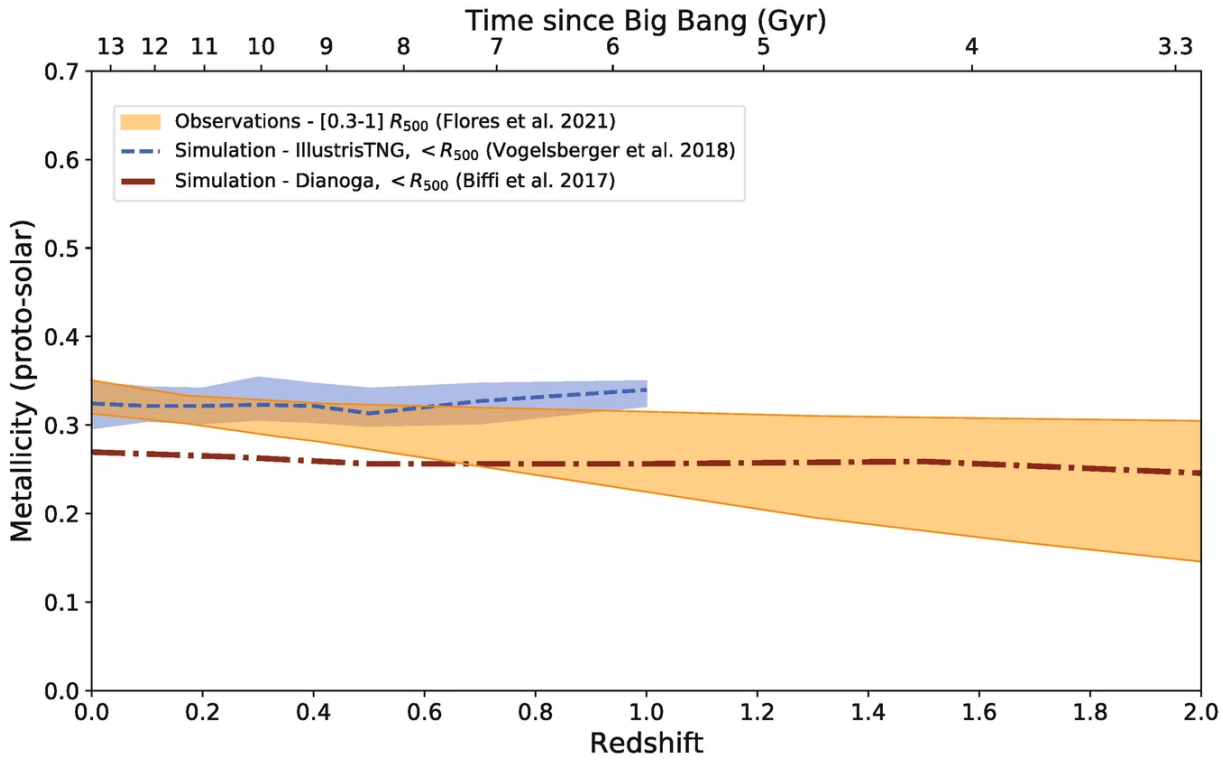

Figure 1.12: Reproduced from Mernier & Biffi (2022). Redshift evolution of cluster metallicities, as seen by recent observations (Flores et al., 2021) and as predicted by cosmological simulations – DIANOGA (Biffi et al., 2017) and ILLUSTRISTNG (Vogelsberger et al., 2018). Metallicities are all expressed in units of Asplund et al. (2009).

enrichment scenario, although, again, contributions from both processes are likely required to explain the detailed metal abundance profiles (de Plaa, 2013; Mernier et al., 2018a).

Cosmological simulations are not yet at the level to consistently and robustly predict and constrain detailed features of abundance profiles, in particular their slopes; nonetheless, they can provide great insight into the physical processes, such as stellar and AGN feedback, that may play a role in such observations. It is of interest to investigate the degree to which the details and realism of a chemical enrichment model are also central to the redistribution of metals in the IGrM and setting their abundance profiles.

Several studies involving cosmological simulations have specifically investigated IGrM abundance profiles (e.g. Kapferer et al. (2007, 2009), Guo & Mathews (2010), McCarthy et al. (2010) (OWLS), Rasia et al. (2015), Biffi et al. (2017, 2018b) (DIANOGA), Barnes et al. (2017) and Pearce et al. (2021) (CLUSTER-EAGLE), Barnes et al. (2018) and Vogelsberger et al. (2018) (ILLUSTRISTNG), Robson & Davé (2020) and Padawer-Blatt et al. (2025) (SIMBA/SIMBA-C), Nelson et al. (2024) (TNG-CLUSTER), Braspenning et al. (2024)

(FLAMINGO)), although they rarely focus on the chemical enrichment model employed and only sometimes investigate the abundances of individual elements besides Fe. This is in part due to the relatively large uncertainties inherent to key components of these models, like metal yields. Their general results include:

- Limited late-time abundance profile evolution in the outer regions of groups and clusters, consistent with the idea of early enrichment (Kapferer et al., 2007, 2009; Guo & Mathews, 2010; Barnes et al., 2018; Vogelsberger et al., 2018; Pearce et al., 2021; Braspenning et al., 2024).

- Overall approximate agreement with observations for high mass groups and clusters, including both Fe abundance profiles and additionally α element abundance profiles, but greater discrepancy at the group scale (Barnes et al., 2017; Vogelsberger et al., 2018; Pearce et al., 2021; Nelson et al., 2024; Braspenning et al., 2024; Padawer-Blatt et al., 2025).

- The need for AGN feedback on top of stellar feedback to produce flat outskirt abundance profiles in the ICM (e.g. McCarthy et al., 2010; Biffi et al., 2017, 2018b).

- Relatively flat, close to Solar, radial X/Fe profiles[24] (Biffi et al., 2017; Vogelsberger et al., 2018; Pearce et al., 2021).

From these findings, it is clear that cosmological simulations have improved to a point at which they are sufficient to match and potentially predict observations of the ICM, at the high masses and temperatures of closed-box systems like galaxy clusters. On the other hand, there are fewer simulation-based studies of the metal content of the IGrM at the group scale, and those that do exist find larger discrepancy with observations. Deeper understanding of the physics and mechanisms driving the enrichment of the IGrM is critical to improve sub-grid models in simulations. This includes the complex processes and pathways of chemical enrichment and stellar feedback.

[24]X/Fe corresponds to the ratio of the abundance of some metal X to that of Fe. It is commonly used in observational astronomy because Fe is well-constrained, and most other X-ray-measurable metals are α elements that largely originate from core-collapse SNe, whereas Fe largely originates from SNe Ia, thus providing a view of the relative contributions of these two sources to the overall enrichment. C and N lines are occasionally accessible in spectral observations as well, and these metals mostly come from AGB stars, so C/Fe and N/Fe are additionally useful ratios.

1.7.4 The Chem5 Model

Chem5 is the "version-5" of a self-consistent[25] 3D chemodynamical enrichment model developed by Kobayashi (2004); Kobayashi et al. (2007); Taylor & Kobayashi (2014), with continued development by Kobayashi & Nakasato (2011) and Kobayashi et al. (2020a,b). It is the key upgrade in the new SIMBA-C cosmological simulation, overhauling the "instantaneous recycling of metals" approximation used in SIMBA (see Sec. 1.8.1 for a definition). In this section, I will provide a very brief overview of the components of this model, but the interested reader may refer to Kobayashi et al. (2020a,b) for an in-depth description, including the full yield tables, or to Hough et al. (2023) or Padawer-Blatt et al. (2025) for a succinct summary.

Chem5 tracks the production and cycling of all elements on the periodic table from hydrogen (H) to germanium (Ge). It implements various physical processes accounting for a diverse array of stellar feedback channels and enrichment pathways, including those from core-collapse SNe (covering SNe II, hypernovae (HNe), and "failed" SNe), SNe Ia, and stellar winds from stars of all masses (including AGB and super-AGB stars).

In Chem5, stellar winds (which for nomenclature purposes covers both "true" stellar winds from stars and SN-induced outflows when discussing Chem5) are the mechanism through which both processed metals (i.e. those formed through nucleosynthesis within a star) and unprocessed metals (i.e. those locked in a star's envelope since its formation) are returned to the ISM. Only the former are included in the yields for SNe, while both are included for AGB stars (Kobayashi et al., 2020b). The mass ejected by stellar winds, which contains the metals, is given by

$$M_{\rm wind} = M_{\rm init} - M_{\rm remnant} - \sum_i p_{z_i m} \tag{1.1}$$

where $M_{\rm init}$ is the initial stellar mass, $M_{\rm remnant}$ is the remaining mass (e.g. of a black hole, neutron star, or white dwarf) that is left over after a star "dies" or ejects winds, and $p_{z_i m}$ is the nucleosynthetic yield of element i (i.e. the mass of element i released from a given stellar feedback event, dependent on the enrichment channel). Therefore, the mass of the winds is the difference between the initial mass of a star and whatever "remains" after it has gone through some stellar feedback event (i.e. the remnant and the mass of metals injected into nearby ISM gas that does not form a wind). For stars of $M_{\rm init} = 0.7\,{\rm M}_\odot$ and $M_{\rm init} = 0.9\,{\rm M}_\odot$, the helium core mass is set to $M_{\rm remnant} = 0.459\,{\rm M}_\odot$ and $M_{\rm remnant} = 0.473\,{\rm M}_\odot$, respectively, with $p_{z_i m} = 0$.

Through their evolution, stars pass through the thermally pulsing AGB phase, which

[25] Self-consistent here means that the metal return from stars follows a detailed stellar evolution model with mass- and metal-dependent yields.

can occur for stellar masses of $\sim 0.9 - 8\,M_\odot$ depending on the metallicity. These stars can produce various metals on their surface, such as ^{12}C, ^{14}N, ^{23}Na, and Al, via proton-capture nucleosynthesis in the convective envelope and the subsequent mixing of core and envelope metals due to an unstable He-burning shell (producing ^{12}C); they then undergo such processes as the CNO, NeNa, and MgAl cycles to produce other elements. Stellar winds eject these metals over the star's lifetime. These yields are calculated in `Chem5` as the difference between the amount of the element in the wind and the initial amount in the progenitor star's envelope.

The metal production and enrichment pathways of super-AGB stars - stars with initial masses between 8 and 10 $M_\odot$ - are currently less certain (Doherty et al., 2014b). The upper mass limit of AGB stars is accepted to be the minimum mass required for C ignition, $M_{\rm up,C} \sim 10\,M_\odot$. Below this, C and Ne ignition, either off-centre or in the core depending on the mass, can result in WDs if the outer shell is lost through stellar winds. The yields for these processes up to Ni from Doherty et al. (2014a,b) are included in `Chem5`.

For SNe Ia yields, `Chem5` assumes that all SNe Ia progenitors are Chandrasekhar-mass WDs (as opposed to sub-Chandrasekhar-mass), which is reasonable since this pathway occurs the majority of the time ($> 75\%$; Kobayashi et al. (2020a)). In particular, a singly-degenerate system, in which a WD's mass grows by accreting mass from a H-rich companion (instead of the doubly-degenerate scenario of two merging WDs) is assumed. Because the energy and mass output of SNe Ia are known to often occur delayed relative to the time of WD formation, a SN Ia lifetime distribution function[26] is computed, taking into account the metallicity dependence of WD winds (Kobayashi et al., 1998) and the mass stripping effect on the binary companion (Kobayashi & Nomoto, 2009). This results in a double peak, the times of which depend on the type of WD companion; these times are $\sim 0.1 - 1$ Gyr for main sequence stars and $\sim 1 - 20$ Gyr for red giants (Kobayashi & Nomoto, 2009; Kobayashi et al., 2020a). The associated metal yields are calculated with simulations of delayed detonations in Chandrasekhar-mass WDs for various metallicities and solar-scaled initial compositions (Kobayashi et al., 2020a).

Core-collapse SNe yields are computed from 1D simulations (Kobayashi et al., 2006, 2011), in which the yields for the individual types of massive star SNe are taken from Woosley & Weaver (1995), Nomoto et al. (1997), and Limongi et al. (2003), and constantly being updated. To address uncertainties in the yields, quantities such as explosion energy and ^{56}Ni mass are constrained independently through light curve and spectral fitting of an observed SN (Kobayashi et al., 2006; Nomoto et al., 2013; Kobayashi et al., 2020b). As a consequence

[26] A lifetime distribution function parametrizes the typical lifetimes of stars with different masses, and thus when they actively eject mass, metals, and energy.

of this, hypernovae (HNe; Kobayashi et al., 2020b), which are core-collapse SNe with masses $M > 20\,M_{\odot}$ and explosion energies greater than $10\times$ that of a regular SN, are included in `Chem5`. Of note, HNe produce more Fe and α elements (e.g. Si, S, Ar, Ca) than regular SNe II. The nucleosynthesis yields of SNe II and HNe are provided separately as a function of progenitor mass and metallicity.

Lastly, a new pathway, called 'failed' SNe, is introduced to take into account SNe II from stars with initial mass $M > 30\,M_{\odot}$ (Kobayashi et al., 2020b), for which it is observationally unclear (as well as from simulations) whether they can occur. For these yields, it is assumed the stellar CO cores fall onto black holes and are not ejected into the ISM, thus leaving the upper mass limit as a free parameter. The yields and upper mass limit for HNe are separate and not affected by this.

1.8 Cosmological Simulations and the `SIMBA` Suite

Cosmological hydrodynamic simulations are the test bed for investigating the results of different galaxy formation and evolution models, and whether these results match observations. These simulations have collisionless dark matter, star, and SMBH particles whose dynamics are determined by gravitational physics, and collisional gas particles additionally subject to a range of baryonic processes including cooling and heating, star formation, stellar feedback, AGN feedback, and metal enrichment (Somerville & Davé, 2015; Vogelsberger et al., 2020; Crain & van de Voort, 2023). Using such galaxy formation models, it is possible to simulate galaxy formation and evolution in a cosmological context, capturing important processes like galaxy mergers, gaseous fueling of galaxies via large-scale flows, galactic winds, and the evolution of galaxies in different environments. The main challenge is to ensure that galaxy formation simulations produce realistic results.

While I do not dive into the details of different types of cosmological simulations (e.g. mesh-based, particle-based), I describe here their primary components. The foundation on which they are built is the concept of N-body simulations. An N-body simulation is a computational method employed to model the gravitational interactions of a large number of particles (or "bodies") that represent components of a system. In these simulations, the forces (e.g. gravity) between all pairs of particles are calculated, and their positions and velocities are updated over time. The complexity of N-body simulations grows significantly with the number of particles, requiring sophisticated algorithms and powerful computing resources to handle the computations efficiently.

In cosmological simulations, both gravitational and hydrodynamic components are crucial

for accurately modeling the large-scale structure of the universe and the evolution of galaxies. The gravitational component tracks the motion of particles under mutual gravitational attraction according to Newton's laws. It typically uses algorithms like tree codes, particle-mesh (PM) methods, or hybrid methods that combine tree and grid-based approaches to compute the forces. For example, the tree code reduces computational cost by approximating the gravitational influence of distant particles as a single mass, while PM methods solve for gravitational potential on a grid (Vogelsberger et al., 2020).

The hydrodynamic component, on the other hand, models the behavior of gas within the universe as a fluid, taking into account processes like compression, shock waves, and cooling. This is implemented using techniques like Smoothed Particle Hydrodynamics (SPH), which treats fluid elements as particles, or grid-based methods like Adaptive Mesh Refinement (AMR), which solve the equations of fluid dynamics on a spatial grid that adapts to the resolution required. SPH is more suitable for simulations with complex geometries, while AMR provides higher accuracy in regions of interest by increasing the grid resolution where needed.

One of the drawbacks - or some may argue, the single greatest drawback - of cosmological-scale simulations is the coarseness at which they must be constructed due to computational limitations. The N-body approach requires the discretization of the simulation, and thus engenders the idea of numerical resolution, forcing one to choose a specific number of simulation elements, the value of which must compromise between the available computational resources and the resolution necessary to capture the desired processes. Similarly, the gravity and hydrodynamics components entail placing a lower limit on the spatial lengths considered (determined by the "softening length" for gravity, and by the grid size in grid-based methods or the "smoothing length" in SPH for hydrodynamics), the particle masses (specifically, for dark matter and gas), and the timesteps of the simulation. The physical drivers of many processes and feedback systems occur on spatial, mass, or temporal scales below these resolution thresholds. Consequently, sub-grid models are employed as representative calculations, and are implemented to reproduce the effects of these processes. They are commonly characterized by various normalizing parameters that are unknown ab initio, which are calibrated to chosen observations.

This approach works well for many galaxy properties, with different galaxy formation models generating successes across a range of cosmic epochs and environments. For an overview of recent progress, achievements, and problems, we refer the reader to Vogelsberger et al. (2020); Oppenheimer et al. (2021); Crain & van de Voort (2023), and references therein. However, there are known issues. One stems from the range of scales over which sub-grid

models are calibrated. Galaxy formation models are generally not calibrated to very low-mass systems (dwarf galaxies) or very high-mass systems (groups or clusters of galaxies). This leads to some of these systems' simulated physical properties being incorrect.

In the rest of this section, I introduce and describe the SIMBA and SIMBA-C cosmological hydrodynamic simulations (the two simulations with which I perform my analysis in Chapter 2), and briefly motivate the development of SIMBA-C. Table 2.1 lists all key differences between the sub-grid models of SIMBA and SIMBA-C.

1.8.1 SIMBA Simulation and Galaxy Formation Model

SIMBA[27] (Davé et al., 2019) - the successor to MUFASA (Davé et al., 2016) - is a large-volume cosmological hydrodynamic simulation and galaxy formation model built on the N-body gravity+hydrodynamics solver `GIZMO` in its meshless finite mass (MFM) mode (Hopkins, 2015, 2017). It is run with `MUSIC`-generated initial conditions from a redshift of $z = 249$ to $z = 0$, assuming a Planck Collaboration et al. (2020) flat ΛCDM cosmology with $\Omega_m = 0.3$, $\Omega_\Lambda = 0.7$, $\Omega_b = 0.048$, and $H_0 = 68\,\mathrm{km\,s^{-1}\,Mpc^{-1}}$.

GIZMO evolves dark matter and gas elements together with gravity and pressure forces, handling shocks via a Riemann solver with no artificial viscosity. The mass within each fluid element is preserved during evolution, enabling detailed tracking of gas flows, and performs well in standard hydrodynamics tests (Hopkins, 2015). In this way, it brings together the advantages of particle-based codes like adaptivity in space and time, with the hydrodynamics accuracy of Riemann solver-based mesh codes.

The main SIMBA suite is composed of seven different runs:

1. The flagship run in a box of volume $V = (100\,h^{-1}\mathrm{Mpc})^3$ with 2×1024^3 particles (1024^3 dark matter and 1024^3 gas) and full SIMBA physics. It uses a minimum Plummer-equivalent gravitational softening length of $0.5\,h^{-1}$kpc, an initial gas element mass resolution of $1.82 \times 10^7\,M_\odot$, a dark matter particle mass resolution of $9.6 \times 10^7\,M_\odot$, and has a minimum stellar mass of a resolved galaxy of $5.8 \times 10^8\,M_\odot$. This is the run I employ for comparison with SIMBA-C.

2. A $V = (50\,h^{-1}\mathrm{Mpc})^3$ box of 2×512^3 particles, with five feedback variants, namely full SIMBA physics, no X-ray AGN feedback (SIMBA NO-X), no X-ray or jet feedback (SIMBA NO-JET, just AGN winds), no AGN feedback (SIMBA NO-AGN), and no star formation/stellar feedback or AGN feedback (SIMBA NO-FB); see descriptions of sub-grid feedback models below. They use a minimum gravitational softening length of

[27] https://simba.roe.ac.uk/.

$0.25\,h^{-1}$kpc, an initial gas element mass resolution of $2.28 \times 10^6\,M_\odot$, a dark matter particle mass resolution of $1.2 \times 10^7\,M_\odot$, and have a minimum stellar mass of a resolved galaxy of $7.3 \times 10^7\,M_\odot$.

3. A high-resolution box of $V = (25\,h^{-1}\mathrm{Mpc})^3$ with 2×512^3 particles and full SIMBA physics. It uses a minimum gravitational softening length of $0.125\,h^{-1}$kpc, an initial gas element mass resolution of $2.85 \times 10^5\,M_\odot$, a dark matter particle mass resolution of $1.5 \times 10^6\,M_\odot$, and has a minimum stellar mass of a resolved galaxy of $9.1 \times 10^6\,M_\odot$.

Other simulations employing the SIMBA model, or components of it, exist, such as the HYENAS suite of "zoom" cosmological simulations[28] (Cui et al., 2024), the GIZMO-SIMBA runs of THE THREE HUNDRED PROJECT (Cui et al., 2022), the OBSIDIAN model (Rennehan et al., 2024), and SIMBA-C (Hough et al., 2023, 2024; Padawer-Blatt et al., 2025).

The following is a list of short descriptions of the sub-grid models in SIMBA:

- **Cooling and Heating:** The GRACKLE-3.1 library (Smith et al., 2017) is employed to model radiative cooling and photoionization heating, including metal cooling and non-equilibrium evolution of primordial elements.

- **Star Formation:** The sub-grid model of Krumholz & Gnedin (2011), with some modifications in Davé et al. (2016) to account for variations in numerical resolution, is used to compute the H_2 fraction for an H_2-based star formation rate (SFR), given by $\mathrm{SFR} = \varepsilon_* \rho_{H_2}/t_{\mathrm{dyn}}$ with $\varepsilon_* = 0.02$ (Kennicutt, 1998). Additionally, SIMBA uses artificial ISM pressurization at a minimum level required to resolve the Jeans mass in star-forming gas, as it can become smaller then the mass resolution at high densities and large cooling rates. Above a density threshold n_{th}, at which the temperature is assumed to be $T_0 = 10^4$ K the temperature, the gas element temperature is set to the Jeans minimum temperature $T_{\mathrm{JMT}} = T_0(n/n_{\mathrm{th}})^{1/3}$ (Davé et al., 2016).

- **Chemical Enrichment:** SIMBA tracks 11 elements (H, He, C, N, O, Ne, Mg, Si, S, Ca, and Fe), with production by SNe II, SNe Ia, and AGB stars and yield tables from Nomoto et al. (2006) for SNII, Iwamoto et al. (1999) for SNIa, and following Oppenheimer & Davé (2006) for AGBs. SNII and the prompt component of SNIa enrichment occurs in the instantaneous recycling approximation, in which the metals

[28]The zoom-in technique identifies a region of interest in a cosmological simulation, such as a galaxy group, and re-simulates it at higher resolution, while the surrounding cosmic environment is simulated at lower resolution.

are injected into the ISM by adding them to gas elements that are eligible for star formation (Oppenheimer & Davé, 2008; Davé et al., 2016). Specifically these gas elements "self-enrich" prior to turning into a star particle - effectively converting some of their hydrogen and helium mass into metal mass - at each timestep they are eligible for star formation. This is implemented under the assumption that all stars more massive than $1\,M_\odot$ die and explode instantaneously, while all stars less massive live forever (Matteucci, 2016), and that expelled gas and metals are instantly recycled back into the star-forming phase of the ISM[29]. On the other hand, AGB stars and the delayed component of SNIa provide enrichment from star particles that is delayed relative to the time of star formation. This is achieved by adding metals to the 16 gas elements nearest to a given star, in a kernel-weighted manner; for AGB stars, this is computed following the mass-loss rate assuming a Chabrier IMF (Chabrier, 2003).

- **Stellar Feedback:** SIMBA uses kinetic two-phase star formation-driven galactic winds, generated by SNe and AGB stars, in which 30% of wind particles are ejected "hot" (with a temperature set by the SN energy minus the wind kinetic energy) and 70% remain at the ISM temperature. This fixed fraction of 30% heated wind particles are hydrodynamically decoupled from their environment for some time, with radiative cooling turned off such that when they recouple they deposit their thermal energy into the CGM. The main recoupling criterion for a wind gas element is that it has a velocity difference with respect to the surrounding gas of less than 50% of the local sound speed. In cases where this has not been satisfied by the time a gas element has been decoupled for a duration of $0.02t_{\rm H}(z_{\rm launch})$, or if its surrounding gas density reaches 1% of the ISM threshold density (i.e. $0.01n_{\rm th}$), recoupling is also triggered. The mass loading factor η scales with stellar mass according to an analysis via particle tracking of the Feedback In Realistic Environments (FIRE) suite of simulations (Anglés-Alcázar et al., 2017b), which can be well fit by a redshift-independent broken power law at $M_0 = 5.2 \times 10^9\,M_\odot$ as

$$\eta(M_*) \propto \begin{cases} 9(M_*/M_0)^{-0.317}, & M_* < M_0 \\ 9(M_*/M_0)^{-0.761}, & M_* > M_0 \end{cases} \tag{1.2}$$

[29] In general, the equations of chemical evolution can be considerably simplified using the instantaneous recycling approximation, in which stars are divided into two classes: those below some mass m that live forever, and those above m that die as soon as they are born, immediately releasing their nucleosynthesis products (Talbot & Arnett, 1971). In this approximation, the immediately ejected metals are instantaneously recycled back into the star-forming gas that will go on to produce future stellar populations. However, this model can fail in various scenarios; see the review by Tinsley (2022) for details.

Below a galaxy stellar mass corresponding to 16 star particles, $\eta(M_*)$ is set to be flat to account for poorly resolved galaxies being unable to grow due to overly strong stellar feedback. On top of this, at $z > 3$, to allow for early galaxy growth, the mass loading is suppressed by a factor of $(a/0.25)^{f_a}$, where a is the cosmological scale factor and f_a is a value tuned based on the simulation resolution. The winds are artificially enriched by extracting some metals from nearby particles in a kernel-weighted manner (but always keeping the total metal mass conserved) according to $dZ = f_{\rm SNII} y_{\rm SNII}/{\rm MAX}(\eta, 1)$ to represent local enrichment by SNe-driven outflows, where $f_{\rm SNII} = 0.18$ is the stellar mass fraction lost to SNe, $y_{\rm SNII}$ is the metal-dependent SNII yield for each element, and η is the mass loading factor. The wind velocity is dependent on v_{circ} (determined with a scaling based on the baryonic Tully-Fisher relation) following Muratov et al. (2015), with an increased normalization of 1.6, and an additional velocity component corresponding to the potential difference between the launch point and one-quarter of the virial radius (Davé et al., 2016). The equation is

$$v_{\rm wind} = 1.6(v_{\rm circ}/200\,{\rm km\,s^{-1}})^{0.12} + \Delta(0.25 R_{\rm vir}), \tag{1.3}$$

with the wind speed attenuated when the kinetic energy of the wind exceeds the available energy from SNe in the galaxy. Similar to the enrichment channels in SIMBA, SNe II and the prompt component of SNe Ia release mass and energy into the star-forming gas elements of the ISM at the time of star formation through these stellar winds. The amount of mass and energy is dictated by the above equations for SNe II, whereas the energy for SNe Ia is set to 10^{51} erg. On the other hand, star particles, through AGB stars and the delayed component of SNe Ia, inject energy into the 16 nearest neighbours with a delay relative to the time of star formation.

- **Black Hole Formation:** Black holes (BHs) are dynamically seeded in galaxies that reach a stellar mass $M_* > \gamma_{BH} M_{\rm seed}$ (where $\gamma_{\rm BH} = 3 \times 10^5$ and $M_{\rm seed} = 10^4\,h^{-1}{\rm M}_\odot$ such that these galaxies have $M_* \gtrsim 10^{9.5}\,{\rm M}_\odot$) and do not already contain a BH particle. If this condition is met, the star particle closest to the galactic centre of mass is converted into a BH particle. Both a dynamical BH mass (inherited from the star particle that seeded it) and a physical BH mass (with the same value as in SIMBA) are assigned at the time of BH formation. BH particles, if within $4R_0$ (where R_0 is the BH kernel size used for calculating the accretion rate), are repositioned to the location of the potential minimum of the host halo at every time-step as well as set to the centre-of-mass velocity of the host halo, under the assumption that dynamical friction is sufficient to maintain

BHs near the host galaxies' centres.

- **Black Hole Growth:** In SIMBA, the BH mass accretion rate is a linear combination of two modes as $\dot{M}_{BH} = (1-\eta) \times (\dot{M}_{\rm Torque} + \dot{M}_{\rm Bondi})$, where a constant radiative efficiency of $\eta = 0.1$ is adopted (e.g. Yu & Tremaine, 2002). In torque-limited accretion, disc gravitational instabilities drive gas inflows from galactic scales down to the accretion disc surrounding the central BH. This is modelled following Hopkins & Quataert (2011), but only evaluating the relevant equations for cold ($T < 10^5\,{\rm K}$) gas - including all ISM gas (cold gas with $n_H > 0.13\,{\rm cm}^{-3}$ and within 0.5 dex of the pressurized ISM temperature floor) - within the BH kernel radius R_0. Specifically, the equation is

$$\dot{M}_{\rm T} = \epsilon_{\rm Torque} f_d^{5/2} \left(\frac{M_{\rm BH}}{10^8 {\rm M}_\odot}\right)^{1/6} \left(\frac{M_{\rm enc}(R_0)}{10^9\,{\rm M}_\odot}\right) \left(\frac{R_0}{100\,{\rm pc}}\right)^{-3/2} \left(1 + \frac{f_0}{f_{\rm gas}}\right)^{-1} {\rm M}_\odot\,{\rm yr}^{-1} \tag{1.4}$$

where f_d is the disc mass fraction including both gas and stars, $M_{\rm enc}(R_0)$ is the total gas + stellar mass enclosed within R_0, $f_{\rm gas}$ is the mass fraction in the disc component, $f_0 \approx 0.31 f_d^2\ (M_{\rm disc}(R_0)/10^9\,{\rm M}_\odot)^{-1/3}$, and all quantities are evaluated within a distance R_0 of each BH enclosing the nearest 256 gas elements, with an upper limit of $R_0 \leq 2\,h^{-1}$ckpc [30]. Bondi-Hoyle-Lyttleton accretion (commonly abbreviated as Bondi accretion) is computed via the standard Bondi (1952) formula, but only for the hot ($T > 10^5\,{\rm K}$) gas, which is typically more spherically distributed, and is given by

$$\dot{M}_{\rm Bondi} = \epsilon_{\rm m} \frac{4\pi G^2 M_{\rm BH}^2 \rho}{(v^2 + c_s^2)^{3/2}} \tag{1.5}$$

where ρ is the mean density of the hot gas within the BH kernel, c_s is the gas' kernel-averaged sound speed, and v is the gas' kernel-averaged velocity. The normalization factors are related as $\epsilon_{\rm T} = \alpha_{\rm T}\epsilon_{\rm m}$ with $\alpha_{\rm T} = 5$ from Hopkins & Quataert (2011) and $\epsilon_{\rm m} = 0.1$ to match the normalization of the local $M_{\rm BH} - M_*$ relation as in Anglés-Alcázar et al. (2017a). The torque-limited mass accretion rate is capped at 3 times the Eddington limit[31], as non-spherical accretion has been observed to exceed the Eddington limit (Martínez-Aldama et al., 2018), whereas quasi-spherical Bondi accretion is limited to the Eddington rate.

[30] ckpc stands for comoving kpc, where comoving implies the distance is the same fraction of the box size at all redshifts, but with different physical distances.

[31] The Eddington mass accretion rate (or limit) $\dot{M}_{\rm Edd}$ occurs when the outward-acting radiation pressure from matter accreting onto a BH balances the inward-acting gravitational attraction of the BH on this infalling matter, i.e. hydrostatic equilibrium. This in turn defines an Eddington luminosity $L_{\rm Edd}$.

- **Black Hole Feedback:** Feedback from BHs in SIMBA also follows two sub-grid models: bipolar kinetic outflows and X-ray heating. The kinetic model is further divided into a "radiative mode" motivated by observations of multiphase winds from AGNs at velocities $\sim 1000\,\mathrm{km\,s^{-1}}$ (e.g. Sturm et al., 2011; Maiolino et al., 2012; Perna et al., 2017b); and a "jet mode" only at low Eddington ratios ($f_{\rm Edd} \equiv \dot{M}_{\rm BH}/\dot{M}_{\rm Edd} < 0.2$) and high BH masses ($M_{\rm BH}/M_\odot > 10^{7.5}$), where AGNs primarily drive hot gas in collimated jets at velocities of order $\sim 10^4\,\mathrm{km\,s^{-1}}$ (e.g. McNamara & Nulsen, 2007; Fabian, 2012). At $f_{\rm Edd} > 0.2$, radiative AGN winds are produced by ejecting nearby gas particles (within the BH kernel) at the ISM temperature with a variable outflow velocity dependent on the BH mass as

$$v_{\rm wind} = 500 + 500(\log(M_{\rm BH}) - 6)/3\ \mathrm{km\,s^{-1}}. \tag{1.6}$$

On the other hand, the jet velocity is the sum of the radiative wind's velocity and a term inversely dependent on the Eddington ratio as

$$v_{\rm jet} = v_{\rm wind} + 7000\log(0.2/f_{\rm Edd})\ \mathrm{km\,s^{-1}}, \tag{1.7}$$

such that the increase is capped at $7000\,\mathrm{km\,s^{-1}}$, and the jet velocity increases with decreasing $f_{\rm Edd}$ up to a limit of $\sim 8000\,\mathrm{km\,s^{-1}}$. Additionally, since jets are observed to carry hot gas, the ejected gas particles in the jet mode are raised to the Virial temperature of the halo, given by $T_{\rm vir} = 9.52\times10^7(M_{\rm halo}/10^{15}\,\mathrm{M_\odot})^{1/3}\,\mathrm{K}$ (Voit, 2005). The energy injected into AGN winds is set to obtain a momentum output of $\dot{P}_{\rm out} = 20L/c$, where $L = \eta\dot{M}_{\rm BH}c^2$ is the AGN bolometric luminosity, $\eta = 0.1$, and c is the speed of light. Outflows in both the radiative and jet modes are purely bipolar, ejected in a direction (anti-)parallel to the angular momentum vector of the inner disc used to compute BH accretion, and with zero opening angle. A short hydrodynamic and radiative decoupling time of $10^{-4}t_{\rm H}(z_{\rm launch})$ is applied to outflowing gas elements to avoid rapid velocity decrease in the unresolved ISM close to the BH and numerical inaccuracies from high Mach number shocks in very dense gas, resulting in a decoupling distance of up to tens of kpc at the present epoch. In the AGN X-ray feedback sub-grid model, X-rays from the accretion disc input energy into the surrounding gas with a radiative efficiency of 0.1 (Choi et al., 2012), but only when the kinetic jet mode is activated. This heating occurs within the BH accretion kernel and scales inversely with the square of the distance from the BH. Non-ISM gas has its temperature directly increased, while ISM gas receives both a kinetic kick and heating since it would cool quickly if only its temperature was increased due to its low resolution. Additionally, gas-rich galaxies are assumed to

absorb and radiate away the X-ray energy, so X-ray heating only applies to galaxies with a gas fraction $f_{\rm gas} \equiv M_{\rm gas}/M_* < 0.2$.

- **Dust Production, Growth and Destruction:** In SIMBA, dust - with grains of all $a = 0.1\,\mu$m - is passively advected following the gas particles. Following Dwek (1998), metal ejecta from SNe and AGB stars condense into dust, with the condensation efficiency and dust mass produced dependent on the element, whether it is an AGB star or SNII (SNIa are likely not significant sources of dust (Nozawa et al., 2011; Dwek, 2016; Gioannini et al., 2017)) and the C/O mass ratio in AGB stars. Dust grains grow by accreting gas-phase metals in a two-body collisional process, with the grain radius growth rate dependent on the dust mass, metal mass, and accretion time. Dust grains can be destroyed by thermal sputtering, i.e. erosion by colliding with thermally excited gas. Another dust destruction mechanism is implemented to account for unresolved SN blast waves according to the prescription outlined in McKinnon et al. (2016), with the rate dependent on the dust mass, local gas mass, and the mass of local gas shocked to at least $100\,{\rm km\,s^{-1}}$. Additionally, dust and molecular hydrogen are completely destroyed in hot winds during star formation, and any gas impacted by AGN X-ray heating or jets.

1.8.2 Why `SIMBA-C`?

SIMBA-C is the most recent addition to the SIMBA suite, utilizing the `Chem5` model for chemical enrichment and stellar feedback, instead of SIMBA's instantaneous recycling approximation, as well as a few other adjustments to ensure good agreement with observations (see Hough et al., 2023). The primary motivation for developing SIMBA-C concerns how the cooling of metal-enriched gas plays a central role in star formation. Gas must cool to $\sim 10-20$ K for molecular clouds in the ISM to have the chance to collapse into protostellar cores (Kennicutt et al., 2007; Leroy et al., 2008). Molecular H_2 alone is not sufficient to cool the gas to these temperatures (Bromm et al., 2002; Smith et al., 2009) and achieve the star formation rates we observe in galaxies in the local universe (Abel et al., 2002; Stinson et al., 2013; Rasia et al., 2015). Metal-enriched gas is required to lose energy faster and drop the gas to star-forming temperatures (Smith et al., 2008), and thus increase the efficiency of star formation (Kobayashi et al., 2007; Smith et al., 2009).

However, this results in an over-production of stars (Stinson et al., 2013; Rasia et al., 2015) and too many old spheroidal galaxies at $z = 0$ (White & Frenk, 1991; Piontek & Steinmetz, 2011). This is where feedback comes in: feedback processes, like AGN, stellar winds, and

SNe, inject massive amounts of energy into the cold gas clouds, re-heating them (Piontek & Steinmetz, 2011; Stinson et al., 2013) and reducing the rate of star formation (Madau & Dickinson, 2014). Stellar feedback processes also produce and release metals into the ISM, resulting in a self-regulating cycle between star-formation and feedback (see Ceverino & Klypin, 2009; Smith et al., 2009; Piontek & Steinmetz, 2011; Hopkins et al., 2012; Hirschmann et al., 2016; Romano et al., 2019; Lagos et al., 2022, & references therein). Therefore, accurate metal enrichment and self-consistent stellar feedback is vital to reproducing the conditions in the universe necessary to produce the levels of star formation and the galactic stellar masses we observe.

Moreover, the IGrM acts as the galactic interface between the ISM and IGM, coordinating the transfer of baryonic matter into the ISM via large-scale inflows and turbulence-driven condensation and precipitation of cool clouds, and the expulsion of gas, metals, and energy out of the ISM through feedback-driven galactic-scale outflows. The IGrM is thus a vital source of fuel for star formation and AGN activity. The details of these physical processes, like their rates, efficiency, and uniformity, are set by environment as well as such thermodynamic characteristics as the balance between heating and cooling, which in turn are controlled by properties like the abundance and distribution of metals in the IGrM. Chemical enrichment consequently plays a considerable role in the overall self-regulation of galaxy, group, and IGrM evolution. In this way, realistic modelling of chemical enrichment in galaxy formation simulations is potentially crucial to obtain accurate properties of both galaxies and the IGrM.

1.8.3 `SIMBA-C` Simulation and Galaxy Formation Model

SIMBA-C (Hough et al., 2023) employs the same gravity and hydrodynamics code, initial conditions, and cosmology as SIMBA. I use the largest volume box of SIMBA-C available with $V = (100\,h^{-1}\mathrm{Mpc})^3$ and all other general parameters the same as in point 1 of Section 1.8.1. Here, I describe the alterations made to the sub-grid models of SIMBA to obtain those of SIMBA-C:

- **Cooling and Heating:** Same as SIMBA.
- **Star Formation:** Same as SIMBA, except for using an updated value for the star formation efficiency of $\epsilon_* = 0.026$ (Pokhrel et al., 2021).
- **Chemical Enrichment:** This sub-grid model is overhauled in SIMBA-C, replacing it with the `Chem5` model described in Section 1.7.4. SIMBA-C tracks all elements from H to Ge on the periodic table. They are produced by core-collapse SNe (SNe II, HNe,

'failed' SNe), SNe Ia, and stellar winds from AGB/super-AGB stars. Notably, the instantaneous recycling and delayed feedback models from SIMBA are removed, such that gas elements cannot self-enrich nor can they enrich their neighbours; instead, each star particle is treated as an *evolving* stellar population so that metal enrichment of nearby gas elements can only occur *after* a star particle has been spawned from a gas element. For all star particles, the metal yields for each element from each enrichment channel are calculated by `Chem5` at every timestep, and these ejecta are distributed to the 64 gas elements nearest to each star particle in a kernel-weighted manner. Finally, the yield tables for each enrichment channel are updated, with generally reduced yields: Kobayashi et al. (2006) for SNe II and HNe, Kobayashi et al. (2020a) for 'failed' SNe, Kobayashi et al. (2020b) for SNe Ia, and Doherty et al. (2014a,b).

- **Stellar Feedback:** SIMBA-C employs the same two-phase decoupled kinetic wind model, but with some modifications. The stellar mass loss due to SNe II is set to $f_{\rm SNII} = 0$ since the instantaneous recycling models has been removed. As for metals, all energy and mass feedback is computed for each star particle from each stellar feedback channel at every timestep; however, similar to SIMBA, SNe II are assumed to provide the energy for the kinetic self-kick of gas particles into winds (this is the only mode of stellar feedback that is still calculated in the instantaneous recycling approximation). The scaling of the stellar wind velocity is reduced from $a = 1.6$ in SIMBA to $a = 0.85$ in SIMBA-C to match the median value from Muratov et al. (2015). Instead of being fixed at 30%, the fraction of wind particles that are ejected "hot" and hydrodynamically decoupled is made to follow the trend found with the model of Pandya et al. (2023) after having been calibrated to the FIRE-2 simulation, such that it depends on redshift and halo mass. Lastly, the stellar winds in SIMBA-C are not metal-loaded, as they are in SIMBA.

- **Black Hole Formation:** Same as SIMBA, except that BHs are now seeded as soon as galaxies reach a resolved stellar mass of $M_* \gtrsim 6 \times 10^8\,{\rm M}_\odot$.

- **Black Hole Growth:** Same as SIMBA, except that the initial accretion rate (for $M_{\rm BH} < 3 \times 10^6\,{\rm M}_\odot$) is suppressed by a factor of $e^{-M_{\rm BH}/10^6\,{\rm M}_\odot}$. This change is designed to approximately emulate the behaviour of dwarf galaxies suppressing BH growth, as described in Anglés-Alcázar et al. (2017c) and Hopkins et al. (2022), and ultimately alleviates the "pile-up" of galaxies above the "knee" of the galaxy stellar mass function (GSMF) due to the seeding of BHs and subsequent onset of BH feedback quenching

galaxies and limiting their growth, as seen in SIMBA (Hough et al., 2023).

- **Black Hole Feedback:** Same as SIMBA, with a few modifications. In SIMBA, the jets activated between $M_{\rm BH} = 4 \times 10^7 - 6 \times 10^7\,{\rm M}_\odot$ with a probability scaling from 0 to 1 linearly over that mass range. In SIMBA-C, the jet activation BH mass range is increased to $M_{\rm BH} = 7 \times 10^7 - 10^8\,{\rm M}_\odot$, and a specific jet onset BH mass in that range is effectively assigned to each BH particle, which they retain for the duration of the simulation. The former alteration was decided on through trial-and-error recalibration of SIMBA-C parameters as a consequence of SIMBA-C initially vastly underproducing metals at low redshift compared to observations. The increase in the jet activation BH mass range was therefore introduced as a means to reduce the number of stellar feedback events, allowing a greater amount of star formation and increased metal production (the reduction in the stellar feedback velocity scaling in SIMBA-C, discussed three points back, was introduced in reaction to this change to re-correct the GSMF, which was negatively affected by the change to the jet activation BH mass). Lastly, the maximum jet velocity in SIMBA-C additionally scales with $M_{\rm BH}$ at $f_{\rm Edd} < 0.02$, following

$$v_{\rm jet} = 7000\,{\rm km/s} \times {\rm MIN}(\log_{10}(0.2/f_{\rm Edd}), v_{\rm max}) \tag{1.8}$$

  where $v_{\rm max} = (M_{\rm BH}/10^8\,{\rm M}_\odot)^{1/3}$ is limited to the range $[1, 5]$, such that $v_{\rm jet}$ can become much larger (compared to SIMBA) in very massive halos with very massive BHs, and is capped at $35,000\,{\rm km/s}$ for $M_{\rm BH} \geq 1.25 \times 10^{10}\,{\rm M}_\odot$ and $f_{\rm Edd} \leq 2 \times 10^{-6}$. This change was originally implemented in SIMBA for THE 300 PROJECT as a way to have jet velocities scale with halo escape velocities and thus allow them to penetrate to farther radii in groups and clusters; it was then carried over to SIMBA-C.

- **Dust Production, Growth and Destruction:** Same as SIMBA.

1.9 Thesis Summary

This thesis covers research performed solely by myself over the course of my Master's degree. It focuses on the SIMBA-C simulation, a version of SIMBA with an upgraded chemical enrichment model (`Chem5`), and assessing its prediction of chemical abundance profiles in the IGrM in relation to SIMBA and X-ray observations. Chapter 2 is a paper on this topic published in the journal *Universe*. This work serves to address current issues in predicting observed IGrM abundances and metal distributions, as well as improving our understanding of the contribution of chemical enrichment models to the overall enrichment of the IGrM,

emphasizing the need for physically motivated and realistic sub-grid models. Chapter 3 contains a summary of my findings and conclusions.

Chapter 2

Core to Cosmic Edge: SIMBA-C's New Take on Abundance Profiles in the Intragroup Medium at $z = 0$

Published in *Universe*. This article belongs to the Special Issue *Universe*: Feature Papers 2024–"Galaxies and Clusters".

Authors: Aviv Padawer-Blatt [1,*], Zhiwei Shao [2], Renier Hough [3], Douglas Rennehan [4], Ruxin Barré [1], Vida Saeedzadeh [5], Arif Babul [1,6,7,*], Romeel Davé [8], Chiaki Kobayashi [9], Weiguang Cui [10,11], François Mernier [12,13], and Ghassem Gozaliasl [14,15]

* Correspondence: apadawer@uvic.ca (A.P.-B.); babul@uvic.ca (A.B.)

[1] Department of Physics and Astronomy, University of Victoria, Victoria, BC V8P 1A1, Canada
[2] Department of Astronomy, School of Physics and Astronomy, and Shanghai Key Laboratory for Particle Physics and Cosmology, Shanghai Jiao Tong University, Shanghai 200240, China
[3] Center for Space Research, North-West University, Potchefstroom 2520, South Africa
[4] Center for Computational Astrophysics, Flatiron Institute, New York, NY 10010, USA
[5] Department of Physics & Astronomy, Johns Hopkins University, Baltimore, MD 21218, USA
[6] Leverhulme Visiting Prof., Institute for Astronomy, University of Edinburgh, Royal Observatory, Blackford Hill, Edinburgh EH9 3HJ, UK
[7] Infosys Visiting Chair Professor, Department of Physics, Indian Institute of Science, Bangalore 560012, India
[8] Institute for Astronomy, University of Edinburgh, Royal Observatory, Blackford Hill, Edinburgh EH9 3HJ, UK
[9] Centre for Astrophysics Research, Department of Physics, Astronomy and Mathematics, University of Hertfordshire, Hatfield AL10 9AB, UK
[10] Departamento de Física Téorica, Universidad Autónoma de Madrid, E-28049 Madrid, Spain
[11] Centro de Investigación Avanzada en Física Fundamental (CIAFF), Universidad Autónoma de Madrid, 28049 Madrid, Spain
[12] NASA Goddard Space Flight Center, Greenbelt, MD 20771, USA
[13] Department of Astronomy, University of Marlyand, College Park, MD 20742, USA
[14] Department of Computer Science, Aalto University, P.O. Box 15400, FI-00 076 Espoo, Finland
[15] Department of Physics, University of Helsinki, P.O. Box 64, FI-00014 Helsinki, Finland

Abstract: We employ the SIMBA-C cosmological simulation to study the impact of its upgraded chemical enrichment model (`Chem5`) on the distribution of metals in the intragroup medium (IGrM). We investigate the projected X-ray emission-weighted abundance profiles of key elements over two decades in halo mass ($10^{13} \leq M_{500}/\mathrm{M}_{\odot} \leq 10^{15}$). Typically, SIMBA-C generates lower-amplitude abundance profiles than SIMBA with flatter cores, in better agreement with observations. For low-mass groups, both simulations over-enrich the IGrM with Si, S, Ca, and Fe compared to observations, a trend likely related to inadequate modeling of metal dispersal and mixing. We analyze the 3D mass-weighted abundance profiles, concluding that the lower SIMBA-C IGrM abundances are primarily a consequence of fewer metals in the IGrM, driven by reduced metal yields in `Chem5`, and the removal of the instantaneous recycling of metals approximation employed by SIMBA. Additionally, an increased IGrM mass in low-mass SIMBA-C groups is likely triggered by changes to the AGN and stellar feedback models. Our study suggests that a more realistic chemical enrichment model broadly improves agreement with observations, but physically motivated sub-grid models for other key processes, like AGN and stellar feedback and turbulent diffusion, are required to realistically reproduce observed group environments.

Keywords: galaxy groups; intragroup medium; chemical abundances; metallicity; chemical enrichment; cosmological hydrodynamical simulations; X-ray observations

2.1 Introduction

The majority of galaxies are not born on their own and do not live isolated lives. They often reside and evolve in collections of gravitationally bound groups of galaxies[16] (Eke et al., 2006; Lovisari et al., 2021), with their halos contributing the largest proportion of mass to the total mass in the Universe. These environments are filled with hot diffuse gas that permeates the space between galaxies and extends throughout the dark matter halo, known as the intragroup or intracluster medium. Since we are mainly considering groups in this study, we will refer to this simply as the intragroup medium (IGrM). As a major component of group environments, the IGrM is an important factor in shaping and regulating the evolution of central galaxies (Le Brun et al., 2014; Ragone-Figueroa et al., 2018, 2020; Marini et al., 2021; Martizzi et al., 2014; Remus et al., 2017; Nipoti, 2017; Pillepich et al., 2018; Jackson et al.,

[16]Gravitationally bound collections of galaxies reside in halos whose masses span the range from $\sim 10^{12.5}\, M_{\odot}$ to $\gtrsim 10^{15}\, M_{\odot}$. Historically, lower-mass systems have been referred to as "groups" and higher-mass systems as "clusters". In this paper, we examine both categories of systems, but, for convenience, we will refer to them collectively as "groups", only because the lower-mass systems numerically dominate our simulated samples.

2020; Henden et al., 2020; Bassini et al., 2020).

The IGrM consists of a significant fraction of the bound baryons in the Universe. Due to its high temperatures, the IGrM emits X-rays, primarily from thermal bremsstrahlung, bound-free emission, and line emission from highly ionized trace elements. It is thus observable with X-ray telescopes, permitting studies that illuminate the formation and evolution of groups, including when and how group galaxies and the IGrM were enriched with metals.

A group's thermal, dynamic, and enrichment history plays a role in shaping its late-time metal distributions. Many observational studies find flat, largely sub-solar gas-phase metallicity profiles in the IGrM outskirts ($R \gtrsim 0.3R_{500}$) of local massive groups and clusters (e.g. Werner et al., 2013; Urban et al., 2017; Lovisari & Reiprich, 2019; Ghizzardi et al., 2021; Sarkar et al., 2022). The average amplitudes and slopes for lower-mass groups are not firmly set (e.g. Mernier et al., 2017). Additionally, observations show higher, though generally still sub-solar or solar, enrichment levels in the inner regions of massive groups and clusters, where the central brightest group/cluster galaxies (BGGs/BCGs) typically reside. These core abundances, however, are found to be quite dependent on the thermodynamic state of a group and its cool-core (CC)/non-cool-core (NCC) classification (e.g. Ghizzardi et al., 2021).

The metallicity of the IGrM is directly related to metal production in galaxies via stellar nucleosynthesis, and the subsequent redistribution and mixing through galactic-scale outflows driven by stellar and AGN feedback (Rennehan, 2021; Appleby et al., 2021; Saeedzadeh et al., 2023), ram pressure stripping (Domainko et al., 2006; Saeedzadeh et al., 2023), and outflow-driven turbulence (Prasad et al., 2018; Rennehan et al., 2019; Bennett & Sijacki, 2020; Lochhaas et al., 2020; Rennehan, 2021) as galaxies form and evolve. The distribution of the IGrM abundances therefore critically relies upon all of these physical processes.

Cosmological-scale galaxy formation simulations are the leading approach in modern astronomy to holistically model such processes in a manner enabling them to reproduce observed galaxy properties. They are made up of elements representing dark matter, gas, stars, and supermassive black holes (SMBHs); numerical implementations of gravity and hydrodynamics for particle interactions, and radiative cooling and heating; and sub-grid models[17] for star formation, stellar feedback, chemical enrichment, dust production and destruction, SMBH growth, and AGN feedback, as well as other possibilities (Somerville & Davé, 2015; Vogelsberger et al., 2020; Crain & van de Voort, 2023).

The large dynamic range of physical mechanisms contributing to galaxy evolution (e.g.,

[17]These models, also called sub-resolution models, are denoted as such since they model physical processes occurring on spatial, mass, or temporal scales below the resolution threshold of a simulation. They may be phenomenological physically motivated approximations—or even ad hoc solutions—the validity, realism, and effectiveness of which are subject to debate (for an overview, see Winsberg (2010)).

from the accretion disks around SMBHs to the hot atmospheres in groups) and their complex feedback systems (e.g., metal cooling in gas to feed stellar and AGN feedback), however, make it difficult to improve these simulations with regard to their accuracy across a diversity of properties and observables. With that being said, simulations facilitate experimenting with different methods and sub-grid models to address such numerical challenges, continuously refining and reforming them in an effort to better represent galaxies as we observe them.

Sub-grid models and their parameters are regularly constrained by calibrating simulations to selected observables (e.g. Vogelsberger et al., 2014; McCarthy et al., 2017; Pillepich et al., 2018; Davé et al., 2019; Kugel et al., 2023; Hough et al., 2023). For various reasons (including the idea that, by generating realistic simulated galaxies, structures at other scales should effectively be constrained to the correct properties and features), it is rare to employ group-scale observables in this way[18]. As a result, the properties of simulated samples of galaxy groups are often discrepant with observations (e.g. Vogelsberger et al., 2019; Oppenheimer et al., 2021; Donahue & Voit, 2022; Altamura et al., 2023; Braspenning et al., 2024).

Developing sub-grid models that perform reliably at cosmological resolution, and their continuous testing against observations, is essential for improving the fidelity of simulations, and supports interfacing with observational surveys across an increasingly wide range of wavelengths, scales, and times. Consequently, many studies focus on improving the various sub-grid models by increasing their realism. One such recent step forward is SIMBA-C (Hough et al., 2023, 2024). SIMBA-C employs the SIMBA galaxy formation model (Davé et al., 2019), but with an updated stellar feedback and chemical enrichment model, known as `Chem5` (Kobayashi et al., 2020a,b). SIMBA successfully reproduces a wide range of observations while only being tuned to match the $z = 0$ galaxy stellar mass function (GSMF) and the $M_{\rm BH} - M_*$ relation (Davé et al., 2019). SIMBA-C builds on these successes by implementing a more realistic treatment of galactic chemical enrichment. Additionally, SIMBA-C includes refinements to other sub-grid models, such as a reduced stellar wind velocity scaling and delayed activation of AGN jets, to improve agreement with key observations.

At the galaxy level, SIMBA-C performs better than SIMBA with respect to matching observations (Hough et al., 2023). For example, the SIMBA-C $z = 0$ GSMF matches observations noticeably better than SIMBA, but where SIMBA-C shines is in its predictions of metallicity and chemical abundance (Hough et al., 2023). Specifically, it yields a significantly improved agreement with observed galaxy scaling relations of $[O/Fe] - [Fe/H]$ and $[Mg/Fe] - [Fe/H]$, and a better match to the $z = 0$ stellar mass–metallicity relation at the low-mass end and to

[18]The limited statistics of galaxy groups and clusters compared to individual galaxies in both observations and cosmological simulations additionally play a role in this methodology.

the gas-phase $O/H - M_*$ relation.

Hough et al. (2024) recently demonstrated that, at $z = 0$, compared to SIMBA, the IGrM of SIMBA-C galaxy groups has higher X-ray luminosity, lower entropy, lower Fe and Si mass-weighted global abundances, and larger Si/O abundance ratios. They also found non-trivial differences in the redshift evolution of the $k_{\rm B}T = 1$ keV IGrM metallicity between SIMBA and SIMBA-C. These results indicate that the inclusion of the updated chemical enrichment model, as well as alterations to the feedback models, has substantial impacts on the thermal properties and metal content of the IGrM.

The SIMBA-C galaxy formation model represents a significant improvement compared to SIMBA with regard to stellar feedback and chemical enrichment. It is therefore of interest to investigate how the implementation of `Chem5` in a cosmological simulation and its treatment of physical processes alter the detailed distribution of metals in the IGrM, and if the resulting abundance profiles are in better agreement with observations. Thus, we focus on the radial IGrM metal abundance profiles of SIMBA and SIMBA-C galaxy groups at $z = 0$.

In this article, Section 2.2.1 reviews the simulation methodology and input physics of SIMBA (Davé et al., 2019) and SIMBA-C (Hough et al., 2023), highlighting how they differ. Section 2.2.2 provides a brief overview of the observational samples used in this work. Sections 2.2.3–2.2.5 describe the methods employed to obtain and analyze the simulated and observed galaxy groups and their abundance profiles. Section 2.3 presents the projected emission-weighted abundance profiles. We compare SIMBA and SIMBA-C, noting differences and similarities, and compare their profiles to representative observational results, looking at a variety of astrophysically relevant elements. In Section 2.4, we assess how much SIMBA-C improves over SIMBA, and investigate the simulations' 3D mass-weighted abundance profiles to comment on potential reasons for any changes between SIMBA and SIMBA-C. Finally, we summarize our findings and conclusions in Section 2.5, noting the implications of our results for future simulations, (e.g., new iterations of SIMBA, like KIARA) and future observations of galaxy groups (e.g., the X-Ray Imaging and Spectroscopy Mission (*XRISM*; Team (2020); Tashiro (2022)), the Advanced Telescope for High ENergy Astrophysics (*Athena*; Barcons et al. (2012); Barret et al. (2013, 2020)), the Advanced X-ray Imaging Satellite (*AXIS*; Mushotzky et al. (2019); Reynolds et al. (2023)), and *Lynx* (Gaskin et al., 2019; Schwartz et al., 2019)).

2.2 Methods

2.2.1 Simulation Methodology

Here, we summarize the SIMBA and SIMBA-C cosmological hydrodynamic simulations, their physics, and their galaxy formation models and associated sub-grid models. Detailed descriptions can be found in the works of Davé et al. (2019) and Hough et al. (2023), respectively.

We employ the flagship SIMBA[19] and SIMBA-C runs, each having volumes of side length $100\,h^{-1}$ cMpc with 1024^3 dark matter particles and 1024^3 gas elements. They are run on the same initial conditions from an initial redshift of $z = 249$ down to $z = 0$ assuming a Planck 2018 (Planck Collaboration et al., 2020) flat ΛCDM cosmology with $\Omega_m = 0.3$, $\Omega_\Lambda = 0.7$, $\Omega_b = 0.048$, and $H_0 = 68\,\mathrm{km\,s^{-1}\,Mpc^{-1}}$. Both simulations have a minimum Plummer-equivalent gravitational softening length of $0.5\,h^{-1}$ kpc, an initial gas element mass resolution of $1.82 \times 10^7\,M_\odot$, and a dark matter particle mass resolution of $9.6 \times 10^7\,M_\odot$. SIMBA and SIMBA-C are built on the N-body gravity + hydrodynamics solver GIZMO in its meshless finite-mass (MFM) mode (Lanson & Vila, 2008a,b; Gaburov & Nitadori, 2011; Hopkins, 2015, 2017).

In Table 2.1, we summarize the key differences between the sub-grid models of SIMBA and SIMBA-C[20]. Most importantly, SIMBA-C incorporates an updated chemical enrichment and stellar feedback model (`Chem5`; Kobayashi et al. (2020a,b)) that replaces the *instantaneous recycling approximation* used in SIMBA. This approximation (first described by Talbot & Arnett (1971) and reviewed by Tinsley (2022)) is implemented in SIMBA as a simple sub-grid model according to the following:

1. All gas elements that are eligible to form stars, i.e., the "star-forming ISM" (see Davé et al. (2016) for details), self-enrich with SNII and prompt (concurrent with SNII) SNIa nucleosynthesis products. This occurs at each timestep a gas element is "star forming" and has not spawned a star particle.

2. In the timestep when a star-forming gas element converts to a star particle, no self-enrichment occurs. Also, star particles do not self-enrich.

3. Feedback from stars below $\sim 8\,M_\odot$ is delayed relative to the time of star formation. At 0.7 Gyr, after a star particle is spawned, feedback products (metals and energy) from

[19] https://simba.roe.ac.uk/ (accessed on 1 January 2023).

[20] In Hough et al. (2023), the dust model was excluded from SIMBA-C to remove its possible effects on the metal content in a simulation dedicated to testing a new metal enrichment model. Hough et al. (2024) re-integrated the dust model into SIMBA-C, finding no discernible effects on the global IGrM properties, likely due to the dust sputtering back into metals in the hot diffuse gas.

the delayed component of SNe Ia begin to be added to the 16 nearest gas elements in a kernel-weighted manner. Further, AGB stars slowly release—again to the 16 nearest gas elements—these feedback products (as well as mass, with mass conversation maintained by appropriately reducing a star particle's mass) from a star particle over time, beginning at a delay of ∼15 Myr from the time a star particle spawns.

SIMBA-C also employs recalibrated versions (Hough et al., 2023) of the original AGN and stellar feedback models from SIMBA. Beyond what is discussed in Table 2.1, both simulations employ radiative cooling and photoionization heating from the GRACKLE-3.1 library (Smith et al., 2017), and an H_2-based star formation model with H_2 fractions computed according to the method of Krumholz & Gnedin (2011).

2.2.2 Observational Samples

In this section, we describe the samples of X-ray observational data collected from the literature. This is by no means a comprehensive or exhaustive compilation, but it contains relatively recent results and provides an illustrative representation of the spread across the literature, selection effects due to variations in observing strategy, telescopes and instruments, analysis methods and codes, spectral fitting models, and group-to-cluster scales. Table 2.2 summarizes the key details of each sample.

Werner et al. (2006a) measure core IGrM abundance profiles in the giant elliptical galaxy M87 (near/at the Virgo Cluster center) using high-resolution spectra obtained with the Reflection Grating Spectrometers (RGS; den Herder et al. (2001)) on board *XMM-Newton* (Jansen et al., 2001).

Grange et al. (2011) employ the RGS and EPIC (European Photon Imaging Camera; Strüder et al. (2001); Turner et al. (2001)) instruments on board *XMM-Newton* to measure core IGrM abundances in two galaxy groups, NGC 5044 and NGC 5813.

The CHEmical Evolution RGS Sample (CHEERS) consists of 44 nearby bright cool-core galaxy clusters, groups, and ellipticals observed with *XMM-Newton* (De Plaa et al., 2017). Mernier et al. (2017) perform spectral fitting with the EPIC instrument and construct IGrM abundance profiles centered on the objects' X-ray emission peaks.

Mao et al. (2019) perform spectral fitting of both *XMM-Newton*/RGS and EPIC/MOS instruments to determine core IGrM abundances in CHEERS. The nitrogen abundances could only be well constrained in eight groups, resulting in a smaller sample than CHEERS.

Table 2.1: Summary of key differences between sub-grid models of SIMBA and SIMBA-C.

Sub-Grid Model	SIMBA	SIMBA-C
Star Formation	• SFR $= \varepsilon_* \rho_{\rm H_2}/t_{\rm dyn}$ with $\varepsilon_* = 0.02$ (Kennicutt, 1998).	• Updated value of $\varepsilon_* = 0.026$ (Pokhrel et al., 2021).
Chemical Enrichment	• Elements: H, He, C, N, O, Ne, Mg, Si, S, Ca, Fe. • Metal production by SNe II, SNe Ia, and AGB stars. • Instantaneous recycling of metals model, whereby metals are self-injected into gas elements in the ISM at every timestep they are eligible to form star particles (i.e., above the SF density threshold, where this conversion is performed stochastically), under the assumption that SNe II and the prompt (concurrent with SNe II) SNIa components occur nearly instantaneously after star formation, with the metals being rapidly recycled back into the warm ISM (Davé et al., 2016). • Delayed feedback component of ~ 15 Myr and 0.7 Gyr (relative to time of conversion of gas element into star particle) for AGB stars and SNe Ia, respectively, adding mass, metals, and energy to the 16 nearest neighbors in a kernel-weighted manner (Davé et al., 2016). • Yield tables from Nomoto et al. (2006) for SNe II, Iwamoto et al. (1999) for SNe Ia, and Oppenheimer & Davé (2006) for AGBs.	• Adopts `Chem5` cosmic chemical enrichment model (Kobayashi et al., 2020a,b, and references therein). • Elements: all elements from H to Ge. • Metal production and energetic feedback by core-collapse SNe (SNe II, hypernovae (HNe; high-mass core-collapse SNe whose explosion energy is $>10\times$ that of a regular SN), and 'failed' SNe for most massive stars), SNe Ia, and stellar winds from stars of all masses (including AGB and super-AGB stars). • No instantaneous recycling of metals or delayed feedback models; enrichment occurs only *after* gas element spawns star particle. • Treats each star particle as an evolving stellar population that ejects energy, mass, and metals in a time-resolved sense and distributes these ejecta to the 64 neighboring gas particles in a kernel-weighted fashion, with new analytical models for each enrichment channel (see Kobayashi et al. (2020a,b)). • Updated yield tables (with generally reduced yields) for each enrichment channel. See Kobayashi et al. (2006) for SNe II/HNe, Kobayashi et al. (2020a) for 'failed' SNe, Kobayashi et al. (2020b) for SNe Ia, and Doherty et al. (2014a,b) for AGBs/super AGBs.

to be continued on next page

Table 2.1: (continued from previous page)

Sub-Grid Model	SIMBA	SIMBA-C
Stellar Feedback	• Gas elements eligible for SF can self-kick into a wind, with probability equal to the probability of converting into a star times the mass-loading factor η (as calculated by Davé et al. (2019)), assuming massive stars launch two-phase kinetic winds that drive material out of galaxies through SNe II, radiation pressure, and stellar winds (Davé et al., 2016). • Stellar mass loss due to SNe II of $f_{\rm SNII} = 0.18$ of each gas element's mass, which is released to the warm ISM at each timestep it is eligible for SF. • Wind velocity dependent on $v_{\rm circ}$, based on the study of Muratov et al. (2015), with scaling of $a = 1.6$. • Of the stellar wind particles, 30% are ejected "hot" and hydrodynamically decoupled for a short time. • Ejected winds are metal loaded by extracting some metals from nearby particles to represent local enrichment by SNe, with the metallicity added given by $dZ = f_{\rm SNII} y_{\rm SNII}(Z)/{\rm MAX}(\eta, 1)$. • Long-lived stars provide energetic feedback through SNIa and AGB delayed components by dumping energy and mass into the 16 nearest neighbors in a kernel-weighted manner, heating these gas elements under the assumption that the energy thermalizes rapidly.	• Same two-phase decoupled kinetic wind model, with some changes, as follows. • $f_{\rm SNII} = 0$ due to the removal of the instantaneous recycling approximation. • The assumption that SNe II provide energy for kicking gas elements into stellar winds remains; however, all other stellar channels of energetic feedback are now computed by `Chem5`, with the energy and mass only released in the timesteps after a star particle has formed. • Stellar wind velocity scaling reduced to $a = 0.85$ to match the median value of Muratov et al. (2015). • The fraction of wind particles ejected hot and hydrodynamically decoupled follows the trend from FIRE simulations (Pandya et al., 2023). • Winds are not artificially metal loaded, since they naturally contain metals in `Chem5`.
Black Hole Formation	• BHs are seeded in galaxies not already containing a BH that reach a stellar mass $M_* \gtrsim 3 \times 10^9\,{\rm M}_\odot$, with $M_{\rm BH,seed} = 10^4\,{\rm h}^{-1}\,{\rm M}_\odot$.	• BHs are seeded as soon as galaxies reach a resolved stellar mass of $M_* \gtrsim 6 \times 10^8\,{\rm M}_\odot$, still with $M_{\rm BH,seed} = 10^4\,{\rm h}^{-1}\,{\rm M}_\odot$.

to be continued on next page

Table 2.1: (continued from previous page)

Sub-Grid Model	SIMBA	SIMBA-C
Black Hole Growth	• The BH mass accretion rate is a linear combination of two modes as $\dot{M}_{\rm BH} = (1-\eta) \times (\dot{M}_{\rm Torque} + \dot{M}_{\rm Bondi})$ for each BH's "life", with $\eta = 0.1$.	• BH accretion is the same as in SIMBA, but with the initial accretion rate (for $M_{\rm BH} < 3 \times 10^6 {\rm M}_\odot$) suppressed by a factor of $e^{-M_{\rm BH}/10^6\,{\rm M}_\odot}$, to simulate star formation suppressing BH growth in dwarf galaxies.
Black Hole Feedback	• Two modes: X-ray heating and bipolar kinetic outflows, with the latter divided into jets (only at $f_{\rm Edd} < 0.2$) and radiative winds (see Davé et al. (2019) for details). • Jets activate between $M_{\rm BH,jet,min} = 4 \times 10^7\,{\rm M}_\odot$ and $M_{\rm BH,jet,max} = 6 \times 10^7\,{\rm M}_\odot$, with probability scaling from $0 \rightarrow 1$ over that mass range. • Jet velocity increases with decreasing $f_{\rm Edd}$ as $v_{\rm jet} = 7000\,{\rm km\,s^{-1}} \times \log_{10}\left(0.2/{\rm MAX}(f_{\rm Edd}, 0.02)\right)$ until $f_{\rm Edd} = 0.02$, below which it is capped at $7000\,{\rm km\,s^{-1}}$.	• Same models, with alterations, as follows. • Jet activation range increased to $M_{\rm BH,jet,min} = 7 \times 10^7\,{\rm M}_\odot$ and $M_{\rm BH,jet,max} = 10^8\,{\rm M}_\odot$, with specific jet onset mass assigned to each BH particle. • Maximum jet velocity additionally scales with $M_{\rm BH}$ at $f_{\rm Edd} < 0.02$ as $v_{\rm jet} = 7000\,{\rm km\,s^{-1}} \times {\rm MIN}\left(\log_{10}(0.2/f_{\rm Edd}), v_{\rm max}\right)$, where $v_{\rm max} = \left(M_{\rm BH}/(10^8{\rm M}_\odot)\right)^{1/3}$ is limited to the range $[1, 5]$, such that $v_{\rm jet}$ is capped at $35,000\,{\rm km\,s^{-1}}$ for $M_{\rm BH} \geq 1.25 \times 10^{10}\,{\rm M}_\odot$ and $f_{\rm Edd} \leq 2 \times 10^{-6}$.

The XMM Cluster Outskirts Project (X-COP) consists of observations of the outer regions of 13 massive clusters ($3 \times 10^{14} < M_{500}/{\rm M}_\odot < 9 \times 10^{14}$) at $z = 0.04 - 0.1$ (Eckert et al., 2017a). For objects in X-COP, Ghizzardi et al. (2021) carry out joint spectral fitting with the *XMM-Newton* EPIC/MOS and pn instruments.

Fukushima et al. (2023) measure the core IGrM abundances of 14 CHEERS groups with *XMM-Newton*/RGS.

Lastly, Sarkar et al. (2022) investigate chemical abundances out to $\sim R_{200}$ in the IGrM of four nearby galaxy groups with the *Suzaku* (Mitsuda et al., 2007) X-Ray Imaging Spectrometer (XIS; Koyama et al. (2007)) (for spectral fitting) and *Chandra* (Weisskopf et al., 2000) (for pinning down uncertainty introduced by the Cosmic X-Ray Background (CXB)).

Table 2.2: Selected observational samples containing intragroup medium (IGrM) abundance profiles. Note that telescopes are written in *italics*, while samples and instruments are in capitalized Roman font.

Paper/Sample	**Telescope Instrument(s)**	**X-Ray Band [keV]**	**No. Objects/ Object Names**	**Spatial Extent (Max. Radius)**	**Elements**
Werner et al. (2006a)	*XMM-Newton* RGS	0.8–1.4	M87	$\sim 0.02 R_{500}$	C, N, O, Ne, Fe
Grange et al. (2011)	*XMM-Newton* RGS, EPIC/MOS+pn	∼0.35–10	NGC 5044 NGC 5813	$\sim 0.06 R_{500}$ $\sim 0.08 R_{500}$	C, N, O, Ne, Mg, Si, S, Ar, Ca, Fe, Ni
Mernier et al. (2017) (CHEERS)	*XMM-Newton* EPIC/MOS+pn	0.5–10	44	$\sim 0.6 R_{500}$ (Groups) $\sim 0.9 R_{500}$ (Clusters)	O, Mg, Si, S, Ar, Ca, Fe, Ni
Mao et al. (2019)	*XMM-Newton* RGS, EPIC/MOS	∼0.5–1.8	8	~ 0.01–$0.04 R_{500}$	N, O, Ne, Mg, Fe, Ni
Ghizzardi et al. (2021) (X-COP)	*XMM-Newton* EPIC/MOS+pn	0.5–12	13	$\sim R_{500}$	Fe
Fukushima et al. (2023)	*XMM-Newton* RGS	∼0.5–1.8	14	~ 0.03–$0.07 R_{500}$	N, O, Ne, Mg, Fe, Ni
Sarkar et al. (2022)	*Suzaku* XIS	0.5–7	4	$\sim 2 R_{500}$	O, Mg, Si, S, Fe, Ni

2.2.3 Group Selection

We identify group halos at $z = 0$ as per the method laid out by Jung et al. (2022) and Hough et al. (2024). The AMIGA Halo Finder (AHF; Knebe et al. (2008); Knollmann & Knebe (2009)) is employed to hierarchically identify halos and subhalos, and we find their centers with the shrinking-sphere approach (Power et al., 2003).

We characterize the halos by their halo mass M_Δ, the mass within a sphere of radius R_Δ centered on a halo's center, such that the mean interior mass density is Δ times the critical density of the Universe. We focus on the local universe ($z = 0$), and use $\Delta = 500$ for the characteristic halo masses and radii. The Python package XIGrM[21] (X-ray properties of the IntraGroup Medium) is utilized to calculate the various X-ray halo quantities.

[21] https://xigrm.readthedocs.io/en/latest/ (accessed on 1 January 2023).

Table 2.3: Number of galaxy groups in SIMBA and SIMBA-C for the whole sample, and separately for each mass bin.

Simulation	All Bins	$13 < \log(M_{500}/M_\odot) \leq 13.5$ $0.7 \lesssim k_B T_{\rm spec,corr}\,[keV] \lesssim 1.2$	$13.5 < \log(M_{500}/M_\odot) \leq 14$ $1.2 \lesssim k_B T_{\rm spec,corr}\,[keV] \lesssim 2.2$	$14 < \log(M_{500}/M_\odot) \leq 15$ $2.2 \lesssim k_B T_{\rm spec,corr}\,[keV] \lesssim 7.4$
SIMBA	238	175	54	9
SIMBA-C	258	182	67	9

We select simulated galaxy groups as halos with three or more "luminous" galaxies ($N_{\rm l,gal}$; Hough et al. (2024)), which are defined as having a stellar mass $M_\star \geq 1.16 \times 10^9 {\rm M}_\odot$, equivalent to ≥ 64 star particles. We also restrict the halo mass range to $M_{500}/{\rm M}_\odot \geq 10^{13}$, as the majority of observed groups with measured abundance distributions do not fall below this value. In total, there are 238 halos matching these conditions in SIMBA, and 258 halos in SIMBA-C. There is a negligible number of halos with $M_{500}/{\rm M}_\odot \geq 10^{13}$ and $N_{\rm l,gal} < 3$, indicating that the cut on $N_{l,\rm gal}$ has little impact on the results.

For plotting purposes, we derive R_{2500} and R_{200} from R_{500} using approximate conversion factors from the ratios of the median values of our SIMBA-C group sample, with $\overline{R}_{2500} \approx 182.4\,{\rm kpc}$, $\overline{R}_{500} \approx 414.1\,{\rm kpc}$, and $\overline{R}_{200} \approx 641.2\,{\rm kpc}$[22].

To investigate how the overall statistical properties of abundance profiles change with group mass, we use M_{500} rather than M_{200} or $M_{\rm vir}$, as it is more easily derived from observations of dim groups, and thus better facilitates comparison between simulations and observations. We separate both simulated and observed galaxy groups into three bins in M_{500}: $13 < \log(M_{500}/{\rm M}_\odot) \leq 13.5$, $13.5 < \log(M_{500}/{\rm M}_\odot) \leq 14$, and $14 < \log(M_{500}/{\rm M}_\odot) \leq 15$. See Table 2.3 for the number of simulated halos in each mass bin.

2.2.4 IGrM X-Ray Properties

To compute IGrM properties that would observationally be derived from X-ray luminosity or spectral measurements, we follow the procedure of Hough et al. (2024). We define the simulated IGrM as all gas particles with $T > 5 \times 10^5$ K and a hydrogen number density $n_H < 0.13$ atoms cm^{-3} (below the star formation density threshold in SIMBA and SIMBA-C). Our tests indicate that the derived abundance profiles are relatively robust to the choice of temperature threshold, from $\sim 10^5$–5×10^6 K.

Both SIMBA and SIMBA-C launch hydrodynamically decoupled interstellar particles to represent the heated component of stellar and AGN winds. We exclude these wind particles

[22]Computing the median values of R_{500} separately in our three M_{500} bins results in negligible changes to their ratios compared to using the whole sample.

while they are decoupled in all X-ray analyses in the present study.

X-Ray Luminosity

We calculate the X-ray luminosity of each gas particle using two Python packages. XIGrM computes the temperature of each gas particle based on its internal energy, hydrogen mass fraction, and electron abundance. PyAtomDB[23] (Foster et al., 2016; Foster & Heuer, 2020; Foster et al., 2021) generates each gas particle's X-ray spectrum using their mass, temperature, metallicity, and SPH-weighted[24] density under the assumption that the gas is optically thin and in collisional ionization equilibrium.

To obtain the total X-ray luminosity for a gas particle in a desired energy band $L_{X,E_1-E_2,i}$, where i denotes the particle's id, the photon energy intensities are summed across the specified energy range. We use the total summed line and continuum emission to compute the X-ray luminosities. Additionally, we opt to use the 0.5–10 keV band, as Mernier et al. (2017) use this energy range for spectroscopic fitting. We find negligible differences in the simulated abundance profiles when using other bands.

Abundances

Observationally, gas-phase abundances in the IGrM are primarily derived from spectroscopic fitting (see Gastaldello et al. (2021); Mernier & Biffi (2022), and references therein). Gastaldello et al. (2021) note the importance of carefully choosing the weight w when computing the weighted average metallicity $Z_w = \int wZdV / \int wdV$ in simulated halos and comparing it to observations.

For comparison to observations, we opt to calculate 2D projected emission-weighted abundances (Equation (2.1)). We describe the projecting procedure in Section 2.2.5. Weighting abundance by X-ray luminosity more closely resembles observations than mass or volume weighting, as the spectroscopically inferred abundances are influenced most strongly by bright areas in a group (Biffi et al., 2017).

To compute an element's abundance, we calculate an X-ray luminosity weighted mean:

$$Z_{L_X,q} = \frac{\sum_i Z_{q,i} L_{X,i}}{\sum_i L_{X,i}}, \tag{2.1}$$

where i refers to an individual gas particle's id, q is the element under consideration,

[23]The PyAtomDB documentation can be found at https://atomdb.readthedocs.io/en/master/ (accessed on 1 January 2023).

[24]SPH = smoothed particle hydrodynamics.

$Z_{q,i} = m_{q,i}/m_{gas,i}$ is the mass fraction of element q for particle i, $L_{X,i}$ is the X-ray luminosity calculated as described previously, and the sum runs over all particles within a halo or radial bin. We scale all abundances to the photospheric solar abundances of Asplund et al. (2009), also rescaling observational results that are reported with different solar normalizations.

One can ask whether emission-weighted abundances are comparable to spectroscopic values. Some studies have found little difference between intrinsic abundance profiles and those inferred from mock spectroscopy of simulated groups (e.g. Pearce et al., 2021). Therefore, while it would make for a more realistic comparison, we do not perform full spectral fitting of post-processed synthetic X-ray spectra of galaxy groups (see Jennings & Davé, 2023; Cui et al., 2024; Jennings et al., 2025, for current work).

We emphasize that emission-weighted abundances must be interpreted with caution in the context of metal formation mechanisms and timescales. Hough et al. (2024) show the differences in global mass-weighted and emission-weighted abundances, and demonstrate the bias in measuring abundances only from the X-ray-emitting gas. Consequently, when we compare the abundance profiles of SIMBA and SIMBA-C to investigate the underlying physical processes in Section 2.4.2, we use 3D spherically averaged mass-weighted profiles, as they better represent the intrinsic abundance distributions. These abundances are calculated as

$$Z_{m,q} = \frac{\sum_i Z_{q,i} m_i}{\sum_i m_i} = \frac{M_q}{M_{\rm gas}}, \tag{2.2}$$

where M_q is the total mass of element q in a halo or radial bin, and $M_{\rm gas}$ is the total mass of IGrM gas in the same halo or radial bin.

Global Temperature

In addition to M_{500}, we use an observationally driven global measurement of group temperature to characterize each group. De Plaa et al. (2017) take group temperatures from Chen et al. (2007) and Snowden et al. (2008) for CHEERS objects. As in these studies, IGrM temperatures are typically determined by identifying a single-temperature thermal model whose spectrum best matches the observed spectrum. Reproducing this procedure is involved and time consuming because the observed spectrum is a combined output of emission from gas that spans a range of temperatures. We instead follow the approach adopted by Hough et al. (2024), and use the temperature measure proposed by Vikhlinin (2006), which we will refer to as the "spectroscopic" temperature $T_{\rm spec}$. Vikhlinin (2006) shows that $T_{\rm spec}$ is a good estimate of the temperature derived from fitting the spectrum.

Moreover, the cores of groups and clusters are known to have widely varying temperatures that may not correlate well with their total mass or gravitational potential well depth. Observationally, O'Sullivan et al. (2017) show that the central regions at $R \lesssim 0.15R_{500}$ of both CC and NCC groups exhibit temperature drops or increases, while the temperature profiles outside this core region tend to remain flat to the measured radial extents. Jennings et al. (2025) demonstrate that X-ray AGN bubbles in the HYENAS (Cui et al., 2024) suite of zoom-in cosmological simulations typically sit in the IGrM at ∼20–60 kpc, which roughly corresponds to $\sim 0.05-0.2R_{500}$, agreeing with the extent of the observations. Many observational studies, such as those of Chen et al. (2007) and Snowden et al. (2008), use different methods to excise this inner region from groups with cooling cores when determining group properties. As our primary goal is to sample the gas temperature that is reflective of the gravitational potential, we remove all IGrM particles within $0.15R_{500}$ when computing $T_{\rm spec}$, restricting ourselves to the radial range $0.15 \leq R/R_{500} \leq 1$. We refer to this as the "core-corrected" temperature, or $T_{\rm spec,corr}$, which is found to be more robust than $T_{\rm spec}$ (see Hough et al. (2024) for more details).

We use the $M_{500} - T_{\rm spec,corr}$ scaling relation $\log(M_{500}/\mathrm{M}_\odot) = 1.935\log(k_{\rm B}T_{\rm spec,corr}\ [\mathrm{keV}]) + 13.32$ from SIMBA-C (Hough et al., 2024) to estimate the M_{500} of observed groups from their measured global X-ray temperatures. The calculated M_{500} values are used to place each observed group into its corresponding mass bin. Due to the inherently uncertain nature of the masses calculated with this method, we permit observed groups that are sufficiently close in mass to their neighboring bins to be counted in those bins. Specifically, groups that have a value of M_{500} that is up to 25% of the relevant bin's width in logarithmic scale above or below the edges of that bin are included in the bin. This results in some groups appearing in multiple M_{500} bins or being used in the calculations for more than one average profile. All 44 CHEERS systems end up being included in at least one of our three mass bins, except for one very-low-mass group, NGC 5813.

In supplementary tests, we find that setting this 25% to 0% results in relatively minor changes that are insignificant compared to the scatter and uncertainty already present in simulations and observations. However, we opt to keep the 25% value, as it elevates the statistical significance from averaging.

Temperature measurements for CHEERS objects (including the groups from Werner et al. (2006a) and Grange et al. (2011)) come from De Plaa et al. (2017), who provide emission-weighted global temperatures adapted from Chen et al. (2007) and Snowden et al. (2008). For the group sample from Sarkar et al. (2022), temperature values from the literature are used: Sarkar et al. (2021) for MKW4; Wong et al. (2016) for Antlia; Su et al. (2015) for RX

J1159; and Su et al. (2013) for ESO 3060170. Ghizzardi et al. (2021) provide hydrostatic M_{500} values from Ettori et al. (2019). Because these masses are all well into our high-mass bin, we assume that converting their corresponding temperatures to M_{500} using our $M_{500} - T_{\rm spec,corr}$ relation would not sufficiently change the masses to sit outside the high-mass bin; therefore, we do not go to the effort of finding their X-ray temperatures in the literature.

We also employ the SIMBA-C $M_{500} - T_{\rm spec,corr}$ scaling relation to convert the M_{500} bins into $T_{\rm spec,corr}$ bins (see Table 2.3), since these values are more useful and directly applicable from an observational perspective.

2.2.5 Calculating Abundance Profiles

To explore how SIMBA-C differs from SIMBA in terms of the distribution of metals in the IGrM and how the results compare to observations, we investigate the averaged radial profiles of the gas-phase abundances of various key elements. Mernier et al. (2017) and Sarkar et al. (2022) present projected (2D) profiles, arguing that deprojection assumes spherical symmetry, an assumption that is not necessarily accurate in groups and clusters because they may exhibit non-spherical morphologies. We therefore choose to project our simulated profiles to ensure a like-to-like comparison with observations[25]. For the same reason, we use the projected profiles from Ghizzardi et al. (2021).

For the simulated 2D L_X-weighted abundance profiles of each group, all IGrM particles in a cylinder of radius $3R_{500}$ and total height $3R_{500}$ centered on each group's shrinking-sphere center are projected onto the x-y plane[26]. We bin the particles by halocentric radius into 14 non-overlapping circular annuli. The edges of these bins are identically defined for every group in terms of R_{500}, with the first bin being in the range of 0–0.01R_{500}, 10 equally log-spaced bin edges in the range of 0.01–1R_{500}, and 4 in the range of 1–3R_{500}. We compute X-ray luminosities and metal mass fractions for each IGrM particle, and then the emission-weighted average abundance in each annulus of each group, as described in Section 2.2.4 and Equation (2.1).

For the 3D mass-weighted profiles, the same procedure is carried out with no projection; instead, radial shells are spherically averaged according to Equation (2.2). The same radial bin definitions are employed, with the addition of 10 more equally log-spaced bin edges in

[25]Some studies find projecting simulated profiles to have a significant impact on their shape and/or normalization, generally decreasing and flattening the profiles, especially in the group cores (e.g. Braspenning et al., 2024; Nelson et al., 2024), whereas others find no notable differences (e.g. Vogelsberger et al., 2018; Altamura et al., 2023). Our results follow the former findings.

[26]Choosing the z-axis as the axis of projection results in limited biasing, since any preferential alignment of the halos or spherical asymmetry should be statistically averaged out in each mass bin.

the range of 3–10R_{500}.

Elements that are of special interest to the observational X-ray community include C, N, O, Ne, Mg, Si, S, Ca, Fe, and Ni (Böhringer & Werner, 2010; Werner & Mernier, 2020; Gastaldello et al., 2021). The distributions of the abundances of these metals in galaxy groups and clusters can indicate how and when chemical enrichment occurs, what effects it will have on the future evolution of groups, including cooling and dust formation, and the efficiency of the dispersal and mixing mechanisms at play (e.g. Scannapieco et al., 2005; Tornatore et al., 2007; Wiersma et al., 2009b; Biffi et al., 2017, 2018b, see also Gastaldello et al. (2021); Mernier & Biffi (2022) and references therein). We note that some of these metals, such as C, N, Ne, and Ni, are more difficult to measure due to the lack of strong, well-separated spectral lines in the observed X-ray bands, resulting in limited observations.

Stacking Profiles

To place any sort of statistically significant constraints or draw qualitative or quantitative conclusions, we must make use of average profiles. Simulations and observations suffer from opposite limitations in two major ways in the context of this study, making comparisons slightly more challenging.

First, given the shape of the halo mass function, a fixed volume contains more lower- than higher-mass galaxy groups. Observational samples tend to be weighted towards—or at least have greater statistics for—massive groups and clusters because their X-ray surface brightnesses are larger. Due to this bias, catalogs are more complete at larger halo masses (e.g. Mernier et al., 2017; Ghizzardi et al., 2021). On the other hand, the statistics of cosmological simulations are limited by the volume of the simulation box. Thus, simulation samples have greater statistical significance for lower-mass groups than higher-mass groups, opposite to observational samples.

Second, the outskirts of the observed groups are relatively X-ray dim compared to their cores, where the gas tends to be more dense (e.g. Mulchaey, 2000). Therefore, uncertainties in and the scatter of inferred abundances are often greater in the group outskirts than in the cores. In simulations, however, one of the main factors impacting scatter is the number of resolution elements present in a given annulus or shell: the fewer gas particles, the worse the number statistics, resulting in a greater Poisson uncertainty (see Power et al. (2003); Ludlow et al. (2019) for numerical convergence studies). Since group cores are far more compact than the extended outskirts, there are fewer gas particles in the inner regions. This results in the profiles having larger uncertainties and scatter in the core than the rest of the group, contrary

to what is found for observed profiles.

For these reasons, we use different radial bins and bin sizes for simulations compared to observations. By necessity, for decent statistics, the inner radial bins in simulations are comparatively larger in a log-scaled sense than the outer ones (see Section 2.2.5), and vice versa for the observational profiles. We also take slightly different approaches to determining averages and representational uncertainties in simulated versus observed group samples, as described in the following two sections.

Stacking Observations

To create average observed abundance profiles in each M_{500} bin, we adapt the procedure described by Mernier et al. (2017), first proposed by Leccardi & Molendi (2008). In the study of Mernier et al. (2017), since the spectral analysis to compute the abundance profiles of individual groups was performed within annuli of fixed angular sizes, regardless of the distance or redshift, the resulting profiles rescaled to each group's R_{500} have different radial bins. Thus, this method requires choosing a set of "reference" radial bins in units of R_{500} for the final average abundance profiles. We employ the radial bins from Mernier et al.'s "group" subsample (Mernier et al., 2017), with bin edges $[0, 0.009, 0.024, 0.042, 0.064, 0.1, 0.15, 0.26, 0.97]R_{500}$.

In each M_{500} bin and reference radial bin, we then compute the median abundances weighted by the individual observation's statistical errors from spectral fitting, as well as a weighting factor between 0 and 1 representing the linear overlapping geometric area fraction of the ith reference radial bin on the jth annulus belonging to the kth galaxy group[27]. The scatter of the average profile is given by the 16th and 84th percentiles weighted by the same quantities, as these converge to 1σ limits in the case of a Gaussian distribution. We find no qualitative differences between the 16th and 84th percentiles compared to the quartiles (25th and 75th percentiles) in terms of the agreement/discrepancy across simulations and observations; quantitatively, there is a minor shrinking of the error bars.

This method reduces the effect of uncertain measurements on the final average profile, and increases the weight of measurements with excellent data quality (e.g., from a very bright group, or from an instrument with higher resolution or sensitivity). As recommended by Mernier et al. (2017), we include radial bins with unphysical negative abundances derived from spectral fitting so as not to bias the averages, but discard certain radial bins from specific groups that do not meet their standards, due to bad data quality, contamination

[27]This overlap factor w is calculated as follows: if the radial bin is fully contained in the reference radial bin (inclusive), $w = 1$; if the bin is fully outside the reference bin, $w = 0$; otherwise, if the bin and reference bin partly overlap, w is the fraction of the radial bin overlapping with the reference bin.

(e.g., from AGN), or poor spectral fitting (details can be found in Mernier et al. (2017)).

In the study of Mernier et al. (2017), Fe was measured in simultaneous *XMM-Newton*/EPIC MOS+pn "global" spectral fits, while O could only be measured with the MOS instruments. The rest of the elements were measured separately with both MOS and pn ("local" fits). While Mernier et al. (2017) devised a method to combine the measurements from the MOS and pn instruments, we opt to keep these separate for the elements that have both, since they are sometimes found to provide systematically different values. As the true abundances are not known a priori, there is no way to pick one of these instruments over the other. Therefore, we take any spread between the MOS and pn stacked profiles, on top of their individual scatter, to be representative of the uncertainty.

We employ the same method of error-weighted averaging for the core abundance results from Mao et al. (2019) and Fukushima et al. (2023), albeit with only a single reference radial bin at small radii. All groups in the X-COP sample of Ghizzardi et al. (2021) fall into our high-mass bin; therefore, we simply use the mean profiles reported directly in their paper[28]. We do not stack the profiles from Sarkar et al. (2022), as their sample only consists of four objects.

In supplementary tests, we find minimal changes in the averaged observed abundance profiles and little impact on the agreement between simulated and observed abundance profiles when altering some of the choices we make for averaging. This includes the choice of reference radial bins, whether negative abundances are excluded from averaging, and whether certain groups with excellent data quality (that may bias the average profile towards their values) are excluded.

Stacking Simulations

Ideally, for a consistent comparison, simulated profiles would be averaged in the same manner as observations. However, the uncertainties in the simulated abundance profiles decrease with increasing halo mass, as the number of particles increases[29]. Hence, performing an error-weighted average would bias the resulting abundance profiles towards the higher-mass groups. Thus, we do not weight the average abundance profiles from simulations by uncertainty. Rather, we calculate the abundance profiles of each group individually, and then find the median values of each radial bin in each M_{500} bin. We again take the 16th and 84th percentiles to represent the uncertainty.

[28] Ghizzardi et al. (2021) find negligible differences between the mean and median Fe profiles of the X-COP sample.

[29] Because the number of groups decreases with increasing M_{500} in cosmological simulations, the scatter in the median profiles also increases; however, this does not necessarily introduce any bias.

To address numerical resolution concerns, particularly in the high-density/low-particle-number group cores, we implement four cuts, described in the following list. According to Davé et al. (2016), SIMBA and SIMBA-C employ GIZMO with a 64-neighbor cubic spline kernel for hydrodynamics, and, similarly, a 64-particle kernel for adaptive gravitational softening. For this reason, here, "resolved" refers to a radial bin that contains at least 64 resolution elements.

1. Unresolved individual radial bins of individual groups are excluded from averaging. In the case of projected profiles, if a 2D annulus has any contributions from any unresolved 3D shells in the group, the annulus is also considered unresolved. The reason for this is that, spectroscopic observations being effectively X-ray emission weighted and L_X increasing towards the center of a group, the abundances in annuli have greater contributions from the inner spherical shells. Therefore, in our simulations, if these inner shells are unresolved, it can impact the resultant projected abundance values significantly[30].

2. Per group, radial bins that are thinner than the *physical* minimum gravitational softening length are excluded. The physical value is the Plummer-equivalent value multiplied by 2.8, to account for the conversion to the actual smoothing kernel radius (Davé et al., 2016). Here, this gives $0.5\,\mathrm{h}^{-1}$ kpc "Plummer-equivalent" $= 0.5/0.68 \times 2.8\,\mathrm{kpc} \approx 2\,\mathrm{kpc}$.

3. Similar to Braspenning et al. (2024), we require at least 16% of the groups in a radial bin to be resolved. Below this point, the 1σ error can no longer be reliably determined. If this condition is not met, the radial bin is fully ignored and does not appear in the averaged profile. Note that this may result in the averaged profiles for different mass bins, and for SIMBA and SIMBA-C, having different inner stopping radii.

4. There must be a minimum of five resolved individual radial bins contributing to a given radial bin of the average profile; otherwise, the radial bin is ignored overall. This condition is imposed to ensure that radial bins that undergo the prior cuts still contain sufficient statistics to consider the average as representative of the population.

[30]We find that using the total number of particles projected into an annulus as the resolution cut criterion for each annulus results in insignificant changes to the projected abundance profiles in comparison to using the number of particles in each spherical shell that contributes to the annulus (our approach discussed in this text). The former method generally leads to slightly higher median amplitudes in the innermost radial bins, and—as expected—produces far fewer unresolved radial bins (i.e., the profiles extend further in towards the group cores). Any qualitative conclusions we draw are robust to the choice of resolution cut method.

2.3 Results

Our results focus on IGrM abundance profiles. We compare SIMBA-C and SIMBA to each other and to the observational samples outlined in Section 2.2.2. Kobayashi et al. (2020a) describe the setup of the `Chem5` model and the proportion of each element that originates from different astrophysical sources across cosmic time, which, for the purposes of the present study, constitute AGB stars, core-collapse SNe (SNe II and HNe), and SNe Ia. Based on their results, and focusing only on those metals observable in X-ray and for which we have observational data, we split up the metals according to their origins as follows:

- The iron-peak elements **Fe and Ni** are produced largely by SNe Ia. In `Chem5`, about 60% of Fe comes from SNe Ia, with the rest mainly produced by HNe. Also, an appreciable amount of Ni comes from core-collapse SNe. We focus heavily on Fe, since it is the most robustly constrained metal from X-ray observations, and has been shown to be a good tracer of overall IGrM metallicity (Renzini, 1997; Urban et al., 2017; Vogelsberger et al., 2018; Pearce et al., 2021; Gastaldello et al., 2021; Mernier & Biffi, 2022).

- **C and N** are produced primarily by AGB stars, with considerable amounts from core-collapse SNe (up to ∼40% for C at $z \sim 0$).

- The light α elements **O, Ne, and Mg** originate largely from core-collapse SNe.

- The heavy α elements **Si, S, and Ca**, similar to the other α elements, are mainly produced by core-collapse SNe, but with a significant proportion (∼20–40%) originating from SNe Ia.

For each grouping of metals, we compare the SIMBA abundance profiles to those of observations, followed by a comparison of SIMBA-C and observations (emphasizing the differences found for SIMBA-C), and finally compare the SIMBA-C and SIMBA abundance profiles.

2.3.1 Iron-Peak Elements: Fe and Ni

SIMBA-C tracks all of the Fe-peak elements, while SIMBA only tracks Fe. To the best of our knowledge, on top of Fe, X-ray observational data of Fe-peak elemental abundances in the IGrM are only available for Cr, Mn, and Ni[31]. Figure 2.1 shows the simulated average

[31]For Cr and Mn, we can only find abundance *ratios* (e.g., X/Fe) in the literature, not *absolute* abundances. However, the simulated Cr and Mn abundance profiles have similar amplitudes, shapes, and trends with M_{500} as Ni.

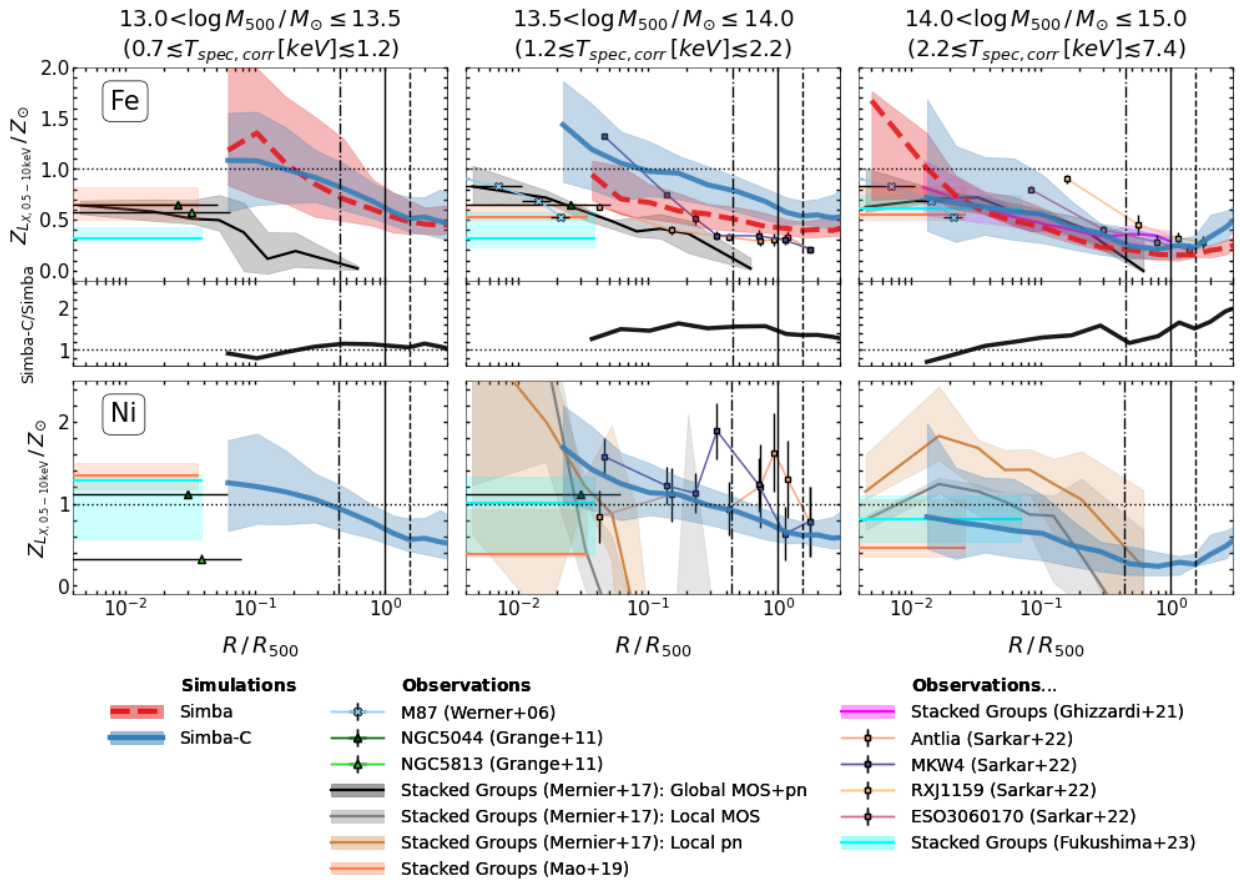

Figure 2.1: Median 2D projected Fe (*upper row*) and Ni (*lower row*) abundance profiles from SIMBA and SIMBA-C, as well as a compilation of observational results. Note that SIMBA does not track Ni. Abundance profiles of individual groups are emission weighted by the IGrM X-ray luminosity in the 0.5–10 keV band, and are scaled to the solar abundances of Asplund et al. (2009). Shaded regions represent the 16th–84th percentiles in the scatter. The three columns split all data into our three bins in group mass M_{500}, with their corresponding approximate temperatures $T_{\rm spec,corr}$ indicated. The vertical solid line is R_{500}, and the vertical dot-dashed and long-dashed lines are our approximations for R_{2500} and R_{200}, respectively, using the median values from our two simulated samples. The horizontal dotted line is solar abundance $Z_\odot$. The radial axes extend in the range of 0.004–3R_{500}. The upper limit, just above R_{200}, cuts out the IGM, as we focus primarily on the IGrM in this study. The lower 40% of each panel in the top row shows the ratio of the SIMBA-C to SIMBA abundance profiles, highlighting their relative amplitudes across radii.

IGrM Fe and Ni abundance profiles of all selected galaxy groups in SIMBA and SIMBA-C, as well as the observational samples. The lower 40% of each individual panel plots the ratio of the SIMBA-C to SIMBA abundance profiles, which is useful for a direct comparison of the amplitude and shape of the two simulated profiles.

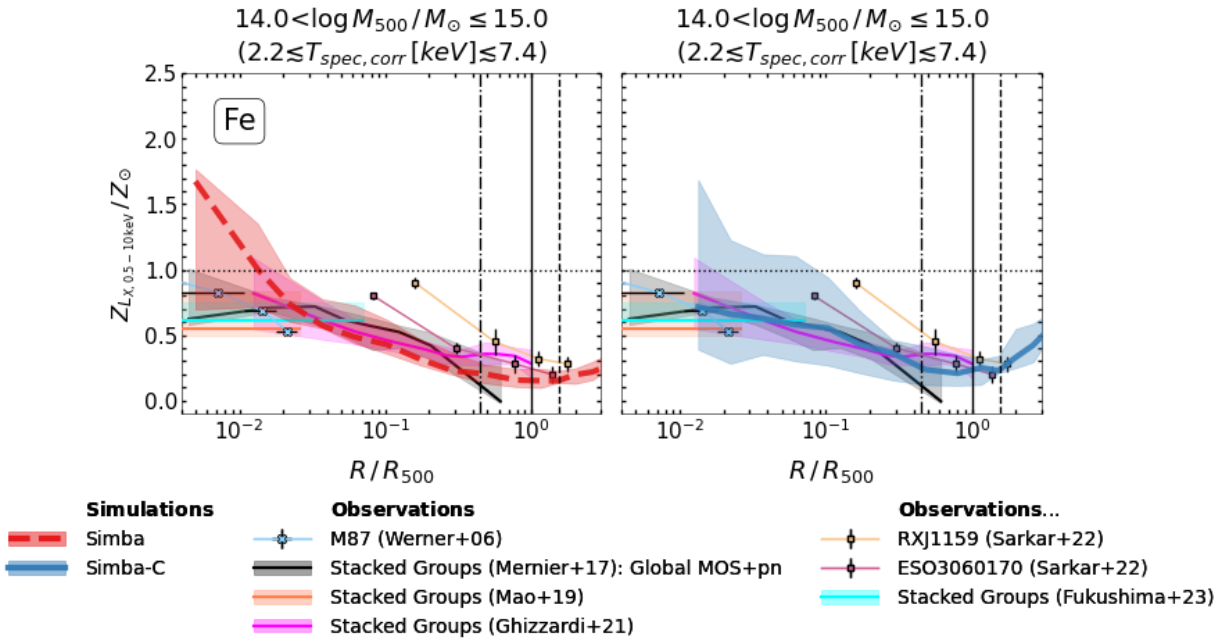

Figure 2.2: Projected L_X-weighted Fe abundance profiles of SIMBA and SIMBA-C in the high-mass bin, separated by simulation: SIMBA (*left*) and SIMBA-C (*right*). Both subplots show the same set of observational samples. This figure is meant to separate out and clarify the comparison of the simulated and observed abundance profiles from the first row, third column in Figure 2.1, which is quite crowded. All other characteristics of the plot are the same as in Figure 2.1. The vertical solid line is R_{500}, and the vertical dot-dashed and long-dashed lines are our approximations for R_{2500} and R_{200}, respectively, using the median values from our two simulated samples. The horizontal dotted line is the solar abundance $Z_\odot$.

Figure 2.2 shows the simulated and observed Fe abundance profiles in the high-mass bin, separated by simulation (see caption), since this panel in Figure 2.1 is quite crowded.

SIMBA–Observation Comparison

On average, the low-mass SIMBA groups (leftmost bin) are discrepant with observations at $R \gtrsim 0.1R_{500}$, being around a factor of 2–5 too high. SIMBA and observations become more similar in amplitude in the intermediate-mass bin (middle column) through a slight decrease and increase, respectively. With respect to CHEERS (Mernier et al., 2017), however, SIMBA is still inconsistent at $>1\sigma$.

In the high-mass bin (rightmost column), in the outskirts at $R \lesssim R_{200}$, SIMBA and observations converge to $\sim$0.1–0.3 $Z_{\mathrm{Fe},\odot}$, similar to other studies of massive groups and clusters in the literature, both simulation based (e.g. Barnes et al., 2017; Biffi et al., 2017, 2018b; Vogelsberger et al., 2018; Braspenning et al., 2024) and observational (e.g. Urban

et al., 2017; Lovisari & Reiprich, 2019; Ghizzardi et al., 2021; Sarkar et al., 2022; Gatuzz et al., 2023). This can be seen clearly in Figure 2.2. Notably, the median SIMBA Fe abundance rises steeply towards the center at $R \lesssim 0.03R_{500}$, whereas observations remain flatter and sub-solar, although the lower bound of the uncertainty limits still overlaps with observations.

SIMBA-C–Observation Comparison

In the low-mass bin, the SIMBA-C Fe profile is similar to that of SIMBA, and equally inconsistent with observations. Unlike SIMBA, however, SIMBA-C changes very little from the low- to intermediate-mass bins, in which it has a higher-amplitude median profile than SIMBA and is in less agreement with observations.

In high-mass groups, SIMBA-C exhibits excellent agreement with observations across all radii[32]. As with SIMBA, SIMBA-C converges with observations in the outskirts. Unlike SIMBA, SIMBA-C remains flatter, sub-solar, and in agreement with observations at $R \lesssim 0.03R_{500}$ (see Figure 2.2). At this mass scale, SIMBA-C is a clear improvement over SIMBA.

The SIMBA-C profiles for Ni follow similar trends to Fe (i.e., abundances at $R \gtrsim 0.1R_{500}$ decreasing and core abundances flattening from the intermediate- to high-mass bin), and the two have similar amplitudes. This is expected because Ni is itself an Fe-peak element, and the ratio of the Fe and Ni yields is roughly constant across stellar metallicity for both core-collapse SNe and SNe Ia. Observational profiles for Ni, especially for lower-mass groups, are highly uncertain because the Ni-L shell emission lines are largely unresolved with current CCD instruments (e.g. Gu et al., 2018; Gastaldello et al., 2021)[33]. Although the SIMBA-C abundance profiles of Fe and Ni are similar in amplitude, by extrapolating radially inwards, the Ni profiles better agree with observations in the low-mass bin than those of Fe. This is due to a greater abundance of Ni compared to Fe in the cores of the observed lower-mass groups. In the intermediate-mass bin, SIMBA-C appears to produce slightly high core abundances (consistent with the more uncertain results of Mernier et al. (2017)), but agrees well with the outskirt values, and is broadly consistent with observations in the high-mass bin. The agreement in the intermediate-mass bin at $R \gtrsim 0.1R_{500}$ should be interpreted as preliminary due to low observational statistics; more high-quality observations are required.

[32]Note that the innermost radial bin of each group in the Sarkar et al. (2022) sample includes all data from the center of the group out to the first bin edge, which tend to be a fair bit larger than the first bin edges of the simulated and other observed profiles. In this way, there are contributions to the inner Sarkar et al. (2022) radial bins from the core, where the abundances tend to be higher, but, due to the log scaling of the radial axes, these values then appear at larger radii.

[33]CHEERS has measurements of Ni abundance profiles at low group masses, but, as they are quite limited, we have opted not to show them.

SIMBA-C–SIMBA Comparison

At $R \gtrsim 0.1R_{500}$, SIMBA Fe abundance gradually decreases with increasing M_{500}. Simultaneously, the SIMBA abundance profiles become more centrally peaked, potentially indicating that the deepening gravitational potentials are more efficiently retaining metals in the inner regions.

As stated, SIMBA-C, in contrast, alters minimally from the low- to intermediate-mass bins, such that the two simulations become largely discrepant at $\gtrsim 1\sigma$. This is followed by an abrupt decrease in the SIMBA-C abundance profile amplitude in the high-mass bin, with the profile amplitude and shape being broadly comparable to that of SIMBA for $R \gtrsim 0.1R_{500}$ but significantly flatter at $R \lesssim 0.1R_{500}$[34,35].

Additionally, at high masses, the outer regions of SIMBA-C groups contain, on average, somewhat greater abundances of Fe than in SIMBA. Combined with the different core abundances between SIMBA and SIMBA-C, this suggests that, in the high-mass groups of SIMBA-C, Fe is expelled to larger radii more efficiently, whereas, in SIMBA, the Fe is confined substantially more to the core region. On the other hand, in low-mass groups, outflows appear to be shuttling metals to the group outskirts more equally in the two simulations.

Overall, the improved agreement for SIMBA-C at high masses notwithstanding, the simulation–observation discrepancy in Fe abundance profiles at low masses for both SIMBA and SIMBA-C indicates that there exist persistent issues in our simulations at the group scale that still need to be addressed.

2.3.2 C and N

Figure 2.3 depicts the C and N abundance profiles in SIMBA and SIMBA-C, and core abundances of these metals in observations.

SIMBA–Observation Comparison

SIMBA produces group cores over-enriched in N by up to factors of ~ 4 in the low- and high-mass bins. The disagreement is less extreme in the intermediate bin but still evident. We note, however, that observations also find highly super-solar abundances of N in the IGrM.

[34]Since there are only nine groups in each simulated sample in the high-mass bin, we test removing different groups from this bin, and find that the median profiles in SIMBA and SIMBA-C change minimally, preserving the trends we find and confirming that they are statistically robust.

[35]In the high-mass bin, due to the resolution cuts, SIMBA-C "stops" one radial bin above SIMBA. Without these cuts, the trends already found are further exaggerated, indicating that it is unlikely that SIMBA-C would show a rapid increase in core Fe abundance (similar to SIMBA) if the simulation resolution were enhanced.

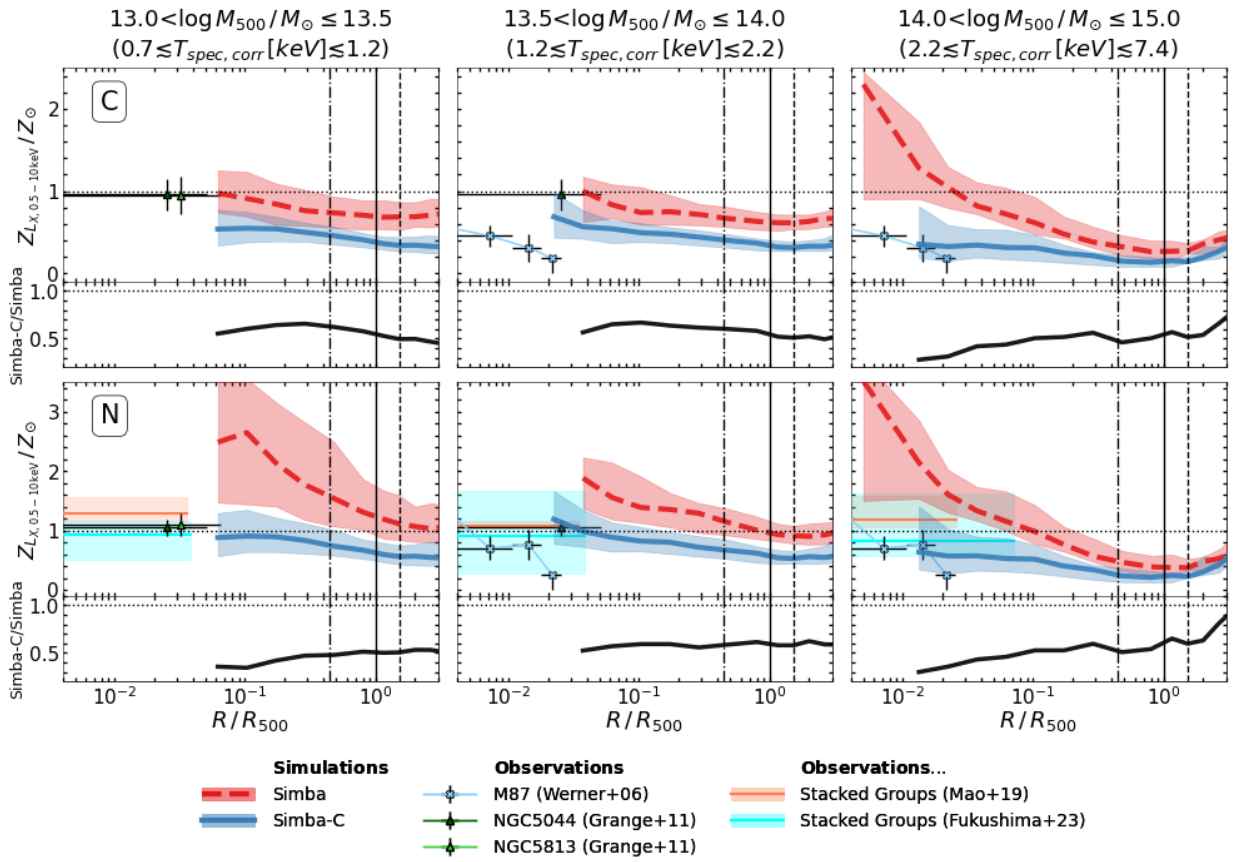

Figure 2.3: Same as Figure 2.1 but for C (*upper row*) and N (*lower row*). The vertical solid line is R_{500}, and the vertical dot-dashed and long-dashed lines are our approximations for R_{2500} and R_{200}, respectively, using the median values from our two simulated samples. The horizontal dotted line is solar abundance $Z_{\odot}$.

For example, some groups in the Mao et al. (2019) and Fukushima et al. (2023) samples have N abundances of up to $\sim 2Z_{\mathrm{N},\odot}$, while NGC 1404 was found to have abundances of around $2-3Z_{\mathrm{N},\odot}$ (Mernier et al., 2022).

Observations of IGrM C abundances are generally too limited to draw conclusions confidently. At lower masses, extrapolating radially inwards, SIMBA appears to match observations, while, similar to N, it generally over-enriches high-mass groups in terms of C. A more comprehensive study, collecting all data from the literature and/or using the upcoming observations from *XRISM*, will be carried out in the future.

SIMBA-C–Observation Comparison

Unlike SIMBA, SIMBA-C agrees well with observations of N core abundances across all masses (extrapolating radially inward in the low-mass bin), and with C core abundances in the intermediate- and high-mass bins. However, SIMBA-C appears to under-enrich low-mass groups with C, making it slightly less consistent with observations than SIMBA.

C and N are primarily produced by AGB stars. Therefore, the overhauled treatment of AGB stars in CHEM5 in SIMBA-C improves concretely on the enrichment of the IGrM with N, and potentially with C, in particular in group cores.

SIMBA-C–SIMBA Comparison

Figure 2.3 shows that both C and N feature one similar trend to Fe: from the two lower-mass bins to the high-mass bin, the SIMBA profiles become highly centrally concentrated, whereas the SIMBA-C profiles remain flat in the core.

In contrast to Fe though, at all M_{500} and all radii, the profiles of SIMBA have statistically ($\gtrsim 1\sigma$) larger amplitudes than those of SIMBA-C. This is particularly clear in the inner regions, where SIMBA largely produces inwardly increasing abundance profiles while the SIMBA-C profiles are flatter and may even hint at a "turn over" moving into the core.

2.3.3 Light α Elements: O, Ne, and Mg

Figure 2.4 shows the IGrM abundance profiles of O, Ne, and Mg for SIMBA, SIMBA-C, and observations.

SIMBA–Observation Comparison

In the low-mass bin, for all three metals, SIMBA produces abundance profiles that are too high in amplitude compared to observations. Additionally, the SIMBA profiles show an inwardly increasing trend toward super-solar abundances, taking it further away from the sub-solar abundances observed in galaxy group cores.

While the same is true in the intermediate-mass bin, the profiles from SIMBA and the data from *XMM-Newton* are slightly closer. For O and Mg, the observations from the study of Sarkar et al. (2022) with *Suzaku* are relatively consistent with SIMBA, bounding the simulation from above (at least at $R \lesssim R_{2500}$ for O). On the other hand, the SIMBA profiles exhibit an upturn in abundance at $R \gtrsim R_{500}$, a feature that again brings them away from the radially flat or decreasing trends of outskirt observations of O and Mg abundances.

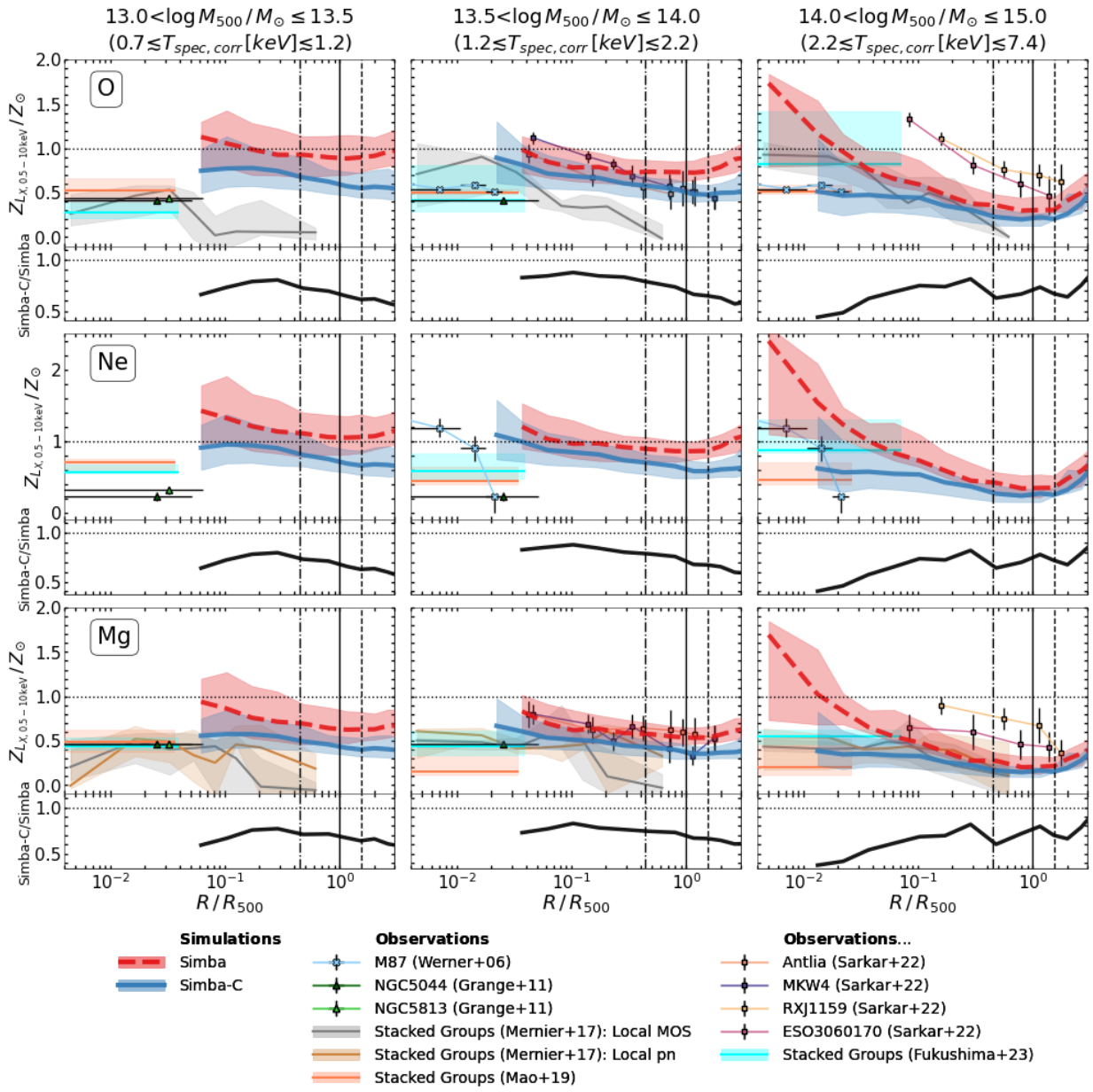

Figure 2.4: Same as Figure 2.1 but for O (*upper row*), Ne (*middle row*), and Mg (*lower row*). The vertical solid line is R_{500}, and the vertical dot-dashed and long-dashed lines are our approximations for R_{2500} and R_{200}, respectively, using the median values from our two simulated samples. The horizontal dotted line is solar abundance $Z_{\odot}$.

In the high-mass bin, SIMBA generally produces overly enriched cores at $R \lesssim 0.1R_{500}$, but is still more or less consistent with observations. It is again bounded by the two observational samples at $R \gtrsim 0.1R_{500}$, the CHEERS sample (Mernier et al., 2017) below and the Sarkar et al. (2022) sample above, respectively.

SIMBA-C–Observation Comparison

At low group masses, SIMBA-C shows hints of a central downturn in abundance, which is non-existent in SIMBA. Extrapolating this trend inward suggests that SIMBA-C may agree with observations of core abundances where SIMBA does not. Although both simulations produce profiles that are too high in O abundance at $R \gtrsim 0.1R_{500}$ compared to stacked group observations (Mernier et al., 2017), SIMBA-C's lower amplitude is regardless an improvement over SIMBA. Furthermore, for the same reason, while SIMBA sits largely discrepant with observations of Mg at $R \gtrsim 0.1R_{500}$, SIMBA-C shows considerably more overlap.

In the intermediate-mass bin, the central downturn in SIMBA-C has disappeared, but SIMBA-C remains more consistent than SIMBA due to its lower abundance profile amplitudes. In particular, the SIMBA-C outskirt O and Mg abundances at $R \gtrsim 0.1R_{500}$ are within the spread of observations more consistently than SIMBA and over a larger range of radii. Further, SIMBA-C does not show the upturn in abundances at large radii found for SIMBA.

High-mass SIMBA-C groups are again in excellent agreement with observations across the range of radii investigated. Note that observed central O abundances have more diversity than the other α elements, permitting SIMBA to also be consistent with these observations, although the shallower slope of SIMBA-C remains a better match.

Overall, SIMBA-C is in better agreement than SIMBA with observations of O, Ne, and Mg abundances at all group masses.

SIMBA-C–SIMBA Comparison

As with C and N, SIMBA-C has lower amplitude and generally flatter profiles than SIMBA. SIMBA therefore constrains its IGrM metals to a greater extent in both low-mass and massive group cores, while SIMBA-C distributes them more uniformly. This is unsurprising because a significant fraction of C and N is produced by core-collapse SNe, the main producer of O, Ne, and Mg, so the stellar winds and SNe feedback can spread these metals similarly throughout the IGrM.

2.3.4 Heavy α Elements: Si, S, and Ca

Figure 2.5 presents the simulated and observed abundance profiles of Si, S, and Ca[36].

[36]Observations of Ar abundance in the IGrM exist; however, SIMBA does not track Ar, and the Ar profiles exhibit similar amplitudes, shapes, and trends with M_{500} as Si, S, and Ca.

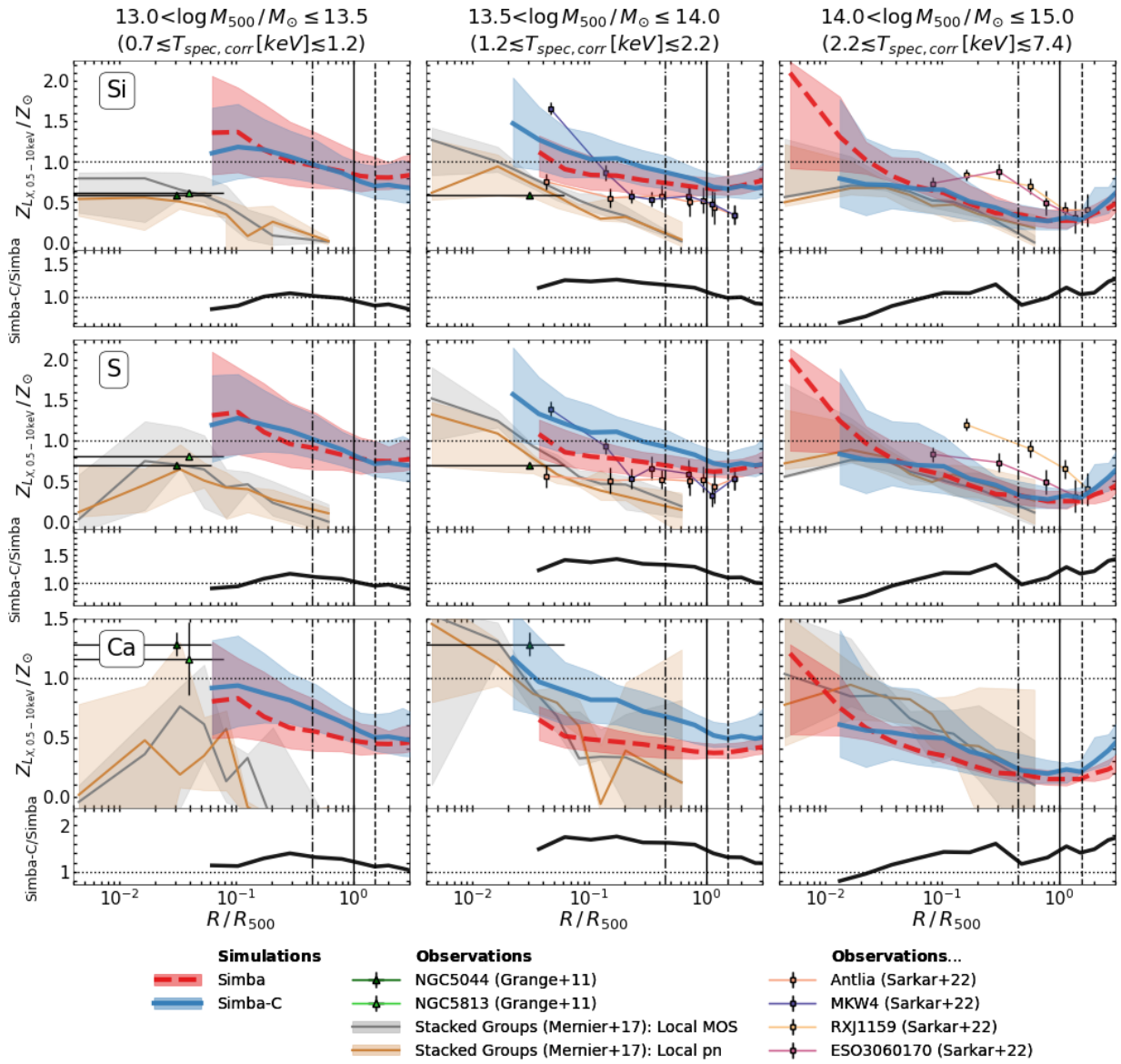

Figure 2.5: Same as Figure 2.1 but for Si (*upper row*), S (*middle row*), and Ca (*lower row*). The vertical solid line is R_{500}, and the vertical dot-dashed and long-dashed lines are our approximations for R_{2500} and R_{200}, respectively, using the median values from our two simulated samples. The horizontal dotted line is solar abundance $Z_{\odot}$.

SIMBA–Observation Comparison

The Si and S profiles show a similar behavior to Fe. SIMBA produces abundance profiles in the low-mass bin that have a high amplitude and are discrepant with observations. The SIMBA abundance profile amplitudes drop slightly from the low- to the intermediate-mass bin, resulting in SIMBA's increased agreement with observations. The abundance profiles in

the high-mass groups of SIMBA are steep in the cores, and thus largely do not agree with observations, but are quite consistent with observations at $R \gtrsim 0.1R_{500}$. This overarching similarity is understandable since, like Fe, a modest fraction of the production of Si and S is from SNe Ia according to Kobayashi et al. (2020a).

Compared to Si and S, the simulated Ca abundance profiles are reduced in amplitude relative to the observed profiles. The effect is an overall improved agreement of SIMBA and observations in the two lower-mass bins, and a trade-off in the high-mass bin. Specifically, in the intermediate-mass bin, SIMBA agrees well with observations at $R \gtrsim 0.03R_{500}$. In the high-mass bin, while the shape of the SIMBA Ca abundance profile does not match that of observations, and its amplitude outside the core largely falls somewhat below observed abundances, the simulated and observed core abundances overlap.

SIMBA-C–Observation Comparison

Like SIMBA, the SIMBA-C Si and S abundance profiles follow the same trends as the SIMBA-C Fe profiles. This includes substantial discrepancy between simulation and observations in the low- and intermediate-mass bins (with the intermediate-mass groups of SIMBA-C at greater discordance with observations than those of SIMBA) but strong agreement in the high-mass bin—much better than SIMBA in the group cores.

For Ca, the overlap of the SIMBA-C and observed abundance profiles again increases relative to Si and S in the two lower-mass bins. In particular, in the low-mass bin, the degree of improvement is similar to that for SIMBA; however, in the intermediate-mass bin, SIMBA-C is more consistent than SIMBA with observations of Ca abundance at $R \lesssim 0.1R_{500}$ in both amplitude and slope, while SIMBA remains in better agreement at $R \gtrsim 0.1R_{500}$. Moreover, in the high-mass bin, SIMBA-C is now in better agreement with observed profiles at $R \gtrsim 0.1R_{500}$. In this bin, while SIMBA-C still better matches the flatter observed core abundance profiles of Ca than SIMBA, SIMBA better matches the core amplitude. Thus, the clear improvement from SIMBA to SIMBA-C found for Si, S, and Fe in high-mass groups becomes muddled for Ca.

SIMBA-C–SIMBA Comparison

The evolution of the abundance profiles with increasing group mass for Si, S, and Ca is commensurate with that for Fe. SIMBA-C and SIMBA show similar profiles in the low-mass bin, which switches in the intermediate-mass bin to SIMBA-C having steeper and higher-amplitude profiles, and then switches again to flatter central SIMBA-C profiles in the high-mass bin. These results are consistent with the notion that SIMBA-C retains its metals to a larger degree

in the cores of high-mass groups compared to SIMBA, but does not do so in low-mass groups.

2.4 Discussion

In this section, we qualitatively assess which simulation is most in agreement with observations, and investigate and discuss potential reasons for the differences and similarities we find between SIMBA and SIMBA-C.

2.4.1 Does SIMBA-C Improve on Agreement with Observations?

In terms of measuring and constraining resolved X-ray abundances with low uncertainty (i.e., high spatial and spectral resolution), observations are still relatively in their adolescence. Cosmological simulations, while advanced and successful in many ways, also have their limitations, e.g., low-resolution group cores, ad hoc models for stellar and AGN feedback, and, in our case, the neglect of metal diffusion (a process that is likely vital in the real universe for distributing metals). Many of these are being addressed with the advent of faster gravity and hydrodynamics codes (e.g., SWIFT (Schaller et al., 2024), which will be employed by KIARA), high-resolution simulations (e.g., HYENAS (Cui et al., 2024; Jennings et al., 2025), ROMULUS (Tremmel et al., 2017; Jung et al., 2022; Saeedzadeh et al., 2023), TNG-CLUSTER (Nelson et al., 2024; Ayromlou et al., 2024; Truong et al., 2024; Lehle et al., 2024; Rohr et al., 2025)), and increasingly realistic and physically motivated sub-grid models, like the AGN model of OBSIDIAN (Rennehan et al., 2024).

At the moment, though, asking which simulation is in better agreement with data may not always yield robust answers. In particular, metals like C, N, Ne, Ar, Cr, Mn, and Ni—elements that are especially difficult to pick out of the noise and thermal continuum in low-mass/low-temperature group spectra—observationally have low statistics, large scatter, and a lack of abundance measurements extending past group cores. However, as shown in Section 2.3, our results broadly demonstrate improvement from SIMBA to SIMBA-C in the ability to predict metal abundances and their trends across a range of radii and masses.

For C, N, O, Ne, and Mg, the metals that are produced primarily by AGB stars or core-collapse SNe, the SIMBA-C abundance profiles have substantially lower amplitudes than SIMBA in the low-mass groups, generally bringing them into better agreement with observations. The high-mass group profiles are flatter in SIMBA-C than in SIMBA, improving agreement between SIMBA-C and observations. This strongly suggests that the upgrades implemented in SIMBA-C have a positive impact on the mechanisms that bring these metals to and distribute them in the IGrM.

On the other hand, as noted, Si, S, Ca, and Fe, the metals most produced by SNe Ia of those that we consider, are too abundant in the IGrM of low-mass groups in both SIMBA and SIMBA-C, to a similar degree. For these same metals, increasing M_{500} by about 0.5 dex causes the SIMBA IGrM abundances in the range of $0.1 \lesssim R/R_{500} \lesssim 1$ to noticeably decrease, bringing them more in line with observations. SIMBA-C, on the other hand, changes little across that mass range, and remains discrepant with observations. The reason for this is currently not clear, but may have something to do with differences in the distribution of metals with L_X across IGrM gas elements between SIMBA-C and SIMBA. As before, in the high-mass bin, it appears that SIMBA is confining these metals largely in the group cores, whereas SIMBA-C spreads them out more uniformly, permitting it to better match observations. This is potentially a consequence of delayed SNIa enrichment being more sensitive to the (altered) details of feedback than prompt enrichment.

The SIMBA-C Ni abundance profiles broadly match existing observations, and, where they do not, observations are limited with large scatter and/or uncertainty. Therefore, SIMBA-C and the `Chem5` model hold promise for predicting the IGrM abundance distributions of many metals.

Lastly, observations display a flattening of the Fe abundance profiles in group cores across a range of masses (e.g., the X-COP sample (Ghizzardi et al., 2021), as shown in the study of Braspenning et al. (2024), and the samples of Sun (2012), Sasaki et al. (2014), Mernier et al. (2017), and Lovisari & Reiprich (2019), as plotted by Gastaldello et al. (2021)). SIMBA-C better reflects this feature than SIMBA, in particular at high group masses, and, as such, is an improvement.

Partial forward modeling of our simulated abundance profiles is key for accurately comparing simulations to observations. However, attempting to ascribe reasons for the different trends between SIMBA and SIMBA-C is not necessarily meaningful, as the projection and L_X weighting of abundances do not necessarily transparently reflect the underlying metal enrichment and distribution mechanisms. For example, the differences between SIMBA and SIMBA-C may be over- or under-exaggerated, or skewed because metal abundance and gas X-ray luminosity do not strictly track each other (see, e.g., the study of Braspenning et al. (2024), who compare X-ray luminosity, mass, and volume weighting). We leave this to Section 2.4.2.

It is pertinent to mention that other biases have been shown to be important to take into account when comparing simulated and observed abundance profiles, in particular, the CC/NCC dichotomy. In both simulations (Fabjan et al., 2010; Rasia et al., 2015; Biffi et al., 2017; Vogelsberger et al., 2018; Barnes et al., 2017, 2018; Braspenning et al., 2024) and

observations (Leccardi & Molendi, 2008; Johnson et al., 2011; Ettori et al., 2015; Mernier et al., 2017; Ghizzardi et al., 2021), CC clusters tend to exhibit higher metallicity cores and more negative metallicity gradients than NCC clusters. To our knowledge, statistical studies of the correlation of core metallicity with CC/NCC status at the *group* scale have not been conducted; however, a similar characteristic may exist.

Additionally, there is preferential inclusion of CC systems in X-ray-selected samples due to their dense, bright centers (see Pearson et al. (2017); Henden et al. (2018)). The same biases may be responsible for at least part of the discrepancy between simulations and observations. While unknown currently for SIMBA-C, the SIMBA $z = 0$ galaxy group population consists of primarily NCC systems, possibly a result of the overly efficient feedback (Oppenheimer et al., 2021). On the other hand, CHEERS comprises *only* CC groups and three out of four groups in the Sarkar et al. (2022) sample are CC, thus potentially making the simulation–observation comparison not strictly "like to like".

This merits a deeper investigation of CC/NCC classifications in SIMBA and SIMBA-C and how it impacts their abundance profiles, as well as the incorporation of a wider range of groups into our comparison observational samples that better represent the true distribution of CC and NCC groups in the Universe. This is out of the scope of the present study, but will be explored in the future.

2.4.2 Potential Reasons for Changes from `SIMBA-C` to `SIMBA-C`

The new `Chem5` model in SIMBA-C is more complex than the instantaneous recycling of metals model of SIMBA. It is therefore difficult to trace changes in the results to their source. To attempt to decipher the primary drivers of these changes, we conduct some preliminary tests and refer to the recent results from SIMBA-C (Hough et al., 2023, 2024). Subsequent studies will more deeply explore the origins of these changes.

As such, we compute spherically averaged (3D) mass-weighted IGrM abundance profiles (Figure 2.6) to investigate the differences between the two simulations, since these better represent the intrinsic abundance distributions than the projected L_X-weighted profiles. We include only those elements that are tracked in both simulations, and order them by atomic number. Additionally, we now extend the upper radial limit to $10R_{500}$, enabling us to assess the extent to which the different mass bins and two simulations converge in and beyond group outskirts.

Abundance Profile Amplitudes

Figure 2.6 indicates there are relatively minor changes in the outer region ($R \gtrsim R_{2500}$, up to $10R_{500}$) abundances of both SIMBA and SIMBA-C groups as M_{500} increases, with a slight but noticeable drop from the intermediate-mass bin (purple lines) to the high-mass bin (green lines), similar to the L_X-weighted profiles. On the other hand, as demonstrated by the ratio profiles, the abundances of SIMBA-C are essentially never greater than those of SIMBA, contrary to what we find for the L_X-weighted profiles of Si, S, Ca, and Fe in the intermediate-mass bin. These results suggest that some trends found in the 2D L_X-weighted profiles may be strongly impacted by the emission weighting and/or projecting. In supplementary tests, we find that both emission weighting and projecting can contribute significantly to differences, although emission weighting tends to dominate.

In Section 2.3, we found that, for most metals (excluding C, N, and Ni), both SIMBA and SIMBA-C over-enrich the outer regions of the IGrM ($R \gtrsim 0.1R_{500}$) in low-mass groups. Braspenning et al. (2024) attribute a similar discrepancy in the FLAMINGO simulations to unduly high assumed nucleosynthetic yields, or to the total stellar masses being too high in the simulations and over-producing metals. As with the L_X-weighted profiles, Figure 2.6 demonstrates that the lighter elements, like C and N, exhibit noticeably lower abundance profile amplitudes in SIMBA-C than in SIMBA in all mass bins by up to ~ 0.5 dex. This is likely a consequence of the new yields in `Chem5` being lower overall than those in SIMBA.

Another possible reason contributing to this is as follows: Via the instantaneous recycling of metals in SIMBA, gas elements could self-enrich before forming stars through SNII and prompt SNIa feedback, with further enrichment from nearby stars (i.e., due to delayed feedback if the gas element in question is one of the 16 nearest neighbors to a star particle) and metal-loaded stellar winds (Davé et al., 2016, 2019). This may result in highly enriched gas escaping galaxies to join the IGrM. In contrast, SIMBA-C eliminates self-enrichment and metal-loaded winds, with metallicity only increasing via nearby star particles' feedback. Consequently, stars and gas (both ISM and IGrM) in SIMBA-C are expected to be less enriched. After the implementation of `Chem5`, Hough et al. (2023) performed recalibrations on SIMBA-C to improve low-redshift metal production and the agreement of the simulated and observed GSMFs. Optimizing between these two resulted in lower ISM (Hough et al., 2023) and IGrM (Hough et al., 2024) gas-phase metallicities in SIMBA-C than in SIMBA, by up to $\sim$0.2 dex.

That said, as atomic number increases, the IGrM abundance profiles of SIMBA and SIMBA-C approach each other. This culminates with Ca and Fe, for which there is significant overlap

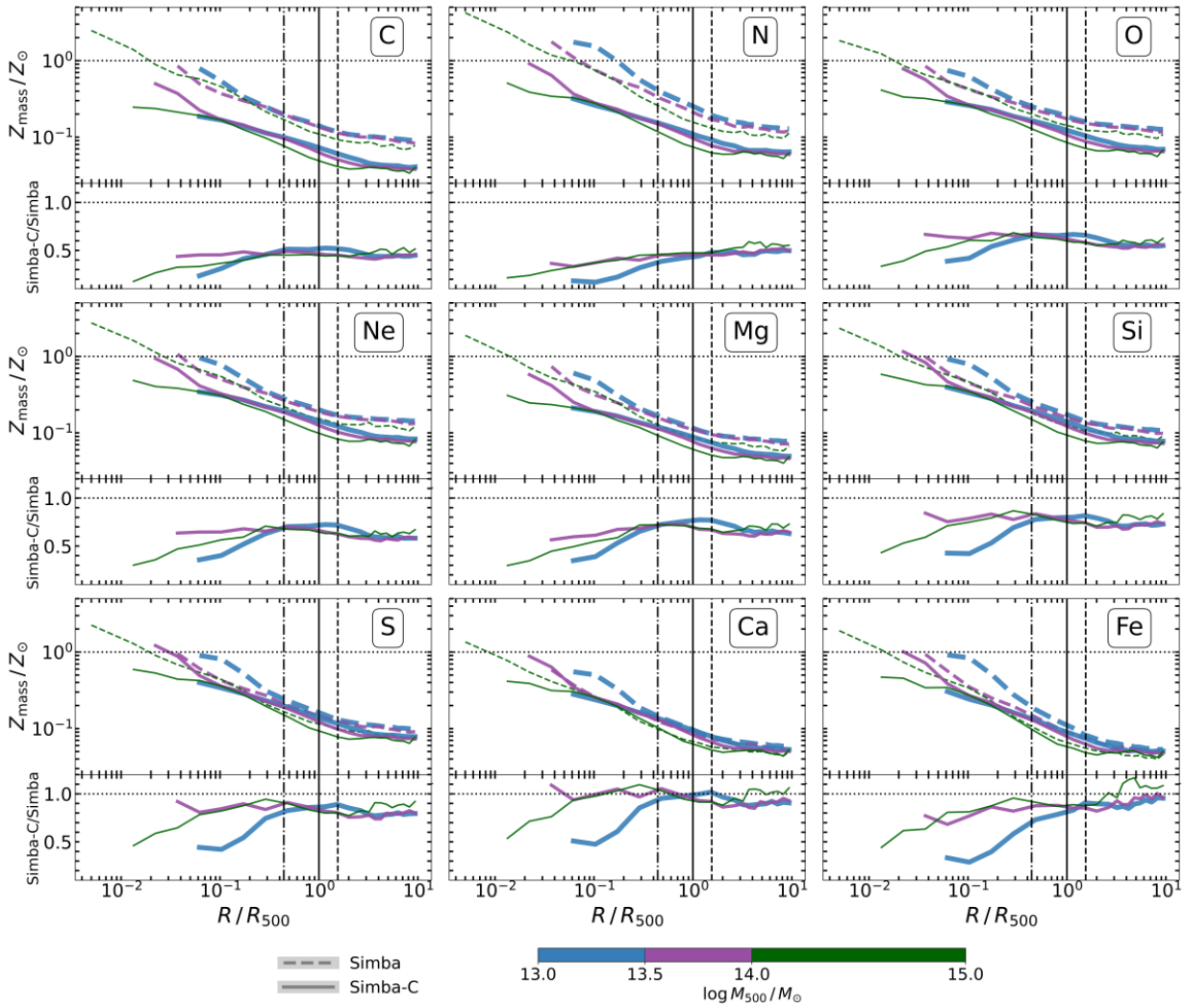

Figure 2.6: Median 3D mass-weighted logarithmically scaled metal abundance profiles for all metals in both SIMBA and SIMBA-C, in our three previously defined M_{500} bins. These profiles are scaled by their solar abundances from Asplund et al. (2009). The 16th–84th percentile regions are omitted for clarity; however, comparing SIMBA-C to SIMBA profiles, they generally exhibit discordance at the level of $\gtrsim 1\sigma$ at $R \lesssim R_{2500}$ and $\gg 1\sigma$ at $R \gtrsim R_{2500}$ for C, N, O, Ne, and Mg; and $\sim 1\sigma$ at $R \lesssim R_{2500}$ and $\gtrsim 1\sigma$ at $R \gtrsim R_{2500}$ for Si, S, Ca, and Fe. The lower part of the subplot for each element shows the ratios of the SIMBA-C and SIMBA profiles in each mass bin.

between the two simulations, especially in the group outskirts. Thus, for these metals, there is no reduction in the abundance profile amplitudes that would enable SIMBA-C to better match low-mass group observations than SIMBA. We postulate this may be a consequence of the inclusion of HNe in `Chem5`, which is not included in SIMBA. HNe produce a greater amount of Fe and α elements than the lower-energy SNe II (Kobayashi et al., 2020a; Hough

et al., 2023). On the other hand, for metals including and heavier than O, there is a net reduction of SNe II yields from SIMBA to SIMBA-C due to the inclusion of 'failed' SNe yields. It is possible that the "extra" HNe products make up the difference between the SIMBA yields and the lower SIMBA-C yields of the heavier metals.

These points highlight systematic issues with sub-grid models at the group scale. The pervasive nature of this issue from SIMBA to SIMBA-C, at least for the heavier metals, hints at the source being a sub-grid model that has been minimally altered or not changed in the upgrade to SIMBA-C, such as AGN feedback, the stellar-wind-powered dispersal of metals, radiative cooling and heating, or the lack of metal diffusion.

Along these same lines, the nature of feedback processes and their interaction with group environments may play a significant role. Lower-mass groups, with their shallower gravitational potentials, are thought to be more easily impacted by AGN or stellar feedback (Oppenheimer et al., 2021). Even though components of the AGN feedback model were altered from SIMBA to SIMBA-C, the overall model did not change. Similarly, although there was an overhaul in the stellar feedback model, the general treatment of stellar winds remained unchanged. Therefore, it is plausible that, at the low-mass group scale, (inappropriately modeled) feedback is important for setting the metal distribution.

Hough et al. (2023) find sizable differences going from SIMBA to SIMBA-C in both their galactic gas-phase and stellar abundances and abundance ratios, which lead to improvements with respect to observations. This may imply that, although the enrichment within galaxies is improved in SIMBA-C relative to SIMBA, the mechanisms that bring metals out of the ISM phases and disperse them into the IGrM phase (in temperature and location), such as stellar winds and turbulent mixing, remain inadequately modeled at the group scale.

To this point, Rennehan et al. (2019) present and test a new method for dynamically calculating turbulent diffusivity. Subsequently, Rennehan (2021) implements an anisotropic eddy viscosity and metal-mixing model into a Lagrangian astrophysical simulation. Most relevantly, they show that the hot diffuse gas around individual galaxies (known as the circumgalactic medium, or CGM) is particularly sensitive to the treatment of turbulent diffusion, and their models result in earlier metal mixing and more lower-metallicity gas in the metal distribution functions of the CGM than other models, including the oft-employed constant coefficient Smagorinsky model. As discussed, both SIMBA and SIMBA-C produce over-enriched low-mass groups for most metals. Extending the results of Rennehan et al. (2019) and Rennehan (2021) from the CGM to the low-mass IGrM suggests that explicit and realistic sub-grid modeling of metal diffusion could help remedy this. Further, other recent studies find that turbulence may be important for generally producing realistic galaxies in

simulations, in particular in the ISM, as well as generating realistic turbulent properties of the IGrM (e.g. Groth et al., 2025; Sotira et al., 2024; Kempf & Rincon, 2024; Beattie et al., 2024, 2025).

Abundance Profile Slopes

The shapes of abundance profiles are noteworthy, often considered to impart information about the degree of mixing in the IGrM and when enrichment occurs. Although neither cosmological simulations nor observations are at the level of precision necessary for comparing them on equal footing, it is of interest to start to take a look at this.

In Figure 2.6, similar to the L_X-weighted abundance profiles, the SIMBA-C mass-weighted profiles are generally less steep in the group inner regions than those of SIMBA. Further, the abundance profiles of all metals in all mass bins in both SIMBA and SIMBA-C exhibit flattening at $R \gtrsim R_{200}$. Resolved X-ray observations of *cluster* ($M_{500} \gtrsim 10^{14}\,\mathrm{M}_\odot$) outskirts also find flat metallicity profiles (e.g. Werner et al., 2013; Urban et al., 2017; Ghizzardi et al., 2021). At the *group* scale ($M_{500} \lesssim 10^{14}\,\mathrm{M}_\odot$), observations are less robust and more varied. Some lower-mass group samples, like those of Sarkar et al. (2022), exhibit relatively flat outskirt profiles, while others, like those of Rasmussen & Ponman (2007) and Mernier et al. (2017), cannot formally constrain the outskirts[37].

The *XRISM*/Resolve X-ray spectrometer, with the highest spectral resolution of any current similar instrument, has the ability to reduce abundance uncertainties significantly and improve observations of different radial regions in groups and clusters (Ishisaki et al., 2018). In the near future, the *Athena* X-ray Integral Field Unit spatially resolved spectrometer (Barret et al., 2023) and *AXIS* (Mushotzky et al., 2019; Reynolds et al., 2023) will further improve on this, the former obtaining highly accurate abundance profiles through high spectral and spatial resolutions and the latter measuring ICM abundances in various spatial regions with high sensitivity. Without these facilities, statistically confirming the outskirt abundance profile slopes in observations of low-mass groups—and comparing them with simulations like SIMBA and SIMBA-C—would be difficult given the current technological limitations.

Some studies find that the production of $z = 0$ metallicity profiles with flat outskirts in zoom cosmological simulations of clusters requires an "early enrichment scenario" (e.g. Sijacki & Springel, 2006a; Fabjan et al., 2010; Biffi et al., 2017, 2018b). Specifically, early

[37]According to Mernier et al. (2017), neither flat nor decreasing outskirt profiles are favored over the other in CHEERS. On the other hand, the Sarkar et al. (2022) sample contains more robust outskirt abundance profiles due to *Suzaku*'s stable particle background and high spectral sensitivity below 1 keV (Koyama et al., 2007). This latter sample, however, is quite small.

($z \gtrsim 2-3$) AGN feedback is needed to sufficiently expel enriched gas from galaxies into the IGrM and quench star formation, keeping metals in the hot diffuse phase and preventing them from being locked back in the stellar phase (Fabjan et al., 2010).

AGN feedback is found to be more efficient than stellar feedback in distributing metal-rich gas to large cluster-centric distances in small high-z halos (prior to the assembly of $z = 0$ groups and clusters), reducing the build-up of high-metallicity cores and increasing outskirt abundances (Biffi et al., 2017, 2018b). Gas dynamical processes—associated with the merging of these halos and continued energy output from feedback—promote the mixing of the pre-enriched and hot diffuse gas into relatively uniform distributions (Fabjan et al., 2010).

It is important to note that, in all of these studies, AGN feedback is not *required* to disperse metals from galaxies out to the CGM or IGrM in their cosmological simulations. Those without AGN feedback can still exhibit low-to-moderate abundances in galaxy, group, or cluster outskirts when only accounting for star formation and stellar feedback. In fact, high-resolution simulations that track the evolution of high-velocity nuclear outflows (e.g. Faucher-Giguère & Quataert, 2012; Gabor & Bournaud, 2014) demonstrate that these outflows transition into an expanding wind of shocked gas before escaping the central region of galaxies. When they subsequently encounter the galactic disk, they follow the path of least resistance, resulting in their preferential expulsion perpendicular to the disk. As such, the metal-rich ISM is found to be affected only to a limited degree by AGN outflows. However, the cost of removing the AGN is the production of overly star-forming BGGs with ∼2–4× too many stars (e.g. McCarthy et al., 2010).

Critically, most of these simulations, including SIMBA and SIMBA-C, do not include any explicit implementation of metal mixing, a process potentially crucial for setting metal distributions in the real IGrM. Rennehan et al. (2019) and Rennehan (2021) demonstrate that improved models of turbulent diffusion result in the rapid mixing of fluid properties, including metals. This reveals that, not only can the implementation of metal mixing have an impact on the timing of enrichment, but also that observables (like abundance profile shapes) are not necessarily good indicators of the time or efficiency of mixing because metals may be able to mix uniformly on short timescales regardless of when enrichment occurs.

Additionally, SIMBA and SIMBA-C employ hydrodynamically decoupled winds and jets for AGN feedback, meaning AGN feedback should not be capable of bringing metal-enriched gas from the ISM of the central galaxy out to larger radii (unless the gas located near the SMBH is enriched). Other mechanisms, like mergers or stellar feedback with metal-enriched winds, are required. Once the enriched gas particles are at sufficiently large radii, where the AGN wind and jet particles can recouple, AGN feedback could then ostensibly redistribute

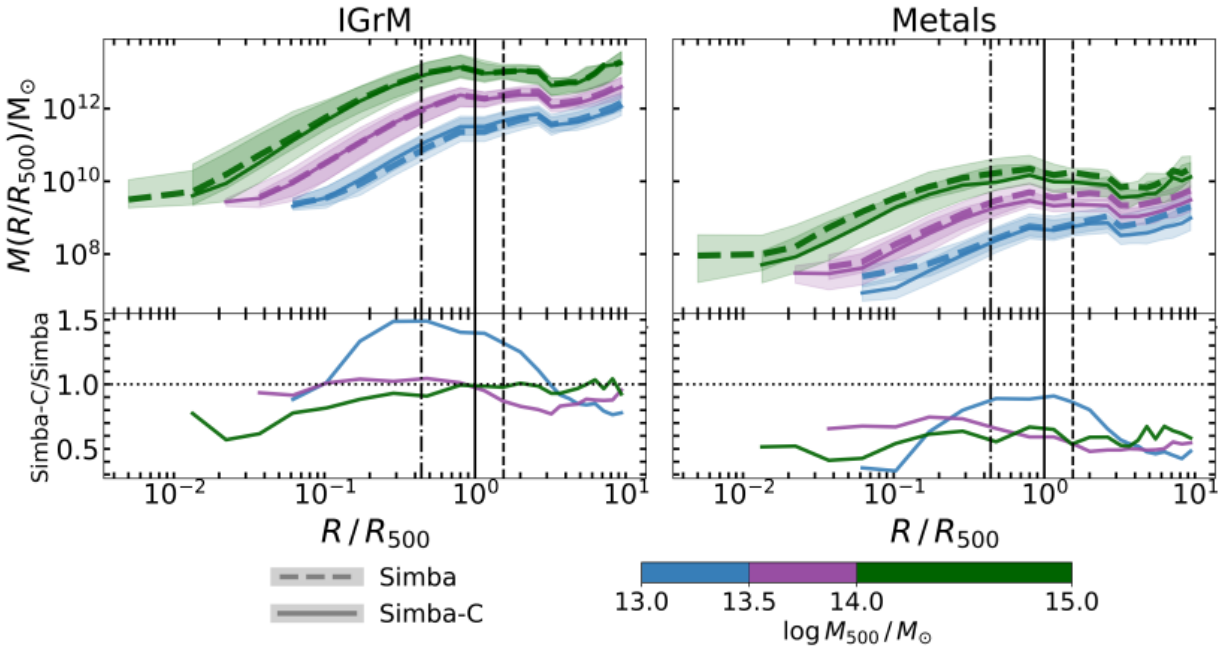

Figure 2.7: Median mass profiles of the IGrM (*left*) and the sum total of IGrM-phase metals (*right*) in SIMBA and SIMBA-C, in our three M_{500} bins. Shaded regions represent the 16th–84th percentiles of the scatter. The lower half of each subplot shows the ratios of the SIMBA-C and SIMBA profiles for each mass bin.

the metal-enriched gas. Therefore, a complex blend of physical processes, such as cooling, turbulence, star formation, and AGN and stellar feedback (most of which are not well modeled in cosmological simulations), as well as potentially simulation resolution, is likely responsible for setting the particular distribution of metals in the IGrM.

IGrM Mass and Metal Mass Profiles

Next, in Figure 2.7, we investigate the separate components that form the abundance profiles, namely, the total mass profile of IGrM-phase metals (summed together) and the mass profile of all gas in the IGrM. We find that, in the low-mass bin (blue lines), the IGrM mass profile increases from SIMBA to SIMBA-C at most radii. Looking at the intermediate-mass bin (purple lines), we note that there is no increase in IGrM mass within R_{500} and, instead, a slight decrease at larger radii. The high-mass bin (green lines) yields the opposite, i.e., a decrease within R_{500} and no change outside R_{500}.

The dependence on the halo mass of the $M_{\rm IGrM}$ SIMBA-C–SIMBA ratio profiles, as well as the two simulations' identical cosmologies, indicates that alterations to the feedback models in SIMBA-C are plausible candidates for the origin of these differences. The altered stellar wind

feedback likely contributes, in particular, the reduction in the stellar wind velocity scaling a in SIMBA-C by a factor of $\sim$2 compared to SIMBA. As previously noted, the gas in lower-mass groups is more prone to feedback and other baryonic processes than that in higher-mass groups (Oppenheimer et al., 2021). This implies that a change in feedback strength will be more noticeable in the gas properties of these lower-mass groups. Specifically, a lower fraction of gas may be blown to larger radii (or even out of the groups altogether), allowing them to retain more IGrM mass. Hence, we observe an increase in IGrM mass in the low-M_{500} bin, but more limited changes in the higher-mass bins.

For $R \lesssim R_{500}$, the low-mass bin shows an overall increase in IGrM mass from SIMBA to SIMBA-C, while the intermediate- and high-mass bins show minimal change (in the high-mass bin, the decrease is largely confined to the group cores, which contribute little to the total mass). This is consistent with the findings of Hough et al. (2024), who find a higher IGrM mass fraction ($M_{\rm IGrM,500}/M_{500}$) in SIMBA-C than in SIMBA for halos in the range $10^{13} \lesssim M_{500}/\mathrm{M}_\odot \lesssim 10^{13.5}$ but negligible differences at higher masses.

Moreover, Khrykin et al. (2024) show that, in SIMBA, the jet mode AGN feedback is key in distributing baryons between the CGM and IGM at $z = 0$–1, increasing the IGM baryon fraction by $\sim$20% relative to SIMBA NOJET. They also find that AGN feedback is the most effective mechanism for this redistribution in halos with masses $10^{12} \lesssim M_{200}/\mathrm{M}_\odot \lesssim 10^{14}$ (approximately $5 \times 10^{11} \lesssim M_{500}/\mathrm{M}_\odot \lesssim 5 \times 10^{13}$), but that the baryon distribution in halos outside this mass range is only weakly sensitive to the specific feedback prescription. This is in very good agreement with our results, which also exhibit significant changes in the IGrM mass profiles of similarly low-mass groups but minor changes above this mass range.

Relative to SIMBA, we find that IGrM metal mass decreases by $\sim$10–70% across all radii and halo masses in SIMBA-C. The reduced metal content leads to the lower mass-weighted abundances in Figure 2.6, since the IGrM masses do not simultaneously decrease. As before, this decrease may reflect the overall reduced nucleosynthetic yields and the lack of self-enrichment in `Chem5`.

It is possible that the lower metal cooling rates in SIMBA-C (due to reduced abundances) keep more gas in the hot diffuse phase of the IGrM, which could help explain the IGrM gas mass increase from SIMBA to SIMBA-C for low-mass groups (Hough et al., 2023, 2024). However, we note that, Fe being the primary coolant for the hot diffuse gas (at least around its virial temperature), and there being minimal differences between the SIMBA and SIMBA-C mass-weighted Fe abundance profiles in Figure 2.6, it is unlikely that these changes can fully account for the observed differences in the IGrM mass profiles.

More feasibly, the alterations to the AGN and stellar feedback models impacted the timing

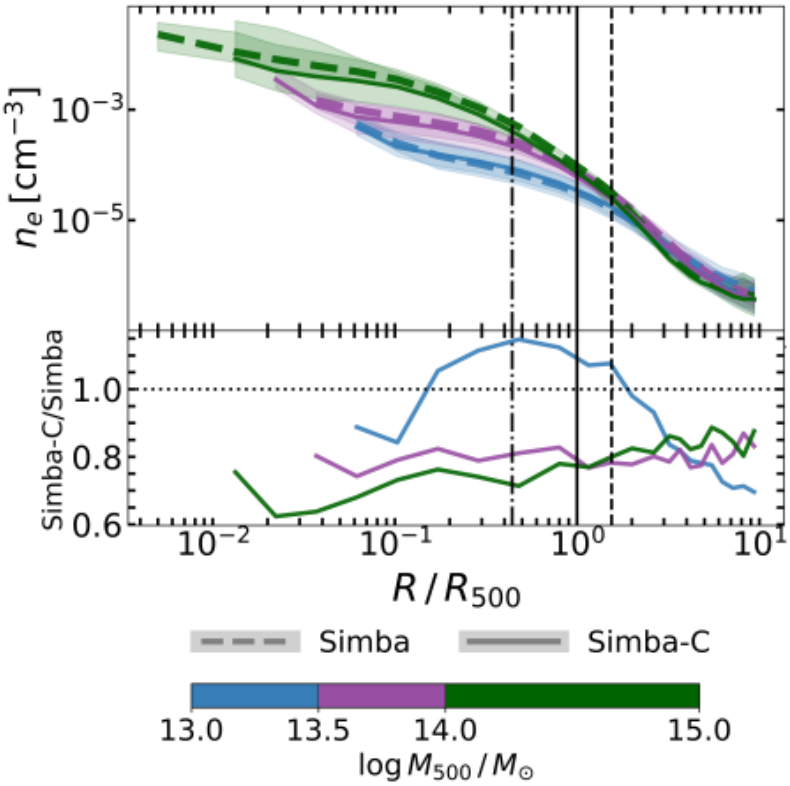

Figure 2.8: Median electron number density profiles of the IGrM in SIMBA and SIMBA-C, in our three M_{500} bins. Shaded regions represent the 16th–84th percentiles of the scatter. The lower half of the figure shows the ratios of the SIMBA-C and SIMBA profiles for each mass bin.

of mass assembly in the groups, resulting in a build-up of hot diffuse gas in low-mass groups. In SIMBA-C, for example, the reduced stellar wind velocity normalization and the effectively delayed AGN jet activation may allow the group gravitational potentials to deepen rapidly prior to feedback being able to blow gas out of the groups. In SIMBA, stellar feedback may be too strong or AGN jets may activate too early, blowing gas out and leaving little behind in the IGrM. Hough et al. (2024) find quite low IGrM mass fractions in low-mass groups, particularly in SIMBA.

Further, changes in the IGrM gas density may alter the IGrM mass. In Figure 2.8, we find that SIMBA-C produces IGrM gas density profiles that are ∼25% lower in amplitude than SIMBA in the intermediate- and high-mass bins. On the other hand, it is more variable in the low-mass bin; at $R \lesssim 0.2R_{500}$ and $R \gtrsim R_{200}$, the gas density is slightly reduced in SIMBA-C, whereas, at $0.2R_{500} \lesssim R \lesssim R_{200}$, there is a slight increase.

The volumetric gas cooling rate is proportional to n_e and Z as $\dot{E} \propto n_e^2 \Lambda(Z,T)$, where $\Lambda(Z,T)$ is the cooling function. Smaller differences in n_e become more important, while

changes in Z are less so because $\dot{E}$ is only linearly proportional to it. The rate of cooling contributes heavily to the evolution and state of the IGrM, including its total mass and mass profile. Increased densities enhance the cooling rate, drawing more gas out of the hot diffuse phase, and vice versa. However, in this case, differences in gas density between SIMBA and SIMBA-C are likely sub-dominant to the effects of the altered AGN and stellar sub-grid feedback models because the changes in density are not substantial.

Putting this all together, it appears that the lower-amplitude mass-weighted abundance profiles in high-mass SIMBA-C groups (mostly seen with C, N, O, Ne, and Mg) are primarily a consequence of fewer metals in the IGrM in SIMBA-C. On the other hand, the same trend in low-mass SIMBA-C groups is additionally driven by an increased IGrM gas mass.

2.5 Conclusion

We conclude that the integration of the `Chem5` chemical enrichment model in SIMBA substantially impacts the abundance and distribution of metals in the IGrM, broadly improving their match to observations across two orders of magnitude in terms of group mass and a wide array of X-ray-relevant elements. SIMBA-C, to the best of our knowledge, makes use of the most realistic chemical enrichment model (`Chem5`) currently feasible to implement in a cosmological simulation. It has also been tested against galaxy-scale properties (Hough et al., 2023), global X-ray observations of the IGrM (Hough et al., 2024), and the distribution of metals in the IGrM (this work), allowing its effects on galaxy formation and evolution to be well characterized across orders of magnitude in scale.

Our main results are as follow:

1. On average, SIMBA-C produces lower-amplitude projected L_X-weighted abundance profiles than SIMBA, with flatter profiles in the inner regions, particularly in high-mass groups but also in low-mass groups for some metals. These characteristics tend to be in better agreement with observations. The scatter within and across observational samples reduces their constraining power and sometimes allows both simulated samples to be consistent with observations. Additionally, in a few instances, SIMBA matches observations better than SIMBA-C. For example, in our intermediate-mass bin, the Fe, Si, and S profiles of SIMBA-C have greater amplitudes than those of SIMBA, resulting in its reduced agreement with observations.

2. Despite the upgrade to SIMBA-C, the low-mass groups ($13 < \log(M_{500}/M_{\odot}) < 14$) are generally in the worst agreement with observations, while the high-mass groups/clusters

$(14 < \log(M_{500}/M_{\odot}) < 15)$ are in the best agreement. This may be a consequence of the increasing importance in the shallower gravitational potential wells of the inadequate modeling of feedback processes, like AGN feedback or stellar winds, or the lack of any explicit implementation of critical physical mechanisms, like metal mixing. Therefore, issues in our cosmological simulations at the group scale continue to persist, and have yet to be addressed.

3. Specifically, SIMBA-C is more consistent with IGrM observations of the abundances of most investigated metals (C, N, O, Ne, Mg, Si, S, Fe) at higher masses, especially in the group cores. SIMBA-C further improves on SIMBA in its agreement with observed abundances of N (and, to some extent, C) across all group masses, suggesting the upgraded treatment of AGB star feedback in CHEM5 enhances the realism of the enrichment of the IGrM. On the other hand, SIMBA and SIMBA-C both exhibit substantial discrepancy with IGrM observations of, for example, Si, S, Ca, and Fe at lower group masses, potentially indicating that further work on the understanding and modeling of core-collapse SN and SNIa feedback and enrichment is required.

4. Some of the features of the 2D emission-weighted abundance profiles are preserved in the 3D mass-weighted profiles, like lower amplitudes and flatter cores in SIMBA-C than in SIMBA, while others are not, such as the aforementioned occasional higher amplitudes in SIMBA-C compared to SIMBA. Additionally, emission weighting results in greater apparent abundances. These results suggest that spectroscopically inferred group abundance profiles are expressive to a limited degree of the underlying physical enrichment mechanisms, and care should be taken in their interpretation.

5. The intrinsically lower IGrM abundances in SIMBA-C than in SIMBA are largely attributed to reduced metal yields and the lack of instantaneous recycling in `Chem5` compared to SIMBA's enrichment model, resulting in a lower mass of IGrM-phase metals in SIMBA-C. On the other hand, the increased IGrM mass in low-mass SIMBA-C groups may be a consequence of the reduced stellar wind velocity normalization and the "delayed" AGN jet activation in SIMBA-C, causing changes in the groups' mass assembly histories.

6. We find that the SIMBA and SIMBA-C mass-weighted abundance profiles draw closer together with increasing atomic number. We connect this to the addition of HNe enrichment in the `Chem5` model, which increases the production of Fe and α elements (e.g., Si, S, Ca), enhancing their abundance profiles to "re-match" those of SIMBA by approximately equaling the aforementioned overall decrease in metals in SIMBA-C.

As demonstrated by Hough et al. (2023), SIMBA-C shows improvements in matching observed galaxy properties, such as the galaxy stellar mass function and the stellar mass–metallicity relation, compared to the original SIMBA simulation. Hough et al. (2024) and the present study reveal that SIMBA-C also improves on both global and detailed properties of the IGrM at the group scale. This indicates progress in directly addressing an enduring challenge in cosmological simulations: accurately and simultaneously reproducing galaxy-scale and group-scale observables.

The results of SIMBA-C at the group scale additionally confirm the necessity of greater constraining power from observations to distinguish between different models of cosmic chemical enrichment, in particular at lower halo masses and for harder-to-observe metals in X-ray like C, N, Ne, Ca, and Ni. Current and upcoming X-ray missions, such as *XRISM* (Team, 2020; Tashiro, 2022), *Athena* (Barcons et al., 2012; Barret et al., 2013, 2020), *AXIS* (Mushotzky et al., 2019; Reynolds et al., 2023), and *Lynx* (Gaskin et al., 2019; Schwartz et al., 2019), aim to close this gap through increased sensitivity and spectral and spatial resolutions. These technological improvements will reduce the uncertainty of abundance and temperature measurements, enable the mapping of the IGrM out to larger radii, pick out the X-ray faint IGrM, make group and cluster X-ray samples more complete, and remove substantial observational biases. Concurrently, SIMBA-C and future iterations will help guide observations regarding in which regions of the IGrM certain metals are likely to be found and in what abundances.

With the continuing progression in computational resources, algorithms, and numerical methods—as well as improved observing capabilities—sub-grid models must keep up. Realistic and self-consistent modeling of physical processes, such as AGN and stellar feedback, appears critical to reproducing observed enrichment of the hot diffuse gas in group environments. We therefore require not just accurate and physically motivated sub-grid models, like `Chem5`, but also improved treatment of key processes like turbulent diffusion (Rennehan et al., 2019; Rennehan, 2021) to be implemented in the next generation of cosmological simulations.

Author Contributions: Conceptualization, A.P.-B. and A.B.; data curation, A.P.-B. and F.M.; formal analysis, A.P.-B.; funding acquisition, A.P.-B. and A.B.; investigation, A.P.-B.; methodology, A.P.-B., Z.S., R.T.H., A.B. and W.C.; project administration, A.P.-B.; resources, D.R., A.B. and W.C.; software, A.P.-B., Z.S., R.T.H., D.R., R.D., C.K. and W.C.; supervision, A.B.; validation, A.P.-B.; visualization, A.P.-B.; writing—original draft, A.P.-B.; writing—review and editing, Z.S., R.T.H., D.R., R.B., V.S., A.B., R.D., C.K., W.C., F.M. and G.G. All authors have read and agreed to the published version of the manuscript.

Funding: This research was funded by a Natural Sciences and Engineering Research Council of Canada (NSERC) Canada Graduate Scholarship—Masters (CGS-M), grant number 585656/2023.

Data Availability Statement: The SIMBA-C simulation data underlying this article are publicly available at the Flatiron Institute upon reasonable request to Douglas Rennehan (drennehan@flatironinstitute.org). The published SIMBA simulations are available in the SIMBA simulation repository at http://Simba.roe.ac.uk/ (accessed on 1 January 2023).

Acknowledgments: The simulations and analyses reported in this article were enabled by HPC resources provided by the Digital Research Alliance of Canada (alliancecan.ca) award to A.B., specifically SciNet and the Niagara computing cluster. The SIMBA-C simulation was run on the Flatiron Institute's research computing facilities (the Iron compute cluster), supported by the Simons Foundation. A.P.B. also acknowledges the SIMBA collaboration for the use of their simulations. A.B. acknowledges the support of the Natural Sciences and Engineering Research Council of Canada (NSERC) through its Discovery Grant program. A.B. also acknowledges support from the Infosys Foundation via an endowed Infosys Visiting Chair Professorship at the Indian Institute of Science and from the Leverhulme Trust via the Leverhulme Visiting Professorship at the University of Edinburgh. W.C. is supported by the Atracción de Talento contract no. 2020-T1/TIC19882 granted by the Comunidad de Madrid in Spain, and the science research grants from the China Manned Space Project. He also thanks the Ministerio de Ciencia e Innovación (Spain) for financial support under project grant PID2021-122603NB-C21 and HORIZON EUROPE Marie Sklodowska-Curie Actions for supporting the LACEGAL-III project with grant number 101086388. C.K. acknowledges funding from the UK Science and Technology Facility Council through grant ST/Y001443/1. For observational comparisons with CHEERS, the material is based upon work supported by NASA under award number 80GSFC24M0006. We thank A. Sarkar for directly contributing observational data. Finally, we acknowledge the lək̓ʷəŋən peoples on whose traditional territory the University of Victoria stands, and the Songhees, Equimalt, and WSÁNEĆ peoples whose historical relationships with the land continue to this day.

Conflicts of Interest: The authors declare no conflicts of interest. The funders had no role in the design of the study; in the collection, analyses, or interpretation of data; in the writing of the manuscript; or in the decision to publish the results.

Personal Contribution Clarification: I performed all research and analysis independently for this chapter. Renier Hough created and provided the SIMBA-C simulation. Zhiwei Shao provided the base script from `XIGRM`, off of which I built my pipeline to calculate and average abundance profiles. Weiguang Cui executed memory-intensive scripts that were not able to be run on the Niagara Compute Cluster. Arif Babul, Romeel Davé, Weiguang Cui, Renier Hough, and Zhiwei Shao provided scientific guidance and feedback.

Chapter 3

Conclusion

I conclude this thesis with a summary of my results and how they are situated within the literature. I have investigated how upgrading the SIMBA cosmological hydrodynamic simulation of galaxy formation and evolution to a more realistic and self-consistent stellar feedback and chemical enrichment sub-grid model (`Chem5`) impacts the distribution of metals in the intra-group medium (IGrM). This new cosmological simulation is called SIMBA-C.

To compare to a selected compilation of X-ray observations, I project and X-ray luminosity-weight the IGrM abundance profiles of C, N, O, Ne, Mg, Si, S, Ca, Fe, and Ni, and average these profiles across different groups in three bins of halo mass $M_{500}/M_{\odot} = 10^{13} - 10^{13.5} - 10^{14} - 10^{15}$. I find improved agreement with observations across all of these metals (except for Ni, which SIMBA does not track) for SIMBA-C compared to SIMBA for groups with halo masses $M_{500} > 10^{14}\,M_{\odot}$. Specifically, the core abundances are substantially lower and the inner region abundance profiles are flatter in SIMBA-C. For N, O, Ne, and Mg, SIMBA-C additionally is in better agreement with simulations at lower group masses $10^{13} < M_{500}/M_{\odot} \leq 10^{14}$ through reduced abundance profile amplitudes, flatter abundance profiles in SIMBA-C compared to unrealistically rising profiles in SIMBA at $R \gtrsim R_{500}$, and the indication of a central downturn in the SIMBA-C abundance profiles of groups with masses $10^{13} < M_{500}/M_{\odot} \leq 10^{13.5}$. On the other hand, the abundance profiles of Si, S, Ca, and Fe in the low mass bin show effectively no differences between SIMBA and SIMBA-C. Moreover, the SIMBA-C abundance profiles of those same metals in the intermediate mass bin have larger amplitudes than in SIMBA, worsening the agreement of SIMBA-C with observations.

I next turn to deciphering the physical mechanisms driving these changes by studying the spherically averaged (3D) mass-weighted abundance profiles, which better represent the intrinsic distribution of metals in the IGrM. Compared to SIMBA, the SIMBA-C abundance profiles have lower amplitudes at nearly all radii and M_{500}. This indicates that the lack of differences between SIMBA-C and SIMBA emission-weighted abundance profiles in low mass

groups, and particularly their increased amplitudes in intermediate mass groups in SIMBA-C compared to SIMBA, are likely a consequence of the emission-weighting, possibly due to changing gas density with group mass.

I decompose the abundance profiles into their constituents, the IGrM mass and total metal mass profiles. My results show that metal mass in the IGrM decreases from SIMBA to SIMBA-C at all radii and M_{500}, likely a consequence of the reduced metal yields in `Chem5` and its removal of SIMBA's instantaneous recycling approximation. Additionally, the difference in amplitude of the mass-weighted abundance profiles between SIMBA and SIMBA-C decreases with increasing atomic number, i.e. moving from C to Fe on the periodic table. I attribute this to the addition of hypernovae in `Chem5`, which greatly increases the production of Fe and α elements like Si, S, and Ca. Further, within R_{500}, the IGrM mass only significantly changes (specifically, increasing) in the low mass groups. This suggests that changes to the stellar and AGN feedback models in SIMBA-C play a role in altering the abundance profiles, because the gas in low mass galaxy groups is more susceptible to thermodynamic processes than that in high mass groups and clusters. In particular, a later onset of AGN feedback and decreased stellar wind velocities in SIMBA-C are likely candidates.

My results are well-placed in the literature. We are at a time when the next generation of X-ray telescopes, with enhanced resolutions and sensitivities, are being conceived; the X-ray Imaging and Spectroscopy Mission (*XRISM*) is already taking science data, and improved measurements of metal abundances in the ICM should be available soon, with those in the IGrM planned for the near future. Simultaneously, new algorithms are allowing cosmological simulations to run faster and with higher resolutions, e.g. the SPH With Inter-dependent Fine-grained Tasking (*SWIFT*) gravity and hydrodynamics code. My work shows that a realistic and physically motivated stellar feedback and chemical enrichment sub-grid model can have considerable impact on the metal content and distribution of the IGrM. While its effect is an overall improvement with regard to observations, the various sub-grid and feedback models are all linked, and therefore it is imperative that they all concurrently be upgraded for a holistically better representation of galaxy groups in the real universe.

Bibliography

Abel, T., Bryan, G. L., & Norman, M. L. 2002, Science, 295, 93, doi: 10.1126/science.295.5552.93

Abell, G. O. 1958, Astrophys. J. Suppl. Ser., 3, 211, doi: 10.1086/190036

Aharonian, F., Akamatsu, H., Akimoto, F., et al. 2017, Nature, 551, 478, doi: 10.1038/nature24301

Albert, C. E., White, R. A., & Morgan, W. W. 1977, Astrophys. J., 211, 309, doi: 10.1086/154935

Albrecht, A., & Steinhardt, P. J. 1982, Phys. Rev. Lett., 48, 1220, doi: 10.1103/PhysRevLett.48.1220

Albuquerque, I. S., Frusciante, N., Pace, F., & Schimd, C. 2024, Phys. Rev. D, 109, 023535, doi: 10.1103/PhysRevD.109.023535

Altamura, E., Kay, S. T., Bower, R. G., et al. 2023, Mon. Not. R. Astron. Soc., 520, 3164, doi: 10.1093/mnras/stad342

Anglés-Alcázar, D., Davé, R., Faucher-Giguère, C.-A., Özel, F., & Hopkins, P. F. 2017a, Monthly Notices of the Royal Astronomical Society, 464, 2840, doi: 10.1093/mnras/stw2565

Anglés-Alcázar, D., Faucher-Giguère, C.-A., Kereš, D., et al. 2017b, Monthly Notices of the Royal Astronomical Society, 470, 4698, doi: 10.1093/mnras/stx1517

Anglés-Alcázar, D., Faucher-Giguère, C.-A., Quataert, E., et al. 2017c, Monthly Notices of the Royal Astronomical Society: Letters, 472, L109, doi: 10.1093/mnrasl/slx161

Appleby, S., Davé, R., Sorini, D., Storey-Fisher, K., & Smith, B. 2021, Mon. Not. R. Astron. Soc., 507, 2383, doi: 10.1093/mnras/stab2310

Arnaud, K. A. 1996, 101, 17

Arnett, D. 1996, 92, 337

Arribas, S., Colina, L., Bellocchi, E., Maiolino, R., & Villar-Martín, M. 2014, A&A, 568, A14, doi: 10.1051/0004-6361/201323324

Ascasibar, Y., & Markevitch, M. 2006, ApJ, 650, 102, doi: 10.1086/506508

Aschenbach, B. 1991, Rev. Mod. Astron., 4, 173, doi: 10.1007/978-3-642-76750-0_13

Asplund, M., Grevesse, N., Sauval, A. J., & Scott, P. 2009, Annu. Rev. Astron. Astrophys., 47, 481, doi: 10.1146/annurev.astro.46.060407.145222

Ayromlou, M., Nelson, D., Pillepich, A., et al. 2024, A&A, 690, A20, doi: 10.1051/0004-6361/202348612

Babul, A., Balogh, M. L., Lewis, G. F., & Poole, G. B. 2002, Monthly Notices of the Royal Astronomical Society, 330, 329, doi: 10.1046/j.1365-8711.2002.05044.x

Babul, A., & Rees, M. J. 1992, Monthly Notices of the Royal Astronomical Society, 255, 346, doi: 10.1093/mnras/255.2.346

Bahé, Y. M., Barnes, D. J., Dalla Vecchia, C., et al. 2017, Monthly Notices of the Royal Astronomical Society, 470, 4186, doi: 10.1093/mnras/stx1403

Balogh, M. L., Babul, A., & Patton, D. R. 1999, Monthly Notices of the Royal Astronomical Society, 307, 463, doi: 10.1046/j.1365-8711.1999.02608.x

Banerjee, N., & Sharma, P. 2014, Monthly Notices of the Royal Astronomical Society, 443, 687, doi: 10.1093/mnras/stu1179

Barai, P., Martel, H., & Germain, J. 2011, ApJ, 727, 54, doi: 10.1088/0004-637X/727/1/54

Barcons, X., Barret, D., Decourchelle, A., et al. 2012, Athena (Advanced Telescope for High ENergy Astrophysics) Assessment Study Report for ESA Cosmic Vision 2015-2025, arXiv, doi: 10.48550/arXiv.1207.2745

Bardeen, J. M., Bond, J. R., Kaiser, N., & Szalay, A. S. 1986, Astrophys. J., 304, 15, doi: 10.1086/164143

Barnes, D. J., Kay, S. T., Bahé, Y. M., et al. 2017, Monthly Notices of the Royal Astronomical Society, 471, 1088, doi: 10.1093/mnras/stx1647

Barnes, D. J., Vogelsberger, M., Kannan, R., et al. 2018, Monthly Notices of the Royal Astronomical Society, 481, 1809, doi: 10.1093/mnras/sty2078

Barret, D., Decourchelle, A., Fabian, A., et al. 2020, Astron. Nachrichten, 341, 224, doi: 10.1002/asna.202023782

Barret, D., Nandra, K., Barcons, X., et al. 2013, Athena+: The First Deep Universe X-ray Observatory (eprint: arXiv:1310.3814), 447–453, doi: 10.48550/arXiv.1310.3814

Barret, D., Albouys, V., den Herder, J.-W., et al. 2023, Exp Astron, 55, 373, doi: 10.1007/s10686-022-09880-7

Bassini, L., Feldmann, R., Gensior, J., et al. 2023, Monthly Notices of the Royal Astronomical Society, 525, 5388, doi: 10.1093/mnras/stad2617

Bassini, L., Rasia, E., Borgani, S., et al. 2020, A&A, 642, A37, doi: 10.1051/0004-6361/202038396

Baumgartner, W. H., Loewenstein, M., Horner, D. J., & Mushotzky, R. F. 2005, ApJ, 620, 680, doi: 10.1086/427158

Beattie, J. R., Federrath, C., Klessen, R. S., Cielo, S., & Bhattacharjee, A. 2024, Magnetized Compressible Turbulence with a Fluctuation Dynamo and Reynolds Numbers over a Million, arXiv. https://arxiv.org/abs/2405.16626

Beattie, J. R., Kolborg, A. N., Ramirez-Ruiz, E., & Federrath, C. 2025, So Long Kolmogorov: The Forward and Backward Turbulence Cascades in a Supernovae-Driven, Multiphase Interstellar Medium, arXiv, doi: 10.48550/arXiv.2501.09855

Behroozi, P., Wechsler, R. H., Hearin, A. P., & Conroy, C. 2019, Monthly Notices of the Royal Astronomical Society, 488, 3143, doi: 10.1093/mnras/stz1182

Bennett, J. S., & Sijacki, D. 2020, Mon. Not. R. Astron. Soc., 499, 597, doi: 10.1093/mnras/staa2835

Benson, A. J. 2010, Physics Reports, 495, 33, doi: 10.1016/j.physrep.2010.06.001

Biermann, P., & Kronberg, P. P. 1983, Astrophys. J., 268, L69, doi: 10.1086/184031

Biermann, P., Kronberg, P. P., & Madore, B. F. 1982, Astrophys. J., 256, L37, doi: 10.1086/183791

Biffi, V., Mernier, F., & Medvedev, P. 2018a, Space Sci Rev, 214, 123, doi: 10.1007/s11214-018-0557-7

Biffi, V., Planelles, S., Borgani, S., et al. 2018b, Monthly Notices of the Royal Astronomical Society, 476, 2689, doi: 10.1093/mnras/sty363

—. 2017, Monthly Notices of the Royal Astronomical Society, 468, 531, doi: 10.1093/mnras/stx444

Bildfell, C., Hoekstra, H., Babul, A., & Mahdavi, A. 2008, Monthly Notices of the Royal Astronomical Society, 389, 1637, doi: 10.1111/j.1365-2966.2008.13699.x

Binney, J. 1977, Astrophys. J., 215, 483, doi: 10.1086/155378

Birnboim, Y., & Dekel, A. 2003, Monthly Notices of the Royal Astronomical Society, 345, 349, doi: 10.1046/j.1365-8711.2003.06955.x

Blackwell, A. E., & Bregman, J. N. 2025, ApJ, 979, 74, doi: 10.3847/1538-4357/ad9826

Böhringer, H., & Werner, N. 2010, Astron Astrophys Rev, 18, 127, doi: 10.1007/s00159-009-0023-3

Bondi, H. 1952, Monthly Notices of the Royal Astronomical Society, 112, 195, doi: 10.1093/mnras/112.2.195

Borgani, S., Diaferio, A., Dolag, K., & Schindler, S. 2008, Space Sci Rev, 134, 269, doi: 10.1007/s11214-008-9317-4

Borodina, O., Ni, Y., Bennett, J. S., et al. 2025, You Shall Not Pass! The Propagation of Low/Moderate Powered Jets through a Turbulent Interstellar Medium, arXiv, doi: 10.48550/arXiv.2501.14062

Bourne, M. A., & Sijacki, D. 2017, Monthly Notices of the Royal Astronomical Society, 472, 4707, doi: 10.1093/mnras/stx2269

Bradley, L., Davé, R., Cui, W., Smith, B., & Sorini, D. 2022, High-Ionisation Oxygen Absorption from the Warm-Hot Intergalactic Medium in Simba, arXiv, doi: 10.48550/arXiv.2203.15055

Bradshaw, E. J., Almaini, O., Hartley, W. G., et al. 2013, Monthly Notices of the Royal Astronomical Society, 433, 194, doi: 10.1093/mnras/stt715

Bradt, H., Mayer, W., Naranan, S., Rappaport, S., & Spada, G. 1967, Astrophys. J., 150, L199, doi: 10.1086/180125

Braspenning, J., Schaye, J., Schaller, M., Kugel, R., & Kay, S. T. 2025, Monthly Notices of the Royal Astronomical Society, 536, 3784, doi: 10.1093/mnras/stae2798

Braspenning, J., Schaye, J., Schaller, M., et al. 2024, Mon. Not. R. Astron. Soc., doi: 10.1093/mnras/stae1436

Brauer, K., Emerick, A., Mead, J., et al. 2024, AEOS: Star-by-Star Cosmological Simulations of Early Chemical Enrichment and Galaxy Formation, arXiv, doi: 10.48550/arXiv.2410.16366

Bromm, V., Coppi, P. S., & Larson, R. B. 2002, Astrophys. J., 564, 23, doi: 10.1086/323947

Brooks, A. M., Governato, F., Quinn, T., Brook, C. B., & Wadsley, J. 2009, ApJ, 694, 396, doi: 10.1088/0004-637X/694/1/396

Bryan, G. L., & Norman, M. L. 1998, ApJ, 495, 80, doi: 10.1086/305262

Brzycki, B., & ZuHone, J. 2019, ApJ, 883, 118, doi: 10.3847/1538-4357/ab3983

Buote, D. A. 1999, Monthly Notices of the Royal Astronomical Society, 309, 685, doi: 10.1046/j.1365-8711.1999.02886.x

—. 2000a, ApJ, 539, 172, doi: 10.1086/309224

—. 2000b, Monthly Notices of the Royal Astronomical Society, 311, 176, doi: 10.1046/j.1365-8711.2000.03046.x

—. 2002, ApJ, 574, L135, doi: 10.1086/342532

Buote, D. A., Brighenti, F., & Mathews, W. G. 2004, ApJ, 607, L91, doi: 10.1086/422097

Buote, D. A., Lewis, A. D., Brighenti, F., & Mathews, W. G. 2003, ApJ, 595, 151, doi: 10.1086/377256

Burns, J. O., Gregory, S. A., & Holman, G. D. 1981, Astrophys. J., 250, 450, doi: 10.1086/159392

Byram, E. T., Chubb, T. A., & Friedman, H. 1966, Science, 152, 66

Carniani, S., Venturi, G., Parlanti, E., et al. 2024, A&A, 685, A99, doi: 10.1051/0004-6361/202347230

Cautun, M., Benítez-Llambay, A., Deason, A. J., et al. 2020, Monthly Notices of the Royal Astronomical Society, 494, 4291, doi: 10.1093/mnras/staa1017

Cavaliere, A. G., Gursky, H., & Tucker, W. H. 1971, Nature, 231, 437, doi: 10.1038/231437a0

Ceverino, D., & Klypin, A. 2009, Astrophys. J., 695, 292, doi: 10.1088/0004-637X/695/1/292

Chabrier, G. 2003, PASP, 115, 763, doi: 10.1086/376392

Chen, Y., Reiprich, T. H., Böhringer, H., Ikebe, Y., & Zhang, Y. Y. 2007, Astron. Astrophys., 466, 805, doi: 10.1051/0004-6361:20066471

Chisholm, J., Tremonti, C., & Leitherer, C. 2018, Monthly Notices of the Royal Astronomical Society, 481, 1690, doi: 10.1093/mnras/sty2380

Chiu, I., Mohr, J. J., McDonald, M., et al. 2018, Monthly Notices of the Royal Astronomical Society, 478, 3072, doi: 10.1093/mnras/sty1284

Choi, E., Brennan, R., Somerville, R. S., et al. 2020, ApJ, 904, 8, doi: 10.3847/1538-4357/abba7d

Choi, E., Ostriker, J. P., Naab, T., & Johansson, P. H. 2012, ApJ, 754, 125, doi: 10.1088/0004-637X/754/2/125

Connelly, J. L., Wilman, D. J., Finoguenov, A., et al. 2012, ApJ, 756, 139, doi: 10.1088/0004-637X/756/2/139

Cooke, B. A., Ricketts, M. J., Maccacaro, T., et al. 1978, Monthly Notices of the Royal Astronomical Society, 182, 489, doi: 10.1093/mnras/182.3.489

Crain, R. A., McCarthy, I. G., Frenk, C. S., Theuns, T., & Schaye, J. 2010, Monthly Notices of the Royal Astronomical Society, 407, 1403, doi: 10.1111/j.1365-2966.2010.16985.x

Crain, R. A., & van de Voort, F. 2023, Annu. Rev. Astron. Astrophys., 61, 473, doi: 10.1146/annurev-astro-041923-043618

Cresci, G., Tozzi, G., Perna, M., et al. 2023, A&A, 672, A128, doi: 10.1051/0004-6361/202346001

Croton, D. J., Springel, V., White, S. D. M., et al. 2006, Monthly Notices of the Royal Astronomical Society, 365, 11, doi: 10.1111/j.1365-2966.2005.09675.x

Cui, W., Jennings, F., Dave, R., Babul, A., & Gozaliasl, G. 2024, Monthly Notices of the Royal Astronomical Society, 534, 1247, doi: 10.1093/mnras/stae2115

Cui, W., Knebe, A., Yepes, G., et al. 2018, Monthly Notices of the Royal Astronomical Society, 480, 2898, doi: 10.1093/mnras/sty2111

Cui, W., Dave, R., Knebe, A., et al. 2022, Mon. Not. R. Astron. Soc., 514, 977, doi: 10.1093/mnras/stac1402

Curtis, H. D. 1988, PASP, 100, 6, doi: 10.1086/132128

Dalla Vecchia, C., Bower, R. G., Theuns, T., et al. 2004, Monthly Notices of the Royal Astronomical Society, 355, 995, doi: 10.1111/j.1365-2966.2004.08381.x

Dan, K. Y., Seebeck, J., Veilleux, S., et al. 2025, ApJ, 979, 68, doi: 10.3847/1538-4357/ad9a50

Davé, R. 2008, Monthly Notices of the Royal Astronomical Society, 385, 147, doi: 10.1111/j.1365-2966.2008.12866.x

Davé, R., Anglés-Alcázar, D., Narayanan, D., et al. 2019, Mon. Not. R. Astron. Soc., 486, 2827, doi: 10.1093/MNRAS/STZ937

Davé, R., Finlator, K., & Oppenheimer, B. D. 2006, Monthly Notices of the Royal Astronomical Society, 370, 273, doi: 10.1111/j.1365-2966.2006.10464.x

Davé, R., Oppenheimer, B. D., & Sivanandam, S. 2008, Mon. Not. R. Astron. Soc., 391, 110, doi: 10.1111/j.1365-2966.2008.13906.x

Davé, R., Thompson, R., & Hopkins, P. F. 2016, Mon. Not. R. Astron. Soc., 462, 3265, doi: 10.1093/mnras/stw1862

David, L. P., Jones, C., Forman, W., & Daines, S. 1994, Astrophys. J., 428, 544, doi: 10.1086/174264

David, L. P., O'Sullivan, E., Jones, C., et al. 2011, ApJ, 728, 162, doi: 10.1088/0004-637X/728/2/162

Davies, R. L., Schreiber, N. M. F., Übler, H., et al. 2019, ApJ, 873, 122, doi: 10.3847/1538-4357/ab06f1

Davis, D. S., Mulchaey, J. S., & Mushotzky, R. F. 1999, ApJ, 511, 34, doi: 10.1086/306665

Davis, D. S., Mulchaey, J. S., Mushotzky, R. F., & Burstein, D. 1996, Astrophys. J., 460, 601, doi: 10.1086/176995

Davis, D. S., Mushotzky, R. F., Mulchaey, J. S., et al. 1995, Astrophys. J., 444, 582, doi: 10.1086/175632

Davis, M., Efstathiou, G., Frenk, C. S., & White, S. D. M. 1985, Astrophys. J., 292, 371, doi: 10.1086/163168

de Plaa, J. 2013, Astron. Nachrichten, 334, 416, doi: 10.1002/asna.201211870

de Plaa, J., Werner, N., Bykov, A. M., et al. 2006, A&A, 452, 397, doi: 10.1051/0004-6361:20053864

De Plaa, J., Kaastra, J. S., Werner, N., et al. 2017, Astron. Astrophys., 607, A98, doi: 10.1051/0004-6361/201629926

de Vaucouleurs, A. 1965, The Observatory, 85, 75

Dekel, A., & Birnboim, Y. 2006, Monthly Notices of the Royal Astronomical Society, 368, 2, doi: 10.1111/j.1365-2966.2006.10145.x

Dekel, A., Sari, R., & Ceverino, D. 2009a, ApJ, 703, 785, doi: 10.1088/0004-637X/703/1/785

Dekel, A., Birnboim, Y., Engel, G., et al. 2009b, Nature, 457, 451, doi: 10.1038/nature07648

dell'Antonio, I. P., Geller, M. J., & Fabricant, D. G. 1994, Astron. J., 107, 427, doi: 10.1086/116864

den Herder, J. W., Brinkman, A. C., Kahn, S. M., et al. 2001, Astron. Astrophys., 365, L7, doi: 10.1051/0004-6361:20000058

Doe, S. M., Ledlow, M. J., Burns, J. O., & White, R. A. 1995, Astron. J., 110, 46, doi: 10.1086/117496

Doherty, C. L., Gil-Pons, P., Lau, H. H. B., Lattanzio, J. C., & Siess, L. 2014a, Monthly Notices of the Royal Astronomical Society, 437, 195, doi: 10.1093/mnras/stt1877

Doherty, C. L., Gil-Pons, P., Lau, H. H. B., et al. 2014b, Monthly Notices of the Royal Astronomical Society, 441, 582, doi: 10.1093/mnras/stu571

Dolag, K., Mevius, E., & Remus, R.-S. 2017, Galaxies, 5, 35, doi: 10.3390/galaxies5030035

Domainko, W., Mair, M., Kapferer, W., et al. 2006, Astron. Astrophys., 452, 795, doi: 10.1051/0004-6361:20053921

Donahue, M., & Voit, G. M. 2022, Phys. Rep., 973, 1, doi: 10.1016/j.physrep.2022.04.005

Dopita, M. A., & Sutherland, R. S. 2003, in Astrophysics of the Diffuse Universe, ed. M. A. Dopita & R. S. Sutherland (Berlin, Heidelberg: Springer), 101–123, doi: 10.1007/978-3-662-05866-4_5

Doria, A., Gitti, M., Ettori, S., et al. 2012, ApJ, 753, 47, doi: 10.1088/0004-637X/753/1/47

Duan, X., & Guo, F. 2024, ApJ, 972, 41, doi: 10.3847/1538-4357/ad5bdf

Duan, X., Wu, L., Zhang, R., & Li, J. 2024, Formation of Giant Radio Sources in Galaxy Clusters, arXiv, doi: 10.48550/arXiv.2410.04467

Dubois, Y., Devriendt, J., Teyssier, R., & Slyz, A. 2011, Monthly Notices of the Royal Astronomical Society, 417, 1853, doi: 10.1111/j.1365-2966.2011.19381.x

Dubois, Y., Pichon, C., Welker, C., et al. 2014, Monthly Notices of the Royal Astronomical Society, 444, 1453, doi: 10.1093/mnras/stu1227

Dwek, E. 1998, ApJ, 501, 643, doi: 10.1086/305829

—. 2016, ApJ, 825, 136, doi: 10.3847/0004-637X/825/2/136

Eckert, D., Ettori, S., Pointecouteau, E., et al. 2017a, Astron. Nachrichten, 338, 293, doi: 10.1002/asna.201713345

Eckert, D., Gaspari, M., Gastaldello, F., Le Brun, A. M., & O'Sullivan, E. 2021, Universe 2021 Vol 7 Page 142, 7, 142, doi: 10.3390/UNIVERSE7050142

Eckert, D., Ettori, S., Coupon, J., et al. 2016, A&A, 592, A12, doi: 10.1051/0004-6361/201527293

Eckert, D., Gaspari, M., Owers, M. S., et al. 2017b, A&A, 605, A25, doi: 10.1051/0004-6361/201730555

Eckert, D., Ghirardini, V., Ettori, S., et al. 2019, A&A, 621, A40, doi: 10.1051/0004-6361/201833324

Edwards, D., & Heath, D. 1976, Astrophys Space Sci, 41, 183, doi: 10.1007/BF00684580

Efstathiou, G., Sutherland, W. J., & Maddox, S. J. 1990, Nature, 348, 705, doi: 10.1038/348705a0

Ehlert, S., Werner, N., Simionescu, A., et al. 2013, Monthly Notices of the Royal Astronomical Society, 430, 2401, doi: 10.1093/mnras/stt060

Einasto, M., Einasto, J., Tenjes, P., et al. 2024, A&A, 681, A91, doi: 10.1051/0004-6361/202347504

Eke, V. R., Baugh, C. M., Cole, S., Frenk, C. S., & Navarro, J. F. 2006, Monthly Notices of the Royal Astronomical Society, 370, 1147, doi: 10.1111/j.1365-2966.2006.10568.x

Elvis, M. 1976, Monthly Notices of the Royal Astronomical Society, 177, 7P, doi: 10.1093/mnras/177.1.7P

Erfanianfar, G., Finoguenov, A., Furnell, K., et al. 2019, A&A, 631, A175, doi: 10.1051/0004-6361/201935375

Ettori, S. 2015, Monthly Notices of the Royal Astronomical Society, 446, 2629, doi: 10.1093/mnras/stu2292

Ettori, S., Baldi, A., Balestra, I., et al. 2015, A&A, 578, A46, doi: 10.1051/0004-6361/201425470

Ettori, S., Donnarumma, A., Pointecouteau, E., et al. 2013, Space Sci Rev, 177, 119, doi: 10.1007/s11214-013-9976-7

Ettori, S., & Eckert, D. 2022, A&A, 657, L1, doi: 10.1051/0004-6361/202142638

Ettori, S., Ghirardini, V., Eckert, D., et al. 2019, Astron. Astrophys., 621, A39, doi: 10.1051/0004-6361/201833323

Fabian, A. C. 1994, Annu. Rev. Astron. Astrophys., 32, 277, doi: 10.1146/annurev.aa.32.090194.001425

—. 2012, Annu. Rev. Astron. Astrophys., 50, 455, doi: 10.1146/annurev-astro-081811-125521

Fabjan, D., Borgani, S., Tornatore, L., et al. 2010, Monthly Notices of the Royal Astronomical Society, 401, 1670, doi: 10.1111/j.1365-2966.2009.15794.x

Fall, S. M., & Efstathiou, G. 1980, Monthly Notices of the Royal Astronomical Society, 193, 189, doi: 10.1093/mnras/193.2.189

Faucher-Giguère, C.-A., & Quataert, E. 2012, Monthly Notices of the Royal Astronomical Society, 425, 605, doi: 10.1111/j.1365-2966.2012.21512.x

Ferrara, A. 2024, A&A, 684, A207, doi: 10.1051/0004-6361/202348321

Finlator, K., & Davé, R. 2008, Monthly Notices of the Royal Astronomical Society, 385, 2181, doi: 10.1111/j.1365-2966.2008.12991.x

Finlator, K., Davé, R., & Özel, F. 2011a, ApJ, 743, 169, doi: 10.1088/0004-637X/743/2/169

Finlator, K., Oppenheimer, B. D., & Davé, R. 2011b, Monthly Notices of the Royal Astronomical Society, 410, 1703, doi: 10.1111/j.1365-2966.2010.17554.x

Finoguenov, A., David, L., & Ponman, T. 1999, Astron. Nachrichten, 320, 286, doi: 10.1002/1521-3994(199908)320:4/5<286::AID-ASNA286>3.0.CO;2-C

Fiore, F., Feruglio, C., Shankar, F., et al. 2017, A&A, 601, A143, doi: 10.1051/0004-6361/201629478

Flores, A. M., Mantz, A. B., Allen, S. W., et al. 2021, Monthly Notices of the Royal Astronomical Society, 507, 5195, doi: 10.1093/mnras/stab2430

Fluetsch, A., Maiolino, R., Carniani, S., et al. 2021, Monthly Notices of the Royal Astronomical Society, 505, 5753, doi: 10.1093/mnras/stab1666

Ford, A. B., Davé, R., Oppenheimer, B. D., et al. 2014, Monthly Notices of the Royal Astronomical Society, 444, 1260, doi: 10.1093/mnras/stu1418

Forman, W., Kellogg, E., Gursky, H., Tananbaum, H., & Giacconi, R. 1972, Astrophys. J., 178, 309, doi: 10.1086/151791

Foster, A., Smith, R. K., Brickhouse, N. S., et al. 2016, AAS, 227, 211.08

Foster, A. R., & Heuer, K. 2020, At. 2020 Vol 8 Page 49, 8, 49, doi: 10.3390/ATOMS8030049

Foster, A. R., Heuer, K., & Smith, R. 2021, Bull. AAS, 53

Fritz, G., Davidsen, A., Meekins, J. F., & Friedman, H. 1971, Astrophys. J., 164, L81, doi: 10.1086/180697

Fukazawa, Y., Makishima, K., Tamura, T., et al. 1998, Publ. Astron. Soc. Jpn., 50, 187, doi: 10.1093/pasj/50.1.187

Fukazawa, Y., Makishima, K., Matsushita, K., et al. 1996, Publ. Astron. Soc. Jpn., 48, 395, doi: 10.1093/pasj/48.3.395

Fukushima, K., Kobayashi, S. B., & Matsushita, K. 2023, ApJ, 953, 112, doi: 10.3847/1538-4357/ace16a

Gabor, J. M., & Bournaud, F. 2014, Monthly Notices of the Royal Astronomical Society, 441, 1615, doi: 10.1093/mnras/stu677

Gaburov, E., & Nitadori, K. 2011, Monthly Notices of the Royal Astronomical Society, 414, 129, doi: 10.1111/j.1365-2966.2011.18313.x

Gaskin, J. A., Swartz, D., Vikhlinin, A. A., et al. 2019, JATIS, 5, 021001, doi: 10.1117/1.JATIS.5.2.021001

Gaspari, M., Brighenti, F., D'Ercole, A., & Melioli, C. 2011a, Monthly Notices of the Royal Astronomical Society, 415, 1549, doi: 10.1111/j.1365-2966.2011.18806.x

Gaspari, M., & Churazov, E. 2013, A&A, 559, A78, doi: 10.1051/0004-6361/201322295

Gaspari, M., Melioli, C., Brighenti, F., & D'Ercole, A. 2011b, Monthly Notices of the Royal Astronomical Society, 411, 349, doi: 10.1111/j.1365-2966.2010.17688.x

Gaspari, M., Ruszkowski, M., & Oh, S. P. 2013, Monthly Notices of the Royal Astronomical Society, 432, 3401, doi: 10.1093/mnras/stt692

Gaspari, M., Temi, P., & Brighenti, F. 2017, Monthly Notices of the Royal Astronomical Society, 466, 677, doi: 10.1093/mnras/stw3108

Gaspari, M., Tombesi, F., & Cappi, M. 2020, Nat Astron, 4, 10, doi: 10.1038/s41550-019-0970-1

Gaspari, M., Eckert, D., Ettori, S., et al. 2019, ApJ, 884, 169, doi: 10.3847/1538-4357/ab3c5d

Gastaldello, F., & Molendi, S. 2002, ApJ, 572, 160, doi: 10.1086/340283

Gastaldello, F., Simionescu, A., Mernier, F., et al. 2021, Universe, 7, 208, doi: 10.3390/universe7070208

Gatuzz, E., Sanders, . J. S., Dennerl, K., et al. 2023, Mon. Not. R. Astron. Soc., 525, 6394, doi: 10.1093/MNRAS/STAD2716

Geach, J. E., Hickox, R. C., Diamond-Stanic, A. M., et al. 2014a, Nature, 516, 68, doi: 10.1038/nature14012

Geach, J. E., Bower, R. G., Alexander, D. M., et al. 2014b, ApJ, 793, 22, doi: 10.1088/0004-637X/793/1/22

Geller, M. J., & Huchra, J. P. 1983, Astrophys. J. Suppl. Ser., 52, 61, doi: 10.1086/190859

Gendron-Marsolais, M., Kraft, R. P., Bogdan, A., et al. 2017, ApJ, 848, 26, doi: 10.3847/1538-4357/aa8a6f

Ghirardini, V., Eckert, D., Ettori, S., et al. 2019, Astron. Astrophys., 621, A41, doi: 10.1051/0004-6361/201833325

Ghizzardi, S., Rossetti, M., & Molendi, S. 2010, A&A, 516, A32, doi: 10.1051/0004-6361/200912496

Ghizzardi, S., Molendi, S., van der Burg, R., et al. 2021, A&A, 646, A92, doi: 10.1051/0004-6361/202038501

Giacconi, R., Gursky, H., Paolini, F. R., & Rossi, B. B. 1962, Phys. Rev. Lett., 9, 439, doi: 10.1103/PhysRevLett.9.439

Giacconi, R., Murray, S., Gursky, H., et al. 1972, Astrophys. J., 178, 281, doi: 10.1086/151790

Gianfagna, G., Rasia, E., Cui, W., et al. 2023, Monthly Notices of the Royal Astronomical Society, 518, 4238, doi: 10.1093/mnras/stac3364

Gianolli, V. E., Bianchi, S., Petrucci, P.-O., et al. 2024, A&A, 687, A235, doi: 10.1051/0004-6361/202348908

Gioannini, L., Matteucci, F., Vladilo, G., & Calura, F. 2017, Monthly Notices of the Royal Astronomical Society, 464, 985, doi: 10.1093/mnras/stw2343

Girelli, G., Pozzetti, L., Bolzonella, M., et al. 2020, A&A, 634, 135, doi: 10.1051/0004-6361/201936329

Gitti, M., O'Sullivan, E., Giacintucci, S., et al. 2010, ApJ, 714, 758, doi: 10.1088/0004-637X/714/1/758

Gonzalez, A. H., Sivanandam, S., Zabludoff, A. I., & Zaritsky, D. 2013, ApJ, 778, 14, doi: 10.1088/0004-637X/778/1/14

Grandi, S. D., & Molendi, S. 2001, ApJ, 551, 153, doi: 10.1086/320098

—. 2009, A&A, 508, 565, doi: 10.1051/0004-6361/200912745

Grange, Y. G., de Plaa, J., Kaastra, J. S., et al. 2011, Astron. Astrophys., 531, A15, doi: 10.1051/0004-6361/201016187

Groth, F., Valentini, M., Steinwandel, U. P., Vallés-Pérez, D., & Dolag, K. 2025, A&A, 693, A263, doi: 10.1051/0004-6361/202451803

Gu, J., Xu, H., Gu, L., et al. 2007, ApJ, 659, 275, doi: 10.1086/512180

Gu, L., Zhuravleva, I., Churazov, E., et al. 2018, Space Sci Rev, 214, 108, doi: 10.1007/s11214-018-0544-z

Guedes, J., Callegari, S., Madau, P., & Mayer, L. 2011, ApJ, 742, 76, doi: 10.1088/0004-637X/742/2/76

Gunn, J. E. 1977, Astrophys. J., 218, 592, doi: 10.1086/155715

Gunn, J. E., & Gott, J. R. 1972, Astrophys. J., 176, 1, doi: 10.1086/151605

Guo, F., & Mathews, W. G. 2010, ApJ, 717, 937, doi: 10.1088/0004-637X/717/2/937

Gursky, H., Kellogg, E. M., Leong, C., Tananbaum, H., & Giacconi, R. 1971, Astrophys. J., 165, L43, doi: 10.1086/180713

Guth, A. H. 1981, Phys. Rev. D, 23, 347, doi: 10.1103/PhysRevD.23.347

Harris, C. R., Millman, K. J., van der Walt, S. J., et al. 2020, Nature, 585, 357, doi: 10.1038/s41586-020-2649-2

Harrison, C. M., Alexander, D. M., Mullaney, J. R., & Swinbank, A. M. 2014, Monthly Notices of the Royal Astronomical Society, 441, 3306, doi: 10.1093/mnras/stu515

Heath, D. J. 1977, Monthly Notices of the Royal Astronomical Society, 179, 351, doi: 10.1093/mnras/179.3.351

Heckman, T. M., Alexandroff, R. M., Borthakur, S., Overzier, R., & Leitherer, C. 2015, ApJ, 809, 147, doi: 10.1088/0004-637X/809/2/147

Heckman, T. M., Armus, L., & Miley, G. K. 1990, Astrophys. J. Suppl. Ser., 74, 833, doi: 10.1086/191522

Heckman, T. M., Lehnert, M. D., Strickland, D. K., & Armus, L. 2000, ApJS, 129, 493, doi: 10.1086/313421

Helsdon, S. F., & Ponman, T. J. 2000a, Monthly Notices of the Royal Astronomical Society, 319, 933, doi: 10.1046/j.1365-8711.2000.03916.x

—. 2000b, Monthly Notices of the Royal Astronomical Society, 315, 356, doi: 10.1046/j.1365-8711.2000.03396.x

Henden, N. A., Puchwein, E., Shen, S., & Sijacki, D. 2018, Mon. Not. R. Astron. Soc., 479, 5385, doi: 10.1093/mnras/sty1780

Henden, N. A., Puchwein, E., & Sijacki, D. 2020, Monthly Notices of the Royal Astronomical Society, 498, 2114, doi: 10.1093/mnras/staa2235

Henry, J. P., Gioia, I. M., Huchra, J. P., et al. 1995, Astrophys. J., 449, 422, doi: 10.1086/176067

Henson, M. A., Barnes, D. J., Kay, S. T., McCarthy, I. G., & Schaye, J. 2017, Monthly Notices of the Royal Astronomical Society, 465, 3361, doi: 10.1093/mnras/stw2899

Hirschmann, M. 2016, 317, 247, doi: 10.1017/S1743921315008613

Hirschmann, M., & De Lucia, G. 2016, 319, 26, doi: 10.1017/S1743921315009928

Hirschmann, M., De Lucia, G., & Fontanot, F. 2016, Mon. Not. R. Astron. Soc., 461, 1760, doi: 10.1093/mnras/stw1318

Hirschmann, M., Naab, T., Davé, R., et al. 2013, Monthly Notices of the Royal Astronomical Society, 436, 2929, doi: 10.1093/mnras/stt1770

Hoekstra, H., Herbonnet, R., Muzzin, A., et al. 2015, Monthly Notices of the Royal Astronomical Society, 449, 685, doi: 10.1093/mnras/stv275

Holmberg, E. 1950, Medd. Fran Lunds Astron. Obs. Ser. II, 128, 5

Hopkins, P. F. 2015, Mon. Not. R. Astron. Soc., 450, 53, doi: 10.1093/mnras/stv195

—. 2017, A New Public Release of the GIZMO Code, doi: 10.48550/arXiv.1712.01294

Hopkins, P. F., Chan, T. K., Ji, S., et al. 2021, Monthly Notices of the Royal Astronomical Society, 501, 3640, doi: 10.1093/mnras/staa3690

Hopkins, P. F., Kereš, D., Oñorbe, J., et al. 2014, Monthly Notices of the Royal Astronomical Society, 445, 581, doi: 10.1093/mnras/stu1738

Hopkins, P. F., & Quataert, E. 2011, Monthly Notices of the Royal Astronomical Society, 415, 1027, doi: 10.1111/j.1365-2966.2011.18542.x

Hopkins, P. F., Quataert, E., & Murray, N. 2012, Mon. Not. R. Astron. Soc., 421, 3522, doi: 10.1111/j.1365-2966.2012.20593.x

Hopkins, P. F., Torrey, P., Faucher-Giguère, C.-A., Quataert, E., & Murray, N. 2016, Monthly Notices of the Royal Astronomical Society, 458, 816, doi: 10.1093/mnras/stw289

Hopkins, P. F., Wellons, S., Anglés-Alcázar, D., Faucher-Giguère, C.-A., & Grudić, M. Y. 2022, Mon. Not. R. Astron. Soc., 510, 630, doi: 10.1093/mnras/stab3458

Hough, R. T., Rennehan, D., Kobayashi, C., et al. 2023, Monthly Notices of the Royal Astronomical Society, 525, 1061, doi: 10.1093/mnras/stad2394

Hough, R. T., Shao, Z., Cui, W., et al. 2024, Monthly Notices of the Royal Astronomical Society, 532, 476, doi: 10.1093/mnras/stae1435

Hu, D., Xu, H., Kang, X., et al. 2019, ApJ, 870, 61, doi: 10.3847/1538-4357/aaf16c

Hubble, E. P. 1926, Astrophys. J., 64, 321, doi: 10.1086/143018

—. 1929, Astrophys. J., 69, 103, doi: 10.1086/143167

—. 1936, Realm of the Nebulae

Huchra, J. P., & Geller, M. J. 1982, Astrophys. J., 257, 423, doi: 10.1086/160000

Hudson, D. S., Mittal, R., Reiprich, T. H., et al. 2010, A&A, 513, A37, doi: 10.1051/0004-6361/200912377

Humason, M. L. 1956, Vistas in Astronomy, 2, 1620, doi: 10.1016/0083-6656(56)90089-7

Humason, M. L., Mayall, N. U., & Sandage, A. R. 1956, Astron. J., 61, 97, doi: 10.1086/107297

Humphrey, P. J., Buote, D. A., Brighenti, F., et al. 2012, ApJ, 748, 11, doi: 10.1088/0004-637X/748/1/11

Hunter, J. D. 2007, Comput. Sci. Eng., 9, 90, doi: 10.1109/MCSE.2007.55

Hurier, G., & Angulo, R. E. 2018, A&A, 610, L4, doi: 10.1051/0004-6361/201731999

Hwang, U., Mushotzky, R. F., Burns, J. O., Fukazawa, Y., & White, R. A. 1999, ApJ, 516, 604, doi: 10.1086/307147

Ishisaki, Y., Ezoe, Y., Yamada, S., et al. 2018, J Low Temp Phys, 193, 991, doi: 10.1007/s10909-018-1913-4

Iwamoto, K., Brachwitz, F., Nomoto, K., et al. 1999, ApJS, 125, 439, doi: 10.1086/313278

Jackson, T. M., Pasquali, A., Pacifici, C., et al. 2020, Monthly Notices of the Royal Astronomical Society, 497, 4262, doi: 10.1093/mnras/staa2306

Jansen, F., Lumb, D., Altieri, B., et al. 2001, A&A, 365, L1, doi: 10.1051/0004-6361:20000036

Jennings, F., & Davé, R. 2023, Mon. Not. R. Astron. Soc., 526, 1367, doi: 10.1093/mnras/stad2666

Jennings, F. J., Babul, A., Davé, R., Cui, W., & Rennehan, D. 2025, Monthly Notices of the Royal Astronomical Society, 536, 145, doi: 10.1093/mnras/stae2592

Johnson, R., Finoguenov, A., Ponman, T. J., Rasmussen, J., & Sanderson, A. J. 2011, Mon. Not. R. Astron. Soc., 413, 2467, doi: 10.1111/J.1365-2966.2011.18317.X

Johnson, R., Ponman, T. J., & Finoguenov, A. 2009, Mon. Not. R. Astron. Soc., 395, 1287, doi: 10.1111/J.1365-2966.2009.14644.X

Jung, S. L., Rennehan, D., Saeedzadeh, V., et al. 2022, Mon. Not. R. Astron. Soc., 515, 22, doi: 10.1093/MNRAS/STAC1622

Kahn, S. M. 1999, 4, 12.02

Kapferer, W., Kronberger, T., Weratschnig, J., et al. 2007, A&A, 466, 813, doi: 10.1051/0004-6361:20066804

Kapferer, W., Kronberger, T., Breitschwerdt, D., et al. 2009, A&A, 504, 719, doi: 10.1051/0004-6361/200912099

Katz, H., Kimm, T., Ellis, R. S., Devriendt, J., & Slyz, A. 2023, Monthly Notices of the Royal Astronomical Society, 524, 351, doi: 10.1093/mnras/stad1903

Katz, N. 1992, Astrophys. J., 391, 502, doi: 10.1086/171366

Katz, N., Keres, D., Davé, R., & Weinberg, D. H. 2003, in The IGM/Galaxy Connection: The Distribution of Baryons at Z=0, ed. J. L. Rosenberg & M. E. Putman (Dordrecht: Springer Netherlands), 185–192, doi: 10.1007/978-94-010-0115-1_34

Kay, S. T., Braspenning, J., Chluba, J., et al. 2024, Monthly Notices of the Royal Astronomical Society, 534, 251, doi: 10.1093/mnras/stae1991

Kay, S. T., Thomas, P. A., Jenkins, A., & Pearce, F. R. 2004, Monthly Notices of the Royal Astronomical Society, 355, 1091, doi: 10.1111/j.1365-2966.2004.08383.x

Kazuyo, T., Sato, K., Ishisaki, Y., et al. 2008, Publications of the Astronomical Society of Japan, 60, S317, doi: 10.1093/pasj/60.sp1.S317

Kelleher, R., & Lelli, F. 2024, A&A, 688, A78, doi: 10.1051/0004-6361/202449968

Kelley, R. L., Mitsuda, K., Allen, C. A., et al. 2007, Publications of the Astronomical Society of Japan, 59, S77, doi: 10.1093/pasj/59.sp1.S77

Kellogg, E., Gursky, H., Tananbaum, H., Giacconi, R., & Pounds, K. 1972, Astrophys. J., 174, L65, doi: 10.1086/180950

Kempf, J. M., & Rincon, F. 2024, Non-Linear Saturation and Energy Transport in Global Simulations of Magneto-Thermal Turbulence in the Stratified Intracluster Medium, arXiv, doi: 10.48550/arXiv.2411.16242

Kennicutt, Jr, R. C. 1998, ApJ, 498, 541, doi: 10.1086/305588

Kennicutt, Jr., R. C., Calzetti, D., Walter, F., et al. 2007, Astrophys. J., 671, 333, doi: 10.1086/522300

Kereš, D., Katz, N., Fardal, M., Davé, R., & Weinberg, D. H. 2009, Monthly Notices of the Royal Astronomical Society, 395, 160, doi: 10.1111/j.1365-2966.2009.14541.x

Kereš, D., Katz, N., Weinberg, D. H., & Davé, R. 2005, Monthly Notices of the Royal Astronomical Society, 363, 2, doi: 10.1111/j.1365-2966.2005.09451.x

Khrykin, I. S., Sorini, D., Lee, K.-G., & Davé, R. 2024, Monthly Notices of the Royal Astronomical Society, 529, 537, doi: 10.1093/mnras/stae525

Kim, D.-W., & Fabbiano, G. 2004, ApJ, 613, 933, doi: 10.1086/423266

Kirkpatrick, C. C., Gitti, M., Cavagnolo, K. W., et al. 2009, ApJ, 707, L69, doi: 10.1088/0004-637X/707/1/L69

Kirkpatrick, C. C., McNamara, B. R., & Cavagnolo, K. W. 2011, ApJL, 731, L23, doi: 10.1088/2041-8205/731/2/L23

Knebe, A., Draganova, N., Power, C., et al. 2008, Mon. Not. R. Astron. Soc., 386, L52, doi: 10.1111/j.1745-3933.2008.00459.x

Knollmann, S. R., & Knebe, A. 2009, Astrophys. J. Suppl. Ser., 182, 608, doi: 10.1088/0067-0049/182/2/608

Kobayashi, C. 2004, Mon. Not. R. Astron. Soc., 347, 740, doi: 10.1111/j.1365-2966.2004.07258.x

Kobayashi, C., Karakas, A. I., & Lugaro, M. 2020a, Astrophys. J., 900, 179, doi: 10.3847/1538-4357/abae65

Kobayashi, C., Karakas, A. I., & Umeda, H. 2011, Mon. Not. R. Astron. Soc., 414, 3231, doi: 10.1111/j.1365-2966.2011.18621.x

Kobayashi, C., Leung, S.-C., & Nomoto, K. 2020b, Astrophys. J., 895, 138, doi: 10.3847/1538-4357/ab8e44

Kobayashi, C., & Nakasato, N. 2011, Astrophys. J., 729, 16, doi: 10.1088/0004-637X/729/1/16

Kobayashi, C., & Nomoto, K. 2009, Astrophys. J., 707, 1466, doi: 10.1088/0004-637X/707/2/1466

Kobayashi, C., Springel, V., & White, S. D. M. 2007, Monthly Notices of the Royal Astronomical Society, 376, 1465, doi: 10.1111/j.1365-2966.2007.11555.x

Kobayashi, C., Tsujimoto, T., Nomoto, K., Hachisu, I., & Kato, M. 1998, Astrophys. J., 503, L155, doi: 10.1086/311556

Kobayashi, C., Umeda, H., Nomoto, K., Tominaga, N., & Ohkubo, T. 2006, Astrophys. J., 653, 1145, doi: 10.1086/508914

Komatsu, E., Dunkley, J., Nolta, M. R., et al. 2009, ApJS, 180, 330, doi: 10.1088/0067-0049/180/2/330

Komatsu, E., Smith, K. M., Dunkley, J., et al. 2011, ApJS, 192, 18, doi: 10.1088/0067-0049/192/2/18

Komiyama, M., Sato, K., Nagino, R., Ohashi, T., & Matsushita, K. 2009, Publications of the Astronomical Society of Japan, 61, S337, doi: 10.1093/pasj/61.sp1.S337

Koyama, K., Tsunemi, H., Dotani, T., et al. 2007, Publications of the Astronomical Society of Japan, 59, S23, doi: 10.1093/pasj/59.sp1.S23

Kraft, R. P., Forman, W. R., Churazov, E., et al. 2004, ApJ, 601, 221, doi: 10.1086/380427

Kraft, R. P., Jones, C., Nulsen, P. E. J., & Hardcastle, M. J. 2006, ApJ, 640, 762, doi: 10.1086/500123

Kravtsov, A. V., & Borgani, S. 2012, Annu. Rev. Astron. Astrophys., 50, 353, doi: 10.1146/annurev-astro-081811-125502

Kravtsov, A. V., Vikhlinin, A. A., & Meshcheryakov, A. V. 2018, Astron. Lett., 44, 8, doi: 10.1134/S1063773717120015

Kriss, G. A., Canizares, C. R., McClintock, J. E., & Feigelson, E. D. 1980, Astrophys. J., 235, L61, doi: 10.1086/183159

Kriss, G. A., Cioffi, D. F., & Canizares, C. R. 1983, Astrophys. J., 272, 439, doi: 10.1086/161311

Krumholz, M. R., & Gnedin, N. Y. 2011, ApJ, 729, 36, doi: 10.1088/0004-637X/729/1/36

Krumholz, M. R., & Thompson, T. A. 2013, Monthly Notices of the Royal Astronomical Society, 434, 2329, doi: 10.1093/mnras/stt1174

Kugel, R., Schaye, J., Schaller, M., et al. 2023, Mon. Not. R. Astron. Soc., 526, 6103, doi: 10.1093/mnras/stad2540

Kurinchi-Vendhan, S., Farcy, M., Hirschmann, M., & Valentino, F. 2024, Monthly Notices of the Royal Astronomical Society, 534, 3974, doi: 10.1093/mnras/stae2297

Laganá, T. F., Lovisari, L., Martins, L., et al. 2015, A&A, 573, A66, doi: 10.1051/0004-6361/201424821

Lagos, P., Loubser, S. I., Scott, T. C., et al. 2022, Mon. Not. R. Astron. Soc., 516, 5487, doi: 10.1093/mnras/stac2535

Lahav, O., Lilje, P. B., Primack, J. R., & Rees, M. J. 1991, Mon. Not. R. Astron. Soc., 251, 128, doi: 10.1093/mnras/251.1.128

Lanson, N., & Vila, J.-P. 2008a, SIAM J. Numer. Anal., 46, 1912, doi: 10.1137/S0036142903427718

—. 2008b, SIAM J. Numer. Anal., 46, 1935, doi: 10.1137/S003614290444739X

Le Brun, A. M. C., McCarthy, I. G., Schaye, J., & Ponman, T. J. 2014, Monthly Notices of the Royal Astronomical Society, 441, 1270, doi: 10.1093/mnras/stu608

Lea, S. M., Mushotzky, R., & Holt, S. S. 1982, Astrophys. J., 262, 24, doi: 10.1086/160392

Leccardi, A., & Molendi, S. 2008, Astron. Astrophys., 487, 461, doi: 10.1051/0004-6361:200810113

Lehle, K., Nelson, D., Pillepich, A., Truong, N., & Rohr, E. 2024, A&A, 687, A129, doi: 10.1051/0004-6361/202348609

Leroy, A. K., Walter, F., Brinks, E., et al. 2008, Astron. J., 136, 2782, doi: 10.1088/0004-6256/136/6/2782

Lewis, G. F., Babul, A., Katz, N., et al. 2000, ApJ, 536, 623, doi: 10.1086/308954

Liang, L., Durier, F., Babul, A., et al. 2016, Mon. Not. R. Astron. Soc., 456, 4266, doi: 10.1093/MNRAS/STV2840

Limongi, M., Chieffi, A., & Bonifacio, P. 2003, ApJ, 594, L123, doi: 10.1086/378734

Linde, A. D. 1982, Physics Letters B, 108, 389, doi: 10.1016/0370-2693(82)91219-9

Liu, A., Tozzi, P., Ettori, S., et al. 2020, A&A, 637, A58, doi: 10.1051/0004-6361/202037506

Lochhaas, C., Bryan, G. L., Li, Y., Li, M., & Fielding, D. 2020, Mon. Not. R. Astron. Soc., 493, 1461, doi: 10.1093/mnras/staa358

Loubser, S. I., Hoekstra, H., Babul, A., & O'Sullivan, E. 2018, Monthly Notices of the Royal Astronomical Society, 477, 335, doi: 10.1093/mnras/sty498

Lovisari, L., Ettori, S., Gaspari, M., & Giles, P. A. 2021, Universe, 7, 139, doi: 10.3390/universe7050139

Lovisari, L., & Reiprich, T. H. 2019, Mon. Not. R. Astron. Soc., 483, 540, doi: 10.1093/MNRAS/STY3130

Lovisari, L., Reiprich, T. H., & Schellenberger, G. 2015, Astron. Astrophys., 573, A118, doi: 10.1051/0004-6361/201423954

Ludlow, A. D., Schaye, J., & Bower, R. 2019, Mon. Not. R. Astron. Soc., 488, 3663, doi: 10.1093/mnras/stz1821

Madau, P., & Dickinson, M. 2014, Annu. Rev. Astron. Astrophys., 52, 415, doi: 10.1146/annurev-astro-081811-125615

Mahdavi, A., Böhringer, H., Geller, M. J., & Ramella, M. 1997, ApJ, 483, 68, doi: 10.1086/304237

—. 2000, ApJ, 534, 114, doi: 10.1086/308740

Mahdavi, A., Hoekstra, H., Babul, A., & Henry, J. P. 2008, Monthly Notices of the Royal Astronomical Society, 384, 1567, doi: 10.1111/j.1365-2966.2007.12796.x

Maiolino, R., Gallerani, S., Neri, R., et al. 2012, Monthly Notices of the Royal Astronomical Society: Letters, 425, L66, doi: 10.1111/j.1745-3933.2012.01303.x

Maiolino, R., Scholtz, J., Witstok, J., et al. 2024, Nature, 1, doi: 10.1038/s41586-024-07052-5

Maller, A. H., & Bullock, J. S. 2004, Monthly Notices of the Royal Astronomical Society, 355, 694, doi: 10.1111/j.1365-2966.2004.08349.x

Mantz, A. B., Allen, S. W., Morris, R. G., et al. 2017, Monthly Notices of the Royal Astronomical Society, 472, 2877, doi: 10.1093/mnras/stx2200

Mao, J., de Plaa, J., Kaastra, J. S., et al. 2019, A&A, 621, A9, doi: 10.1051/0004-6361/201730931

Marini, I., Borgani, S., Saro, A., et al. 2021, Monthly Notices of the Royal Astronomical Society, 507, 5780, doi: 10.1093/mnras/stab2518

Markevitch, M., & Vikhlinin, A. 2007, Physics Reports, 443, 1, doi: 10.1016/j.physrep.2007.01.001

Markevitch, M., Vikhlinin, A., & Forman, W. R. 2003, 301, 37, doi: 10.48550/arXiv.astro-ph/0208208

Martin, C. L. 1999, ApJ, 513, 156, doi: 10.1086/306863

—. 2006, ApJ, 647, 222, doi: 10.1086/504886

Martin, C. L., Shapley, A. E., Coil, A. L., et al. 2012, ApJ, 760, 127, doi: 10.1088/0004-637X/760/2/127

Martín, M. V., Cobá, C. L., Cazzoli, S., Montero, E. P., & Lavers, A. C. 2024, A&A, 690, A397, doi: 10.1051/0004-6361/202449621

Martínez-Aldama, M. L., del Olmo, A., Marziani, P., et al. 2018, Astron. Astrophys., 618, A179, doi: 10.1051/0004-6361/201833541

Martizzi, D., & Agrusa, H. 2016, Mass Modeling of Galaxy Clusters: Quantifying Hydrostatic Bias and Contribution from Non-Thermal Pressure, arXiv, doi: 10.48550/arXiv.1608.04388

Martizzi, D., Hahn, O., Wu, H.-Y., et al. 2016, Mon. Not. R. Astron. Soc., 459, 4408, doi: 10.1093/mnras/stw897

Martizzi, D., Jimmy, Teyssier, R., & Moore, B. 2014, Monthly Notices of the Royal Astronomical Society, 443, 1500, doi: 10.1093/mnras/stu1233

Materne, J. 1979, Astron. Astrophys., 74, 235

Matsushita, K., Ohashi, T., & Makishima, K. 2000, Publ. Astron. Soc. Jpn., 52, 685, doi: 10.1093/pasj/52.4.685

Matteucci, F. 2016, 703, 012004, doi: 10.1088/1742-6596/703/1/012004

Mazzotta, P., Rasia, E., Moscardini, L., & Tormen, G. 2004, arXiv e-prints, astro, doi: 10.48550/arXiv.astro-ph/0409618

McCabe, T., & Borthakur, S. 2023, Bull. AAS, 55

McCabe, T., Borthakur, S., Heckman, T., et al. 2021, ApJ, 923, 189, doi: 10.3847/1538-4357/ac283c

McCarthy, I. G., Babul, A., Bower, R. G., & Balogh, M. L. 2008a, Mon. Not. R. Astron. Soc., 386, 1309, doi: 10.1111/J.1365-2966.2008.13141.X/2/MNRAS0386-1309-F12.JPEG

—. 2008b, Monthly Notices of the Royal Astronomical Society, 386, 1309, doi: 10.1111/j.1365-2966.2008.13141.x

McCarthy, I. G., Schaye, J., Bird, S., & Le Brun, A. M. C. 2017, Mon. Not. R. Astron. Soc., 465, 2936, doi: 10.1093/mnras/stw2792

McCarthy, I. G., Schaye, J., Bower, R. G., et al. 2011, Monthly Notices of the Royal Astronomical Society, 412, 1965, doi: 10.1111/j.1365-2966.2010.18033.x

McCarthy, I. G., Schaye, J., Ponman, T. J., et al. 2010, Monthly Notices of the Royal Astronomical Society, 406, 822, doi: 10.1111/j.1365-2966.2010.16750.x

McCarthy, P. J., van Breugel, W., & Heckman, T. 1987, Astron. J., 93, 264, doi: 10.1086/114309

McCourt, M., Sharma, P., Quataert, E., & Parrish, I. J. 2012, Monthly Notices of the Royal Astronomical Society, 419, 3319, doi: 10.1111/j.1365-2966.2011.19972.x

McDonald, M., Bulbul, E., de Haan, T., et al. 2016, ApJ, 826, 124, doi: 10.3847/0004-637X/826/2/124

McKinnon, R., Torrey, P., & Vogelsberger, M. 2016, Monthly Notices of the Royal Astronomical Society, 457, 3775, doi: 10.1093/mnras/stw253

McNamara, B. R., & Nulsen, P. E. J. 2007, Annu. Rev. Astron. Astrophys., 45, 117, doi: 10.1146/annurev.astro.45.051806.110625

McQuinn, Kristen. B. W., van Zee, L., & Skillman, E. D. 2019, ApJ, 886, 74, doi: 10.3847/1538-4357/ab4c37

Meekins, J. F., Fritz, G., Chubb, T. A., Friedman, H., & Henry, R. C. 1971, Nature, 231, 107, doi: 10.1038/231107a0

Mernier, F., & Biffi, V. 2022, Handb. X-Ray Gamma-Ray Astrophys., 1, doi: 10.1007/978-981-16-4544-0_123-1

Mernier, F., de Plaa, J., Pinto, C., et al. 2016, Astron. Astrophys., 592, A157, doi: 10.1051/0004-6361/201527824

Mernier, F., De Plaa, J., Kaastra, J. S., et al. 2017, A&A, 603, 80, doi: 10.1051/0004-6361/201630075

Mernier, F., Biffi, V., Yamaguchi, H., et al. 2018a, Space Sci. Rev., 214, doi: 10.1007/s11214-018-0565-7

Mernier, F., Werner, N., de Plaa, J., et al. 2018b, Mon. Not. R. Astron. Soc. Lett., 480, L95, doi: 10.1093/MNRASL/SLY134

Mernier, F., De Plaa, J., Werner, N., et al. 2018c, Mon. Not. R. Astron. Soc. Lett., 478, L116, doi: 10.1093/MNRASL/SLY080

Mernier, F., Cucchetti, E., Tornatore, L., et al. 2020, A&A, 642, A90, doi: 10.1051/0004-6361/202038638

Mernier, F., Werner, N., Su, Y., et al. 2022, Mon. Not. R. Astron. Soc., 511, 3159, doi: 10.1093/MNRAS/STAC253

Messier, C. 1781, Catalogue Des Nébuleuses et Des Amas d'Étoiles (Catalog of Nebulae and Star Clusters), Tech. rep.

Migkas, K., Kox, D., Schellenberger, G., et al. 2024, A&A, 688, A107, doi: 10.1051/0004-6361/202349006

Mitchell, R. J., Culhane, J. L., Davison, P. J. N., & Ives, J. C. 1976, Monthly Notices of the Royal Astronomical Society, 175, 29P, doi: 10.1093/mnras/175.1.29P

Mitsuda, K., Bautz, M., Inoue, H., et al. 2007, Publications of the Astronomical Society of Japan, 59, S1, doi: 10.1093/pasj/59.sp1.S1

Mo, H. J., Mao, S., & White, S. D. M. 1998, Monthly Notices of the Royal Astronomical Society, 295, 319, doi: 10.1046/j.1365-8711.1998.01227.x

Mok, A., Balogh, M. L., McGee, S. L., et al. 2013, Monthly Notices of the Royal Astronomical Society, 431, 1090, doi: 10.1093/mnras/stt251

Molendi, S., Eckert, D., De Grandi, S., et al. 2016, A&A, 586, A32, doi: 10.1051/0004-6361/201527356

Moll, R., Schindler, S., Domainko, W., et al. 2007, A&A, 463, 513, doi: 10.1051/0004-6361:20066386

Morgan, W. W., Kayser, S., & White, R. A. 1975, Astrophys. J., 199, 545, doi: 10.1086/153721

Mori, M., Ferrara, A., & Madau, P. 2002, ApJ, 571, 40, doi: 10.1086/339913

Mota, D. F. 2004, A&A, 421, 71, doi: 10.1051/0004-6361:20041090

Muñoz-Echeverría, M., Macías-Pérez, J. F., Pratt, G. W., et al. 2024, A&A, 682, A147, doi: 10.1051/0004-6361/202347584

Mulchaey, J. S. 2000, Annu. Rev. Astron. Astrophys., 38, 289, doi: 10.1146/annurev.astro.38.1.289

Mulchaey, J. S., Colbert, E., Wilson, A. S., Mushotzky, R. F., & Weaver, K. A. 1993a, Astrophys. J., 414, 144, doi: 10.1086/173063

Mulchaey, J. S., Davis, D. S., Mushotzky, R. F., & Burstein, D. 1993b, Astrophys. J., 404, L9, doi: 10.1086/186731

—. 1996, Astrophys. J., 456, 80, doi: 10.1086/176629

Mulchaey, J. S., & Zabludoff, A. I. 1998, ApJ, 496, 73, doi: 10.1086/305356

Muratov, A. L., Kereš, D., Faucher-Giguère, C.-A., et al. 2015, Monthly Notices of the Royal Astronomical Society, 454, 2691, doi: 10.1093/mnras/stv2126

Murray, N., Quataert, E., & Thompson, T. A. 2005, ApJ, 618, 569, doi: 10.1086/426067

—. 2009, ApJ, 709, 191, doi: 10.1088/0004-637X/709/1/191

Mushotzky, R., Aird, J., Barger, A. J., et al. 2019, Bull. AAS, 51

Mushotzky, R. F., Holt, S. S., Boldt, E. A., Serlemitsos, P. J., & Smith, B. W. 1981, Astrophys. J., 244, L47, doi: 10.1086/183477

Naab, T., & Ostriker, J. P. 2017, Annu. Rev. Astron. Astrophys., 55, 59, doi: 10.1146/annurev-astro-081913-040019

Nagai, D., Kravtsov, A. V., & Vikhlinin, A. 2007, ApJ, 668, 1, doi: 10.1086/521328

Nelson, D., Pillepich, A., Ayromlou, M., et al. 2024, Astron. Astrophys., 686, A157, doi: 10.1051/0004-6361/202348608

Nelson, D., Pillepich, A., Springel, V., et al. 2019, Monthly Notices of the Royal Astronomical Society, 490, 3234, doi: 10.1093/mnras/stz2306

Nelson, K., Lau, E. T., & Nagai, D. 2014, ApJ, 792, 25, doi: 10.1088/0004-637X/792/1/25

Nipoti, C. 2017, Monthly Notices of the Royal Astronomical Society, 467, 661, doi: 10.1093/mnras/stx112

Nolthenius, R., & White, S. D. M. 1987, Monthly Notices of the Royal Astronomical Society, 225, 505, doi: 10.1093/mnras/225.3.505

Nomoto, K., Hashimoto, M., Tsujimoto, T., et al. 1997, Nuclear Physics A, 616, 79, doi: 10.1016/S0375-9474(97)00076-6

Nomoto, K., Kobayashi, C., & Tominaga, N. 2013, Annu. Rev. Astron. Astrophys., 51, 457, doi: 10.1146/annurev-astro-082812-140956

Nomoto, K., Tominaga, N., Umeda, H., Kobayashi, C., & Maeda, K. 2006, Nuclear Physics A, 777, 424, doi: 10.1016/j.nuclphysa.2006.05.008

Nozawa, T., Maeda, K., Kozasa, T., et al. 2011, ApJ, 736, 45, doi: 10.1088/0004-637X/736/1/45

Nugent, J. M., Dai, X., & Sun, M. 2020, ApJ, 899, 160, doi: 10.3847/1538-4357/aba691

Nusser, A., Silk, J., & Babul, A. 2006, Monthly Notices of the Royal Astronomical Society, 373, 739, doi: 10.1111/j.1365-2966.2006.11061.x

Ocvirk, P., Pichon, C., & Teyssier, R. 2008, Monthly Notices of the Royal Astronomical Society, 390, 1326, doi: 10.1111/j.1365-2966.2008.13763.x

Opik, E. 1922, Astrophys. J., 55, 406, doi: 10.1086/142680

Oppenheimer, B. D., Babul, A., Bahé, Y., Butsky, I. S., & McCarthy, I. G. 2021, Universe, 7, doi: 10.3390/universe7070209

Oppenheimer, B. D., & Davé, R. 2006, Monthly Notices of the Royal Astronomical Society, 373, 1265, doi: 10.1111/j.1365-2966.2006.10989.x

—. 2008, Monthly Notices of the Royal Astronomical Society, 387, 577, doi: 10.1111/j.1365-2966.2008.13280.x

—. 2009, Monthly Notices of the Royal Astronomical Society, 395, 1875, doi: 10.1111/j.1365-2966.2009.14676.x

Oppenheimer, B. D., Davé, R., & Finlator, K. 2009, Monthly Notices of the Royal Astronomical Society, 396, 729, doi: 10.1111/j.1365-2966.2009.14771.x

Ostriker, J. P., & Steinhardt, P. J. 1995, Nature, 377, 600, doi: 10.1038/377600a0

O'Sullivan, E., David, L. P., & Vrtilek, J. M. 2014, Monthly Notices of the Royal Astronomical Society, 437, 730, doi: 10.1093/mnras/stt1926

O'Sullivan, E., Giacintucci, S., David, L. P., Vrtilek, J. M., & Raychaudhury, S. 2011, Monthly Notices of the Royal Astronomical Society, 411, 1833, doi: 10.1111/j.1365-2966.2010.17812.x

O'Sullivan, E., Ponman, T. J., & Collins, R. S. 2003a, Monthly Notices of the Royal Astronomical Society, 340, 1375, doi: 10.1046/j.1365-8711.2003.06396.x

O'Sullivan, E., Schellenberger, G., Burke, D. J., et al. 2019, Monthly Notices of the Royal Astronomical Society, 488, 2925, doi: 10.1093/mnras/stz1711

O'Sullivan, E., Vrtilek, J. M., Harris, D. E., & Ponman, T. J. 2007, ApJ, 658, 299, doi: 10.1086/511778

O'Sullivan, E., Vrtilek, J. M., & Kempner, J. C. 2005a, ApJ, 624, L77, doi: 10.1086/430600

O'Sullivan, E., Vrtilek, J. M., Kempner, J. C., David, L. P., & Houck, J. C. 2005b, Monthly Notices of the Royal Astronomical Society, 357, 1134, doi: 10.1111/j.1365-2966.2005.08749.x

O'Sullivan, E., Vrtilek, J. M., Read, A. M., David, L. P., & Ponman, T. J. 2003b, Monthly Notices of the Royal Astronomical Society, 346, 525, doi: 10.1046/j.1365-2966.2003.07108.x

O'Sullivan, E., Giacintucci, S., Babul, A., et al. 2012, Monthly Notices of the Royal Astronomical Society, 424, 2971, doi: 10.1111/j.1365-2966.2012.21459.x

O'Sullivan, E., Ponman, T. J., Kolokythas, K., et al. 2017, Mon. Not. R. Astron. Soc., 472, 1482, doi: 10.1093/mnras/stx2078

Pace, F., Meyer, S., & Bartelmann, M. 2017, J. Cosmol. Astropart. Phys., 2017, 040, doi: 10.1088/1475-7516/2017/10/040

Padawer-Blatt, A., Shao, Z., Hough, R. T., et al. 2025, Universe, 11, 47, doi: 10.3390/universe11020047

Panagoulia, E. K., Sanders, J. S., & Fabian, A. C. 2015, Mon. Not. R. Astron. Soc., 447, 417, doi: 10.1093/mnras/stu2469

Pandya, V., Fielding, D. B., Bryan, G. L., et al. 2023, Astrophys. J., 956, 118, doi: 10.3847/1538-4357/acf3ea

Pearce, F. A., Kay, S. T., Barnes, D. J., Bahé, Y. M., & Bower, R. G. 2021, Mon. Not. R. Astron. Soc., 507, 1606, doi: 10.1093/mnras/stab2194

Pearson, R. J., Ponman, T. J., Norberg, P., et al. 2017, Monthly Notices of the Royal Astronomical Society, 469, 3489, doi: 10.1093/mnras/stx1081

Peeples, M., Behroozi, P., Bordoloi, R., et al. 2019, Bull. AAS, 51

Percival, W. J. 2005, A&A, 443, 819, doi: 10.1051/0004-6361:20053637

Perna, M., Lanzuisi, G., Brusa, M., Cresci, G., & Mignoli, M. 2017a, A&A, 606, A96, doi: 10.1051/0004-6361/201730819

Perna, M., Lanzuisi, G., Brusa, M., Mignoli, M., & Cresci, G. 2017b, A&A, 603, A99, doi: 10.1051/0004-6361/201630369

Perrotta, S., Coil, A. L., Rupke, D. S. N., et al. 2023, ApJ, 949, 9, doi: 10.3847/1538-4357/acc660

Pillepich, A., Nelson, D., Truong, N., et al. 2021, Monthly Notices of the Royal Astronomical Society, 508, 4667, doi: 10.1093/mnras/stab2779

Pillepich, A., Nelson, D., Hernquist, L., et al. 2018, Mon. Not. R. Astron. Soc., 475, 648, doi: 10.1093/mnras/stx3112

Piontek, F., & Steinmetz, M. 2011, Mon. Not. R. Astron. Soc., 410, 2625, doi: 10.1111/j.1365-2966.2010.17637.x

Planck Collaboration, Aghanim, N., Akrami, Y., et al. 2020, Astron. Astrophys., 641, A6, doi: 10.1051/0004-6361/201833910

Planelles, S., Borgani, S., Fabjan, D., et al. 2014, Monthly Notices of the Royal Astronomical Society, 438, 195, doi: 10.1093/mnras/stt2141

Pokhrel, R., Gutermuth, R. A., Krumholz, M. R., et al. 2021, ApJL, 912, L19, doi: 10.3847/2041-8213/abf564

Ponman, T. J., & Bertram, D. 1993, Nature, 363, 51, doi: 10.1038/363051a0

Ponman, T. J., Bourner, P. D. J., & Ebeling, H. 1996a, X-Ray Properties of Compact Galaxy Groups., 357–360

Ponman, T. J., Bourner, P. D. J., Ebeling, H., & Böhringer, H. 1996b, Mon. Not. R. Astron. Soc., 283, 690, doi: 10.1093/mnras/283.2.690

Ponman, T. J., Sanderson, A. J. R., & Finoguenov, A. 2003, Mon. Not. R. Astron. Soc., 343, 331, doi: 10.1046/j.1365-8711.2003.06677.x

Pontzen, A., Roškar, R., Stinson, G., & Woods, R. 2013, Astrophys. Source Code Libr., ascl:1305.002

Power, C., Navarro, J. F., Jenkins, A., et al. 2003, Monthly Notices of the Royal Astronomical Society, 338, 14, doi: 10.1046/j.1365-8711.2003.05925.x

Prasad, D., Sharma, P., & Babul, A. 2015, Astrophys. J., 811, 108, doi: 10.1088/0004-637X/811/2/108

—. 2017, Mon. Not. R. Astron. Soc., 471, 1531, doi: 10.1093/mnras/stx1698

—. 2018, Astrophys. J., 863, 62, doi: 10.3847/1538-4357/aacce8

Pratt, G. W., & Arnaud, M. 2002, A&A, 394, 375, doi: 10.1051/0004-6361:20021032

Pratt, G. W., Croston, J. H., Arnaud, M., & Böhringer, H. 2009, A&A, 498, 361, doi: 10.1051/0004-6361/200810994

Press, W. H., & Schechter, P. 1974, Astrophys. J., 187, 425, doi: 10.1086/152650

Price, R., Duric, N., Burns, J. O., & Newberry, M. V. 1991, Astron. J., 102, 14, doi: 10.1086/115854

Rafferty, D. A., Bîrzan, L., Nulsen, P. E. J., et al. 2013, Monthly Notices of the Royal Astronomical Society, 428, 58, doi: 10.1093/mnras/sts007

Ragone-Figueroa, C., Granato, G. L., Borgani, S., et al. 2020, Monthly Notices of the Royal Astronomical Society, 495, 2436, doi: 10.1093/mnras/staa1389

Ragone-Figueroa, C., Granato, G. L., Ferraro, M. E., et al. 2018, Monthly Notices of the Royal Astronomical Society, 479, 1125, doi: 10.1093/mnras/sty1639

Ramella, M., Geller, M. J., Huchra, J. P., & Thorstensen, J. R. 1995a, Astron. J., 109, 1458, doi: 10.1086/117375

—. 1995b, Astron. J., 109, 1469, doi: 10.1086/117376

Randall, S. W., Nulsen, P. E. J., Jones, C., et al. 2015, ApJ, 805, 112, doi: 10.1088/0004-637X/805/2/112

Rasia, E., Lau, E. T., Borgani, S., et al. 2014, ApJ, 791, 96, doi: 10.1088/0004-637X/791/2/96

Rasia, E., Borgani, S., Murante, G., et al. 2015, Astrophys. J., 813, L17, doi: 10.1088/2041-8205/813/1/L17

Rasmussen, J., & Ponman, T. J. 2007, Mon. Not. R. Astron. Soc., 380, 1554, doi: 10.1111/J.1365-2966.2007.12191.X

—. 2009, Mon. Not. R. Astron. Soc., 399, 239, doi: 10.1111/J.1365-2966.2009.15244.X/2/MNRAS0399-0239-F20.JPEG

Rees, M. J., & Ostriker, J. P. 1977, Monthly Notices of the Royal Astronomical Society, 179, 541, doi: 10.1093/mnras/179.4.541

Reiprich, T. H., Basu, K., Ettori, S., et al. 2013, Space Sci Rev, 177, 195, doi: 10.1007/s11214-013-9983-8

Remus, R.-S., Dolag, K., & Hoffmann, T. L. 2017, Galaxies, 5, 49, doi: 10.3390/galaxies5030049

Rennehan, D. 2021, Mon. Not. R. Astron. Soc., 506, 2836, doi: 10.1093/MNRAS/STAB1813

Rennehan, D., Babul, A., Hopkins, P. F., Davé, R., & Moa, B. 2019, Mon. Not. R. Astron. Soc., 483, 3810, doi: 10.1093/mnras/sty3376

Rennehan, D., Babul, A., Moa, B., & Davé, R. 2024, Monthly Notices of the Royal Astronomical Society, 532, 4793, doi: 10.1093/mnras/stae1785

Renzini, A. 1997, ApJ, 488, 35, doi: 10.1086/304696

Reynolds, C. S., Balbus, S. A., & Schekochihin, A. A. 2015, ApJ, 815, 41, doi: 10.1088/0004-637X/815/1/41

Reynolds, C. S., Kara, E. A., Mushotzky, R. F., et al. 2023, in UV X-Ray Gamma-Ray Space Instrum. Astron. XXIII, Vol. 12678 (SPIE), 421–442, doi: 10.1117/12.2677468

Robson, D., & Davé, R. 2020, Mon. Not. R. Astron. Soc., 498, 3061, doi: 10.1093/mnras/staa2394

—. 2021, arXiv, arXiv:2107.01206, doi: 10.48550/ARXIV.2107.01206

Roediger, E., Brüggen, M., Rebusco, P., Böhringer, H., & Churazov, E. 2007, Monthly Notices of the Royal Astronomical Society, 375, 15, doi: 10.1111/j.1365-2966.2006.11300.x

Roediger, E., Brüggen, M., Simionescu, A., et al. 2011, Monthly Notices of the Royal Astronomical Society, 413, 2057, doi: 10.1111/j.1365-2966.2011.18279.x

Roediger, E., Kraft, R. P., Forman, W. R., Nulsen, P. E. J., & Churazov, E. 2013, ApJ, 764, 60, doi: 10.1088/0004-637X/764/1/60

Roediger, E., Vaezzadeh, I., & Nulsen, P. 2024, Mon. Not. R. Astron. Soc., 529, 563, doi: 10.1093/mnras/stae493

Rohr, E., Pillepich, A., Nelson, D., et al. 2025, Monthly Notices of the Royal Astronomical Society, 536, 1226, doi: 10.1093/mnras/stae2536

Romano, D., Calura, F., D'Ercole, A., & Few, C. G. 2019, Astron. Astrophys., 630, A140, doi: 10.1051/0004-6361/201935328

Rossetti, M., Eckert, D., Gastaldello, F., et al. 2024, A&A, 686, A68, doi: 10.1051/0004-6361/202348853

Rupke, D. S., Veilleux, S., & Sanders, D. B. 2005, ApJS, 160, 115, doi: 10.1086/432889

Ruszkowski, M., & Pfrommer, C. 2023, Astron Astrophys Rev, 31, 4, doi: 10.1007/s00159-023-00149-2

Saeedzadeh, V., Jung, S. L., Rennehan, D., et al. 2023, Monthly Notices of the Royal Astronomical Society, 525, 5677, doi: 10.1093/mnras/stad2637

Salehirad, S., Reines, A. E., & Molina, M. 2025, ApJ, 979, 26, doi: 10.3847/1538-4357/ad9a57

Sanderson, A. J. R., O'Sullivan, E., Ponman, T. J., et al. 2013, Monthly Notices of the Royal Astronomical Society, 429, 3288, doi: 10.1093/mnras/sts586

Saracco, P., & Ciliegi, P. 1995, Astron. Astrophys., 301, 348, doi: 10.48550/arXiv.astro-ph/9412040

Sarazin, C. L. 1986, Rev. Mod. Phys., 58, 1, doi: 10.1103/RevModPhys.58.1

Sarkar, A., Su, Y., Randall, S., et al. 2021, Mon. Not. R. Astron. Soc., 501, 3767, doi: 10.1093/MNRAS/STAA3858

Sarkar, A., Su, Y., Truong, N., et al. 2022, Mon. Not. R. Astron. Soc., 516, 3068, doi: 10.1093/mnras/stac2416

Sasaki, T., Matsushita, K., & Sato, K. 2014, Astrophys. J., 781, 36, doi: 10.1088/0004-637X/781/1/36

Sato, K., Kawaharada, M., Nakazawa, K., et al. 2010, Publications of the Astronomical Society of Japan, 62, 1445, doi: 10.1093/pasj/62.6.1445

Sato, K., Matsushita, K., & Gastaldello, F. 2009a, Publications of the Astronomical Society of Japan, 61, S365, doi: 10.1093/pasj/61.sp1.S365

Sato, K., Matsushita, K., Ishisaki, Y., et al. 2009b, Publications of the Astronomical Society of Japan, 61, S353, doi: 10.1093/pasj/61.sp1.S353

Scannapieco, C., Tissera, P. B., White, S. D. M., & Springel, V. 2005, Monthly Notices of the Royal Astronomical Society, 364, 552, doi: 10.1111/j.1365-2966.2005.09574.x

Schaller, M., Borrow, J., Draper, P. W., et al. 2024, Monthly Notices of the Royal Astronomical Society, 530, 2378, doi: 10.1093/mnras/stae922

Schaye, J., Crain, R. A., Bower, R. G., et al. 2015, Mon. Not. R. Astron. Soc., 446, 521, doi: 10.1093/mnras/stu2058

Schellenberger, G., Reiprich, T. H., Lovisari, L., Nevalainen, J., & David, L. 2015, A&A, 575, A30, doi: 10.1051/0004-6361/201424085

Schindler, S., & Diaferio, A. 2008, Space Sci Rev, 134, 363, doi: 10.1007/s11214-008-9321-8

Schure, K. M., Kosenko, D., Kaastra, J. S., Keppens, R., & Vink, J. 2009, A&A, 508, 751, doi: 10.1051/0004-6361/200912495

Schwartz, D. A., Schwarz, J., & Tucker, W. 1980, Astrophys. J., 238, L59, doi: 10.1086/183258

Schwartz, D. A., Vikhlinin, A., Tananbaum, H., et al. 2019, in UV X-Ray Gamma-Ray Space Instrum. Astron. XXI, Vol. 11118 (SPIE), 148–159, doi: 10.1117/12.2533637

Sell, P. H., Tremonti, C. A., Hickox, R. C., et al. 2014, Monthly Notices of the Royal Astronomical Society, 441, 3417, doi: 10.1093/mnras/stu636

Sembolini, F., Yepes, G., De Petris, M., et al. 2013, Monthly Notices of the Royal Astronomical Society, 429, 323, doi: 10.1093/mnras/sts339

Serlemitsos, P. J., Smith, B. W., Boldt, E. A., Holt, S. S., & Swank, J. H. 1977, Astrophys. J., 211, L63, doi: 10.1086/182342

Shapiro, P. R., Giroux, M. L., & Babul, A. 1994, Astrophys. J., 427, 25, doi: 10.1086/174120

Sharma, P., Chandran, B. D. G., Quataert, E., & Parrish, I. J. 2009, AIP Conference Proceedings, 1201, 363, doi: 10.1063/1.3293077

Sharma, P., McCourt, M., Quataert, E., & Parrish, I. J. 2012, Monthly Notices of the Royal Astronomical Society, 420, 3174, doi: 10.1111/j.1365-2966.2011.20246.x

Sheardown, A., Fish, T. M., Roediger, E., et al. 2019, ApJ, 874, 112, doi: 10.3847/1538-4357/ab0c06

Short, C. J., Thomas, P. A., & Young, O. E. 2013, Monthly Notices of the Royal Astronomical Society, 428, 1225, doi: 10.1093/mnras/sts107

Sijacki, D., & Springel, V. 2006a, Monthly Notices of the Royal Astronomical Society, 366, 397, doi: 10.1111/j.1365-2966.2005.09860.x

—. 2006b, Monthly Notices of the Royal Astronomical Society, 371, 1025, doi: 10.1111/j.1365-2966.2006.10752.x

Silk, J. 1977a, Astrophys. J., 211, 638, doi: 10.1086/154972

—. 1977b, Astrophys. J., 214, 152, doi: 10.1086/155240

—. 1977c, Astrophys. J., 214, 718, doi: 10.1086/155301

Simionescu, A., Werner, N., Böhringer, H., et al. 2009, A&A, 493, 409, doi: 10.1051/0004-6361:200810225

Simionescu, A., Werner, N., Finoguenov, A., Böhringer, H., & Brüggen, M. 2008, A&A, 482, 97, doi: 10.1051/0004-6361:20078749

Simionescu, A., Werner, N., Forman, W. R., et al. 2010, Monthly Notices of the Royal Astronomical Society, 405, 91, doi: 10.1111/j.1365-2966.2010.16450.x

Simionescu, A., Werner, N., Mantz, A., Allen, S. W., & Urban, O. 2017, Monthly Notices of the Royal Astronomical Society, 469, 1476, doi: 10.1093/mnras/stx919

Simionescu, A., Nakashima, S., Yamaguchi, H., et al. 2019, Monthly Notices of the Royal Astronomical Society, 483, 1701, doi: 10.1093/mnras/sty3220

Sivanandam, S., Zabludoff, A. I., Zaritsky, D., Gonzalez, A. H., & Kelson, D. D. 2009, ApJ, 691, 1787, doi: 10.1088/0004-637X/691/2/1787

Slipher, V. M. 1913, Lowell Obs. Bull., 2, 56

—. 1915, Pop. Astron., 23, 21

Smith, B., Sigurdsson, S., & Abel, T. 2008, Mon. Not. R. Astron. Soc., 385, 1443, doi: 10.1111/j.1365-2966.2008.12922.x

Smith, B. D., Turk, M. J., Sigurdsson, S., O'Shea, B. W., & Norman, M. L. 2009, Astrophys. J., 691, 441, doi: 10.1088/0004-637X/691/1/441

Smith, B. D., Bryan, G. L., Glover, S. C. O., et al. 2017, Monthly Notices of the Royal Astronomical Society, 466, 2217, doi: 10.1093/mnras/stw3291

Snowden, S. L., Mushotzky, R. F., Kuntz, K. D., & Davis, D. S. 2008, Astron. Astrophys., 478, 615, doi: 10.1051/0004-6361:20077930

Sokołowska, A., Babul, A., Mayer, L., Shen, S., & Madau, P. 2018, ApJ, 867, 73, doi: 10.3847/1538-4357/aae43a

Sokołowska, A., Capelo, P. R., Fall, S. M., et al. 2017, ApJ, 835, 289, doi: 10.3847/1538-4357/835/2/289

Sokołowska, A., Mayer, L., Babul, A., Madau, P., & Shen, S. 2016, ApJ, 819, 21, doi: 10.3847/0004-637X/819/1/21

Somerville, R. S., & Davé, R. 2015, Annu. Rev. Astron. Astrophys., 53, 51, doi: 10.1146/annurev-astro-082812-140951

Sotira, S., Vazza, F., & Brighenti, F. 2024, On the Impact of AGN Feedback Modes onto the Turbulent Properties of the Multiphase ICM, arXiv, doi: 10.48550/arXiv.2410.07314

Springel, V. 2005, Mon. Not. R. Astron. Soc., 364, 1105, doi: 10.1111/j.1365-2966.2005.09655.x

Springel, V., di Matteo, T., & Hernquist, L. 2005, Monthly Notices of the Royal Astronomical Society, 361, 776, doi: 10.1111/j.1365-2966.2005.09238.x

Springel, V., Pakmor, R., Pillepich, A., et al. 2018, Monthly Notices of the Royal Astronomical Society, 475, 676, doi: 10.1093/mnras/stx3304

Stewart, K. R. 2017, in Gas Accretion onto Galaxies, ed. A. Fox & R. Davé (Cham: Springer International Publishing), 249–270, doi: 10.1007/978-3-319-52512-9_11

Stinson, G. S., Brook, C., Macciò, A. V., et al. 2013, Mon. Not. R. Astron. Soc., 428, 129, doi: 10.1093/mnras/sts028

Strüder, L., Briel, U., Dennerl, K., et al. 2001, Astron. Astrophys., 365, L18, doi: 10.1051/0004-6361:20000066

Sturm, E., González-Alfonso, E., Veilleux, S., et al. 2011, ApJL, 733, L16, doi: 10.1088/2041-8205/733/1/L16

Su, K.-Y., Hopkins, P. F., Hayward, C. C., et al. 2019a, Monthly Notices of the Royal Astronomical Society, 487, 4393, doi: 10.1093/mnras/stz1494

Su, Y., Buote, D., Gastaldello, F., & Brighenti, F. 2015, Astrophys. J., 805, 104, doi: 10.1088/0004-637X/805/2/104

Su, Y., White, R. E., & Miller, E. D. 2013, Astrophys. J., 775, 89, doi: 10.1088/0004-637X/775/2/89

Su, Y., Kraft, R. P., Roediger, E., et al. 2017, ApJ, 834, 74, doi: 10.3847/1538-4357/834/1/74

Su, Y., Kraft, R. P., Nulsen, P. E. J., et al. 2019b, AJ, 158, 6, doi: 10.3847/1538-3881/ab1d51

Sun, M. 2012, New J. Phys., 14, 045004, doi: 10.1088/1367-2630/14/4/045004

Sun, M., Voit, G. M., Donahue, M., et al. 2009, Astrophys. J., 693, 1142, doi: 10.1088/0004-637X/693/2/1142

Sun, X., Wang, X., Ma, X., et al. 2024, The Physical Origin of Positive Metallicity Radial Gradients in High-Redshift Galaxies: Insights from the FIRE-2 Cosmological Hydrodynamic Simulations, arXiv, doi: 10.48550/arXiv.2409.09290

Sunyaev, R. A., & Zeldovich, Ya. B. 1970, Astrophys Space Sci, 7, 20, doi: 10.1007/BF00653472

Takahashi, T., Mitsuda, K., Kelley, R., et al. 2014, ASTRO-H White Paper - Introduction, arXiv, doi: 10.48550/arXiv.1412.2351

Takahashi, T., Kokubun, M., Mitsuda, K., et al. 2016, in Space Telesc. Instrum. 2016 Ultrav. Gamma Ray, Vol. 9905 (SPIE), 212–228, doi: 10.1117/12.2232379

Talbot, Jr., R. J., & Arnett, W. D. 1971, Astrophys. J., 170, 409, doi: 10.1086/151228

Tanaka, Y., Inoue, H., & Holt, S. S. 1994, Publ. Astron. Soc. Jpn., 46, L37

Tashiro, M. S. 2022, Int. J. Mod. Phys. D, 31, 2230001, doi: 10.1142/S0218271822300014

Taylor, P., & Kobayashi, C. 2014, Mon. Not. R. Astron. Soc., 442, 2751, doi: 10.1093/mnras/stu983

—. 2015, Mon. Not. R. Astron. Soc., 452, L59, doi: 10.1093/mnrasl/slv087

Team, X. S. 2020, Science with the X-ray Imaging and Spectroscopy Mission (XRISM), arXiv, doi: 10.48550/arXiv.2003.04962

Thölken, S., Lovisari, L., Reiprich, T. H., & Hasenbusch, J. 2016, Astron. Astrophys., 592, A37, doi: 10.1051/0004-6361/201527608

Tinsley, B. M. 2022, doi: 10.48550/arXiv.2203.02041

Tittley, E. R., & Henriksen, M. 2005, ApJ, 618, 227, doi: 10.1086/425952

Tomczak, A. R., Quadri, R. F., Tran, K. V. H., et al. 2014, Astrophys. J., 783, 85, doi: 10.1088/0004-637X/783/2/85

Tornatore, L., Borgani, S., Dolag, K., & Matteucci, F. 2007, Monthly Notices of the Royal Astronomical Society, 382, 1050, doi: 10.1111/j.1365-2966.2007.12070.x

Torres-Papaqui, J. P., Coziol, R., Robleto-Orús, A. C., Cutiva-Alvarez, K. A., & Roco-Avilez, P. 2024, AJ, 168, 37, doi: 10.3847/1538-3881/ad43db

Tremmel, M., Karcher, M., Governato, F., et al. 2017, Monthly Notices of the Royal Astronomical Society, 470, 1121, doi: 10.1093/mnras/stx1160

Trinchieri, G., Fabbiano, G., & Kim, D. W. 1997, Astron. Astrophys., 318, 361

Trümper, J. 1982, Advances in Space Research, 2, 241, doi: 10.1016/0273-1177(82)90070-9

Truong, N., Pillepich, A., Nelson, D., et al. 2024, A&A, 686, A200, doi: 10.1051/0004-6361/202348562

Truong, N., Rasia, E., Biffi, V., et al. 2019, Monthly Notices of the Royal Astronomical Society, 484, 2896, doi: 10.1093/mnras/stz161

Tully, R. B. 1987, Astrophys. J., 321, 280, doi: 10.1086/165629

Tumlinson, J., Peeples, M. S., & Werk, J. K. 2017, doi: 10.1146/annurev-astro-091916

Tuominen, T., Nevalainen, J., Heinämäki, P., et al. 2023, A&A, 671, A103, doi: 10.1051/0004-6361/202244508

Turner, D. J., Giles, P. A., Romer, A. K., et al. 2025, Monthly Notices of the Royal Astronomical Society, 537, 1404, doi: 10.1093/mnras/staf007

Turner, M. J. L., Abbey, A., Arnaud, M., et al. 2001, Astron. Astrophys., 365, L27, doi: 10.1051/0004-6361:20000087

Turner, M. L., Schaye, J., Steidel, C. C., Rudie, G. C., & Strom, A. L. 2014, Monthly Notices of the Royal Astronomical Society, 445, 794, doi: 10.1093/mnras/stu1801

Urban, O., Werner, N., Allen, S. W., Simionescu, A., & Mantz, A. 2017, Mon. Not. R. Astron. Soc., 470, 4583, doi: 10.1093/MNRAS/STX1542

Urban, O., Werner, N., Simionescu, A., Allen, S. W., & Böhringer, H. 2011, Monthly Notices of the Royal Astronomical Society, 414, 2101, doi: 10.1111/j.1365-2966.2011.18526.x

van de Voort, F., Schaye, J., Booth, C. M., Haas, M. R., & Dalla Vecchia, C. 2011, Monthly Notices of the Royal Astronomical Society, 414, 2458, doi: 10.1111/j.1365-2966.2011.18565.x

van Uitert, E., Cacciato, M., Hoekstra, H., et al. 2016, Monthly Notices of the Royal Astronomical Society, 459, 3251, doi: 10.1093/mnras/stw747

Vayner, A., Díaz-Santos, T., Eisenhardt, P. R. M., et al. 2024, Powerful Nuclear Outflows and Circumgalactic Medium Shocks Driven by the Most Luminous Quasar in the Universe, arXiv, doi: 10.48550/arXiv.2412.02862

Veilleux, S., Meléndez, M., Sturm, E., et al. 2013, ApJ, 776, 27, doi: 10.1088/0004-637X/776/1/27

Vikhlinin, A. 2006, ApJ, 640, 710, doi: 10.1086/500121

Villar Martín, M., Emonts, B., Humphrey, A., Cabrera Lavers, A., & Binette, L. 2014, Monthly Notices of the Royal Astronomical Society, 440, 3202, doi: 10.1093/mnras/stu448

Virtanen, P., Gommers, R., Oliphant, T. E., et al. 2020, Nat Methods, 17, 261, doi: 10.1038/s41592-019-0686-2

Vogelsberger, M., Marinacci, F., Torrey, P., & Puchwein, E. 2020, Nat Rev Phys, 2, 42, doi: 10.1038/s42254-019-0127-2

Vogelsberger, M., McKinnon, R., O'Neil, S., et al. 2019, Mon. Not. R. Astron. Soc., 487, 4870, doi: 10.1093/mnras/stz1644

Vogelsberger, M., Genel, S., Springel, V., et al. 2014, Mon. Not. R. Astron. Soc., 444, 1518, doi: 10.1093/mnras/stu1536

Vogelsberger, M., Marinacci, F., Torrey, P., et al. 2018, Monthly Notices of the Royal Astronomical Society, 474, 2073, doi: 10.1093/mnras/stx2955

Voges, W. 1992, in Digit. Opt. Sky Surv., ed. H. T. MacGillivray & E. B. Thomson (Dordrecht: Springer Netherlands), 453–463, doi: 10.1007/978-94-011-2472-0_57

Voit, G. M. 2005, Advances in Space Research, 36, 701, doi: 10.1016/j.asr.2005.02.042

—. 2018, ApJ, 868, 102, doi: 10.3847/1538-4357/aae8e2

Wechsler, R. H., & Tinker, J. L. 2018, Annu. Rev. Astron. Astrophys., 56, 435, doi: 10.1146/annurev-astro-081817-051756

Weiner, B. J., Coil, A. L., Prochaska, J. X., et al. 2009, ApJ, 692, 187, doi: 10.1088/0004-637X/692/1/187

Weisskopf, M. C., Tananbaum, H. D., Speybroeck, L. P. V., & O'Dell, S. L. 2000, in X-Ray Opt. Instrum. Missions III, Vol. 4012 (SPIE), 2–16, doi: 10.1117/12.391545

Weldon, A., Reddy, N. A., Coil, A. L., et al. 2024, Monthly Notices of the Royal Astronomical Society, 531, 4560, doi: 10.1093/mnras/stae1428

Werner, N., Böhringer, H., Kaastra, J. S., et al. 2006a, A&A, 459, 353, doi: 10.1051/0004-6361:20065678

Werner, N., de Plaa, J., Kaastra, J. S., et al. 2006b, A&A, 449, 475, doi: 10.1051/0004-6361:20053868

Werner, N., Durret, F., Ohashi, T., Schindler, S., & Wiersma, R. P. C. 2008, Space Sci Rev, 134, 337, doi: 10.1007/s11214-008-9320-9

Werner, N., & Mernier, F. 2020, Rev. Front. Mod. Astrophys., 279, doi: 10.1007/978-3-030-38509-5_10

Werner, N., Urban, O., Simionescu, A., & Allen, S. W. 2013, Nature, 502, 656, doi: 10.1038/nature12646

White, S. D. M., & Frenk, C. S. 1991, Astrophys. J., 379, 52, doi: 10.1086/170483

White, S. D. M., Navarro, J. F., Evrard, A. E., & Frenk, C. S. 1993, Nature, 366, 429, doi: 10.1038/366429a0

White, S. D. M., & Rees, M. J. 1978, Monthly Notices of the Royal Astronomical Society, 183, 341, doi: 10.1093/mnras/183.3.341

Wiersma, R. P. C., Schaye, J., & Smith, B. D. 2009a, Monthly Notices of the Royal Astronomical Society, 393, 99, doi: 10.1111/j.1365-2966.2008.14191.x

Wiersma, R. P. C., Schaye, J., Theuns, T., Dalla Vecchia, C., & Tornatore, L. 2009b, Monthly Notices of the Royal Astronomical Society, 399, 574, doi: 10.1111/j.1365-2966.2009.15331.x

Wijers, N. A., Faucher-Giguère, C.-A., Stern, J., Byrne, L., & Sultan, I. 2024, ApJ, 973, 99, doi: 10.3847/1538-4357/ad63a0

Williams, C. C., Giavalisco, M., Lee, B., et al. 2015, ApJ, 800, 21, doi: 10.1088/0004-637X/800/1/21

Winsberg, E. 2010, Science in the Age of Computer Simulation (Chicago, IL: University of Chicago Press)

Wolf, M. 1901, Astron. Nachrichten, 155, 127, doi: 10.1002/asna.19011550608

—. 1902, Publ. Astrophys. Inst. Koenigstuhl-Heidelb., 1, 125

—. 1906, Astron. Nachrichten, 170, 211

Wong, K.-W., Irwin, J. A., Wik, D. R., et al. 2016, Astrophys. J., 829, 49, doi: 10.3847/0004-637X/829/1/49

Woosley, S. E., & Weaver, T. A. 1995, Astrophys. J. Suppl. Ser., 101, 181, doi: 10.1086/192237

Xu, X., Heckman, T., Yoshida, M., Henry, A., & Ohyama, Y. 2023, ApJ, 956, 142, doi: 10.3847/1538-4357/acfa71

Xue, Y.-J., Böhringer, H., & Matsushita, K. 2004, A&A, 420, 833, doi: 10.1051/0004-6361:20035760

Yates, R. M., Thomas, P. A., & Henriques, B. M. 2017, Mon. Not. R. Astron. Soc., 464, 3169, doi: 10.1093/MNRAS/STW2361

Yu, Q., & Tremaine, S. 2002, Monthly Notices of the Royal Astronomical Society, 335, 965, doi: 10.1046/j.1365-8711.2002.05532.x

Zeldovich, Ya. B., & Sunyaev, R. A. 1969, Astrophys Space Sci, 4, 301, doi: 10.1007/BF00661821

Zhan, H., Fang, L.-Z., & Burstein, D. 2003, ApJ, 592, L1, doi: 10.1086/377442

Zhuravleva, I., Churazov, E., Schekochihin, A. A., et al. 2014, Nature, 515, 85, doi: 10.1038/nature13830

ZuHone, J. A. 2011, ApJ, 728, 54, doi: 10.1088/0004-637X/728/1/54

ZuHone, J. A., Kunz, M. W., Markevitch, M., Stone, J. M., & Biffi, V. 2014, ApJ, 798, 90, doi: 10.1088/0004-637X/798/2/90

ZuHone, J. A., Markevitch, M., & Lee, D. 2011, ApJ, 743, 16, doi: 10.1088/0004-637X/743/1/16

ZuHone, J. A., Markevitch, M., Ruszkowski, M., & Lee, D. 2012, ApJ, 762, 69, doi: 10.1088/0004-637X/762/2/69

ZuHone, J. A., Markevitch, M., & Zhuravleva, I. 2016a, ApJ, 817, 110, doi: 10.3847/0004-637X/817/2/110

ZuHone, J. A., Miller, E. D., Simionescu, A., & Bautz, M. W. 2016b, ApJ, 821, 6, doi: 10.3847/0004-637X/821/1/6

ZuHone, J. A., & Roediger, E. 2016, J. Plasma Phys., 82, 535820301, doi: 10.1017/S0022377816000544

Appendix A

Additional Information

All codes used in this thesis are available upon request. The analyses were performed using the Python programming language (Python Software Foundation) and following packages: NumPy (Harris et al., 2020), Matplotlib (Hunter, 2007), Pynbody (Pontzen et al., 2013), SciPy (Virtanen et al., 2020), PyAtomDB (Foster et al., 2021), `XIGrM` (XIGrM documentation), and AHF (Knebe et al., 2008; Knollmann & Knebe, 2009). The particle snapshots and Ceasar halo and galaxy catalogues (Caesar Documentation) for SIMBA are publicly available on the SIMBA Simulation Repository, while those for SIMBA-C, as well as the AHF halo catalogues, are available upon request from Douglas Rennehan.